STRUCTURE IN RADIATIVE SHOCK EXPERIMENTS

by

Forrest W. Doss

A dissertation submitted in partial fulfillment
of the requirements for the degree of
Doctor of Philosophy
(Applied Physics)
in The University of Michigan
2011

Doctoral Committee:

Professor R. Paul Drake, Chair
Professor James Holloway
Professor Kenneth Powell
Professor Robert Krasny
Research Scientist Philip Hughes

To my family, who always believed me when I said that I would finish school someday.

TABLE OF CONTENTS

CHAPTER

LIST OF FIGURES

Figure

LIST OF TABLES

Table

LIST OF APPENDICES

Appendix

ABSTRACT

Structure in Radiative Shock Experiments

by

Forrest W. Doss

Chair: R. Paul Drake

The basic radiative shock experiment is a shock launched into a gas of high-atomic-number material (here, xenon) at high velocities (around 200 km/sec), which fulfills the conditions for radiative losses to collapse the post-shock material to high densities (over 20 times the initial gas density). The experiment has lateral dimensions of approximately six hundred microns and length dimensions of two to three millimeters.

Repeatable two- and three-dimensional structure was discovered in the experimental data. One form this took was that of radial boundary effects near the tube walls, extended approximately seventy microns into the system. The cause of this effect - low density wall material which is heated by radiation transport ahead of the shock, launching a new converging shock ahead of the main shock - is apparently unique to high-energy-density experiments. Another form of structure is the appearance of small-scale perturbations in the post-shock layer, modulating the shock and material interfaces and creating regions of enhanced and diminished areal density within the layer. This structure formation has been investigated as a variation of the Vishniac instability of decelerating shocks. This instability mirrors (if one uses

a suitably deformed reflector) effects believed to be present in astronomically scaled systems involving decelerating, diverging supernova remnants.

This thesis gathers data from Omega laser campaigns of July 17, 2007; July 10, 2008; October 23, 2008; July 21, 2009; and August 6, 2010. Each of these experimental campaigns has been undertaken to acquire additional information about the complex structure of the radiating discontinuity.

CHAPTER I

Introduction to Radiative Shocks and Radiative Shock Experiments

The gas-dynamic properties of plane shock waves in gases have been understood since the work of Rankine and Hugoniot in the late 1800s [72], and the properties of oblique shock waves since the work of Prandtl and Meyer in the early 1900s [67]. A shock arises in a system as a response either to supersonic motions within a fluid or to the exposure of a system to a large, impulsive release of energy. Their fundamental property is to increase both the pressure and density of gas which the shock encounters.

Much of the theoretical work of shocks in more complicated geometries and situations has utilized the method of seeking scale-invariant self-similar solutions. The profile of an expanding blast-wave was derived in the 1940s by Taylor and Sedov [89, 85]. Similar scale-invariant solutions for flows including diverging shock waves driven by cylindrical and spherical expanding pistons were found by Lighthill [63], while methods for solving shock waves converging down to a point or a line in spherical or cylindrical geometry were developed by Guderley [34].

Other work has been done to further our understanding of how the system changes when, in addition to the usual gas-dynamic variables, radiation or other means are allowed to transport energy across the shock front. The monograph by Zeldovich and Razier [96] discusses several forms of non-hydrodynamic energy transfer across shocks, including energy transport by heat conduction, radiation, or electric fields, as well as momentum transfer across the shock by viscosity. Radiation transport in particular tends to lead to a variety of regimes and qualitative changes to the shock structure, as well as exhibiting dependence on other complicated properties of the fluid material, namely opacities. Solving radiation transport in the presence of finite but constant mean opacities tends to lead to integral transport equations. This has been undertaken in various regimes in a sequence by Clarke, Ferrari, and Onorato [18, 27, 17], as well as in the specific regime of the experiments in this thesis by McClarren *et al* [65]. Solutions assuming certain power-law dependencies in opacities and other parameters appear in the monograph by Mihalis and Mihalis [68]. The monograph by Drake[24] contains results specialized to conditions with very thin opacity either upstream of the shock or in both directions. Other work specializes in the even more extraordinary, relativistic case where the radiation transport carries not only substantial energy but also momentum across the shock boundary [14]. The radiating shock has also been investigated in the context of astrophysics [48, 49], where they appear in such structures as the Cygnus Loop, accretion flows associated with black holes, and supernovae. These investigations have all found that, in contrast to shocks without radiation, a strongly radiating shock can create very high compressions with low or nonexistent increases in temperature across the shock front, Section 1.2 below discusses how the energy balance across a radiative shock gives it this unusual property.

A third recurring theme in theoretical shock analysis has been the investigation into shock stability. Landau and Lifshitz remind us in *Fluid Dynamics* that “The flows that occur in Nature must not only obey the equations of fluid dynamics, but also be stable,” [60] as possible-but-unstable systems will break apart under little or no provocation by outside influences. Early results proved that plane shocks under ordinary gas-dynamic conditions are indeed strongly self-stabilizing [29, 95], tending to smooth and damp away any perturbations to their surface. However, under the various modifications to geometry or transport listed above, this is not always the case. Traditional work in the field has investigated the stability of the Taylor-Sedov blast wave solutions to instability and fragmentation, major results of which are attributable to Vishniac [92, 94]. Investigations in the case of converging shock geometries have dealt extensively with instabilities such as Rayleigh-Taylor and Richmeyer-Meshkov, and are important to the field of inertial confinement fusion [3]. Other investigations have also been carried out in the cases of added transport mechanisms, such as Bertschinger's considerations [9] of stability in the presence of radiative transfer. The major recurring mechanism for the instability of shocks near a material boundary is explored in Chapter III, and in Chapter VI is given a new viewpoint from within the context of the present body of experimental shock capabilities.

Experimentally, early shocks were often produced in laboratories using wind tunnels (producing regions of supersonic airflow), projectiles such as bullets (traveling themselves supersonically), or by using shock tubes, often driven by diaphragm release or by explosives [86] (delivering large amounts of energy into small volumes). Since the 1980s, Nd:glass laser amplification processes have been advanced to where high-power lasers may not only be used to drive shocks through the application of large amounts of energy to a target, but may also drive terrestrial shocks to the speeds and conditions necessary to explore the physics of radiative shocks [69, 28, 52, 91, 74, 75, 73]. Some details of relevant experiments have been recorded in Table 1.1. Often, these experiments are also performed in one of the non-planar geometries, testing both spherically and cylindrically divergent conditions. These techniques have produced radiative shocks in gases [15, 13], foams [50], and clusters [88]. The experiments have increased in scale and speed along with the laser facilities' increase in power, through facilities on the scale of the Nova [78] and Omega [12] lasers (see also Figure 1.1) to contemporary and future work appearing on the Z Machine [79] and National Ignition Facility [37]. Section 1.3 discusses how these high-energy drivers are able to create a radiative shock system.

Radiative shock experiments on the Omega laser diagnosed by radiography have several years of history before the present work. In particular, the present author inherited the experimental platform of previous students Amy Reighard and Carolyn Kuranz [77, 57], who explored many of the techniques which follow and performed a number of shock experiments between 2002 and 2005 using the core experimental methods outlined below in Sections 1.1 and 1.4. Furthermore, other experiments, among them those by current students Anthony Visco and Channing Huntington, have sought to produce radiative shocks in similar situations but diagnose different variables in the resulting system, including measurements of temperature and ionization, by analyzing spectra.

1.1 Experimental target overview

Figure 1.2(a) shows a CAD model of a typical experimental target. Much of what is shown is acrylic superstructure which serves both as scaffolding to mechanically support the target of interest and as shielding which prevents diagnostics from premature exposure. The vertical stalk tube is in the former category, and is used both to position the target in the chamber and as a fill line for xenon gas. The small stalk section attached to the left in the image is a reference feature used for alignment of the target within the chamber. The xenon gas fills the small yellow PI shock tube, in which the experiment takes place. The large conical acrylic structure and the gold wedges are used to prevent the x-ray diagnostics in the experiment from being exposed to the intense drive event, laser ablation of the thin beryllium disc inset into the acrylic.

The core of the experiment is shown in Figure 1.2(b). Stripped of the experimental

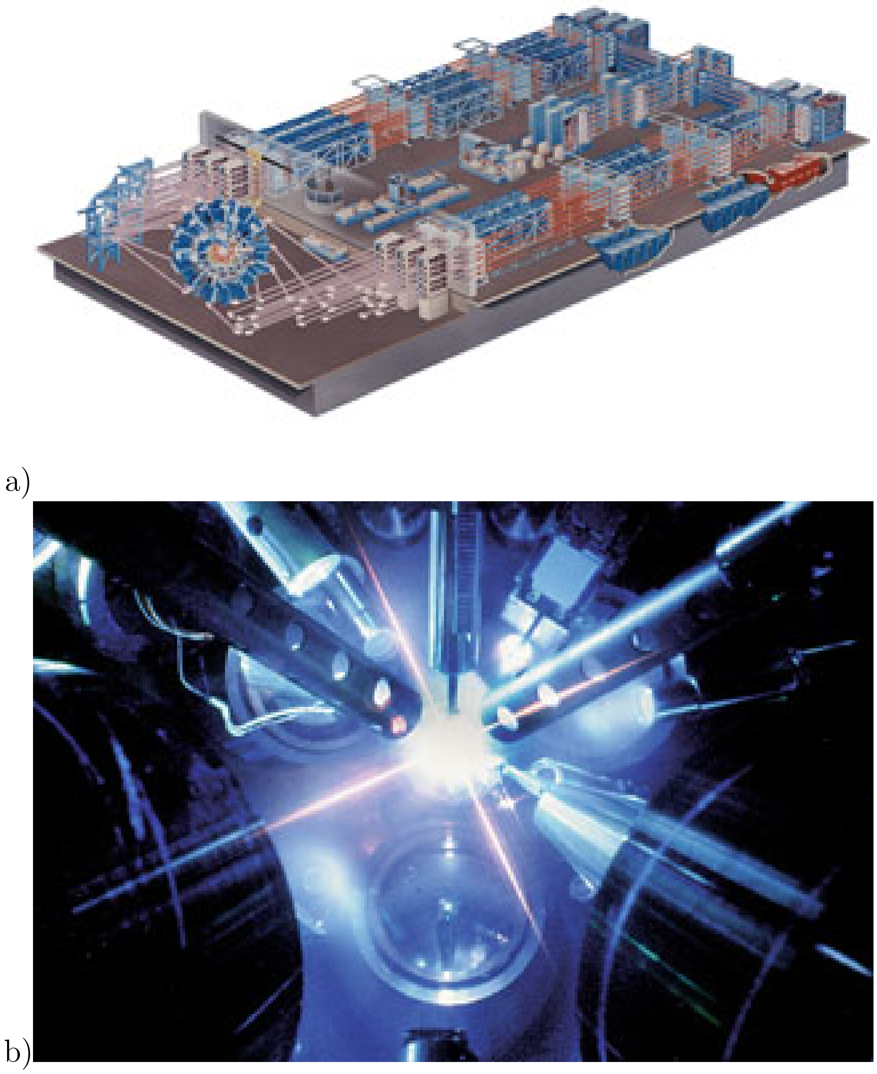

Figure 1.1: a) Schematic of the Omega Laser Facility's laser pathline. c) A target illuminated within the laser chamber. Images reproduced from the Laboratory for Laser Energetics website.

Table 1.1: A selection of high-energy-density experiments relevant to radiative shocks. Groups are listed, along with material used (typically either heavy gases such as xenon or very low-density solid foams) and geometry of the experiment (planar, or cylindrically or spherically divergent). The present work is most similar to the experiments by Reighard[73], driven to greater distances and times and over a larger variety of initial shock speeds.

Citation	Year	Geometry	Material	Notes
Grun[33]	1991	Spherical	Xenon / Nitrogen	Observed instability in a xenon Taylor-Sedov blast wave
Edwards[25]	2001	Cylindrical	Xenon	$\sim$ 8 km/sec
Keiter[50]	2002	Planar	Foam	$\sim$ 70 km/sec
Bailey[4]	2004	Cylindrical	Foam	$\sim$ 350 km/sec, pinch-driven
LULI[13, 52, 91]	2004	Planar	Xenon	$\sim$ 40 km/sec, low density (0.1-0.2 atm) gas
Hansen[35]	2005	Spherical	Xenon	$\sim$ 10km/sec
Reighard[73]	2006	Planar	Xenon	$\sim$ 150 km/sec
Moore[69]	2008	Cylindrical	Xenon clusters	Thermal cooling instability onset
Symes[88]	2010	Cylindrical/Spherical	Xenon clusters	Spatially modulated seeding of instability

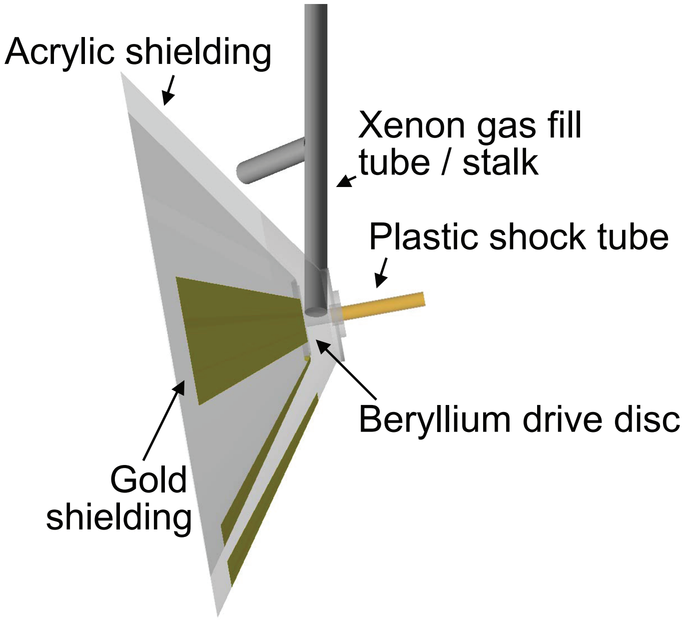

a)

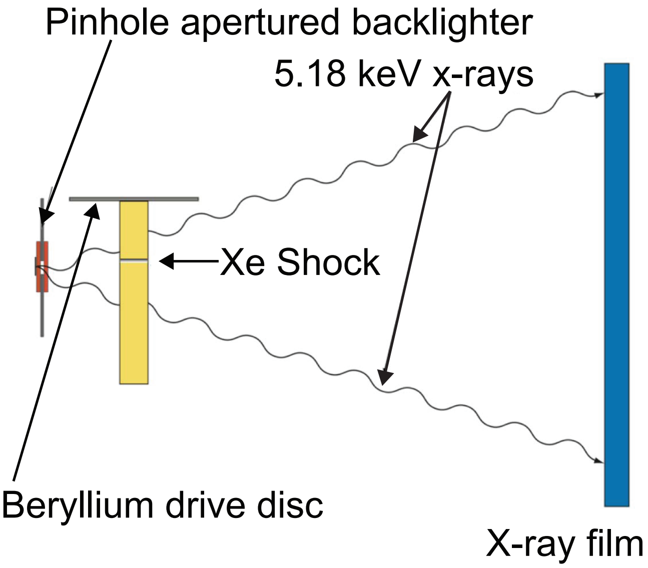

b)

Figure 1.2: Schematic diagram of experimental target used to explore radiative shock physics in July 2007. Figure (b) adapted from [77].

trappings in the previous image, this shows schematically the sites of essential physics. There are three areas of note. First, of greatest importance is the shock tube itself, filled with xenon gas at 1.1 atm, through which propagates the very strong shock which will be the focus of this thesis. Second, the beryllium drive disc at the top of the tube. The shock of interest is launched by irradiating the exterior side of this disc with powerful laser beams, causing a fraction of the beryllium to evaporate and blow off upward at a very high velocity, the reaction forces of which in turn launch the remainder of the disc downward at high speed. For all experiments in this thesis, the laser energy requested to drive ablation totaled ~ 3.8 kJ. The third event of interest is then x-ray backlighting, the diagnostic method for the experiment. Laser beams are used to heat a small piece of vanadium on the far side of a tantalum square. The heated vanadium radiates x-rays in a useful line-emission at 5.18 keV. The x-rays pass through the target and are collected in a piece of x-ray film some distance from the target.

The subsequent sections will investigate generally each of these aspects of the experiment. Section 1.2 addresses the conditions for reaching the radiative regime, and how such a radiating shock becomes of interest for further study. Section 1.3 discusses how such a shock is launched, and how the experimental parameters may be chosen to reflect one's goals. Section 1.4 performs rudimentary calculations regarding the x-ray backlighting scheme, focusing on the production of usable signal for diagnostic purposes.

1.2 Compression of a strongly radiating shock

The post-shock fluid behind a strong shock will, if unhampered by material opacity or other constraints, radiate its energy away, leading to cooling of the material and corresponding decrease in pressure and increase in density. In principle, this procedure could go on indefinitely, leading to collapse of the post-shock fluid to no volume and infinite density [24]. In practice however, the collapse will stop when the post-shock material is no longer optically thin, either because the material has cooled to the point where the relevant wavelengths of blackbody emission are no longer unimpeded, or because the material has increased in density to a state where even a small cross-section of absorption becomes substantial. We will investigate the latter of these cases.

In this section, we derive the effects of radiative transfer on the shock structure when the material is considered optically thin upstream of the shock and optically thick downstream. Of particular interest to us is the final density achieved by the material. The derivation here parallels those found in [96, Chapter 7] and [24, Chapter 7].

Calculations will be made in the moving frame of the shock. We begin with pre-shock flow parameters of density ρ_0, velocity V_s, and enthalpy h_0. The jump conditions ensuring conservation of mass, momentum, and energy can be written as

$$\rho_0 V_s = \rho U \tag{1.1}$$

$$\rho_0 V_s^2 + P_0 = \rho U^2 + P \tag{1.2}$$

$$\frac{\rho_0 V_s^3}{2} + \rho_0 V_s h_0 = \frac{\rho U^3}{2} + \rho U h + S \tag{1.3}$$

where the term S in Equation 1.3 describes all energy flux across the shock not convecting with the fluid, such as by radiation or heat-conduction. These are supplemented by our equation of state, $P = \rho R(1+Z)T$, where R is a species-specific gas constant and Z is the average particle ionization. For such an equation of state, $h = \gamma P/(\rho(\gamma-1))$. We may solve these equations to achieve

$$S = \frac{1}{2}\rho_0 V_s^3 \left(1 + \frac{2P_0\gamma}{\rho_0 V_s^2(\gamma-1)}\left(1-\frac{\rho_0}{\rho}\right) - \frac{2\gamma\rho_0}{(\gamma-1)\rho} + \frac{(\gamma+1)}{(\gamma-1)}\left(\frac{\rho_0}{\rho}\right)^2\right) \tag{1.4}$$

which is a general expression for the evolution of flow parameters beyond the initial state in terms of the non-hydrodynamic flux S, at any later point where the flow has achieved density ρ. Progress is made by assigning $S = 2\sigma T_f^4$, where σ is the Stefan-Boltzmann constant and S is the blackbody radiation from the optically thick post-shock region escaping to infinity on the optically thin side.

With reference to the final state achieved by the fluid, we write the momentum jump condition in Equation 1.2 as

$$\eta \left(V_s^2 + R(1 + Z|_{T_0})T_0 \right) = \eta^2 V_s^2 + R(1 + Z|_{T_f})T_f, \tag{1.5}$$

where $\eta = \rho_0/\rho_f$ and Z is a function of T on each side of the jump. We assume that strong radiation transport will equilibrate the final temperature of the downstream fluid with that of the upstream fluid, $T_f = T_0$. Equation 1.5 now can be solved for the final temperature in terms of shock velocity,

$$T_f = \frac{\eta V_s^2}{R(1 + Z)}. \tag{1.6}$$

Making these substitutions and letting $\rho = \rho_f$ in Equation 1.4, we can then write

$$\frac{2\eta^4 V_s^8 \sigma}{R^4(1 + Z)^4} = \frac{\rho_0 V_s^3}{2}(1 - \eta^2) \tag{1.7}$$

where γ has canceled out of the equation in all instances.

The terms in Equation 1.7 suggest introducing the variable Q,

$$\begin{aligned} Q &= \frac{2\sigma V_s^5}{\rho_0 R^4 (1 + Z)^4} \\ &= \frac{V_s^5}{\rho_0} \left(\frac{\mu}{1 + Z} \right)^4 \frac{\pi^2}{30 c^2 \hbar^3 N_A^4} \end{aligned} \tag{1.8}$$

where μ is the atomic mass of the gas species, $\hbar$ is Planck's constant, c is the speed of light, and N_A is the Avogadro number. In terms of this variable Equation 1.7 becomes

$$2Q\eta^4 + \eta^2 - 1 = 0 \tag{1.9}$$

We may solve this equation for the inverse compression η. There is one real, positive solution for η, which yields a final density

$$\rho_f = \rho_0 \sqrt{\frac{4Q}{\sqrt{1+8Q}-1}}. \tag{1.10}$$

For shocks in xenon at 110 km/sec, $\mu = 131$ g/mol, $Z = 12.6$, and $\rho_0 = 0.006$ g/cm^3, we obtain from Equation 1.10 a compression ratio $\rho_f/\rho_0 = 32$ and a precursor temperature $T_f = 37$ eV. Experimental results, to be found in Chapter IV, confirm that high compression ratios, greater than 20, are achieved.

This compression ratio, predicted for the optically thick-downstream-thin-upstream shock, is substantially above either the high-Mach-number predictions for an ideal monotomic gas $(\gamma+1)/(\gamma-1) = 4$ or models which take into account ionization by introducing an effective $\gamma = 1.2$ for a compression of 11 [24]. This transition to relatively very high compression is the source of many interesting features of these experiments.

1.2.1 Pressure and density corrections from ionization

Further accuracy may also be obtained by eliminating the assumption that ionization Z is a function of temperature only. In reality, the average ionization also depends on the particle density. In this regime, comparing two quantities of plasma at the same thermal temperature, the quantity at higher density will exhibit lower ionization until, at higher densities, continuum lowering will enhance the ionization rate [24]. We then solve Equation 1.5 with Z held at different values before and after the shock and obtain in place of Equation 1.6 the new relation

$$T_f = \frac{V_s^2}{R} \frac{\eta(1-\eta)}{1+Z_f-\eta(1+Z_0)} \tag{1.11a}$$

where Z_f is the average ionization behind the shock and Z_0 is the average ionization ahead of the shock. Inserting this quantity into Equation 1.4 and letting $\rho = \rho_f$ now yields

$$\begin{gathered} 2Q\eta^4 \left(\frac{1-\eta}{1-\epsilon\eta}\right)^4 + \eta^2 - 1 = \frac{2\gamma}{\gamma-1} \left(\frac{\epsilon-1}{1-\epsilon\eta}\right)(1-\eta)\eta \\ \text{where } Q = \frac{2\sigma V_s^5}{\rho_0 R^4 (1+Z_f)^4}, \quad \epsilon = \frac{1+Z_0}{1+Z_f}. \end{gathered} \tag{1.11b}$$

The correction to the solution for η in Equation 1.10 is only a slight perturbation due to corrections from $(\epsilon - 1)$, which remains small. More importantly, in solving Equation 1.11b we learn that the dimensionless parameter Q, in Equation 1.8 a function of Z, is correctly written as a function of the ionization *behind* the shock, Z_f, rather than in front of it, Z_0, when the two are being distinguished. We will also use an equation of state yielding ionizations ahead and behind the shock

$$Z_0 = \mathrm{TF}(T_f, \rho_0) \tag{1.11c}$$

$$Z_f = \mathrm{TF}(T_f, \rho_0/\eta). \tag{1.11d}$$

TF() represents a suitable ionization model, such as Thomas-Fermi [24, 26], evaluated as a function of plasma temperature, density, and (implicitly) ion species. We use results here from the algorithm developed by R. M. More [83, 70]. However, this model does not fully understand atomic shell structure. For example, Argon is unlikely under these conditions to ionize beyond the Ne-like (+8) state, but Table 1.2 finds $Z_0 = 9$ in one case. Armed with such an ionization model, Equations 1.11 form a complete system of nonlinear equations which may be solved numerically to obtain

Table 1.2: Solutions of Equations 1.11 for initial gas conditions given in the leftmost column, including xenon and argon at approximately atmospheric pressure, and dissociated CH (plastic) at 0.04 g/cc. Shown are shock compression, temperature ahead and behind the shock in electron volts, ionization in the precursor immediately ahead of the shock, and ionization in the shocked layer.

Xenon, $\rho_0 = 0.006$ g/cc	$1/\eta$	T_f (eV)	Z_0	Z_f
$V_s = 90$ km/sec	37	32	12	8
$V_s = 110$ km/sec	45	38	13	9
$V_s = 130$ km/sec	52	43	14	9
Argon, $\rho_0 = 0.0017$ g/cc				
$V_s = 90$ km/sec	22	24	7	6
$V_s = 110$ km/sec	26	27	8	6
$V_s = 130$ km/sec	31	31	9	6
CH, $\rho_0 = 0.04$ g/cc				
$V_s = 90$ km/sec	3	51	3	3
$V_s = 110$ km/sec	4	60	3	3
$V_s = 130$ km/sec	4	69	3	3

self-consistent solutions for given ρ_0, V_s, and ion species. For example, with upstream xenon gas with density $\rho = 0.006$ g/cm^3, $\gamma = 5/3$, and shock speed $V_s = 110$ km/sec, we obtain $Q = 2.0 \cdot 10^6, Z_0 = 13, Z_f = 9, \epsilon = 1.4, T_f = 38$ eV, and $\eta = 1/44$. Table 1.2 shows this system evaluated for several additional cases.

A counterintuitive consequence of this is that the sound speed $c_s = \sqrt{\gamma R(1+Z)T}$ will actually *decrease* across the radiative shock by a factor of $\sqrt{(1+Z_f)/(1+Z_0)}$. This is not typical behavior across a shock. Another result of note is that, given that the temperature remains constant at $T_f = T_0$, the pressure $P = \rho R(1+Z)T$ will increase by a factor of $1/\eta \cdot (1+Z_f)/(1+Z_0)$. This ratio is lower than the uncorrected value $1/\eta$ by, at high velocities, approximately 20 percent.

1.3 Laser ablation

This section will explain some aspects of why a laser-driven experiment was a relevant method for creating the strong shocks described in section 1.2. The lasers developed by the Department of Energy's pursuit of inertial confinement fusion data are ideal candidates for such an experiment, being able to deliver large energies (multiple kJ) to relatively small volumes in space and time (fractions of millimeters and single nanoseconds, respectively) [12]. We shall now discuss from basic principles how these energies and powers are converted into a shock wave of interest.

1.3.1 Ablation fronts

We discuss in this section the effects of energy absorption at a shock front and ablation of laser material off the surface of the material. Our earlier expressions in Equations 1.1-1.3 apply equally well here, where S will denote added energy to the rear of the shock. The derivation of basic ablation conditions is found to have similarities with the case of flame propagation in combusting gases, in which the energy source S is energy liberated by a chemical reaction. We assert that material exits the interface at the local sound speed, which will be held at the isothermal sound speed via heating by the incoming energy flux, $U = c_T = (\partial P/\partial \rho)_T$, from which it passes into a rarefaction. Flow which does not exit at this condition is unstable and changes until the outflow is sonic [31].

The interface of energy absorption has characteristics similar to a rarefaction shock, in that it creates a discontinuous drop in density. However, where a rarefaction shock is physically forbidden on grounds of leading to decreases in temperature and net destruction of entropy, the heat transport S into the fluid leads to net increases in temperature and entropy along with the drop in density. The absorption interface, called in this instance a *deflagration*, is preceded by a shock which imparts momentum to the remaining fuel. The opposite case, in which the absorption interface leads to both density and temperature increase, is known as a *detonation* and is not preceded by a shock.

We apply Equation 1.4 across the interface of energy absorption, from region 1 to

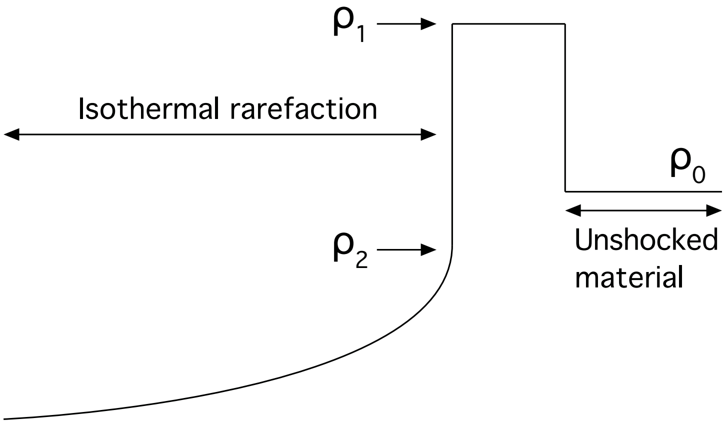

Figure 1.3: Schematic drawing for laser absorption and ablation modeled as a deflagration.

region 2. Region 0 will be taken as the material ahead of both the absorption interface and the shock of acceleration. Figure 1.3 shows the schematic for this calculation. Beginning with Equation 1.4, we make the assignments $\rho_0 \to \rho_1, \rho \to \rho_2$. It will be found useful to express the results in this section in terms of the compression $f = \rho_2/\rho_1$, which for deflagration will be between zero and one (i.e. it will indicate decompression, or lowering of density). We make the replacement $V_s = f \cdot c_T$, and note that the requirement of outflow at the isothermal sound speed implies

$$\frac{P_2}{\rho_2 c_T} = 1$$

and

$$\frac{P_1}{P_2} = (2 - f).$$

Together these changes allow us to write

$$\frac{S}{\rho_2 c_T^3/2} = 3 + \frac{2}{\gamma - 1} - f\left(\frac{4}{\gamma - 1} + 4\right) + f^2\left(\frac{2}{\gamma - 1} + 1\right). \tag{1.12}$$

The left side of Equation 1.12 is the inserted energy flux, normalized against the mechanical energy flowing away from the absorption interface. The purpose of normalizing against this quantity is to easily add in the flux which enters the system but does not reach the absorption interface, which may be similarly normalized. To consider heating by an external source, we define the quantity $q = S + \rho_2 c_T^3$ to represent the total energy influx entering the system. S is the quantity of flux which reaches the absorption front, and $\rho_2 c_T^3$ is the flux required to sustain the stream of ablated material, keeping it isothermal [3]. In terms of this variable,

$$\frac{q}{\rho_2 c_T^3/2} = 5 + \frac{2}{\gamma - 1} - f\left(\frac{4}{\gamma - 1} + 4\right) + f^2\left(\frac{2}{\gamma - 1} + 1\right). \tag{1.13}$$

1.3.2 Laser-plasma interaction

In the last equation of the previous section, the incoming total energy flux q is experimentally set by the parameters and settings of the laser used to drive the system. The remaining free parameters, ρ_2 and c_T, are found using relations from plasma physics. In the laser-heated plasma, we will use the approximation that light will propagate until the local electron density reaches the critical density (in SI units)

$$n_e = \frac{4\pi^2 m_e \epsilon_0 c^2}{e^2 \lambda^2}$$

where e is electron charge, m_e is electron mass, c is the speed of light, ϵ_0 is the permittivity of free space, and λ is the wavelength of the propagating light [53]. Under this approximation, absorption will take place at a material density of

$$\rho_2 = \rho_c = \frac{A m_p}{Z} \cdot n_e = \frac{4\pi^2 A m_p m_e \epsilon_0 c^2}{Z e^2 \lambda^2} \tag{1.14}$$

where A is the mass number of the ion species, Z is its atomic number, and m_p is the proton mass. Given an initial density for the material we are ablating, we can calculate the fractional compression f

$$f = \frac{\rho_2}{\rho_1} = \frac{\gamma - 1}{\gamma + 1} \cdot \frac{\rho_c}{\rho_0}$$

where we have assumed that the acceleration wave ahead of the absorption front is a strong shock. For a typical ablator, such as beryllium, and incoming laser light at 0.35 μm, we have a critical density of 0.0343 g/cc, an initial density of 1.85 g/cc, and $f \approx 0.00464$ when $\gamma = 5/3$. Because the critical density at this wavelength is so much smaller than the solid density of the ablator, f could be regarded as 0 with little loss of accuracy. We now solve Equation 1.13 for c_T to find

$$c_T = \left(\frac{q}{3.977\rho_c} \right)^{1/3}$$

which completes our set of parameters. We may now solve for such quantities as pressure generated by the ablation process,

$$P_1 = 1.995 c_T^2 \rho_c \approx \left(\frac{E}{At} \right)^{2/3} \cdot (0.258\,\mathrm{g}^{1/3}\mathrm{cm}^{-2})$$

mass ablation rate,

$$\dot{m}_2 = \rho_c c_T \approx \left(\frac{E}{At} \right)^{1/3} \cdot (0.0666\,\mathrm{g}^{2/3}\mathrm{cm}^{-2})$$

and a total ablated material depth

$$\Delta m = \frac{\dot{m}_2 t}{\rho_0} \approx \left(\frac{E}{A} \right)^{1/3} t^{2/3} \cdot (0.036\,\mathrm{g}^{-1/3}\mathrm{cm})$$

where E is the total laser energy, delivered in a pulse of time t over an area A. For a laser of 3.8 kJ with a spot size of 820 μm and a pulse length of 1 ns, we obtain a total ablated depth of 6.9 μm removed with an ablation pressure of 31 Mbar.

1.3.3 Rocket equation

We connect these derived quantities to the experiment using the well known "rocket equation"

$$V_f = V_e \ln\left(\frac{m_0}{m_0 - \Delta m}\right). \tag{1.15}$$

The rocket equation describes the final velocity V_f achieved by continuous ejection of material at output speed V_e. For the material parameters discussed so far, with the laser illuminating a Be disc of initial thickness 20 μm, we obtain an output velocity

$$V_e = c_T \approx 374\,\mathrm{km/sec}$$

and a corresponding final disc velocity

$$V_d = c_T \ln\left(\frac{20}{20 - 6.9}\right) \approx 160\,\mathrm{km/sec}.$$

Our ability to reach such high velocities of a substantial mass of our beryllium driver are key to our experiments. This confirms that we can launch an object at velocities such as those considered at the end of section 1.2. The initial velocity may be tuned by controlling the initial thickness of the beryllium disc, as results presented in Chapter V, will indicate.

There is a correction relating the initial velocity of the shock to the initial velocity of the disc. Assuming the accelerated disc acts as a rigid piston with respect to the material within the shock tube,

$$V_s = V_d\left(1 + \eta|_{V_s}\right) \tag{1.16}$$

where the inverse shock compression η is a function of V_s as related by Equations 1.11. Equation 1.16 is an implicit equation for V_s which may be solved numerically. Because the compressions for these shocks are very high, the correction is a small one, typically around 5 km/sec. Table 1.3 shows some predicted disc and shock velocities for typical experimental ablator thicknesses. While this analysis is insufficiently sophisticated to predict the precise speeds that will appear in the experiments, one expects it to be approximately correct and sufficient to better than an order-of-magnitude level.

Table 1.3: Theoretical disc and shock velocities for several thicknesses of beryllium ablators launched into xenon at $\rho_0 = 0.006$ g/cc

Disc (μm)	V_d (km/sec)	V_s (km/sec)
15	230	236
17	195	200
19	169	174
21	149	154
23	133	139
25	121	126
27	110	115
29	102	107
31	94	99

1.4 X-ray radiography

To image a shock traveling over 100 km/sec, in a system only 600 microns in lateral extent, is a task with demanding requirements. To image the range of densities and temperatures present in the system, this author's mechanism of choice is the transmission of x-rays in what might be called the "nearly hard" energy range (1 - 10 keV). In this work we are primarily concerned with the production of 5.18 keV x-rays from the irradiation of vanadium.

Figure 1.4 shows the basic layout of the backlighting scheme. For the experiments discussed in this thesis, the typical dimensions are: a substrate to emitting foil distance of 0.5 mm, a substrate thickness of 50 μm, a pinhole exit diameter of 20 mm, and a substrate to imaging surface distance of 250 mm. In order to resolve the shock

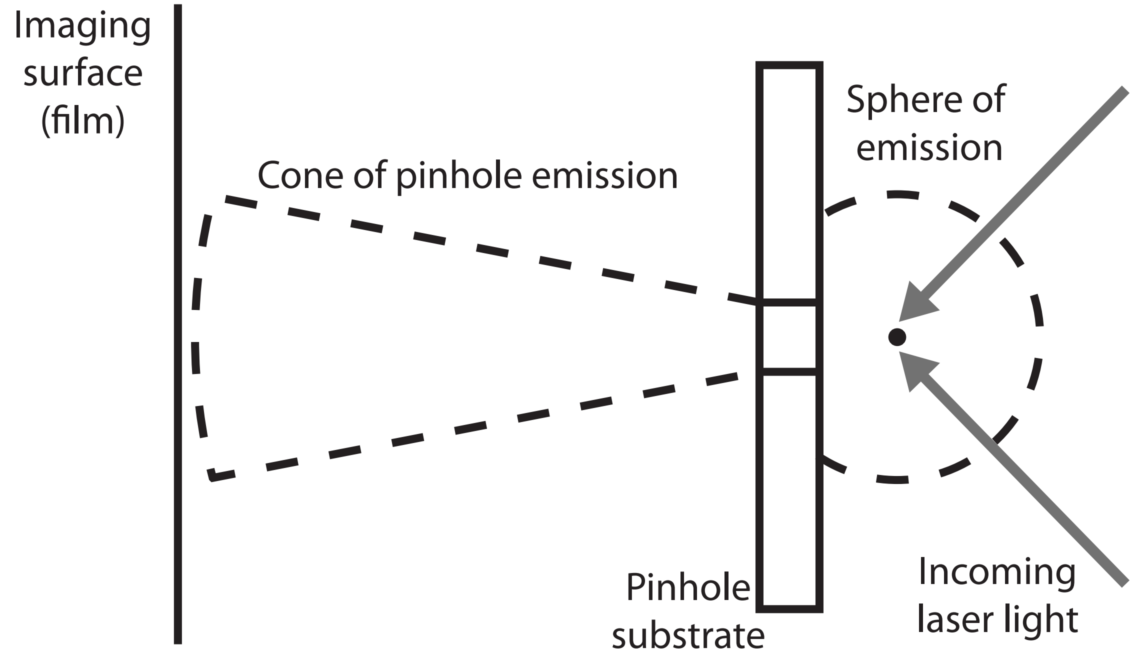

Figure 1.4: Diagram of the backlighting scheme discussed in section 1.4. Lengths are not to scale. The gray lines show incoming laser light irradiating the small foil. The dashed lines show the boundaries of x-ray emission in two stages. The first stage is spherical emission from the backlighter foil, behind the substrate. The second stage are the photons which pass through the small pinhole drilled through the substrate, which pass through the target and reach the imaging surface.

temporally, a short (relative to the drive) laser pulse of 200 ps is used. The substrate is a high Z material which can effectively block many x-rays; tantalum is typically used.

The efficiency of vanadium's conversion of energy to its 5.18 keV x-ray line is ~ 0.004 [41]. For five beams of 70 J each instigating a backlighting event, this would result in $1.69 \cdot 10^{15}$ photons created, but because the beams substantially overfill the emitting foil only $\sim 2.4 \cdot 10^{14}$ are produced.

These photons are spread over the spherical emission behind the foil over a spherical area $3.8 \cdot 10^6 \mu\text{m}^2$, with only a fraction passing through the pinhole of area 314

μm^2. We have at this point $2.0 \cdot 10^{10}$ photons.

These photons are emitted from the foil in a spherical cone of half-angle 16.7°, an angle set by enlarging the foil-side of the pinhole to 50 μm. At a distance of 250 mm, the resulting cap spans $1.57 \cdot 10^{10} \mu$m^2. This yields a final intensity of 1.25 photons / μm^2. The number of usable photons is further reduced by the need for filters. The filters protect the imaging surface both from physical debris and from undesirable photon energies which may either pass through the target without obtaining information, or be emitted from elsewhere in the system (e.g. drive) which may harm or expose the film. These filters may reduce the number of photons at the energy of interest by as much as half to three-quarters, yielding final photon estimates of 0.6 to 0.3 photons/μm^2.

To improve this situation, we strategically place the target much nearer the x-ray source pinhole than to the imaging surface, for a typical magnification of 20x. This results in approximately 240 photons/μm^2 in the plane of the target. When x-ray film is used as the imaging surface, the optical densitometer used to scan the film has a pixel size of 22 μm square, yielding 290 photons/pixel in the scanned image.

Spatial resolution in the target is practically limited by the size of the pinhole. Based on the magnification and scanning resolution quoted above, the scanner-side resolution is approximately 1.1 μm. However, the 20 μm pinhole creates a resolution element of $\sim 14\mu$m, or uncertainty in measurements of $\pm 7\mu$m. Sharper resolution can be obtained, but at the price of shrinking the area through with photons pass, and therefore lowering the quantity of signal.

1.5 Specific heats in ionizing plasmas

An interesting consequence of the radiative shock system is that the Mach number of the shock defined locally in the shock's vicinity is much lower than that of the shock at large distances. A 110 km/sec shock launched into cool xenon at 1/40 eV (room temperature) would be measured as Mach 630. However, because of the radiative heating of the immediately upstream gas, the gas has achieved an ionization of approximately 15 electrons and and an upstream temperature of 50 eV, the speed of sound is $c_s = \sqrt{\gamma R(1+Z)T}$ which depends on the ratio of specific heats γ, but is generally around 30 km/sec. The Mach number of the shock accordingly decreases in its immediate vicinity to around 3.5.

Finding the ratio of specific heats γ is additionally complicated by local ionization Z. A simple model for predicting ionization effects on γ is to add a hydrogen-like energy term to the gas's internal energy, $e_Z = \chi_H \sum_1^Z k^2 = (\chi_H/6)Z(1+Z)(1+2Z)$, where $\chi_H = 13.6$ eV. This results in the expression for γ found in Drake [24],

$$\gamma_{\text{Drake}} = 1 + \frac{P}{\rho e} = \frac{15 + \frac{Z(1+2Z)\chi_H}{kT}}{9 + \frac{Z(1+2Z)\chi_H}{kT}} \tag{1.17}$$

where $P = \rho(1+Z)RT$ is the gas pressure, ρ is the gas density, and e is the gas's internal energy.

Another model, derived in Cox's *Principles of Stellar Structure*, couples the Saha equation for ionization with the thermodynamic derivatives, but remains tractable by assuming only two ionization levels are populated at a given time [20].

$$\gamma_{\text{Cox}} = \frac{5 + \frac{2\left(\frac{\chi}{kT}+\frac{5}{2}\right)^2}{\frac{Z+1}{\lfloor Z\rfloor - \lfloor Z\rfloor^2} + \frac{1}{Z}}}{3 - \frac{Z(\lfloor Z\rfloor - 1)\lfloor Z\rfloor\left(15(kT)^2 + 12kT\chi + 4\chi^2\right)}{2(kT)^2(\lfloor Z\rfloor - \lfloor Z\rfloor^2 + Z^2 + Z)}} \tag{1.18}$$

$\lfloor Z\rfloor$ in Equation 1.18 is the fractional part of Z (e.g. if $Z = 14.4$, $\lfloor Z\rfloor = 0.4$). Z is found in γ_{Cox} using More's Thomas-Fermi solution [70]. χ is the energy needed to liberate the electron for the next level of ionization (e.g. if $Z = 14.4$, $\chi = \chi_{15}$ as tabulated in Figure 1.5 [82]).

Figure 1.6 plots Equations 1.17 and 1.18 for xenon. Both models predict $\gamma \sim 1.2$ for low temperatures, but γ_{Cox} returns to higher average γ at high temperatures. At

50 eV, $\gamma_{\text{Cox}} \sim 1.55$. These estimates will be used through analyses in subsequent chapters.

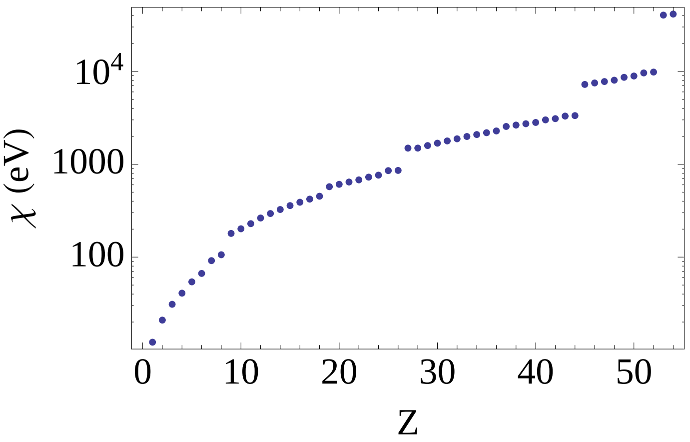

Figure 1.5: Xenon ionization energies from NIST data [82].

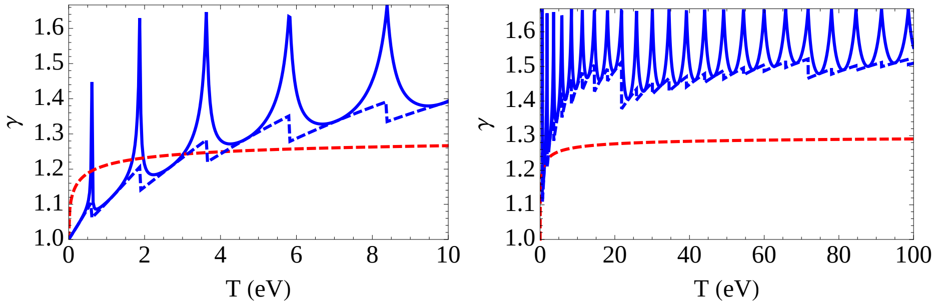

Figure 1.6: Blue solid - γ_{Cox}, Blue dashed - γ_{Cox} with $\lfloor Z \rfloor = 0.5$, Red dashed - γ_{Drake}

1.6 Outline of future chapters

The previous sections have presented results which will be useful in interpreting the subsequent work. The remainder of the text deals with experiments which create radiative shocks and the structure that is observed within them.

Chapter II introduces *wall shocks*, a type of edge effect and boundary condition unique to the radiative experiment. Wall shocks are a medium scale effect with length scales of $\sim 70\mu$m near the shock tube wall. The chapter contains the expanded manuscripts of “Wall shocks in high-energy-density physics experiments,” previously published as *Physics of Plasmas* 16, 112705 (2009), and “Oblique radiative shocks and their interaction with polytropic shocks,” submitted to *Physics of Plasmas* for printing in 2011.

Chapter III discusses a linear theory of perturbations in the post-shock layer, which can lead to instability. Unstable flow patterns coupling the (normally stable) shock front and the material discontinuity at the rear of the post-shock layer lead to rearrangement of areal density from a uniform, flat layer to a non-uniform, clumpy structure. This theoretical section deals with perturbations of infinitesimal amplitude; experimental perturbations seem to be of order 10-30 μm in early time images and potentially substantially larger in late time.

Chapter IV presents experimental campaigns designed to obtain repeatable data and the results of said campaigns. Section 4.1 contains the manuscript of “Repeatability in radiative shock tube experiments,” *High Energy Density Physics*, (2010), which contains the design and results of the October 2008 experiments and is expanded upon in the subsequent sections. Section 4.2 presents an analysis of shock location utilizing heirarchical Bayesian principles. Section 4.3 discusses sources of asymmetrical error in the experiment, and statistical methods which can be used to interpret and mediate their effects, much of which is adapted from the manuscript of “Statistical inference in the presence of an inclination effect in laboratory radiative shock experiments,” submitted to *Astrophysics and Space Sciences* (2010). The chapter concludes in Section 4.4 with discussion of the August 2010 experiments to image the shock with a longer delay after the drive.

Chapter V presents design and data from experimental campaigns which explored the parameter space of shock experiments. Such experiments feature a range of initial shock speeds, controlled by initial thickness of the target beryllium disc, and of times and locations of imaging. Inferences from this spread of data include an estimate of ablated mass during the driving event.

Chapter VI summarizes the links between these experiments and astrophysics. In particular, predictions of instability growth in the post-shock layer, discussed in detail in Chapter III, are scaled to both astrophysical objects and the laser-driven experiments. The data collected in Omega campaigns and discussed in Chapters IV and V are used to point toward future designs of experiments which can be made well-scaled to investigate the instability in the context of supernova remnants.

The Appendices contain detailed parameters used by the laser for a representative shot from each campaign. Each appendix reproduces in full a Shot Request Form used for an experiment. The Shot Request Form contains specifications for laser beam energy, pointing, and driving; diagnostic setup and pointing; and target identification, location, and orientation in the chamber. This information is included so that the interested reader would, in principle, be able to recreate any of the experiments discussed using information in this document. It is included also so that the Omega user may find any technical data that may be of interest, such as beam pointing, laser energy, or temporal pulse shaping.

CHAPTER II

Wall Shocks and Entrained Flow

In Chapter I we introduced the concept of shocks with sufficiently high velocity that their post-shock temperatures begin to drive significant radiation ahead of the shock. It is possible that the corresponding radiation can become strong enough to significantly heat the upstream shock tube wall. Beyond a second threshold speed, discussed further below, the upstream radiation is sufficient to vaporize the tube material some distance ahead of the primary shock. This drives a secondary, radially converging shock, which we name a *wall shock*.

The wall shock can be recognized by a failure of the primary shock to extend to the walls of the tube. Instead, it kinks sharply a finite distance away from the tube walls, indicating a point of interaction with the wall shock. The wall shock itself may also be visible, extending from the kinks ahead of the shock and toward the wall of the shock tube from which it was emitted. This extension of effects far ahead of the primary shock is a feature by which wall shocks may be distinguished from Mach stems and other interactions of shocks with walls [6].

2.1 Simulation of experiments with radiative shocks

Figure 2.1(a) shows an x-ray radiograph of a radiating shock experiment performed on the Omega laser facility at the Laboratory for Laser Energetics, University of

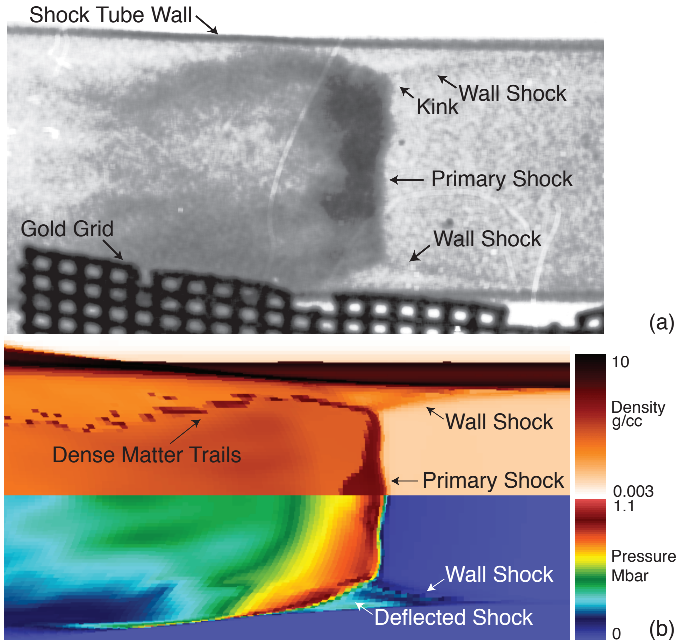

Figure 2.1: (a): Radiating shock experiment featuring wall shocks, as described in the text. (b): 2D HYDRA simulation showing density (log scaled) above and pressure below. The dense Xe feature near the tube axis is an artifact of the rotational symmetry

Rochester [12]. The experimental system is a 20 μm Be drive disc, launched into a 625 μm diameter polyimide tube filled with gaseous Xe at 0.006 g/cc. The image is taken 2 mm down the tube, 14 ns after the laser is turned on, using ungated radiography (as described in [54]) with a 50 μm to 20 μm tapered pinhole backlit by a V source, illuminated by backlighter beams for 200 ps. These experiments are discussed in more detail in Chapter IV

In Figure 2.1(a), the primary shock is the vertical feature near the center of the image, and is at the time of the image moving from left to right at 110 km/sec. The darker region to the left of the primary shock is the shocked Xe, the density of which has increased significantly from radiative effects [76]. Both signatures of a wall shock discussed above are seen here. In previous work with radiating shocks, only the kinks at finite displacements from the tube wall were visible. The improvements in spatial resolution from ungated radiography make the wall shocks themselves visible in the most recent data.

The wall shock interpretation of the kinks and the visible interface is also qualitatively supported by simulations of this experiment using the radiation hydrocode HYDRA [64], shown in Figure 2.1(b). Simulations were performed using diffusion approximated multigroup radiation transport. Fifty log-spaced frequency groups were used, and between approximately 400 to 1000 axial zones in the xenon region. The hydrocode was used primarily in its lagrangian mode, but with substantial relaxation of grid advection in the vicinity of the shock. Tabular opacities were used for the beryllium, xenon, and plastic in the system, while gold was modeled as silver at a modified solid density. The results were found to be sensitive to the distribution of zones in the tube wall, as the expansion of tube wall material into the tube interior caused the lagrangian zones to increase greatly in volume before interacting with the xenon gas. Nevertheless, with sufficiently fine zoning in both the tube interior and its walls, reasonably stable solutions producing wall shocks and shock interactions within the xenon were obtained, though never reaching formal numerical convergence in the usual sense of computer science [43].

2.2 Wall shock analysis

We now consider what can be learned from the wall shock. Figure 2.2 shows two useful constructions of the wall-shock profile. The first, denoted as $\delta(x;t)$, is the wall shock's displacement *vs.* distance from the primary shock, where $x = 0$ is the location of the primary shock at time t. The second, denoted as $\Delta(x)$, is the wall shock's displacement when the primary shock meets it, with distances measured in the lab frame and $x = 0$ marking the origin of the primary shock.

The time-independent viewpoint $\Delta(x)$ is useful for calculating the evolution of the primary shock in a tube modified by the existence of wall shocks. As shown in Figure 2.2, the wall shock has a transient state early in the experiment, after which

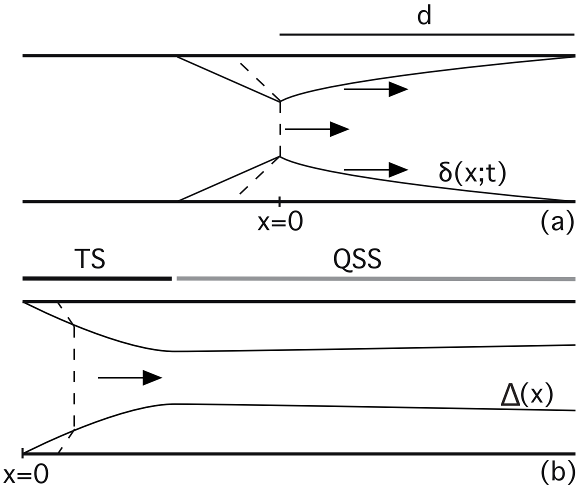

Figure 2.2: Instantaneous (a) and time-independent (b) frameworks of the wall shock, showing the wall shocked tube material interface (solid) and the primary and deflected shocks (dashed). TS = Transient State, QSS = Quasi-Steady State

it is nearly constant. Over long periods of time, the deceleration of the primary shock leads to a decrease in wall shock amplitude. If the speeds of sound of the tube material and the interior gas are very different, then behavior such as expansion fans and shock convergence, consistent with a shock's travel through a duct with profile $\Delta(x)$, might be expected to occur early on [95].

The instantaneous framework $\delta(x;t)$ is useful for considering the dynamics of the wall shock, and is the profile which may be directly observed in an experiment. At a given moment in time, a wall shock has been launched a distance d away from the shock, beyond which $\delta(x > d;t) = 0$. It will then propagate radially inward with speed V_w, assumed constant here, meeting the primary shock at a distance $\delta(0;t)$ from the wall.

2.2.1 Wall shock amplitude

An approximate model provides a useful basis for interpretation. When heating by the shock precursor has produced optically thin upstream material, the intensity of the radiation may be assumed to be falling off spatially in its dominant terms as the square of the distance from the shock. The radiative energy flux from the shock is also proportional to the cube of the steady primary shock speed V_s [24]. The minimum radiation intensity sufficient to vaporize tube material is a value which depends on material factors of the experiment. The blow-out distance d will be the distance from the shock at which that the radiation intensity has fallen off to that minimum. Collecting these dependencies, we see that V_s^3/d^2 will scale proportionally to a constant critical heating parameter. There also exists a minimum speed at which a primary shock radiates strongly enough to launch a wall shock. We may write this scaling in terms of unknown constants C_1, C_2 as

$$d^2 = \frac{C_1}{V_w^2}(V_s - C_2)^3 \tag{2.1}$$

where C_2 is the primary shock speed threshold, and the heating constant C_1 has been normalized against the wall shock speed V_w for later ease in interpretation.

Once launched at a time t_0, a wall shock will travel inward from $\delta(d; t_0) = 0$ along $\delta(d - V_s t; t_0 + t) = V_w t$. Where this segment of the wall shock reaches the primary shock, $\Delta(x) = (V_w/V_s)d$. Substituting from equation 2.1, it follows that $\Delta(x) = C_1^{1/2}(V_s - C_2)^{3/2}/V_s$. For V_s much higher than the threshold velocity, $\Delta(x)^2 \approx C_1(V_s - 3C_2)$. This describes a straight line in the (Δ^2, V_s) plane, from which the two constants may be calibrated to a given experiment by simultaneous measurements of V_s and $\Delta(x) = \delta(0; t)$. Afterwards, $\Delta(x)$, which is the most clearly visible signature of the wall shock, may be used to diagnose V_s.

The threshold C_2 can be no lower than V_w. For two shocks entering a homogenous volume of material, the post-shock temperature will be higher behind the faster shock. If a wall shock were launched by a primary shock with $V_s < V_w$, the wall-shocked material would be at a higher temperature than the primary-shocked material. Since

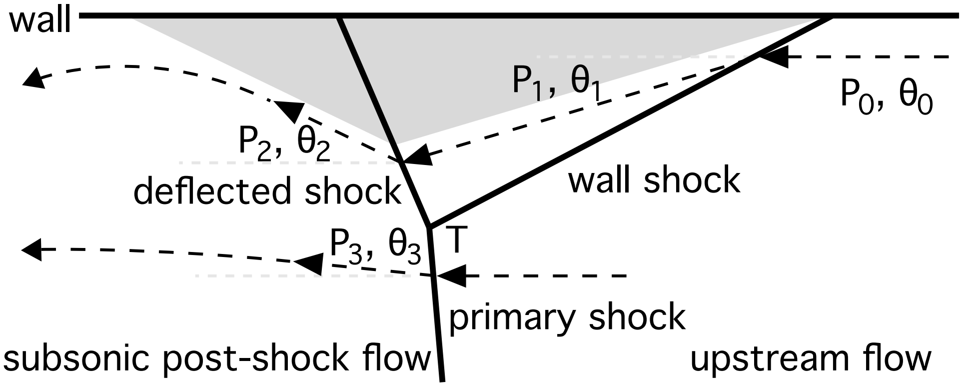

Figure 2.3: Flow diagram for three-shock theory applied to wall shocks in the frame of the primary shock

the wall shock is driven by radiative heat transfer from behind the primary shock, this would contradict the second law of thermodynamics.

2.2.2 Interaction with the primary shock

Now consider interaction of the primary and wall shocks, which is an instance of the well studied three-shock theory [6, 42]. The analysis takes place in the moving frame of the primary shock, approximated as steady, in which flow enters the system from the right at the constant shock speed V_s. Figure 2.3 shows a schematic of the system, in which the wall shock, primary shock, and deflected primary shock all meet at a single, stationary point T. Also shown are the boundaries between ablated wall material (gray) and the interior gas (white), which may be directly observed in the data. The angle of fluid flow in any area is parallel to the visible material interface. Deflections of flow θ are taken to be positive toward the center of the tube (θ_1 is positive). To simplify the analysis, we confine our discussion entirely to the interior gas, acknowledging that shock refraction effects may influence the tube material region [39]. We also neglect any shock reflection phenomena from the wall or changes in flow downstream, focusing in this model only on the local behavior near T.

In the final post-shock flow, there are two distinct regions of Xe gas: one in which the flow has passed through the strong primary shock, and another in which the flow has passed through both the wall shock and deflected primary shock. These two regions may have different flow speeds, densities, and temperatures, but must have equal pressures [6]. In terms of the variables shown in Figure 2.3, $P_3/P_0 = (P_2/P_1) \cdot (P_1/P_0)$, where we have assumed that P_0 is everywhere equal from T to the wall shock. Since the wall shock is localized within the precursor of the primary shock, this equality depends on the assumption that the pressure in the precursor is constant. Any pressure profile $P_0(x)$ will result in curvature in the wall shock profile. As this model depends only on the angles in the immediate vicinity of T, and as long as no nearby profile curvature is experimentally resolvable, any effects due to upstream flow variation are dominated by the existing uncertainty in θ_1. If a finite pressure gradient becomes important, the equality may be modified to include such effects.

Material passing at an angle through a shock experiences a deflection $\Delta\theta$ from its direction of flow and a discontinuous jump in fluid parameters such as pressure P and density ρ. For a polytropic gas with ratio of specific heats γ, the angle of deflection across an oblique shock from flow states i to j may be found as a function of the upstream Mach number M_i and the angle at which the flow meets the shock [24]. Equivalently, we may transform our variables to find the angle of deflection as a function of Mach number and any of the discontinuous ratios which occur at the shock. Choosing for our purposes the pressure ratio P_j/P_i as the second parameter, we obtain

$$\tan(\theta_j - \theta_i) = \frac{\left(\frac{P_j}{P_i} - 1\right)}{\gamma M_i^2 + 1 - \frac{P_j}{P_i}} \sqrt{\frac{2\gamma M_i^2}{(\gamma+1)\frac{P_j}{P_i} + \gamma - 1} - 1} \tag{2.2}$$

Similarly, the ratio of change in Mach number as a flow passes through an oblique shock satisfies [39]

$$\frac{1+\frac{1}{2}(\gamma-1)M_j^2}{1+\frac{1}{2}(\gamma-1)M_i^2} = \frac{(\gamma+1)/(\gamma-1)+(\frac{P_j}{P_i})^{-1}}{(\gamma+1)/(\gamma-1)+\frac{P_j}{P_i}} \tag{2.3}$$

Equations 2.2 and 2.3 hold over each shock encountered in the system. Figure 2.4 shows a plot of equation 2.2 called the *shock polar* for the wall shock. The polar depends on the flow Mach number, the correct value of which will be determined by iteration of this procedure. Flow begins at $(\theta, P_j/P_i) = (0, 1)$, and passes through the wall shock to arrive at point $(\theta_1, P_1/P_0)$ along the wall shock polar. θ_1 may be read from the experimental images. We select the lower branch of the two solutions for pressure on this polar to ensure supersonic flow exiting the wall shock. This is necessary for the flow to immediately pass through an additional shock attached to the same point T as the wall shock.

A second polar, showing states accessible from passing through a second shock, is placed emitting from $(\theta_1, P_1/P_0)$. As the once-shocked flow passes through the deflected shock, it will obtain a final flow state $(\theta_2, P_2/P_0)$ located on the second polar. The angle θ_2 of the post-shock flow, which is the angle of the material interface between shocked interior gas and transparent rarefied wall material, is also read directly from the data.

The pressure jump $P_3/P_0 = P_2/P_0$ across the primary shock may be inferred by first measuring the density jump ρ_3/ρ_0 at the interface, which can be calculated from the ratio of visible volume of the post-shock material to the total distance known to have been travelled by the shock. We assume that the interface between the dense material and the immediate post-shock cooling layer is fixed by the strong transfer of heat at the same temperature as the heated material upstream of the shock, as in Section 1.2.

The deflected shock polar describes, for a chosen upstream Mach number, all of the

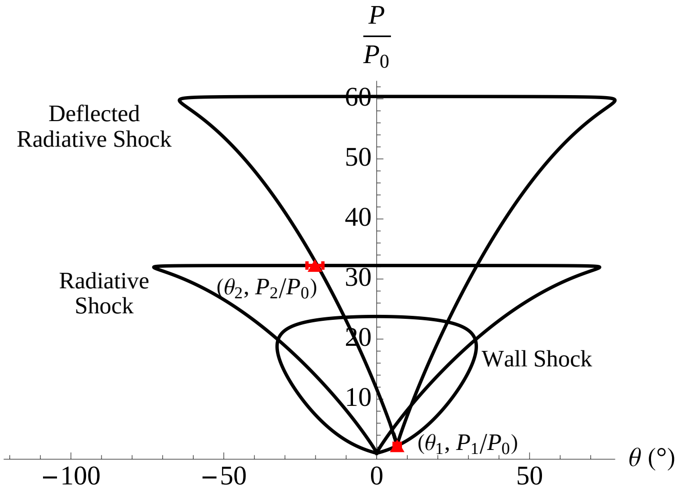

Figure 2.4: Shock polars (black) and data (red) for the radiating shock experiment shown in Figure 2.1(a).

accessible states of the twice-shocked material. Since the flow orientation $(\theta_2, P_2/P_0)$ is known by measurement, the only possible Mach numbers are those that produce shock polars including that point. Two candidate Mach numbers are found, and are referred to as the *weak* and *strong* solutions of the deflected shock, implying respectively supersonic and subsonic flow behind the shock. Detailed calculations in Section 2.3.5 imply that we should take the strong, supersonic solution, and that additional waves will redirect the flow before it impacts the tube wall.

2.3 Interactions of radiative shocks with polytropic shocks

2.3.1 Motivation for considering entrained flow

This section discusses some thoughts, motivated largely by basic physical thinking, on the nature of the *entrained flow* in the radiating shock data. As shown in Figure 2.5, the entrained flow is that dense xenon which is seen near the edges of the shock tube to flow backwards well beyond the normal xenon dense layer width. Measurement of the entrained flows on several different shocks shows that, measuring from the primary shock front, the furthest removed dense xenon is about 4.6 ± .5

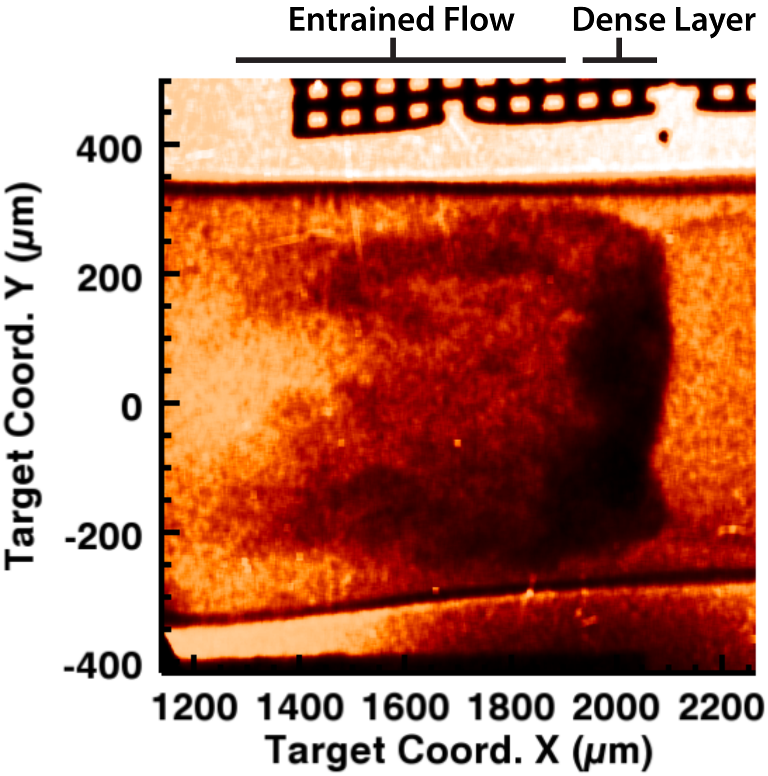

Figure 2.5: Shot 52667. The ‘entrained flow’ is that dense xenon which establishes itself at greater distances from the primary shock than the main Xe/Be interface.

times as far back as the main Xe/Be interface at the rear of the dense layer.

This section contains a motivation for the phenomenon from the viewpoint of wall shocks. In the absence of wall shocks, a no-slip boundary condition along the walls might have been expected to produce such an observation of dense xenon trails clinging to the walls. However, with the wall shocks and the associated ablated plastic tube separating the xenon flow from the rigid wall, modifications to this expectation must be made.

Figure 2.6 shows the three-shock interaction, in the moving frame of the shock system, involved in wall shock analysis. One should pay special attention here to the wall shock amplitude Δ, as it is measured in radiographs such as Figure 2.5. Attention should be called also to the *twice-shocked* xenon which achieves its high

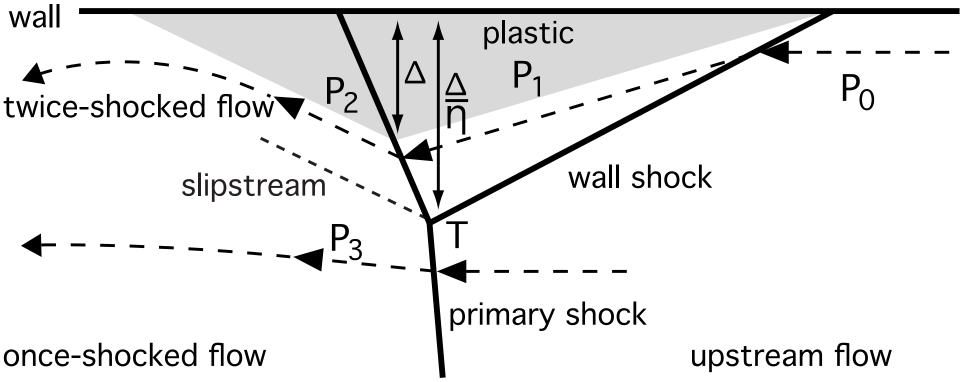

Figure 2.6: Flow diagram for discussing the wall shock - primary shock interactions. Gray indicates the region of ablated wall plastic. Δ is the wall shock amplitude, as measured in radiographs. P_i denotes the pressure in each region, $i = 0, 1, 2, 3$.

density by passing through both the wall shock and the oblique deflected shock, as opposed to the *once-shocked* xenon which passes through the (nearly) normal primary shock.

It is a standard feature of three-shock theory that in such interactions, a vortex sheet (also known as a slipstream) is created which separates the once-shocked and twice-shocked regions and allows them to have different flow velocities. The twice-shocked flow, which has passed through oblique shocks, is typically faster than the once-shocked flow. A standard boundary condition is that $P_2 = P_3$, which in a system with strong temperature conduction by radiation will equally impose $\rho_2 = \rho_3$.

An elementary analysis of mass-conservation in the wall shock geometry yields approximate flow speeds. The geometry takes place in a tube of inner diameter $d = 575\mu$m. Analysis of the CRASH data discussed in Chapter IV suggests an average wall shock amplitude $\Delta = 67\mu$m. It is also helpful here to introduce the parameter η, where now $(1-\eta)^{-1}$ is the compression ratio of the wall shock. The distance Δ/η is therefore the distance from the wall to the shock triple point (one might call Δ the observed, material amplitude and Δ/η the inferred, actual, shock amplitude). Assuming that the wall shock is strong, this parameter η may reasonably be expected to be somewhere between 3/4 and 7/8.

One may construct some appropriate areas of interest:

$$A_0 = \pi \left(\frac{d}{2}\right)^2 \tag{2.4}$$

$$A_1 = \pi \left(\frac{d}{2} - \frac{\Delta}{\eta}\right)^2 \tag{2.5}$$

$$A_2 = \pi \left(\frac{d\,\Delta}{\eta} - \frac{\Delta^2}{\eta^2}\right) \tag{2.6}$$

$$A_3 = \pi \left(d\,\Delta \left(\frac{1}{\eta} - 1\right) - \Delta^2 \left(\frac{1}{\eta^2} - 1\right)\right) \tag{2.7}$$

where A_0 is the total area of the tube, A_1 is the area of the tube encompassed by the primary shock, A_2 is the area of the tube which experiences the wall shock ($A_0 = A_1 + A_2$), and A_3 is the annulus between the triple point and the observed wall shock, the area through which the wall-shocked xenon passes into the deflected shock.

One may construct roughly the ratio of one-shocked to twice-shocked flow,

$$\frac{A_1}{A_0} = \left(1 - \frac{2\Delta}{d\eta}\right)^2 \tag{2.8}$$

For the values discussed above, $A_1/A_0 \sim 0.6$. One accordingly expects 40% of the total xenon mass to have become entrained flow, and 60% of the total mass to be confined to the dense layer. This is referred to as a *mass ratio* of 0.6.

One can now utilize the conservation of mass flow, $\rho u A =$ const. Letting ρ_s be the shocked density, ρ_0 be the unshocked density, u_p be the flow velocity behind the primary shock, u_t be the flow velocity of twice-shocked xenon, and u_0 be the flow velocity ahead of the shock system,

$$\rho_s u_p A_1 = \rho_0 u_0 A_1 \tag{2.9}$$

$$\rho_s u_t A_3 = \rho_0 u_0 A_2 \tag{2.10}$$

Dividing Eqn 2.10 by Eqn 2.9 one obtains,

$$\frac{u_t}{u_p} = \frac{A_2}{A_3} = \frac{d\,\eta - \Delta}{d\,(\eta - \eta^2) - \Delta\,(1 - \eta^2)} \tag{2.11}$$

which yields the expected ratio of twice-shocked flow speed to once-shocked flow speed (the *width ratio*). Entering values $d = 575, \Delta = 67, \eta = 0.75$, one obtains a ratio of 4.64. This is in rather good agreement to the observed ratio of dense entrained flow distance to slow primary-shocked flow distance. For an η of 5/6, this ratio would increase to 6.94; this shows that there is a strong dependence of width ratio on η. Unfortunately, the difference between fine values of η is not reliably radiographically resolvable (the wall-shocked xenon layer being thinner than a resolution element). In actual October 2008 data the observed ratio from typical shocks ranges from around 4.1 to 5.1.

Figure 2.7 shows data extracted for three shots. Lineouts of density are shown for the images, averaged over the widths of the radiographic images. Quality of the lineouts increase with quality of the images. Half-widths of the radiographs are used when one side of the radiograph features an obstruction. The mass ratio (ratio of dense layer mass to total mass) and width ratio (ratio of entrained flow width to dense layer width) are measured for each radiograph. Equations 2.8 and 2.11 are then solved simultaneously for the Δ and η consistent with the measurement and compared with the average measured wall shock amplitude Δ. The measurements confirm an increase in entrained flow effects with larger wall shocks and are all consistent with wall shock η near 0.7. The simple model apparently also consistently overpredicts the necessary wall shock amplitude to produce the effects by about 8 microns ($\sim$ 15%).

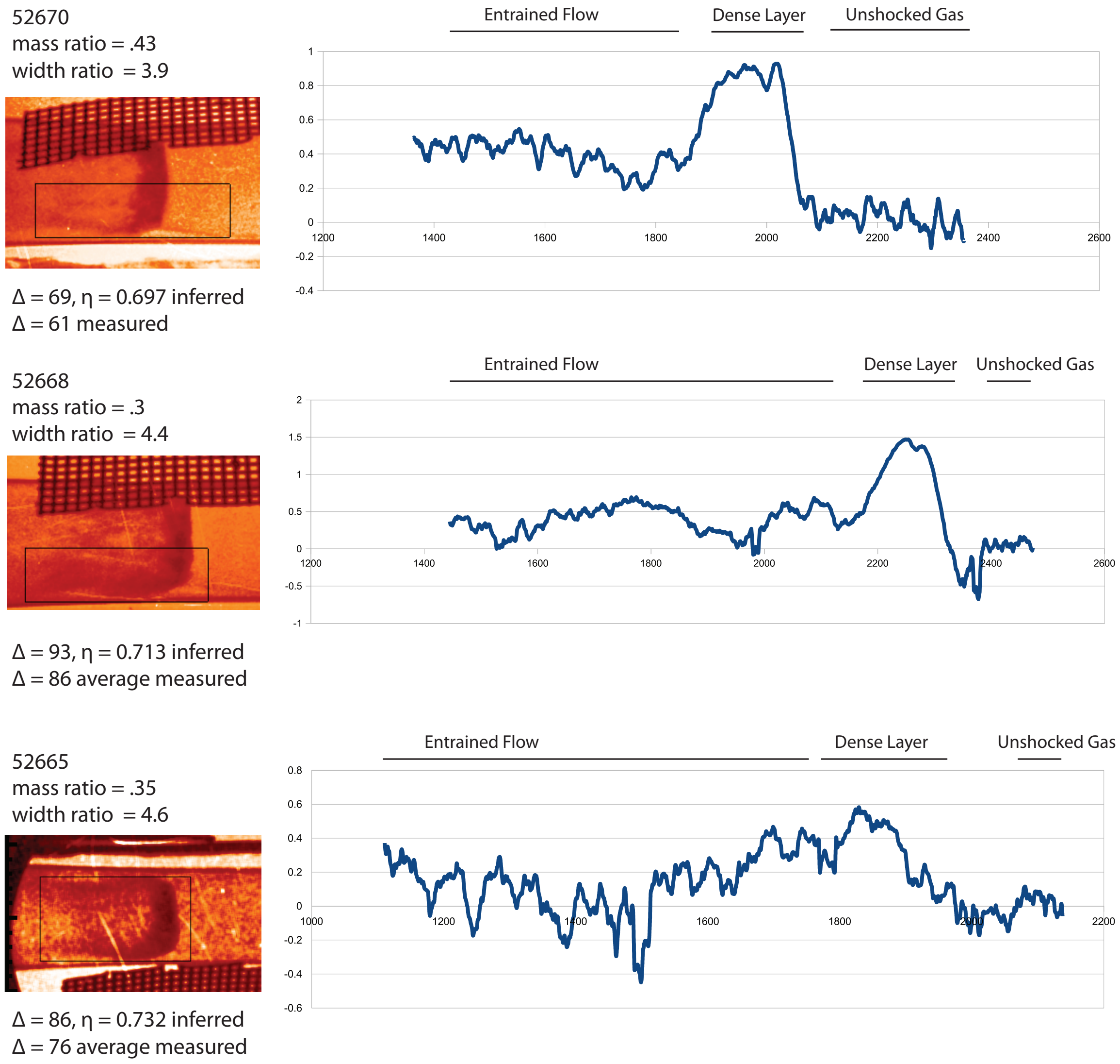

Figure 2.7: Data from shots 52670, 52668, and 52665. Distances (x-axis) are in microns, density (y-axis) is in arbitrary units.

2.3.2 Oblique shock relations

In the theory of oblique shocks in polytropic media without radiation, the passing of flow through the shock is completely described by the flow's incoming Mach number and the angle β at which the flow meets the shock. For a flow passing from state 1 to state 2, deflected through an angle θ, the relations by which one finds the post-shock deflection angle, Mach number, pressure, density, and speed of sound are well-known to be [16, 19]

$$\theta = \tan^{-1}\left(\cot(\beta)\frac{M_1^2\sin^2\beta}{1+\left(\frac{1}{2}(\gamma+1)-\sin^2\beta\right)M_1^2}\right) \tag{2.12a}$$

$$M_2 = \csc(\beta-\theta)\sqrt{\frac{M_1^2(\gamma-1)\sin^2(\beta)+2}{2M_1^2\gamma\sin^2(\beta)-\gamma+1}} \tag{2.12b}$$

$$\frac{P_2}{P_1} = \frac{2M_1^2\gamma\sin^2(\beta)-\gamma+1}{\gamma+1} \tag{2.12c}$$

$$\frac{\rho_2}{\rho_1} = \frac{\frac{1}{2}(\gamma+1)M_1^2\sin^2(\beta)}{\left(\frac{1}{2}(\gamma-1)M_1^2\sin^2(\beta)+1\right)} \tag{2.12d}$$

$$\frac{c_2}{c_1} = \frac{\sqrt{(\gamma-1)M_1^2\sin^2(\beta)+2}\sqrt{2\gamma M_1^2\sin^2(\beta)-\gamma+1}}{(\gamma+1)M_1\sin\beta} \tag{2.12e}$$

where γ is the polytropic index.

For the radiative shock, the relations for polytropes in Equations 2.12 do not apply. Instead, Equations 1.11 give a complete account of jump conditions for a given material given one incoming parameter normal to the shock. Because these conditions define the speed of sound upstream of the shock, the upstream Mach number does not vary simply as a flow approaches a radiative shock at different angles. The material flow velocity V_1 does behave straightforwardly, and will be used in place of the Mach number as the governing parameter for the radiative oblique shock relations. The angular deflection of flow through the oblique radiative shock θ is

$$\theta = \tan^{-1}\left(\frac{(1-\eta)\tan(\beta)}{\eta\tan^2(\beta)+1}\right) \tag{2.13a}$$

where η is the inverse compression ratio now found by solving Equations 1.11 for incoming velocity $V_s = V_1 \sin\beta$. Because the temperature ahead and behind the shock is equilibrated by radiative conduction, the pressure jump is found by

$$\frac{P_2}{P_1} = \frac{(1+Z_2)}{(1+Z_1)\eta} \tag{2.13b}$$

and the total postshock velocity is

$$V_2 = V_1\sqrt{\eta^2 \sin^2(\beta) + \cos^2(\beta)} \tag{2.13c}$$

under the same conditions for η, Z_1, Z_2.

Figure 2.8 shows the deflection angle θ as a function of incident shock angle β for both the radiative and polytropic shocks passing through the same incident flow. The radiative shock, due to its high compression ratio, obtains far higher maximum flow deflections than the polytropic shock. We also note that while the polytropic shock is defined only for $\beta > \sin^{-1} 1/M_1$, the radiative shock polar is defined over all β. In actuality, however, we expect that at some low β the normal component of the flow becomes sufficiently slow that the assumptions of strong radiation transport and thermal equilibrium ahead and behind the shock front are no longer justified. The radiative shock solution should therefore be expected in actuality to approach the polytropic solution for low β. However, for β near normal to the flow, the radiative solutions given here should be accurate.

2.3.3 Shock polars

A common method of investigating oblique shock effects is to construct shock polars [19] in the space of pressure jump *vs.* flow deflection, plotting the locus of flow states which can be reached by solving Equations 2.12 for all β for which the incoming normal flow is supersonic. We can similarly construct the radiative shock

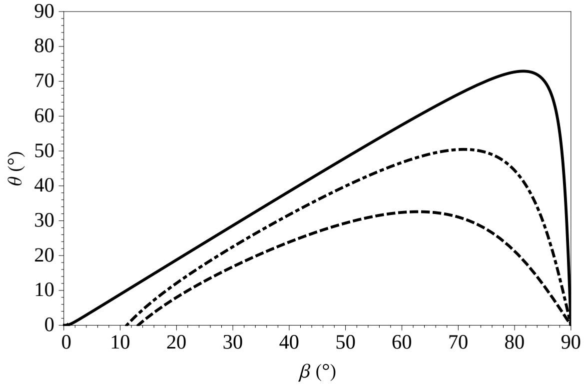

Figure 2.8: Flow deflection θ as a function of incident flow β for (solid curve) radiative flow from Equation 2.13a for xenon with $V_1 = 110$ km/sec and $\rho_1 = 0.006$ g/cm^3, and polytropic flow from Equation 2.12a with (dashed) $\gamma = 5/3$ at $M = 4.4$ and (dot-dashed) $\gamma = 1.2$ at $M = 5.2$, where the Mach numbers are consistent with 110 km/sec in the radiatively preheated case for each γ.

polar by solving Equations 2.13.

In systems containing both a radiative shock and a polytropic shock, certain rules must be established to obtain a unique solution. We define those rules:

1. Polytropic shock polars are parameterized by their flow's upstream Mach number, radiative shock polars are parameterized by their flow's upstream speed.

2. The speed of sound upstream of a radiative shock is a function of the flow speed normal to the radiative shock. If a radiative shock and a polytropic shock are both downstream of a region, then the Mach number upstream of the polytropic shock is a function of the angle at which the flow meets the radiative shock.

3. Flow which passes through a polytropic shock has a speed defined by the immediate post-shock sound speed implied by Equations 2.12. This speed may then be used as the incoming speed for a subsequent radiative shock. The density jump must also be calculated and used as the initial condition for the subsequent radiative shock.

4. Flow which passes through a radiative shock has a postshock Mach number

implied by Equations 1.11 and 2.13, which may then be used as the Mach number for a subsequent polytropic shock.

5. Each region bound by shocks and discontinuities is bound by at most one radiative shock. This prevents inconsistencies arising from multiple radiative shocks sharing an upstream region whose temperature they attempt to set to different values.

The process of solving systems with these rules is illustrated in two examples detailing the collision of a radiative and a polytropic shock.

2.3.4 Four wave interaction

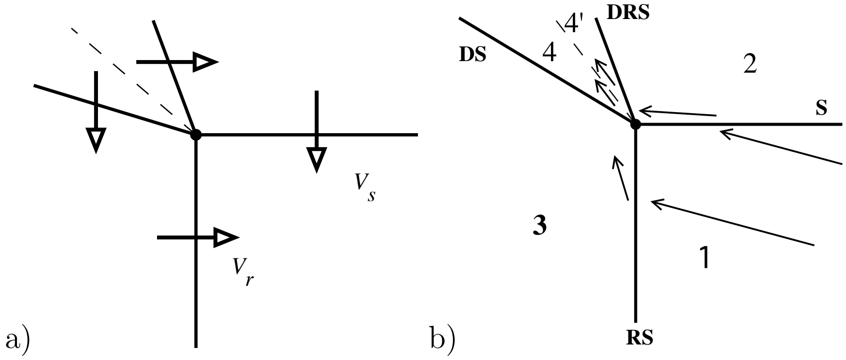

Figure 2.9: Schematic for analyzing the four wave intersection (a) in the frame of the upstream gas and (b) in the frame of the point of intersection. Angles are exaggerated. Solid lines indicate shocks: RS - Incident Radiative Shock, S - Incident Polytropic Shock, DRS - Deflected Radiative Shock, DS - Deflected Polytropic Shock. The dashed line indicates a slipstream.

We consider the four wave interaction shown in Figure 2.9a. In this figure, drawn in the frame of the incident radiating shock, a polytropic shock is advancing orthogonally downward, moving the shock interaction point with it. Figure 2.9b shows the (steady) flow schematic in the frame of the moving interaction point. Because the flow in region 3 is in this frame everywhere supersonic and therefore has no information about the incoming polytropic shock, the incident shock does not become curved and four waves

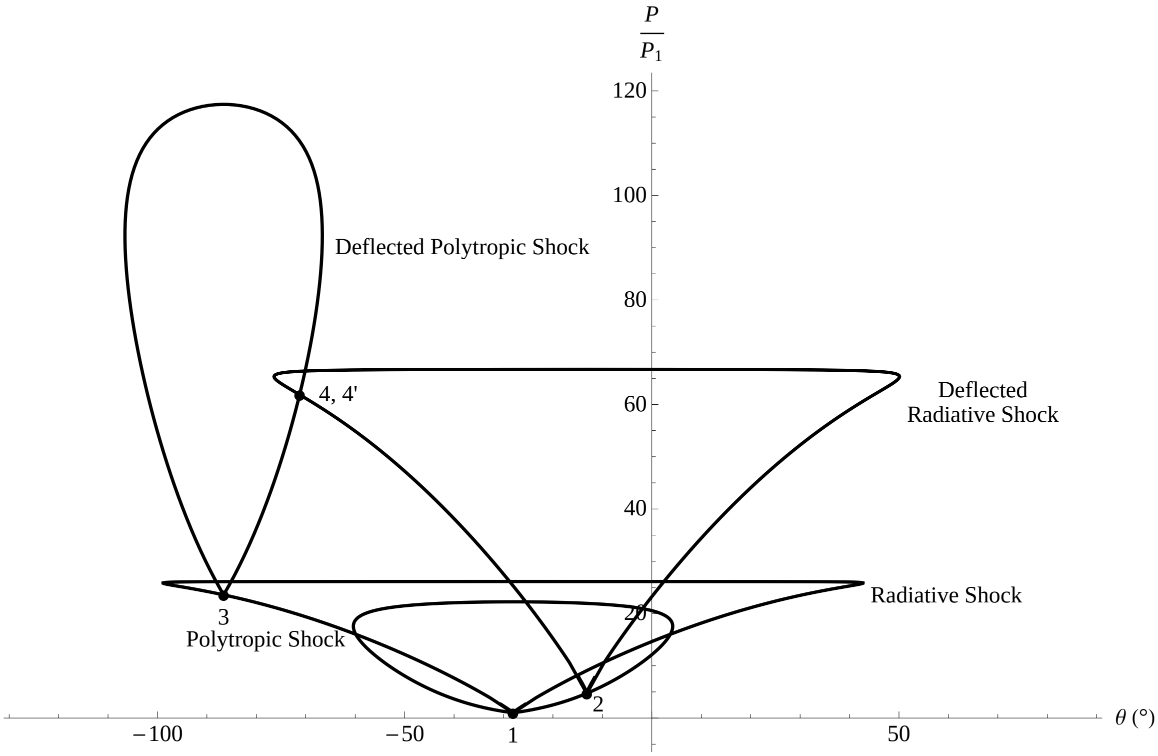

Figure 2.10: Shock polars for the four wave interaction

will meet at the interaction point. When the interaction point is steady or subsonic with respect to the upstream system, the topology changes to that with three waves discussed in Section 2.3.5.

We consider from here on the gas to be xenon at $\rho_1 = 0.006$ g/cm^3 with $\gamma = 5/3$. We consider the initial conditions of, in the frame of the upstream gas in region 1, an incident radiating shock at $V_r = 75$ km/sec, and an incident orthogonal polytropic shock advancing at $V_s = 40$ km/sec. In the frame of the moving interaction point, this is a flow with velocity $V_1 = 85$ km/sec at an angle of 28.1° to the horizontal. The shock polar construction for this flow is shown in Figure 2.10.

The flow through from region 1 to region 3 is first solved in order to obtain the sound speed in region 1. We obtain for region 3 flow moving with $\theta_3 = -86.6°$, $V_3 = 40.1$ km/sec, and $M_3 = 2.67$. As a check, we verify that $V_3 \sin\theta_3 = -V_s = -40$ km/sec, which means that the only velocity in the vertical direction is of the moving frame of the polytropic shock. In the frame of the radiative shock, this is flow entering and exiting the radiative shock normally.

By computing the jump from region 1 to region 3, we also obtain the Mach number of the flow in region 1, $M_1 = 4.24$. It is important in interpreting the Mach number in region 1 to be aware that it refers to the Mach number locally defined in the radiatively heated region immediately upstream of the shock. The Mach number relative to the unheated gas far upstream of the shock would be substantially higher (approximately 480).

Using the solution for M_1, we then pass the flow through the oblique polytropic shock to obtain state 2, in which the flow obtains the values $V_2 = 77.0$ km/sec and $\rho_2/\rho_1 = 2.28$. The angles of the deflected shocks are now both unknown parameters, which will be set by the conditions $\theta_4 = \theta_{4'}$ and $P_4 = P_{4'}$. We construct in the polar diagram a radiative shock polar with state 2 as the origin and a polytropic shock polar with state 3 as the origin. Their point of intersection (for the weaker of the two solutions) is $\theta_4 = -71.2^\circ$, $P_4/P_1 = 61.8$. We may also obtain from this analysis such values as the angle of the deflected wall shock with respect to the horizontal (i.e. the incoming flow in the frame of the incident radiating shock). The shock is found to have $\beta = 47.8^\circ$ to move from state 3 to state 4, where $\beta = 90^\circ$ is normal incidence. Taking this angle from state 3, we find that the deflected shock is inclined 38.8° above the horizontal.

We note that performing this calculation correctly in the pressure-deflection space has required the use of the radiative shock polars, particularly in the case of working with state 3, which requires the additional maximum turning angle of the radiative shock. The calculations involving state 3 take place in regions completely inaccessible to the non-radiative shock polars.

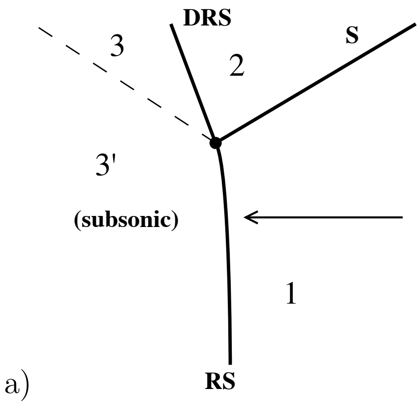

Figure 2.11: a) Schematic for analyzing the three wave intersection in the frame of the shocks. Solid lines indicate shocks: RS - Radiative Shock, S - Polytropic Shock, DRS - Deflected Radiative Shock. The dashed line indicates a slipstream.

2.3.5 Three wave interaction

We next consider the case where an oblique polytropic shock intersects a strong radiative shock, shown in Figure 2.11. A deflected radiative shock and a slipstream (shear flow boundary) exit the point of interaction, and the system is one of steady flow. Because the flow behind the radiative shock is subsonic to all other interactions in the system, the shock can become slightly curved in the vicinity of the triple point, eliminating an additional wave from the system [38]. The situation where this was not the case appeared in Section 2.3.4. Our consideration of this case is heavily influenced by comparison with experiments [23], in which the non-radiative wall shock intersects the primary radiative shock at an oblique angle. Because the triple-point is steady in these experiments, the flow behind the radiative shock will be subsonic, implying that the observed interaction will be of the three-wave type.

We will specify the upstream flow and angle at which the oblique polytropic shock meets the radiative shock and attempt to predict the downstream flow properties including the flow angle in regions 3 and $3'$. The angle of the deflected radiative shock is an unknown parameter in this exercise, and will be calculated from the condition that flow angles and flow pressures must be equal across the slipstream

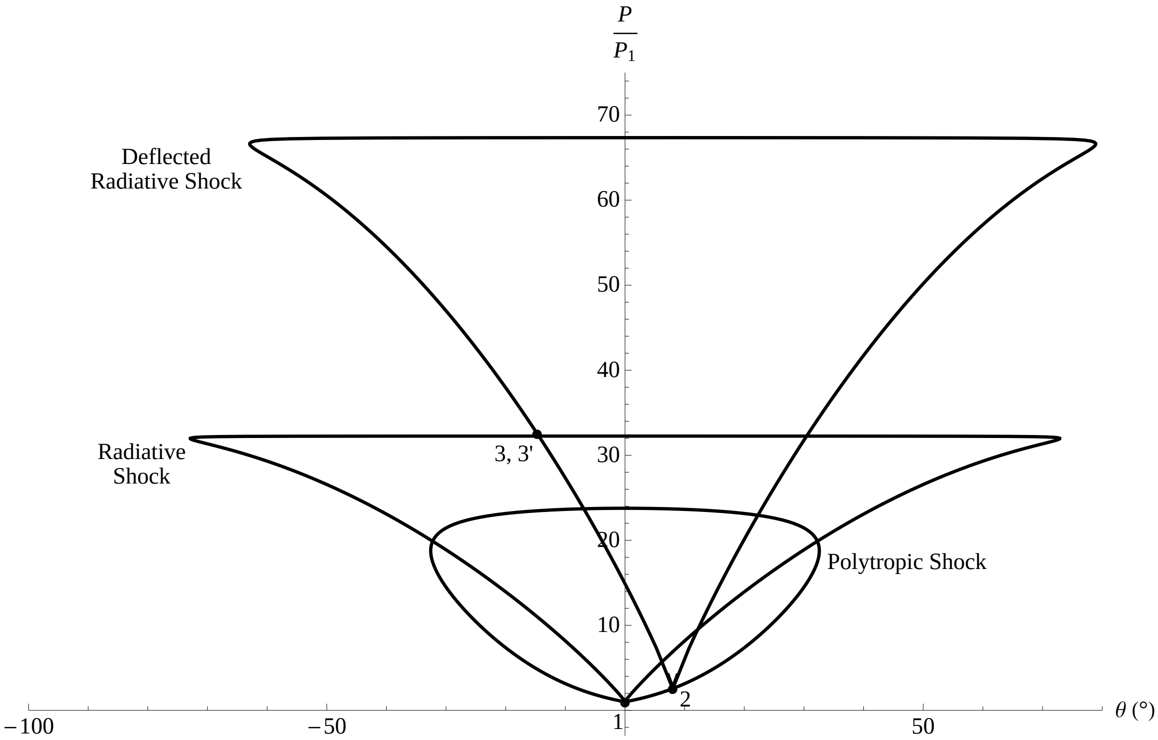

Figure 2.12: Shock polars for the three wave interaction.

separating regions 3 and 3′.

For initial conditions, we consider the incoming flow to have speed $V_1 = 110$ km/sec and to be normal to the lower areas of region 1. We take the angle of the polytropic shock in the system to be 20° with respect to the flow. This number is chosen to produce an angle θ_2 which matches a flow observed behind a non-radiative wall shock in experimental radiography of Omega Shot 52670.

By solving Equations 1.11, we obtain a speed of sound in region 1 of 25.1 km/sec, and an incoming Mach number of 4.38. This calculation also gives us the outgoing speed in region 3′ near the bottom of the figure, which is $V_{3'} = 2.47$ km/sec, or $M_3' = 0.115$. This will be nearly true throughout region 3′. The flow throughout region 3′ is subsonic.

We return to region 1 and solve the flow through the oblique polytropic shock, using the speed of sound in region 1 found above. Because the angle of the polytropic shock is set, we may find the flow in state 2 directly by evaluating Equations 2.13

with $\beta = 20.0°$. We find that $\theta_2 = 8.0°$, $P_2/P_1 = 2.56$, $\rho_2/\rho_1 = 1.71$, and that the flow exits with speed $V_2 = 106$ km/sec.

Because the angle of the deflected radiative shock and the curvature of the incident radiative shock are unknown, we must find them through the conditions $P_3 = P_{3'}$ and $\theta_3 = \theta_{3'}$. This can be done intuitively through the use of shock polars, shown in Figure 2.12. To represent passage through the deflected radiative shock, a radiative shock polar is placed with its origin at flow state 2, using the speed and material properties (i.e. density) and speed of state 2. The initial radiative shock polar intersects this deflected polar at $\theta_3 = -14.7°$, $P_3/P_1 = 32.6$. The flow in region 3 is supersonic.

Once one has obtained the state of region 3 in this method, one may calculate the required curvature of the radiative shock to produce this flow. One finds that the curvature of the radiative shock need only be 0.26°.

In the work by Doss *et al* [23] which first considered the interaction of radiative shocks with wall shocks, it was assumed that the flow in region 3 was subsonic, based on the observation that the flow avoids impacting into the wall. The calculations in Section 2.3.5 show, however, that there is no subsonic solution for flow in that region. The redirection of flow away from the wall therefore requires additional waves to exist in the system, which motivates the construction described in in Section 2.3.6.

2.3.6 Description of the shock tube experiment – six wave interaction

This section presents the steady radiative shock - polytropic shock interaction in the presence of a wall. The experimental system to be modeled is a radiative shock with speed V_r launched in xenon gas contained in a polyimide tube with inner diameter 575 μm. Introducing the wall in the radiative shock system, our previous rules are augmented by the additional item

6. Behind a radiative shock, a wall is a perfect boundary though which fluid does

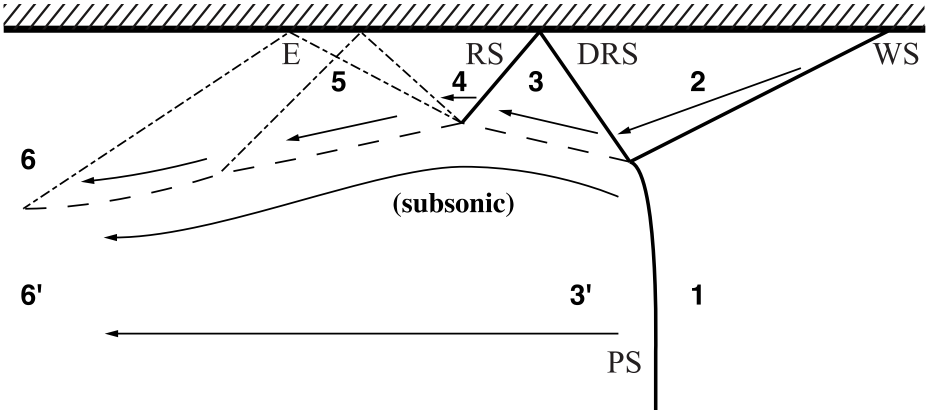

Figure 2.13: Schematic of the wave interactions and flow regions in the radiative shock tube experiment. Solid lines represent shocks, the dashed line represents a slipstream, and the dot-dashed lines represent expansion characteristics. PS - Primary (radiative) shock, WS - Wall shock, DRS - Deflected Radiative Shock, RS - Reflected Shock, E - Expansion region.

not pass. Ahead of a radiative shock, a wall is a material source of fluid propagating (in the frame of the wall) perpendicularly away from the wall.

The strong radiative transport upstream of a radiative shock drives an ablation event of wall material, which then flows into the fluid volume, driving a polytropic 'wall shock' into the system [23]. In the frame of the radiative shock, as shown in Figure 2.13, the wall shock is formed such that flow passing from region 1 to region 2 travels at the same angle as the flow emitted from the wall (with horizontal component V_r to the left and vertical component V_w downward).

We will in this section neglect the difference in materials emitted from the wall and the gas found in region 1. Furthermore, in regions 1 through 5 we will neglect to consider the shock tube an axisymmetric system, treating the area of interest instead as a plane two-dimensional system bounded on the top by a wall and on the bottom by a reflecting boundary condition (*not* a wall!). This simplification is justified while the flow remains at large distances from the tube axis. In the transition from region 5 to region 6, this simplification will be discarded.

The upstream material in region 1 is taken to be xenon at 0.006 g/cm^3 with $\gamma = 5/3$ throughout. The speed of the radiative shock V_r is 110 km/sec and the speed of the wall shock V_w is 49 km/sec (chosen to match $\theta_2 = 8.6$ as seen in Shot 52669). By solving Equations 1.11, the Mach number of the fluid in region 1 is 3.5.

The flow begins as in the three wave interaction, passing from region 2 to region 3 through a deflected radiative shock and from region 1 to subsonic region 3′ through the curved portion of the primary shock. As before, the curvature is found to be 0.5°, producing the outward flow at $\theta_3 = \theta_{3'} = 12.6°$.

Region 4 is bounded by the wall, behind a radiative shock and therefore not ablating. In order to produce flow parallel to the wall, $\theta_4 \neq \theta_3$, a shock reflection occurs producing a reflected shock. On the polar diagram Figure 2.14, the reflected shock is seen emitting from state 3 to a state constrained to $\theta_4 = 0$. We find from the intersection of the reflected shock with the ordinate axis $P_4 = 49\ P_1$.

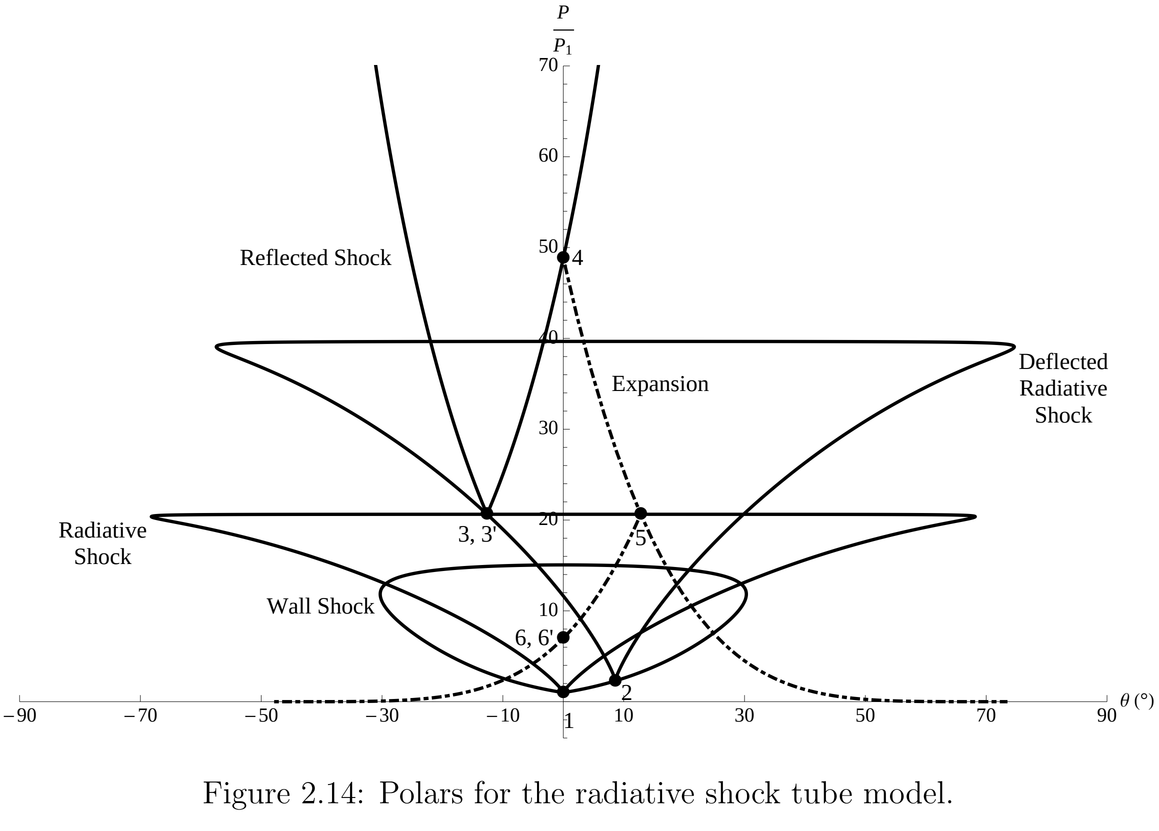

Figure 2.14: Polars for the radiative shock tube model.

Following Figure 2.13 we then see that the reflected shock intersects with the slipstream separating the region of supersonic flow near the wall with the region of subsonic flow near the center of the tube. Such interactions can in principle be quite complex, but we simplify the analysis to the following conditions. In the supersonic region, some form of wave, separating regions 4 and 5, will be reflected back into the supersonic region. No such standing wave can propagate into the subsonic region, and therefore the pressure is unaffected by the interaction. The reflected wave therefore cannot be another shock, which would increase pressure in passing from region 4 to region 5, but must instead be an expansion fan, decreasing the pressure to that in regions 3 and $3'$ [90]. The direction of streamlines in the subsonic region, however, can change in the vicinity of the interaction, and a kink in the subsonic-supersonic streamline will develop. To visualize this process, we may construct in Figure 2.14 a polar representing isentropic expansion of the flow originating in state 4 [19]. The Prandtl-Meyer expansion flow which obtains the final pressure $P_5 = P_3$ obtains an inward flow $\theta_5 = 12.8$. In general θ_5 is close but not equal to the negative of the outward flow in θ_3. Some of this difference comes from the difference between the shapes of Prandtl-Meyer expansion and shock compression polars, as shown in Figure 2.15, but in practice larger differences come from a nonzero θ_4, $\theta_5 \approx -\theta_3 - 2\theta_4$ due to the tube wall beginning its blow-out phase.

Finally, our flow's boundary conditions require that its final state (region 6) must be parallel to the wall ($\theta_6 = 0$). This is obtained by realizing that throughout region 5, where the characteristics of the expansion fan meet the wall they must reflect inward [84]. The reflected expansion curves the flow to again be parallel to the wall. While in general more reflections may result between the slipstream and the wall, the characteristics can terminate on the slipstream if the streamline is suitably curved. It will be assumed that the streamline obtains such a shape that no further reflections occur without any attempt to calculate this shape. Treating the passage through

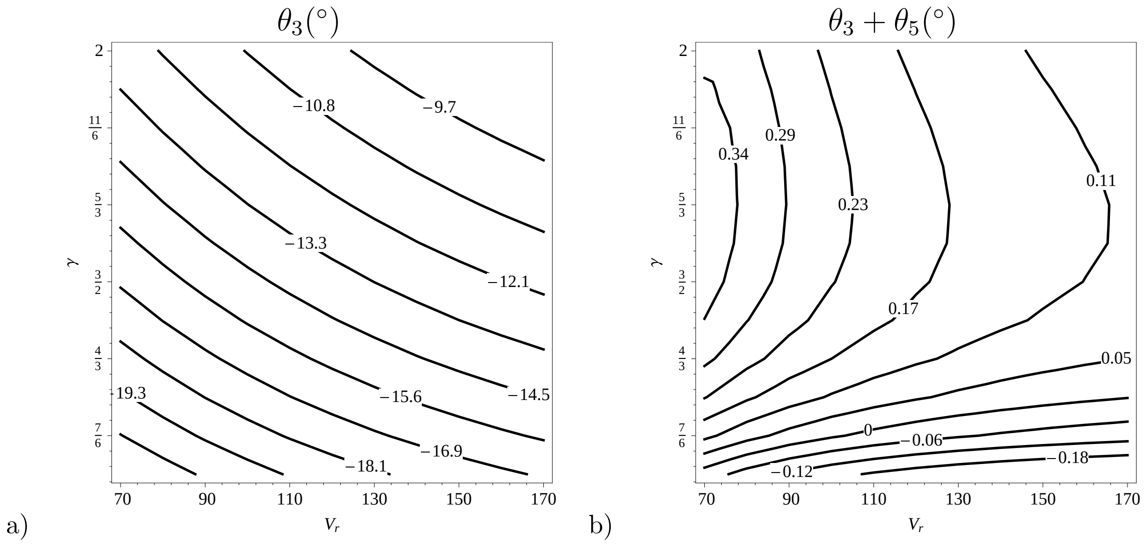

Figure 2.15: Contour plots for $\theta_2 = 8.6^\circ$ of a) θ_3 and b) $\theta_5 + \theta_3$ for varying V_r, γ. We see in the latter that the difference in magnitudes of θ_3 and θ_5 takes a maximum for $\gamma = 5/3$, and does not typically result in large differences.

the second expansion region as a single isentropic expansion, we see in Figure 2.14 that the final pressure is quite low relative to the immediate post-shock pressure, $P_6 = (1/4.6)P_3 = 7\ P_1$.

We will also approximate the effects in the subsonic region of lowering the pressure to $P_{6'}$. Modeling the flow in the subsonic region from region $3'$ to $6'$ as isentropic flow, we can obtain the final diameter of the initial flow. The xenon flow in region $3'$ has a Mach number of 0.1. For additional accuracy, we should regard the xenon as a piston pushing on rarefied beryllium expanded from the laser-absorbing ablator which launched the system, with speed and pressure equal across the material discontinuity. Under these conditions, the beryllium in state $3'$ has a Mach number of 0.05. Given the inner diameter of the tube is 575 μm, with 60 μm around the outside of the tube given to the wall shock and the supersonic region, one finds that to reduce the beryllium pressure from $P_{3'}$ to $P_{6'}$ requires contraction of the subsonic region to a diameter of 140 μm, and that the "subsonic" region has actually reaccelerated to a Mach number of 1.4 in obtaining region 6.

In calculating the states of flow in regions 5 and 6 only the simplest model of the interaction of the subsonic region boundary with the shock and expansion waves has been used. Reflected compression waves from the interaction of the expansion waves reflected off the wall with the slipstream have been neglected. In general, a final pressure boundary condition can be implemented easily by achieving a different final state. For example, a boundary condition requiring P_6 greater than that seen in Figure 2.14 but lower than $P_3 = P_5$, since the pressure in both the subsonic and supersonic regions decreases as the radius of the slipstream decreases, the final pressure will exist for some final radius of the subsonic boundary region.

Experimentally, the interface between shocked xenon and ablated wall material may be used as an optical tracer to image the various angles predicted by this analysis. Regions 1 through 5 are reliably visible in the experimental radiographs as regions of approximately unbent flows directed outward, parallel to the wall, and then inward. Table 2.1 and Figure 2.16 show some comparisons of radiographic data with theoretical predictions.

Measuring region 6 is host to a variety of difficulties, including that at early times the supersonic xenon may not have reached the end of region 5 (the assumption of a steady system has not been achieved), and that at all times distances far behind the tube the wall has began to explode outward under the high pressure, making $\theta_6 = 0$ no longer a reliable boundary condition. All measurements are subject to difficulties such as three-dimensional effects in the initial condition (i.e. non-planar primary shocks).

2.3.7 Inverted experimental case

When θ_2 exceeds a critical value, the solution found in Figure 2.13 changes character to that of the system seen in Figure 2.17. In Figure 2.14, this critical angle can be found as the angle θ_2 which causes the intersection of radiative polars to occur at

Shot Number	Angle	Experiment	Prediction
52665	θ_2	6.7 ±1.0	6.7*
	θ_3	-20.2 ±2.6	-19.7
	θ_4	-1.4 ±2.0	-1.4
	θ_5	13.3 ±1.8	17.6
52669	θ_2	8.6 ±1.3	8.6*
	θ_3	-11.0 ±3.2	-12.6
	θ_4	-0.2 ±3.4	0.0
	θ_5	13.0 ±2.1	12.8
52670	θ_2	8.0 ±1.3	8.0*
	θ_3	-14.4 ±4.3	-14.3
	θ_4	0.2 ±2.2	0.0
	θ_5	9.4 ±1.7	17.23

Table 2.1: Comparison of theoretical predictions to measured quantities. For each shot, the measured value of θ_2 was used to analytically predict the subsequent angles (for $V_r = 110$ km/sec, $\gamma = 5/3$). In shot 52665, the wall was measured to be experiencing blowout and have acquired an angle. Measured wall angles should be taken as having the same measurement error as θ_4.

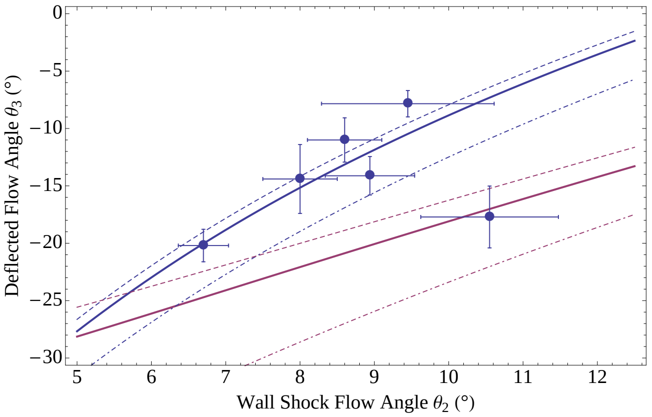

Figure 2.16: θ_2 *vs.* θ_3 measured in the October 2008 dataset and compared to (blue, solid) the radiative shock predictions and (red, solid) the non-radiative, purely polytropic predictions for for $V_r = 120, \gamma = 1.55$. The dashed lines show variation with γ in each case, from $\gamma = 5/3$ (above) to $\gamma = 1.2$ (below).

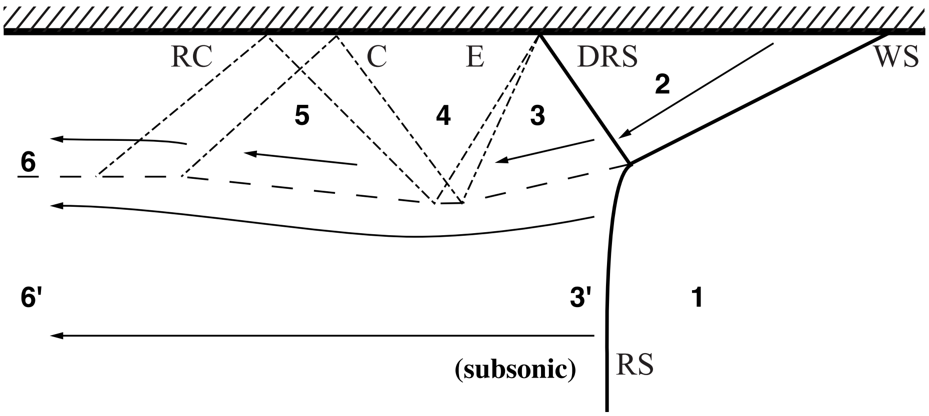

Figure 2.17: Schematic of the wave interactions and flow regions in the case where $\theta_3 > \theta_4 = 0$. Solid lines represent shocks, the dashed line represents a slipstream, and the dot-dashed lines represent isentropic expansion and compression characteristics. RS - Primary radiative shock, WS - Wall shock, DRS - Deflected radiative shock, E - Expansion region, C - Compression region, RC - Reflected compression region.

$\theta_3 = 0$. When $\theta_3 = 0$, no curvature is induced in the primary radiative shock and the flow behind both the primary and deflected radiative shocks is purely axial. No reflected shock is needed to align the flow with the wall, and so for $\theta_2 = \theta_{2c}$ only three waves exist in the system. For $V_r = 110, \gamma = 5/3$, we find that $\theta_{2c} \approx 13.5°$. The polars for this system are shown in Figure 2.18.

For $\theta_2 > \theta_{2c}$, $\theta_3 > 0$ and the flow in region 3 which has passed through the polytropic shock and the deflected radiative shock is still directed inward. In this case, shown in Figure 2.17, in order to accommodate parallel flow to the wall, $\theta_4 \neq \theta_3$, the deflected radiative shock reflects from the wall as an expansion fan. The expansion fan then interacts with the subsonic layer, reflecting as higher-order isentropic compression waves. We again consider the simplest case where the subsonic boundary is treated as a constant pressure boundary condition [84]. These compression waves will then later reflect off of the wall, and the process of reflection will in general continue until $\theta = \theta_4 = 0$ and any final downstream pressure condition is met.

The resulting flow pattern for high θ_2 is therefore inverted around the triple point

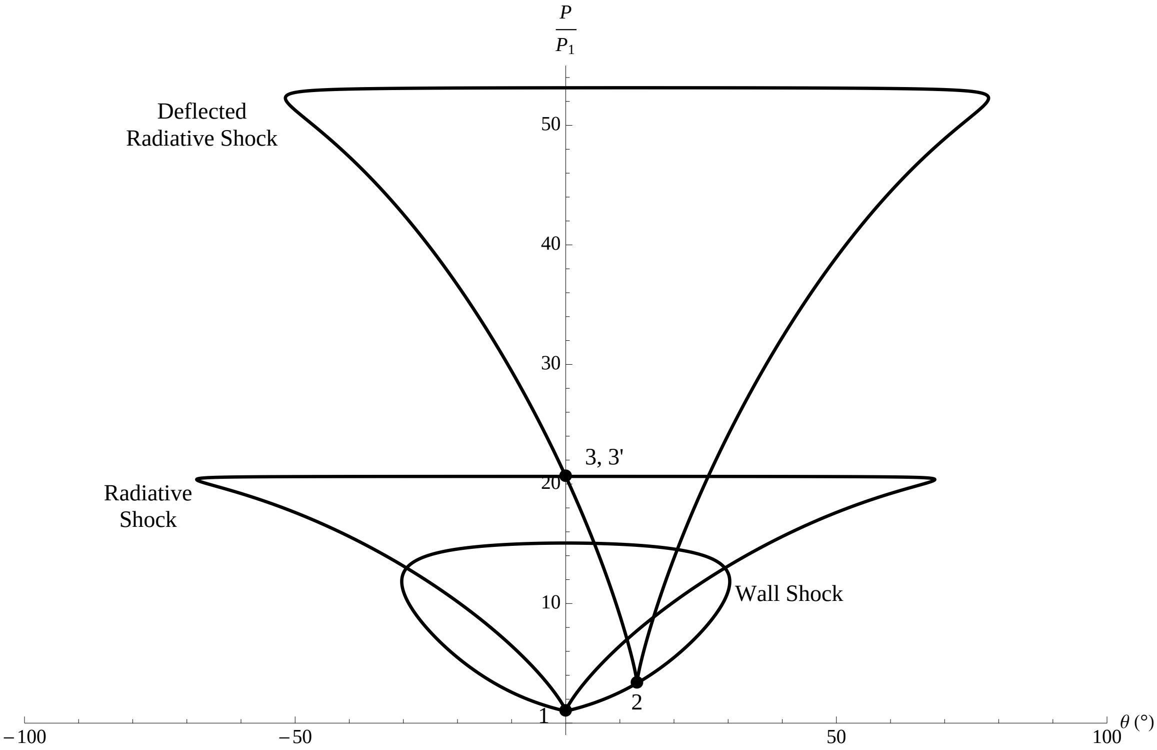

Figure 2.18: Shock polars for $\theta_2 = \theta_{2c}$. θ_3 satisfies the final flow boundary conditions, so only three shocks are needed to describe this system.

as compared to the low θ_2 result. While in Figure 2.13 the flow bows outward toward the wall and then recedes inward, in Figure 2.17 the flow is seen to bow concavely inward immediately after the shock. Figure 2.19 shows the shock polars calculated for this case.

2.3.8 The early primary shock / wall shock interaction

We consider the implications of the preceding analysis as an application to the wall shock [23]. The very early interaction of the wall shock, in which the wall blows out some distance ahead of the primary shock at the initial moment of the experiment, might be modeled as the situation in Figure 2.9a. Later, when the wall shock blowout point is traveling along a fixed distance ahead of the shock, the circumstances change to those in Figure 2.11.

Bridging these scenarios, the likely sequence of events, shown in Figure 2.20, begins

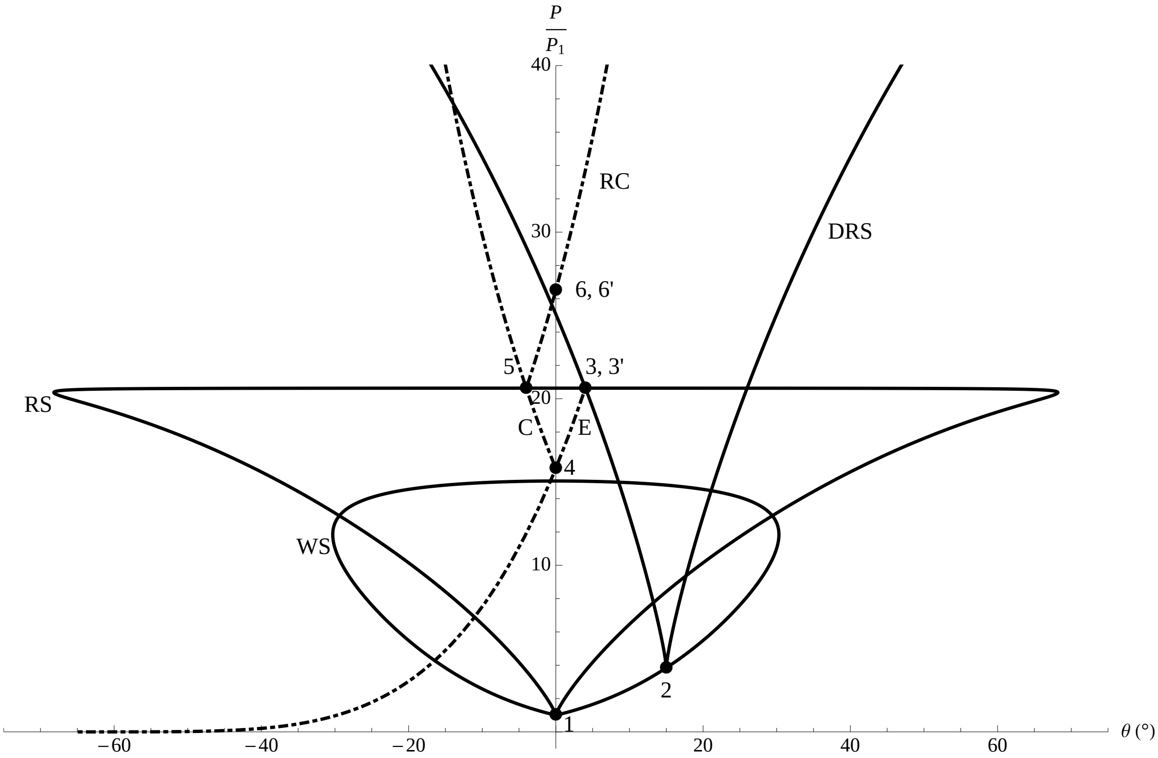

Figure 2.19: Polars for the radiative shock tube model with $\theta_2 > \theta_{2c}$. Polar labels are identified with wave labels used in Figure 2.17.

with the four-wave interaction point separating into two triple points. This process may have some analogy with the transition from regular reflection to Mach reflection in symmetric flows [6]. The area behind both the traveling deflected wall shock and incident primary radiative shock is now strictly subsonic to the system, implying that curvature in the incident shock and diffraction in the traveling shock might both be observed. In the case of the physical experiment, at some point the traveling shock will reach the tube centerline, possibly resulting in a reflection.

2.3.9 Shock refraction at the wall material boundary – thermal percursors

Boundary effects upstream of strong shocks have been observed in various forms since the era of explosively-drive shock tube experiments [86]. It was recognized early

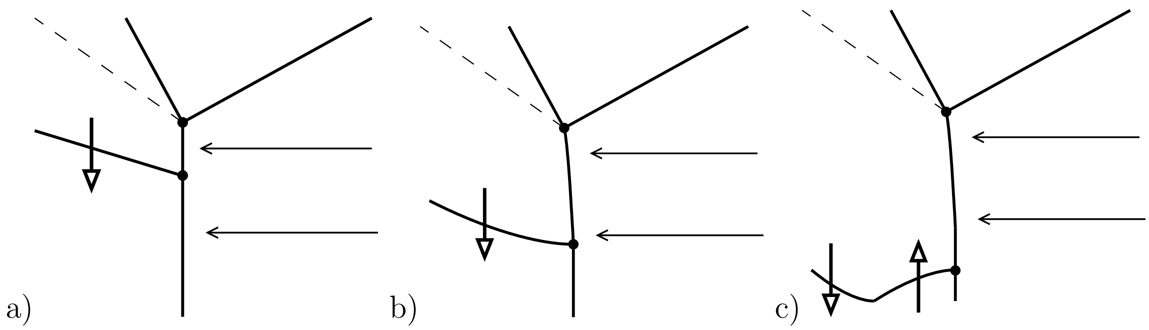

Figure 2.20: Schematics showing (a) the separation of the four-wave solution into two three-wave interactions, including possible (b) diffraction and (c) reflection of the traveling wave as it moves through the system.

on that this was the result of upstream heat propagation creating a thermal layer of evaporated wall material. Analysis of these boundary disturbances has often been paired with the concept of a precursor shock, a shock which may form in the refraction of a shock into a material with higher speed of sound, in which the transmitted portion of the shock detaches and travels freely upstream of the initial shock in the system [40]. The precursor refracts an oblique shock back to the initial shock of the system, which appears upstream of the initial shock.

This distinguishes the effect from that seen in these experiments, in which the upstream material is if the upstream tube material is vaporized and expands into the tube's gas content with supersonic velocity, acting as a piston to drive a new oblique shock into the system. These two mechanisms produce similar, related oblique shocks upstream of the shock, but produce extremely different flows downstream of the shocks. In particular, the thermal precursor leads whenever it appears to completely subsonic flow downstream, while the wall shock may under conditions discussed below lead to supersonic flow downstream.

Analytical and experimental investigations have included models with only thermal precursor shocks [2, 81, 32] but no wall shocks, as well as analyses with both thermal precursors and wall shocks [51, 1, 8]. Some of these were focused on the vortices inevitably generated behind the shocks in these cases. The original paper

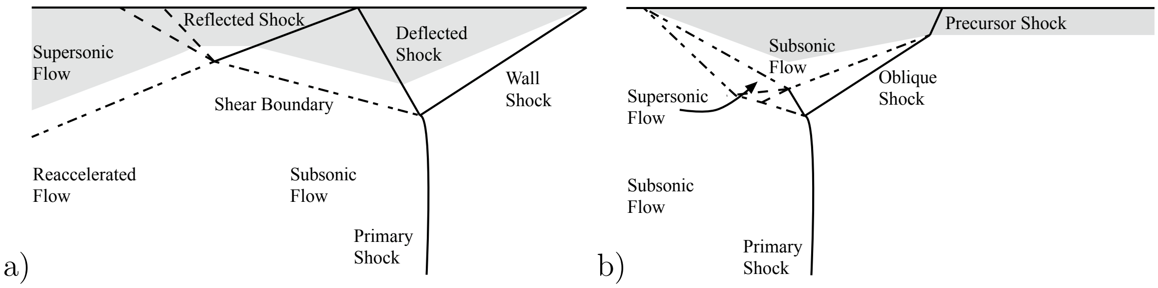

Figure 2.21: a) Shock topology in the radiatively driven wall shock, without refraction, as in Doss *et al* [22]. b) Shock topology in the thermal precursor shock, as in Grun *et al* [32]. The solid lines denote shocks, the dashed lines denote expansions, and the dot-dashed lines denote slipstreams.

of Shreffler and Christian considered only a wall shock without a thermal precursor, but did not go into detail regarding the effects on post-shock flow. The work in Section 2.3.6 analyzing boundary effects in their experiments has also considered only the wall shock, without either a thermal precursor or a refraction event at the material interface.

The two possible cases, with and without a thermal precursor, lead to very different predictions for global downstream behavior. The crucial difference between the two is whether or not the deflected branch of the primary shock encounters a subsonic gas region when it impacts the material composition boundary. The thermal precursor shock necessarily creates subsonic flow to exist at that region, causing the shock's reflected component to have the characteristics of rarefaction rather than compression. If, instead, the shock encounters a material boundary, a refraction event should occur, with both a transmitted component into the low-density tube material and a reflected component back into the gas medium. The reflected component may be a shock. This case is explored below.

The thermal precursor topology (shown in Figure 2.21b) forms a situation in which large regions of subsonic flow surround a small region of possibly supersonic flow (the flow which passes through both the oblique upstream shock and the deflected shock). The enclosed region of flow is convergent, and directed toward the wall, where it is fated to produce shocks, vorticity, and turbulence as it approaches the boundary. This results in subsonic flow throughout the post-shock regions. The reflection of the deflected shock as an expansion fan hastens this development, as it directs the flow more sharply toward the wall. However, as the results from Henderson (and his reproduction of results of a shock refraction experiment by Jahn [46] cf. Figure 13g in Henderson) show, the results of Mach refraction in the absence of the wall shock is already sufficient to create streamlines headed toward the wall which will result in vortices.

The circumstance which can prohibit the formation of a vortex is for a reflected shock (reflected from the refraction at the material interface) to impact a supersonic-subsonic slipstream, reflecting as a Prandtl-Meyer expansion fan. This event redirects the flow away from the tube wall and toward the tube center. The details of the downstream flow, including the expansion's interaction with the subsonic ablated tube wall material, are now a complicated transonic flow problem. It is conceivable that the ablated tube material responds to the expansion fan by reaccelerating into low-pressure supersonic flow (see for example the work in Ben-Dor [6, Figure 2.12] in predicting the height of a Mach stem). However, even if this does not occur, it is possible the resulting small subsonic region may have no further major effects on the system.

When the streamlines do not generate turbulence at the wall but are instead directed inward toward the tube center, the subsonic flow is able to reaccelerate. In principle, this can result in completely supersonic flow throughout the tube downstream of the shock, protecting the shock from a rarefaction from an unsupported source which might otherwise have converted the shock into a blast wave. In some sense, the presence of ablating tube material driving a wall shock may turn the tube into a sort of shock waveguide, allowing the shock to propagate longer distances than otherwise. Of course, this condition can be maintained only as long as the shock continues to radiate thermal energy upstream, which will cause slowing of the shock by radiative cooling and eventually slow the shock to non-radiative speeds.

2.3.10 Mach refraction at a slow-fast material interface in the presence of a wall shock

A numerical analysis using the theory of oblique radiative shocks [22] finds that Mach stem formation in the vicinity of the refraction event generates the necessary features for eventual downstream supersonic conditions. Figure 2.22 shows the geometry of shocks and the analysis using shock polars in the space of pressure increase *vs* flow angle.

A primary shock of speed 110 km/sec is used. The tube gas material is xenon with upstream density of 0.006 g/cm^3, preheated to upstream conditions of mean ionization $Z \approx 12.5$ and speed of sound $c_s \approx 25$ km/sec. The tube wall material is taken to be a mixture of carbon and hydrogen with effective molar mass of 7 g/mol and mean ionization of $Z \approx 3$, with a speed of sound in the vaporized region $c_s \approx 78$ km/sec and a density of 0.04 g/cm^3. Radiative shock models with optically thick-downstream thin-upstream assumptions are used for the primary, deflected, and transmitted shocks in the system.

The heart of the shock refraction is apparent in Figure 2.22b, in which both a radiative shock polar for the deflected shock in xenon as well as the transmitted shock in the tube material are present. The speed of sound is higher in the tube material and radiative effects are diminished due to the lower atomic weight of the tube material components, and the transmitted polar is therefore much smaller than the deflected polar.

Since it is known as part of the analysis that the deflected polar obtains a geometry such that it produces the flow labeled in Figure 2.22 as state 3, additional waves must bridge the states obtainable by the transmitted shock and the deflected shock. The

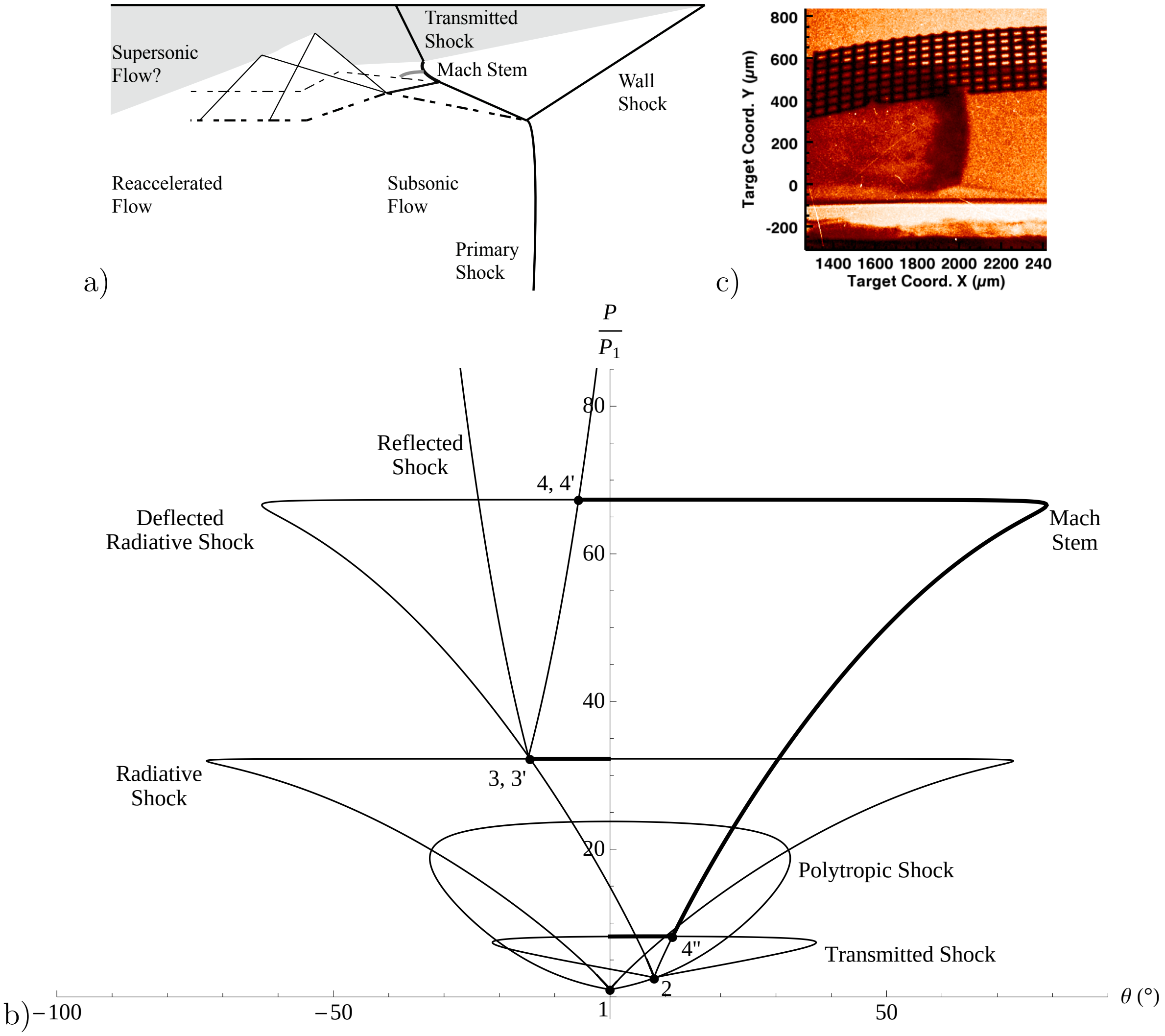

Figure 2.22: a) Schematic drawing of a wall shock's interaction with its driving primary radiative shock in the presence of refraction of the deflected shock at the material interface (compare with Figure 2.21a for labeling of waves common to both systems). The refraction creates a strongly curved Mach stem on the initial gas side and a curved transmitted shock in the tube wall material side and reflects a second straight shock into the initial gas. There is a region of subsonic flow behind part of the Mach stem, shown bounded by a gray curve, which returns to supersonic flow as the flow in the region converges. b) Shock polars for the Mach refraction. Thin curves represent the shock polars. Solid points represent uniform regions of gas accessed by shocks without curvature. Solid curves (most notably the Mach stem) represent regions of gas with continuously varying parameters accessed by curved shocks. Regions are numbered as 1) upstream conditions, 2) supersonic flow downstream of the wall shock, 3) downstream of the deflected shock, having passed through region 2, $3'$) subsonic flow downstream of the primary shock, 4) supersonic flow downstream of the reflected shock which has passed through region 3, $4'$) subsonic flow downstream of the mach stem, and $4''$) supersonic flow downstream of the Mach stem. The transmitted shock in the wall material is curved and spans subsonic states from the $\theta = 0$ axis to $4''$ The primary shock is curved in the vicinity of the shock interaction and accesses subsonic states spanning the $\theta = 0$ axis to $3'$. c)Radiography of Omega Shot 52670 [21], showing on the bottom of the image what appears to be the shock transmitted into the wall material, far downstream of the primary shocks.

theory of shock refraction laid out by Henderson [39] predicts for these conditions a system of curved shocks, and the appearance of a reflected wave and a Mach stem accomplish this, the latter being heavily curved to create a region which matches the pressure and flow direction boundary conditions on both sides. The height of this Mach stem is a free parameter in the current analysis, determined by the details of the downstream flow.

Again, the substantial difference between this and the case of the thermal precursor shock is that a shock has been reflected back into the medium instead of an expansion fan. This would be a minor difference if not for the subsonic-supersonic slipstream boundary between states 3 and $3'$. When the reflected shock reaches this interface and reflects as an expansion fan, it may expand the converging region downstream of the Mach stem before it converges and generates turbulence near the wall.

The downstream experimental radiography in the laser-driven Omega experiments shows the flow of material is initially toward the wall, but then redirects inward toward the tube center, implying the wall shock without thermal precursor case. Additionally, some images (e.g Shots 52670 and 52671) show what may be the transmitted shock in the ablated tube material, occurring well downstream of the primary shock (see Figure 2.22c).

2.4 Experiments with preheat

Interestingly, the visible signature of wall shocks is seen in systems which should not contain radiative shocks, but in which energy is instead deposited throughout the tube as a side-effect of the driving event. This is often referred to as *preheating* [7, 66, 55], and is thought to be the result of hot electrons and/or x-rays generated by laser-plasma interactions at the drive site. We report cases of laser-driven experiments in which the preheat appears to vaporize regions of the tube early in time, with similar consequences as in the radiative shock case. The existence of the preheat-driven wall

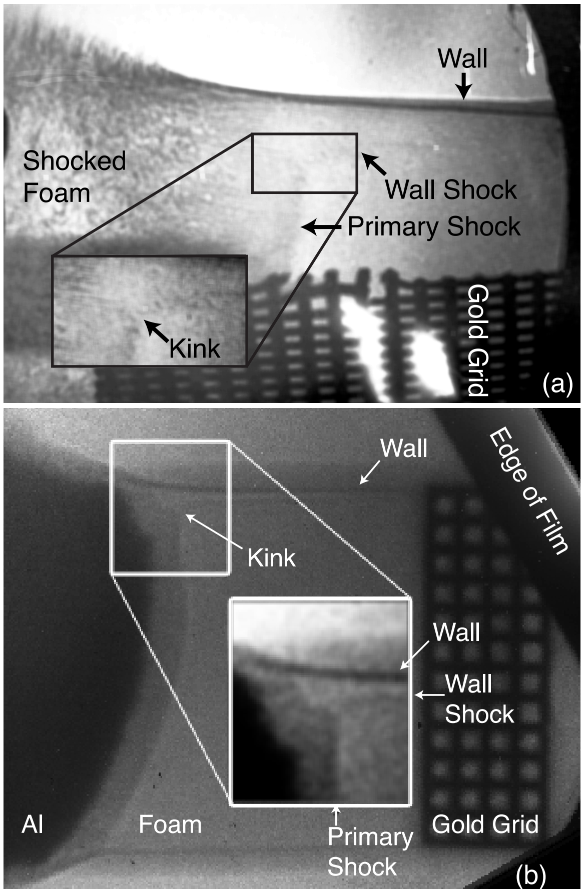

Figure 2.23: Radiographs of (a): an experiment on the Omega laser facility, shock traveling from left to right at ∼50 km/sec. The polyimide tube is 962 μm in diameter and filled with CH foam at .050 g/cc. For details on experiments of this type, see [56], (b): an Early Light experiment on the National Ignition Facility [71], shock traveling from left to right at ∼35 km/sec. The polystyrene tube is 800 μm in diameter and filled with carbon aerogel foam at 0.1 g/cc. For details of these experiments, see [11]

shock will be shown below to offer the experimenter who encounters it a method of diagnosing the degree of preheat.

Figure 2.23 shows wall shocks imaged by x-ray radiography in a supernova-relevant shock experiment (a) and a jet experiment's null test (b) [56, 11]. We notice that in Figure 2.23 the wall shocks extend well beyond the primary shock. By the time the primary shock reaches these later points, the wall shock will have progressed much further into the tube volume. It is possible in preheat-driven wall shocks to have $V_w > V_s$. If this is so, then while $\delta(x;t)$ is similar to that of the radiating shock-driven system, the wall shock position as experienced by the primary shock $\Delta(x)$ will be ever-increasing. Thus, in the preheat driven case the experiment never leaves its transient stage [compare with Figure 2.2(b)]. Shock interaction and convergence phenomena may be expected for the duration of the experiment and may have a significant influence on the long-term evolution of the primary shock.

We may estimate from the profile of the wall shock the temperature of the preheat event. Treating the adiabatic rarefaction of the shock tube material from the wall as a piston driving the wall shock [24], for the experiments shown in Figure 2.23(a) we infer a sound speed at the wall of 1.3 km/sec and wall temperatures on the order of 0.1 eV. This analysis has been carried out in greater detail in [58]. We also often observe these wall shocks to be highly asymmetric with respect to the tube axis, frequently appearing only on one side of the tube, with a Mach stem perhaps appearing elsewhere. The cause for this is presumably related to the details of the preheat event.

CHAPTER III

Instability in the Post-Shock Layer

Vishniac in 1983 [92] outlined a theory of instabilities for a system of a decelerating shock accreting mass, modeled as a thin mass shell layer possessing no internal structure. Later [94], the theory was expanded to include a layer of post-shock material, exponentially attenuating in density. Other work ([9, 59]; among others) has described the perturbation of self-similar solutions for the post-shock flow. The present work complements these investigations, modeling the post-shock flow as a finite thickness layer of constant density and considering both compressible and incompressible post-shock states. This allows us both to more clearly understand which mechanisms depend on the compressibility of the shocked gas and which are common to any shock system undergoing deceleration.

Early in the lifetime of an impulsively driven shock, when the post-shock layer thickness is small compared to its compressible length scale, an exponential scale cannot be formed and the density profile may be closely approximated by a square wave, as a fluid everywhere of constant density. In the shock's frame, upstream fluid is entering the shock with a speed V_s and exiting it with a speed $U = V_s\eta$, where η is the inverse compression ratio associated with the shock, including both the initial density increase of the shock and any subsequent, localized further density increase in consequence of radiative cooling [24].

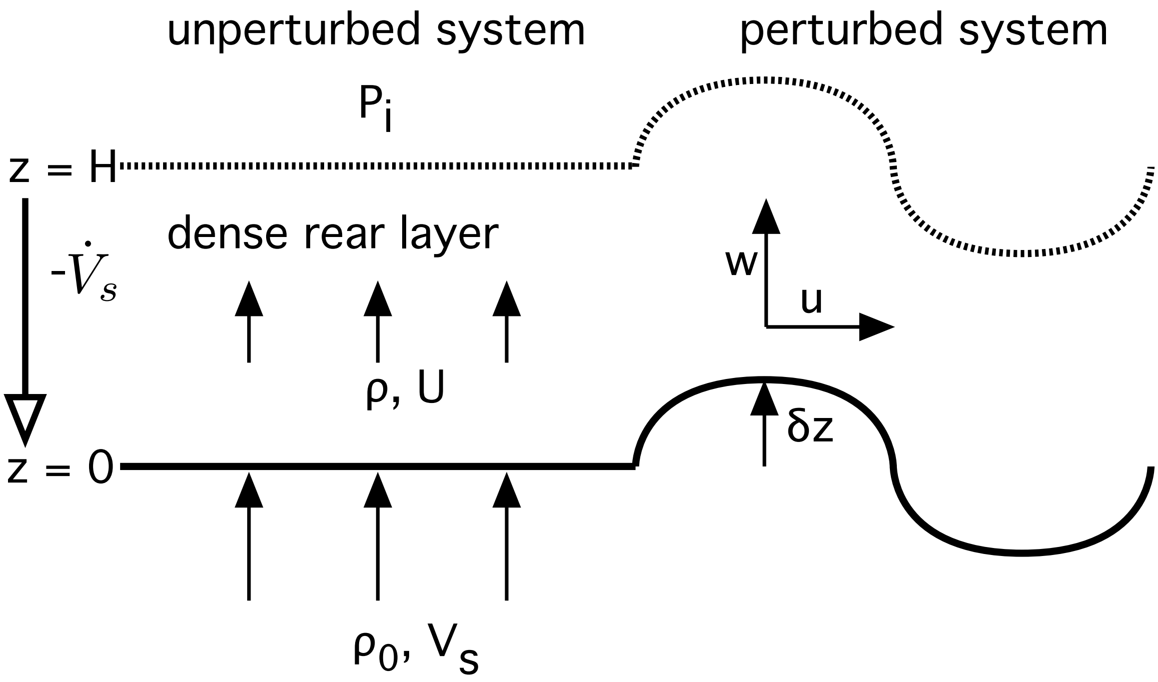

Figure 3.1: Schematic of the decelerating shock system. The solid black line is the shock, the dashed line above the dense rear layer is the rear material interface. The left-hand arrow depicts the in-frame inertial force with acceleration ($-\dot{V}_s$).

3.1 System of a decelerating shock with a dense downstream layer

We consider the shock in its own, decelerating frame. The system is depicted in Figure 3.1. The shock is placed at $z = 0$, with flow entering it from the negative z direction at speed V_s, density ρ_0, and with negligible thermal pressure. Flow is exiting the shock toward positive z with speed U, density ρ, and isotropic pressure P. We will model the downstream, rear layer as a constant density region of finite, increasing thickness from $z = 0$ to $z = H$. The rear surface of the dense layer will be taken to be a free interface at constant pressure. Beyond the rear layer will be taken as a region of constant thermal pressure P_i.

The native surface wave modes in the system will be right- and left-propagating waves on the two surfaces of the dense layer, leading to four modes in total. As drawn in Figure 3.1, the upper surface, a material discontinuity, is stable if the shock frame is decelerating and is characterized by surface gravity modes. The bottom surface, a shock at which compressibility is not suppressed, will feature propagating acoustic modes. The waves which appear in our coupled system will be modifications of these waves which appear on these surfaces in isolation. In particular, the modified acoustic waves along the shock surface will be identified as bending modes of the entire dense layer.

In order to understand the fundamental cause of the instability, we will here be considering the fluid both ahead and behind the shock to be held at (different) densities constant in both space and time. This practice is described and defended by [36], who in their book "consider constant-density hypersonic flows, though we should never consider the fluid in a hypersonic flow as incompressible." The pressure profile behind the shock is hydrostatic, $P(z) = P_i - (H - z)\rho\dot{V}_s$, which leads to increasing pressure at the shock front when the shock is decelerating. Perturbations to density by the waves under investigation will be discussed.

3.2 Linear perturbations of the system

3.2.1 Solutions inside the post-shock fluid

We begin with the inviscid fluid equations

$$\rho(\partial_t \underline{v} + \underline{v} \cdot \nabla \underline{v}) = -\nabla P - \rho \dot{V}_s \hat{z} \tag{3.1}$$

$$\partial_t \rho + \underline{v} \cdot \nabla \rho = -\rho \nabla \cdot \underline{v} \tag{3.2}$$

with total velocity $\underline{v} = (u, 0, w + U)$ and $P = P + \delta P$. We will insert the perturbation $\delta\rho$ only in the continuity equation; the coupling of $\delta\rho$ to the frame's acceleration will be suppressed. This allows us to ignore mode purely internal to the layer, concentrating on the overall shock and layer system. Since $\log\ \rho/\rho_0 \gg \log\ (\rho + \delta\rho)/\rho$

for any reasonable density perturbations, we expect the dynamics of the system to be dominated by the compression at the shock. The omission of the term $\delta\rho\dot{V}_s$ is also required for mathematical consistency with the assumption of our square wave density profile; the system will otherwise begin to evolve into an exponential atmosphere. Since the system *will* in actuality evolve into a compressed density profile, this limits the present analysis to early times. An analysis retaining the effects of this term and the exponential density profile was carried out in Vishniac and Ryu [94], but is mathematically opaque; their results will however be used in Chapter VI. In this chapter, the constant-density model will be investigated to show the conditions of instability and interaction of different physical properties in creating or stabilizing the perturbation growth.

We first let the perturbations $u, w, \delta P$ have time and space dependence as e^{nt+ikx}, with k real and n complex. The perturbations will be growing with time for $\mathrm{Re}(n) > 0$. We then linearize the x- and z- components of the momentum equation to obtain

$$(n + U\partial_z)u = -\frac{ik\delta P}{\rho} \tag{3.3}$$

$$(n + U\partial_z)w + w\partial_z U = -\frac{\partial_z \delta P}{\rho}. \tag{3.4}$$

We expressed the perturbed continuity equation in terms of perturbed pressure,

$$iku + \partial_z w = -\frac{(n + U\partial_z)\delta\rho}{\rho} = -\frac{(n + U\partial_z)\delta P}{\rho c_s^2} \tag{3.5}$$

where $c_s^2 = \partial P/\partial\rho$. We solve Equation 3.3 for δP using Equation 3.5, and discard terms of order U/c_s to obtain

$$\delta P = \frac{\rho}{k^2 + n^2/c_s^2}(n + U\partial_z)(-\partial_z w) \tag{3.6}$$

and insert that into Equation 3.4 to obtain a new equation for z-momentum:

$$(n + U\partial_z)w + w\partial_z U = \partial_z \left(\frac{1}{k^2 + n^2/c_s^2}(n + U\partial_z)(\partial_z w) \right) \tag{3.7}$$

which can now be written as a differential equation for w (taking U and c_s constant throughout the post-shock layer),

$$\left(\frac{U}{k^2 + n^2/c_s^2}\partial_z^3 + \frac{n}{k^2 + n^2/c_s^2}\partial_z^2 - U\partial_z - n \right) w = 0. \tag{3.8}$$

We define

$$j = \sqrt{k^2 + n^2/c_s^2}, \tag{3.9}$$

which describes the effective lateral wavenumber. As a wave approaches the acoustic case, $n^2 = -k^2 c_s^2$, the wave becomes purely longitudinal and j tends toward zero. Equation 3.8 has the general solution

$$w = Ae^{jz} + Be^{-jz} + Ce^{-nz/U}. \tag{3.10}$$

The system accordingly has three boundary conditions at its two interfaces: the shock and the rear surface. We note that the shock frame's acceleration $\dot{V}_s$ does not appear in the general form of the perturbations; it will enter into the system through the boundary conditions.

The last term in Equation 3.10 is a consequence of the background flow U and is closely connected with structures convecting downstream with that velocity. It is instructive to consider the general solution for w in the frame of the rear surface. We introduce the coordinate $z' = Ut - z$. In addition, we will now write explicitly the implicit time-dependence e^{nt}. The general solution is $w = Ae^{(n+jU)t-jz'+nt} + Be^{(n-jU)t+jz'} + Ce^{nz'/U}$. We see that the third term has no time-dependence in the frame of the rear layer. In the frame of the rear surface, these flow structures are generated by perturbations in the shock surface as the shock passes some point in space, and do not evolve further. Therefore, in the frame of the shock, this term describes flow structures convecting downstream through the flow with constant velocity U. We take the shock to have been perfectly planar at the instant, some time past, at which the shock's deceleration and rear layer formation began. This allows us to explicitly set $C = 0$ at the rear layer. We assume however that the perturbation began sufficiently early in time that our treatment using Fourier modes is sufficient, so no further information from initial conditions will be incorporated at this time.

3.2.2 An infinitely thin layer

We recall that the dispersion relation for the thin shell instability in its most simple form, without the effects of compression, is in [94] written in the form

$$n^4 + n^2 c_s^2 k^2 - \frac{k^2 \dot{V}_s P_i}{\sigma} = 0 \tag{3.11}$$

where σ is the areal mass density of the (infinitely) thin layer, and all other variables are as we have defined them. Early work [92] derived this expression for a shock of infinitesimal height but finite areal density. Such a shock, maintaining an infinitely thin layer height while continuing to accrete mass from the incoming flow, would in our analysis be described as the limit of an infinite compression, $\eta \to 0$. We should expect solutions we obtain for layers of finite thickness to approach Equation 3.11 in this limit.

3.2.3 A free rear surface

We construct the boundary condition describing a free layer at $z = H$ by applying $\delta P = \rho(-\dot{V}_s)\delta z$ at $z = H$, with $\partial_t \delta z = w$. Using Equation 3.10 and our earlier expression for δP, Equation 3.6, the boundary condition becomes

$$A(n^2 - j\dot{V}_s)e^{jH} + B(-n^2 - j\dot{V}_s)e^{-jH} = 0 \tag{3.12}$$

where C has been explicitly set to zero as discussed above. Equation 3.12 is a boundary condition well known to generate surface gravity waves, when $j = k$ and when paired with a rigid boundary condition at $z = 0$.

At the shock surface, we must perturb the shock momentum jump condition in the frame of the moving shock. The perturbed shock surface moving upward in Figure 3.1 sees a weaker incoming flow. In addition, by raising the shock surface in the hydrostatic pressure field, the effective post-shock pressure drops by an amount $\dot{V}_s\rho\delta z$. Our jump condition has now become

$$\rho_0(V_s - w)^2 = \rho U^2 + (P + \dot{V}_s\rho\delta z + \delta P), \tag{3.13a}$$

from which we obtain a boundary condition (using $\rho_0 V_s = \rho U$, $\delta z = w/n(1-\eta)$, and our earlier expression for δP in Equation 3.6)

$$\left(\frac{U}{j^2}\partial_z^2 + \frac{n}{j^2}\partial_z - \left(\frac{\dot{V}_s}{n(1-\eta)} + 2U\right)\right) w\bigg|_{z=0} = 0. \tag{3.13b}$$

The expression for $\partial_t\delta z$ comes from conservation of mass across the shock. With density perturbations suppressed, as discussed above, we have a balance of mass flux with $\rho_0 V_s$ entering and $\rho U + w$ leaving the shock, with the shock moving at speed $\partial_t\delta z$.

$$\eta = \frac{U}{V_s} = \frac{U + w - \partial_t\delta z}{V_s - \partial_t\delta z} \tag{3.14a}$$

implying (with $\partial_t = n$)

$$w\bigg|_{z=0} = (1-\eta)n\delta z \tag{3.14b}$$

The third boundary condition comes from oblique shock relations. Letting β be the angle of the shock surface perturbation, continuity of the tangential flow requires to first order $u \approx V_s\beta = (ik)V_s\delta z$. Applying the continuity equation of Equation 3.5 just downstream of the shock, and applying Equations 3.6 and 3.14b

$$\left(\partial_z - \frac{V_s k^2}{n(1-\eta)}\right) w\bigg|_{z=0} = -\frac{(n + U\partial_z)\delta P}{\rho c_s^2} \tag{3.15a}$$

which evaluates to

$$\left(\partial_z - \frac{V_s j^2}{n(1-\eta)}\right)\ w\bigg|_{z=0} = 0 \tag{3.15b}$$

Simultaneously applying these three conditions (equations 3.12, 3.13b, and 3.15b) on w, one demands for nonzero solutions that the determinant of the matrix of coefficients of A, B, and C, shown collected in Equation 3.16, must be zero,

$$\begin{vmatrix} (n^2 - j\dot{V}_s)e^{jH} & (-n^2 - j\dot{V}_s)e^{-jH} & 0 \\ -\frac{n}{j} + U + \frac{\dot{V}_s}{n(1-\eta)} & \frac{n}{j} + U + \frac{\dot{V}_s}{n(1-\eta)} & 2U + \frac{\dot{V}_s}{n(1-\eta)} \\ \frac{1}{j} - \frac{V_s}{n(1-\eta)} & -\frac{1}{j} - \frac{V_s}{n(1-\eta)} & -\frac{n}{Uj^2} - \frac{V_s}{n(1-\eta)} \end{vmatrix} = 0 \tag{3.16}$$

From this one obtains, with some manipulation, the dispersion relation,

$$\begin{gathered} 0 = (1-\eta)n^2 + j^2UV_s + (j\dot{V}_s + 2njU)\times \\ \left(\frac{(n^3 + j^2U\dot{V}_s) - (nj\dot{V}_s + n^2jU)\tanh jH}{(n^3 + j^2U\dot{V}_s)\tanh jH - (nj\dot{V}_s + n^2jU)}\right). \end{gathered} \tag{3.17}$$

We will take, as in [94], the product UV_s to be equivalent to an average sound speed squared $\langle c_s^2\rangle$, which we shall not henceforth distinguish from the sound speed c_s^2 of material compressibility. The qualitative classification of solutions to Equation 3.17 depends strongly on the layer thickness H, specifically on its relation to the compressible scale height $UV_s/|\dot{V}_s| = c_s^2/|\dot{V}_s|$. We shall explore this dependence in what follows, noting again that the assumed density profile is sensible only for $H < c_s^2/|\dot{V}_s|$.

We will now investigate the range in which wavelengths of perturbations are not much shorter than H, and will approximate $\tanh jH \approx jH$. The existence of the critical H is easiest to see in the limit of very strong, highly compressive shocks ($U \to 0$ while $V_s \to \infty$ in such a way that $UV_s = c_s^2$ and $\dot{V}_s$ remain constant). By expanding j, we may write the dispersion relation as,

$$Tn^4 + n^2 \left(k^2 c_s^2 - \frac{\dot{V}_s^2}{c_s^2} SZ \right) - k^2 \dot{V}_s^2 S = 0 \tag{3.18a}$$

where we have introduced scale factors

$$T = 2 - \eta \tag{3.18b}$$

$$S = 1 + \frac{c_s^2/\dot{V}_s}{H} \tag{3.18c}$$

$$Z = 1 - \frac{\eta(S-1)}{S}. \tag{3.18d}$$

For strong shocks, $T \sim (\gamma+3)/(\gamma+1)$, in which any effects of strong radiation are included in γ as an effective polytropic index describing the total density increase at the shock [49]. Z is typically close to 1. Solutions of Equation 3.18, shown in Figure 3.2, yield instability for k in the range $k_1 < k < k_2$, centered around a wavenumber of maximum instability k_m, where

$$k_1 = \frac{|\dot{V}_s|\sqrt{-S}}{c_s^2} \sqrt{2T - Z - 2\sqrt{T^2 - TZ}} \tag{3.19a}$$

$$k_2 = \frac{|\dot{V}_s|\sqrt{-S}}{c_s^2} \sqrt{2T - Z + 2\sqrt{T^2 - TZ}} \tag{3.19b}$$

$$k_m = \frac{|\dot{V}_s|\sqrt{-S}}{c_s^2} \sqrt{T} \tag{3.19c}$$

We find that k_1 and k_2 are real for $S < 0$, requiring $\dot{V}_s < 0$ and $H < c_s^2/|\dot{V}_s|$, conditions defining a decelerating shock and a layer width shorter than a scale height.

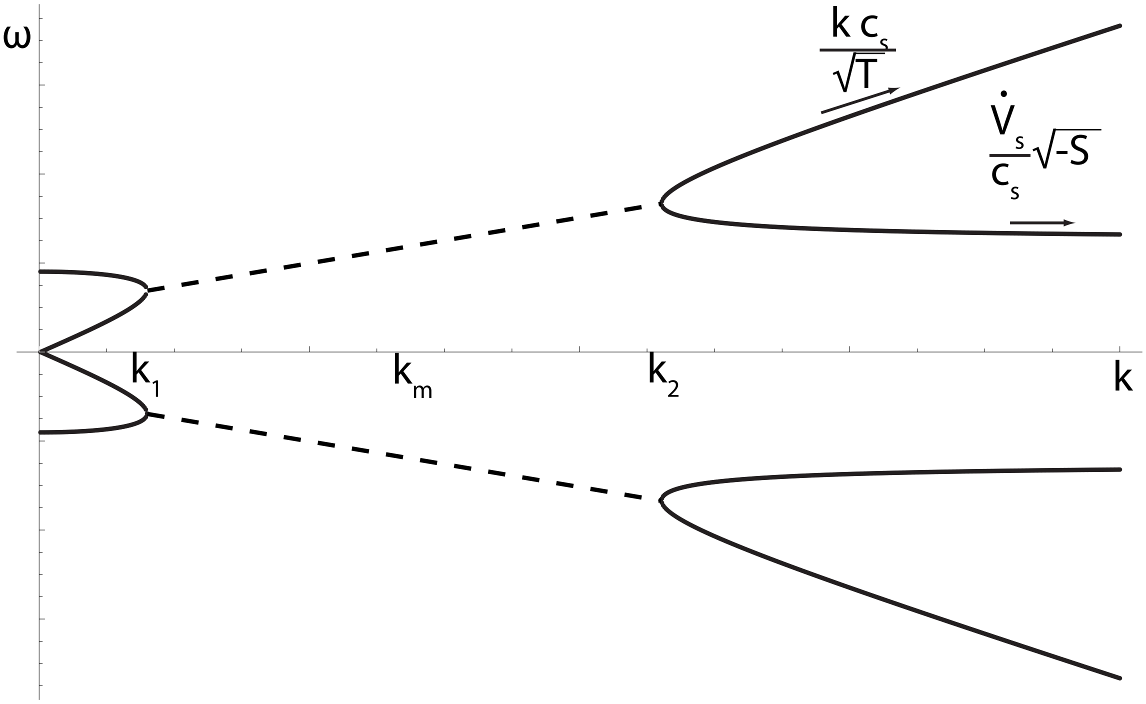

Figure 3.2: Plot showing solutions of Equation 3.18, $\omega = \mathrm{Im}(n)$ *vs.* k. The dashed line denotes the region of instability, where $\mathrm{Re}(n)$ is nonzero.

For the high compression limit $T = 2$, $Z = 1$, the critical wavenumbers take the values

$$k_1 = \frac{|\dot{V}_s|\sqrt{-S}}{c_s^2}\sqrt{3-\sqrt{8}} \sim 0.293 k_m \tag{3.20a}$$

$$k_2 = \frac{|\dot{V}_s|\sqrt{-S}}{c_s^2}\sqrt{3+\sqrt{8}} \sim 1.707 k_m \tag{3.20b}$$

$$k_m = \sqrt{2}\frac{|\dot{V}_s|\sqrt{-S}}{c_s^2} \tag{3.20c}$$

The solutions for growth rate at the fastest growing wavelength are

$$n_m = \pm\left(\sqrt{\frac{1}{8}} \pm i\sqrt{\frac{7}{8}}\right)\frac{|\dot{V}_s|\sqrt{-S}}{c_s} \tag{3.21}$$

which allow us to verify that for $k = k_m$, $jH = (k_m^2 + n_m^2/c_s^2)H$ remains small, validating our assumption.

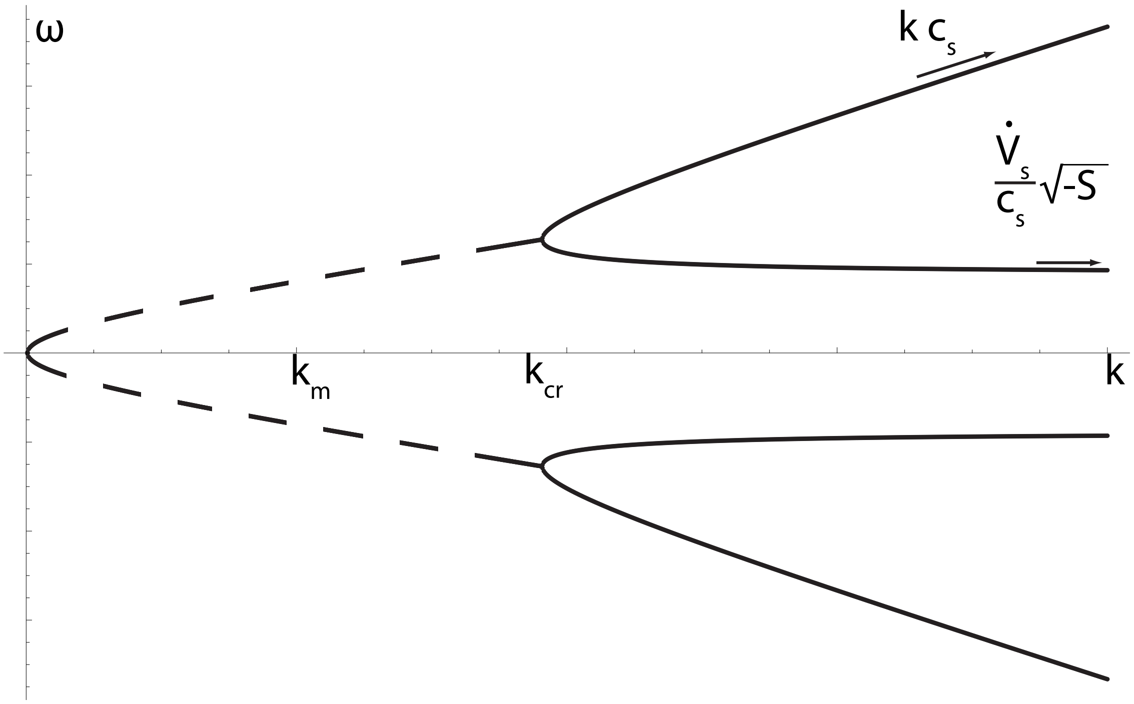

Figure 3.3: Plot showing solutions of Equation 3.23, $\omega = \mathrm{Im}(n)$ *vs.* k. The dashed line denotes the region of instability, $k < k_{cr}$, where $\mathrm{Re}(n)$ is nonzero.

In the opposite limit of shock strength, as $\eta = 1$ and the shock is removed from the system, $T = 1$ and the bending waves asymptotically approach unmodified acoustic waves at high k.

3.2.4 Limiting behavior of solutions

To investigate individually the effect of various terms, we may make several further simplifying assumptions to Equation 3.17. We will consider the system in the combined limit of high shock compression, $\eta \to 0$, as well as the limit of negligible acoustic compressibility, $j^2 \to k^2$. We then obtain from Equation 3.17 the equation

$$\begin{gathered} 0 = n^2 + k^2 c_s^2 + (k\dot{V}_s + 2nkU)\times \\ \left(\frac{(n^3 + k^2 U\dot{V}_s) - (nk\dot{V}_s + n^2 Uk)\tanh kH}{(n^3 + k^2 U\dot{V}_s)\tanh jH - (nk\dot{V}_s + n^2 Uk)} \right). \end{gathered} \tag{3.22}$$

The $2nUk$ term in Equation 3.22, which stems from the same physical source as the term discarded in Equation 6b of [94], contributes to damping and shock stability in the high k limit. It was demonstrated in early work, such as that by [29], that we expect stability for shocks separating two simple spaces of homogenous material. Accordingly, in systems with decelerating shock-bounded dense layers, as we tend to wavelengths short compared to the width of the layer, the dynamics must approach this stable limit [93]. The correct rate of damping is however beyond the scope of our assumptions. Ishizaki and Nishihara [44] have shown that the acoustic modes within the shocked material, which in this section we have suppressed, also play a role in stabilizing the shock.

The limit of an indefinitely thin layer is approached, in the notation of Equation 3.22, by taking the limit of negligible post-shock flow $U \rightarrow 0$, rearranging the dispersion relation as

$$n^4 + n^2 k^2 c_s^2 - k^2 \dot{V}_s^2 \left[1 + \frac{c_s^2/\dot{V}_s}{H} \right] = 0. \tag{3.23}$$

This shows that, in these limits, we regain the form of the Vishniac dispersion relation (Equation 3.11). We also see that, for H less than the scale height and $\dot{V}_s < 0$, the quantity in square brackets becomes negative, while this quantity is positive for large H or positive $\dot{V}_s$. When a shocked layer is accelerating, $\dot{V}_s > 0$, the instability is recognized as the Rayleigh-Taylor instability of the rear layer. When H is greater than a compressible scale height, the analysis, as mentioned above, is invalid, and artificially produces a similarly unstable result.

For the decelerating shock, solutions when $H < -c_s^2/\dot{V}_s$ appear as shown in Figure 3.3. The region of instability is $k < k_{cr}$, with a maximum growth at k_m, where

$$k_{cr} = 2\frac{|\dot{V}_s|\sqrt{-S}}{c_s^2} \tag{3.24a}$$

$$k_m = \frac{|\dot{V}_s|\sqrt{-S}}{c_s^2}. \tag{3.24b}$$

Compared with Equations 3.20 and Figure 3.2, we see that the principal result of removing the effects of compressibility is to eliminate the region of stability near $k = 0$. We also see that the bending modes now travel asymptotically for high k with the full speed of sound, where previously they moved at $c_s^2/\sqrt{T}$.

We note that for $H \ll c_s^2/|\dot{V}_s|$, the rightmost term in Equation 3.23 becomes very large. As H becomes very close to zero, one perhaps expects this term to level off at the value in Equation 3.11; we will explore this limit below.

3.2.5 Post-shock flow patterns

Figure 3.4 shows a numerical solution of Equation 3.22 for a shock system with three different thicknesses. The shock system has a scale height $c_s^2/|\dot{V}_s|$ of $144 \cdot 10^{-6}$ m. One can see that for the very thin layer in Fig 3.4(a), the flow pattern is most similar to that of a surface wave. As the post-shock layer increases in thickness through Figs 3.4(b) and (c), the flow pattern evolves to contain vorticity features. We speculate that the transition at the scale height corresponds to a layer thickness in which a complete cell is localized.

We remark that in the numerical solution of Equation 3.22 we find that the shock and rear surfaces' perturbations achieve different phase. Since the fluid inside the layer is constant in density, this will lead to a corresponding perturbation of areal density of the layer that might be observed. The physical connection is therefore maintained with the theory described by Vishniac [92], in which dynamics causing variation in areal density of the post-shock layer leads to overstability in the shock.

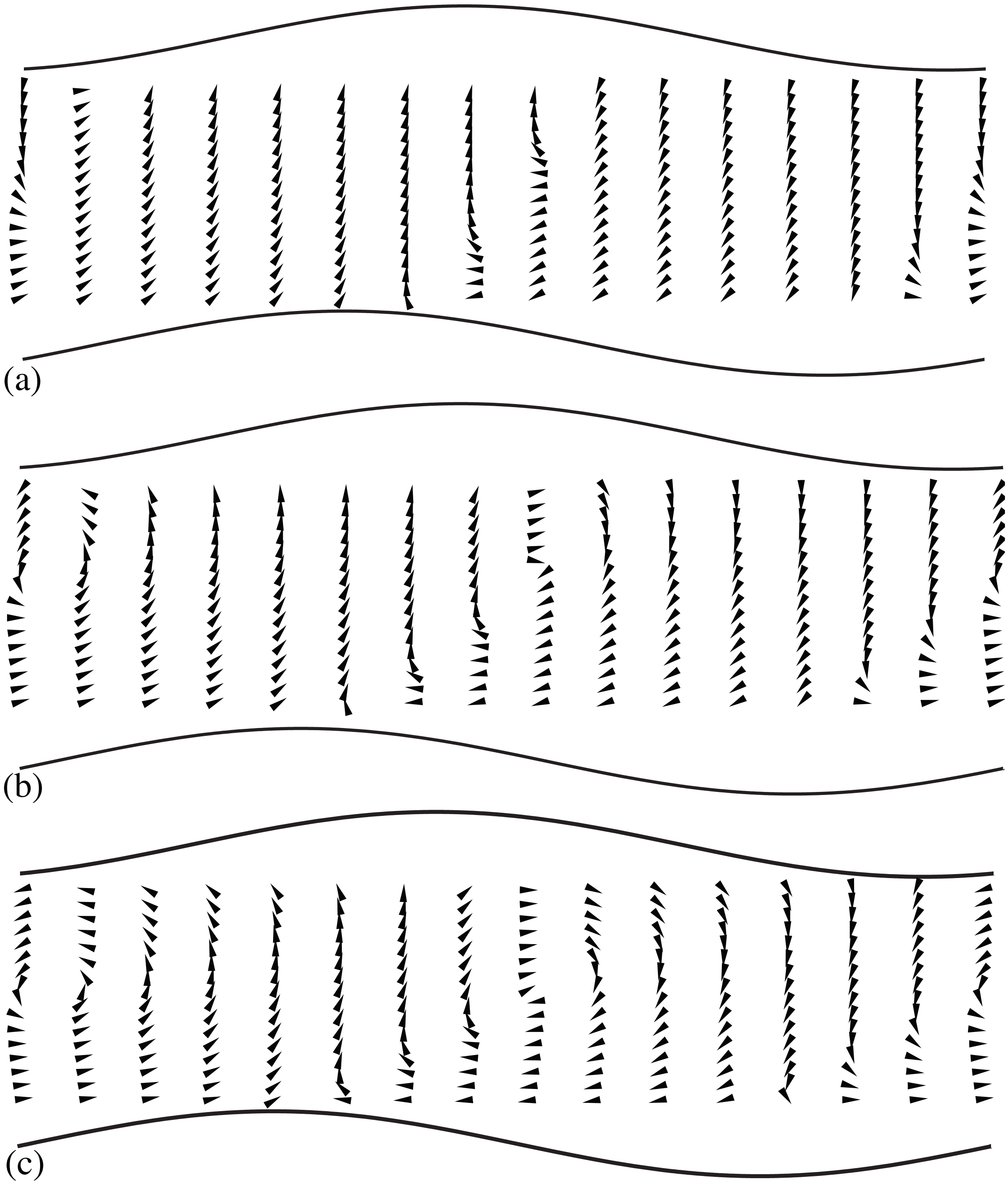

Figure 3.4: Numerical solutions of Equation 3.17, showing flow patterns of the perturbation (u, w) within the layer and relative phase of surface perturbations, with (a) $H = 50 \cdot 10^{-6}$ m, (b) $H = 110 \cdot 10^{-6}$ m, (c) $H = 190 \cdot 10^{-6}$ m, for a shock system with $V_s = 120 \cdot 10^3$ m/sec, $\dot{V}_s = -5 \cdot 10^{12}$ m/sec^2, $\eta = 0.05$, displaying in each case a perturbation with $k = 5210$ m^{-1}.

These plots may be compared with Figures 7-10 of Bertschinger [9], which show similar vortical structure, though without boundary phase shifting.

3.3 Further considerations

3.3.1 Connections to the infinitely thin system

We have seen that the characteristic fourth-order nature of the Vishniac instability, as derived in Equation 3.17, follows from allowing perturbations on both surfaces of the post-shock layer. We note that while the Vishniac derivations contain an instability source in the product $\dot{V}_s P_i/\sigma$, our dispersion relation in Equation 3.17 contains a source term $\dot{V}_s^2$. This difference follows from Vishniac's assumption that the post-shock layer is thin and that the difference between thermal backing pressure and ram pressure together with geometric factors (such as spherical divergence of the shock) are the fundamental sources of the deceleration. We have instead worked with planar shocks and assumed deceleration to stem primarily from mass accumulation and energy loss from the system, for example by strong radiative cooling, and a hydrostatic distribution within the layer to be the dominant contributor to pressure variation.

Despite these differences in approach, we can in fact derive Equation 3.11 from Equation 3.23 immediately. We identify the sound speed at the shock surface with local post-shock fluid variables

$$c_s^2 = \frac{P(0)}{\rho} = \frac{P_i - \rho \dot{V}_s H}{\rho}. \tag{3.25}$$

We have implicity set the polytropic index $\gamma = 1$, which is consistent with our assumption in Equation 3.23 that we are in the infinitely compressive limit $\eta = 0$. However, we do not expect Equation 3.25 to be in general consistent with our other definitions of c_s^2, except in the limit of an infinitely thin shell, $H \to 0$. Keeping this in mind, we see that inserting Equation 3.25 and $\sigma = \rho H$ into the term in square brackets in Equation 3.23, one obtains Equation 3.11. Our derivation therefore is found to agree with the earlier results of Vishniac in the appropriate limits.

The non-oscillating solutions of Equations 3.18 and 3.23 when $\dot{V}_s < 0$ but $H > c_s^2/|\dot{V}_s|$ are of a different nature than the other cases. The system under perturbation was constructed by equating the pressure P immediately behind the shock with the ram pressure of the incoming material. The pressure profile then decreased hydrostatically with distance from the shock. When H exceeds a scale height, the pressure at $z = H$ obtained in this fashion become negative. The "instability" in this case is a response of the system to inconsistent initial conditions, and is the physical interpretation of the consequences resulting from our assuming postulates valid only for $H < c_s^2/|\dot{V}_s|$. In Vishniac's equation, this corresponds to the case where one assigns $\dot{V}_s, P_i < 0$.

Compared to Equation 3.11, Equations 3.17 and 3.23 have the property of being written in terms of the rear layer height and variables defined locally at the compression front, with few assumptions regarding the structure throughout the layer, while Equation 3.11 is properly understood as dealing with quantities averaged over the layer height. This difference allows one to straightforwardly identify from Equation 3.23 the combination of system variables which lead to the transition at the scale height. Equation 3.17 features the same behavior extended to general post-shock U and finite η, with appropriate corrections leading to transition at a fraction of the scale height. We expect the constant density solution to be applicable within a scale height, beyond which modeling the layer as a region of constant density will not be as appropriate as an exponential or self-similar profile.

3.3.2 Experimental observations

We conclude with some discussion of experiments featuring strongly decelerating planar shocks. Experiments which intend to reproduce this instability must feature sufficient lateral space for the growing perturbations. Very early in the experiment's evolution, the post-shock layer thickness will be necessarily small, and we assume $H \ll c_s^2/|\dot{V}_s|$. We see from the results of the proceeding compressible analysis (Equations 3.20 and 3.21) that to allow maximum growth one must afford the experiment lateral dimensions $\lambda > 2\pi c_s\sqrt{H/2|\dot{V}_s|}$, where H is a characteristic or average layer thickness of the system. The evolution will occur within a growth time scale $t = \sqrt{8H/|\dot{V}_s|}$. Conversely, if one wishes to eliminate entirely this instability one should construct an experiment with lateral dimensions $\lambda \lesssim 2.6\ c_s\sqrt{H/|\dot{V}_s|}$. For the experiments discussed above by [73], the values of preferred minimum distance and time to obtain instability are approximately 400 - 500 μm and 9 - 13 ns, conditions which are achievable by the reported experiment.

3.4 Effects of variable speed of sound

The differential equation previously seen in Equation 3.8,

$$(n + U\partial_z)w + w\partial_z U = \partial_z\left(\frac{1}{k^2 + n^2/c_s^2}(n + U\partial_z)(\partial_z w)\right) \tag{3.26}$$

is extended by allowing

$$c_s^2 = c_s^2(z) = c_{s0}^2 + \gamma\dot{V}_s z.$$

We consider the effect of allowing the speed of sound to vary throughout the gas on the relationship between n (specifically, it's imaginary part) and k. We consider first simple sound waves: when c_s is no longer uniform, for a given $\mathrm{Im}(n) = \omega$ the wavenumber of periodicity, $k = \omega/c_s$, must be different at different heights z, or vice-versa if k is held constant. We evidently can no longer choose both ω and k as constants in z in our perturbation ansatz.

We model the effect by defining

$$\begin{aligned} \alpha &= k\ c_s(z), \\ \Gamma^2 &= \alpha^2 + n^2 \end{aligned} \tag{3.27}$$

where α is assumed constant. In effect, we assume that while we do not know the detailed relation between k and $\mathrm{Im}(n)$, we assume it is linear in c_s. We can then rewrite Equation 3.26 as

$$\left(\Gamma^2 - \gamma \dot{V}_s \partial_z - \left({c_{s0}}^2 + \gamma \dot{V}_s z\right) \partial_z^2\right) \left(n + U\partial_z\right) w = 0. \tag{3.28}$$

We identify the two differential operators

$$D_B = \left(\Gamma^2 - \gamma \dot{V}_s \partial_z - \left({c_{s0}}^2 + \gamma \dot{V}_s\right) \partial_z^2\right) \tag{3.29}$$

$$D_t = (n + U\partial_z) \tag{3.30}$$

and rewrite Equation 3.28 as

$$D_B D_t w = 0. \tag{3.31}$$

It is known from the theory of differential equations that a differential equation in the form above has as its general solution the general solutions of its component operators if they are *permutable*. The commutator of our operators is nonvanishing, but

$$[D_B, D_t] \propto \frac{U\dot{V}_s}{nc_s^2} \tag{3.32}$$

will be neglected. The range of validity in neglecting this term is discussed later. Having neglected the commutator, one may then consider the general solutions of each independent operator as the complete general solution to the combined equation. The general solution for D_t is $Ce^{-nz/U}$. The general solution of D_B can be found by a change of variables. If we define

$$\zeta = 2\sqrt{\frac{\Gamma^2 {c_s}^2(z)}{\gamma^2 \dot{V}_s^2}}$$

then the transformation

$$\begin{aligned} c_s^2(z) &= \frac{\zeta^2 \gamma^2 \dot{V}_s^2}{4\Gamma^2} \\ \partial_z &= \frac{2\Gamma^2}{\zeta \gamma \dot{V}_s} \partial_\zeta \\ \partial_z^2 &= \left(\frac{2\Gamma^2}{\gamma \dot{V}_s}\right)^2 \left(\frac{1}{\zeta^2}\partial_\zeta^2 - \frac{1}{\zeta^3}\partial_\zeta\right) \end{aligned}$$

casts D_B as

$$D_B = -\Gamma^2 \left(\partial_\zeta^2 + \frac{1}{\zeta}\partial_\zeta - 1\right) \tag{3.33}$$

which is the operator corresponding to the Modified Bessel's Equation. Solutions to D_B are therefore of the form $A\ I_0\Big(2\sqrt{\frac{\Gamma^2 c_s^2(z)}{\gamma^2 \dot{V}_s^2}}\Big) + B\ K_0\Big(2\sqrt{\frac{\Gamma^2 c_s^2(z)}{\gamma^2 \dot{V}_s^2}}\Big)$, where I_0 and K_0 are the modified Bessel functions.

We take as our approximate general solution[1]

$$w = A\ I_0\left(2\sqrt{\frac{\Gamma^2 c_s^2(z)}{\gamma^2 \dot{V}_s^2}}\right) + B\ K_0\left(2\sqrt{\frac{\Gamma^2 c_s^2(z)}{\gamma^2 \dot{V}_s^2}}\right) + Ce^{-nz/U}. \tag{3.34}$$

The new basis written in modified Bessel's functions is less dissimilar to the pre-

---

[1] If we do not accept the approximate permutability of D_B and D_t, our general solution is found, by use of integrating factors, to be

$$w = e^{-nz/U} \cdot \frac{1}{U} \int e^{nz/U} A'\ I_0\left(2\sqrt{\frac{\Gamma^2 c_s^2(z)}{\gamma^2 \dot{V}_s^2}}\right) + B'\ K_0\left(2\sqrt{\frac{\Gamma^2 c_s^2(z)}{\gamma^2 \dot{V}_s^2}}\right)\ dz$$

where the constant of integration appears as the third arbitrary constant above. The arbitrary constants are written as A' and B' to distinguish them from the approximate case. The integral cannot seem to be expressed as any finite series of elementary or special functions.

vious basis, Equation 3.8, expressed in exponentials, than it appears at first glance. First, to first order in δs and zeroth order in U/c_s, the differential forms of the boundary conditions are changed only cosmetically.

$$0 = \left(n^2 c_s^2(z)\partial_z - \Gamma^2 \dot{V}_s\right) w \,\Big|_{z=H} \tag{3.35}$$

$$0 = \left(\frac{U c_s^2(z)}{\Gamma^2}\partial_z^2 + \frac{n c_s^2(z)}{\Gamma^2}\partial_z - \left(\frac{\dot{V}_s}{n(1-\eta)} + 2U\right)\right) w \,\Bigg|_{z=0} \tag{3.36}$$

$$0 = \left(\frac{c_s^2(z)}{\Gamma^2}\partial_z - \frac{V_s}{n(1-\eta)}\right) w \,\Bigg|_{z=0} \tag{3.37}$$

The first derivatives in z of the Bessel's functions are not unlike those in the exponential case. When $\dot{V}_s < 0$, cancellations yield

$$\partial_z I_0\left(2\sqrt{\frac{\Gamma^2 c_s^2(z)}{\gamma^2 \dot{V}_s^2}}\right) = -j(z)\; I_1\left(2\sqrt{\frac{\Gamma^2 c_s^2(z)}{\gamma^2 \dot{V}_s^2}}\right) \tag{3.38}$$

$$\partial_z K_0\left(2\sqrt{\frac{\Gamma^2 c_s^2(z)}{\gamma^2 \dot{V}_s^2}}\right) = j(z)\; K_1\left(2\sqrt{\frac{\Gamma^2 c_s^2(z)}{\gamma^2 \dot{V}_s^2}}\right) \tag{3.39}$$

which are analogous to e^{-jz} and e^{jz}, respectively, from when there was no z-dependence for j.

A similar result exists for second derivatives. Utilizing recurrence relations for modified Bessel functions

$$\partial_x I_1(x) = I_0(x) - \frac{1}{x} I_1(x) \tag{3.40}$$

$$\partial_x K_1(x) = -K_0(x) - \frac{1}{x} K_1(x) \tag{3.41}$$

we derive expressions for the second derivatives

$$\partial_z^2 I_0\left(2\sqrt{\frac{\Gamma^2 c_s^2(z)}{\gamma^2\dot{V}_s^2}}\right) = j^2(z)\ I_0\left(2\sqrt{\frac{\Gamma^2 c_s^2(z)}{\gamma^2\dot{V}_s^2}}\right) + j(z)\frac{\gamma\dot{V}_s}{c_s^2(z)}\ I_1\left(2\sqrt{\frac{\Gamma^2 c_s^2(z)}{\gamma^2\dot{V}_s^2}}\right) \tag{3.42}$$

$$\partial_z^2 K_0\left(2\sqrt{\frac{\Gamma^2 c_s^2(z)}{\gamma^2\dot{V}_s^2}}\right) = j^2(z)\ K_0\left(2\sqrt{\frac{\Gamma^2 c_s^2(z)}{\gamma^2\dot{V}_s^2}}\right) - j(z)\frac{\gamma\dot{V}_s}{c_s^2(z)}\ K_1\left(2\sqrt{\frac{\Gamma^2 c_s^2(z)}{\gamma^2\dot{V}_s^2}}\right). \tag{3.43}$$

To evaluate these terms at the boundaries, we note that

$$j(H) = j(0)\frac{c_{s0}}{c_s(H)} = j(0)\sqrt{1 - \frac{\gamma\dot{V}_s H}{c_s^2(H)}}.$$

Using these derivatives to evaluate w in the boundary conditions (Equations 3.35 - 3.37), one obtains the dispersion relation as a condition on the determinant of the matrix of coefficients of A, B, and C.

$$\begin{vmatrix} n^2K_1(\zeta_H) - j\dot{V}_s K_0(\zeta_H)\frac{c_{s0}}{c_s(H)} & -n^2 I_1(\zeta_H) - j\dot{V}_s I_0(\zeta_H)\frac{c_{s0}}{c_s(H)} & 0 \\ \begin{matrix} -\frac{n}{j}\left(1-\gamma\frac{U\dot{V}_s}{nc_{s0}^2}\right)K_1(\zeta_0) \\ +\left(U+\frac{\dot{V}_s}{n(1-\eta)}\right)K_0(\zeta_0)\end{matrix} & \begin{matrix} \frac{n}{j}\left(1-\gamma\frac{U\dot{V}_s}{nc_{s0}^2}\right)I_1(\zeta_0) \\ +\left(U+\frac{\dot{V}_s}{n(1-\eta)}\right)I_0(\zeta_0)\end{matrix} & 2U + \frac{\dot{V}_s}{n(1-\eta)} \\ \frac{1}{j}K_1(\zeta_0) - \frac{V_s}{n(1-\eta)}K_0(\zeta_0) & -\frac{1}{j}I_1(\zeta_0) - \frac{V_s}{n(1-\eta)}I_0(\zeta_0) & -\frac{n}{Uj^2} - \frac{V_s}{n(1-\eta)} \end{vmatrix} = 0. \tag{3.44}$$

In Equation 3.44, $j = j(0)$, $\zeta_H = 2\sqrt{\frac{\Gamma^2 c_s^2(H)}{\gamma^2\dot{V}_s^2}}$, and $\zeta_0 = 2\sqrt{\frac{\Gamma^2 c_{s0}^2}{\gamma^2\dot{V}_s^2}}$.

This result has a number of desirable properties. It is interesting to note that any K_n diverges when its argument is 0, explicitly requiring this formulation to apply only for layer heights below a scale height (at which height the sound speed becomes 0). Equation 3.44 reduces to the dispersion relation with constant speed of sound, Equation 3.16, in the limit of $\gamma \to 0$. We see that the only substantial changes are in the terms incorporating the effect of layer height H and the appearance of two terms of $\gamma\frac{U\dot{V}_s}{nc_s^2}$. The latter of these is the same term which was dropped previously in writing Equation 3.32. We will now discuss the actual magnitude of such a term.

We approximate as a lower limit for n either of the two forms kc_s or $\sqrt{k\dot{V}_s}$. In the former case, for variables as seen in our experiments, the term $\gamma\frac{U\dot{V}_s}{nc_s^2}$ is comfortably negligible when $\lambda < 10\text{m}$, and for the latter case, when $\lambda < 1\text{cm}$. Our experiment having lateral dimensions of 0.6 mm removes the need to consider such an effect. This justifies both our solutions in Equation 3.34 and reduces Equation 3.44 to a form which differs from the constant speed of sound case *only* in the terms involving H and in the appearance of the modified Bessel functions.

Taking the limit of $U \to 0$, $V_s \to \infty$, $UV_s \to c_{s0}^2$, we write the dispersion relation as

$$0 = (1-\eta)n^2 + j^2c_{s0}^2 + j\dot{V}_s\left(\frac{n^2 - j\dot{V}_sF_1}{n^2F_2 - j\dot{V}_sF_3}\right) \tag{3.45}$$

where

$$F_1 = \frac{I_0(\zeta_0)K_0(\zeta_H) - K_0(\zeta_0)I_0(\zeta_H)}{I_0(\zeta_0)K_1(\zeta_H) + K_0(\zeta_0)I_1(\zeta_H)}\frac{c_{s0}}{c_s(H)} \tag{3.46}$$

$$F_2 = \frac{I_1(\zeta_0)K_1(\zeta_H) - K_1(\zeta_0)I_1(\zeta_H)}{I_0(\zeta_0)K_1(\zeta_H) + K_0(\zeta_0)I_1(\zeta_H)} \tag{3.47}$$

$$F_3 = \frac{I_1(\zeta_0)K_0(\zeta_H) + K_1(\zeta_0)I_0(\zeta_H)}{I_0(\zeta_0)K_1(\zeta_H) + K_0(\zeta_0)I_1(\zeta_H)}\frac{c_{s0}}{c_s(H)} \tag{3.48}$$

Compared to the previous dispersion relation, F_1 and F_2 are analogous to $\tanh(jH)$ and F_3 was previously equal to one. These identities are preserved if we assign the cylinder functions $I_{0,1}(\zeta_0) = 1, I_{0,1}(\zeta_H) = e^{-jH}$, $K_{0,1}(\zeta_0) = 1, K_{0,1}(\zeta_H) = e^{jH}$, and $\gamma = 0$ (and therefore $c_s(H) = c_{s0}$).

Leaving aside the specific transform of the hyperbolic tangent function to the combinations of modified Bessel functions above, a significant change is the introduction of the amplifying factor $c_{s0}/c_s(H)$. This has a simple physical explanation, which is that the j term on the rear surface boundary condition is, for a given frequency n, made greater proportionally to the drop in the speed of sound. This increase in the local j leads to a corresponding increase in the strength of the instability.

3.5 Rigid rear boundary condition

It is also instructive to consider the case where the rear boundary condition is not free but rather rigid. We will write the boundary condition for a rear surface of a rigid plate at $z = R$,

$$w|_{z=R} = 0,\ C = 0, \tag{3.49}$$

where C has been explicitly set to zero as discussed above. This replaces Equation 3.12 in our earlier derivations, and following the derivation from that point on we obtain an expression for the dispersion relation

$$\begin{vmatrix} e^{jR} & e^{-jR} & 0 \\ -\frac{n}{j} + U + \frac{\dot{V}_s}{n(1-\eta)} & \frac{n}{j} + U + \frac{\dot{V}_s}{n(1-\eta)} & 2U + \frac{\dot{V}_s}{n(1-\eta)} \\ \frac{1}{j} - \frac{V_s}{n(1-\eta)} & -\frac{1}{j} - \frac{V_s}{n(1-\eta)} & -\frac{n}{Uj^2} - \frac{V_s}{n(1-\eta)} \end{vmatrix} = 0 \tag{3.50}$$

or written in its more legible form,

$$(1-\eta)n^2 + j^2c_s^2 + j(\dot{V}_s + 2nU(1-\eta)) \times \frac{(n\tanh(jR) - Uj)}{(n - Uj\tanh(jR))} = 0. \tag{3.51}$$

Since we saw earlier that in this system the waves will always be close to the acoustic solution, $j \ll k$ and we consider only the linear regime of the $\tanh jR$ term, $\tanh jR \approx jR$. We will also consider the limit $\eta \to 0$. We may then rewrite the dispersion relation as

$$n^3 + (n^2 + k^2c_s^2) \times \left(n \left(1 + \frac{R\dot{V}_s}{cs^2} - \frac{2U^2}{c_s^2} \right) - U \left(Rk^2 + \frac{\dot{V}_s}{c_s^2} \right) \right) = 0 \tag{3.52}$$

We may (as we have been) neglect the term of U^2/c_s^2 and write

$$n^3 + (n^2 + k^2c_s^2) \left(n \left(1 + \frac{R\dot{V}_s}{c_s^2} \right) - UR \left(k^2 + \frac{\dot{V}_s}{Rc_s^2} \right) \right) = 0 \tag{3.53}$$

We will elucidate the role of acoustic compressible modes in stabilizing the shock by also considering the analogy of Equation 3.53 for the system, by making a derivation which omits the effects of compressibility. Returning to Equation 3.51 and making the replacement $j \to k$, we obtain

$$n^2 + k^2 U V_s + (k\dot{V}_s + 2nUk) \times \frac{(n \tanh kR - Uk)}{(n - Uk \tanh kR)} = 0 \tag{3.54}$$

and

$$0 = \begin{cases} n^2 + k^2 c_s^2 + k^2 R \dot{V}_s & kR \ll 1 \\ n^2 + k^2 c_s^2 + k\dot{V}_s & kR \gg 1 \end{cases} \tag{3.55}$$

Where the latter limit shows clearly the asymptotic tendency of the modes in the systems to acoustic modes with a small modification proportional to the deceleration. One may experience some surprise on seeing acoustic waves appear in Equation 3.54 despite having suppressed compressibility throughout the rear layer in its derivation. The acoustic waves we have found in Equation 3.54 are not fundamental modes of the post-shock system, but instead are lateral modes of the shock boundary, where compressibility has always been implicitly retained. One may verify that these waves have appeared in the system only through coupling at the shock boundary by the inclusion of V_s, which enters our system of equations only in the shock obliqueness boundary condition in Equation 3.15b, and were rewritten as $c_s^2 = V_s U$.

From Equation 3.55, we obtain the approximate cutoff value predicting instability when $k < |\dot{V}_s|/c_s^2$ or when modes have wavelengths longer than a scale height. For shock conditions $R = 50 \cdot 10^{-6}$ m , $V_s = 120 \cdot 10^3$ m/sec, $\dot{V}_s = -5 \cdot 10^{12}$ m/sec^2, $\eta = 0.05$, this predicts instability for wavelengths above 0.64 mm with real part of n on the order of $2 \cdot 10^7$ sec^{-1}.

By contrast, solutions of the rigid rear layer dispersion relation with fluid compressibility, Equation 3.53, still include growing modes but the growth now appears only on modes longer than 14 meters (for a 50-micron-thick shocked layer), and rate of growth is reduced by factors of $\sim 10^{10}$ to the order of 10^{-3} sec^{-1}. It being unlikely that our assumptions hold over such large scale differences, we may regard this as effectively completely stabilized when the system contains sound waves. This behavior supports the notion [44] that sound waves in the post-shock region play a vital role in stabilizing a shock. The leftmost term in Equation 3.53 controls the cutoff k for instability, resulting in instability when $k^2 < |\dot{V}_s|/Rc_s^2$ for $\dot{V}_s < 0$. When the shock is accelerating, $\dot{V}_s > 0$ and this condition for instability can not be fulfilled.

The "unstable sound-wave-like modes" found in Equation 3.55, and their disappearance when acoustic-mode compression is introduced in the post-shock medium, have a straightforward explanation. In the absence of material compressibility, the lateral acoustic waves create transverse flow patterns which interact with the rear of the layer to produce instability. When compressibility is restored these waves, which move at nearly the sound speed, become almost entirely longitudinal and the destabilizing transverse components of induced flow are suppressed.

3.5.1 Conditions for instability growth

In summary, we have seen that the instability is quite robust with respect to assumptions made in the derivation. The major results of the chapter and in Vishniac's paper with the most robust set of assumptions [94] persist with only small corrections, even when one omits various physical terms, as in Section 3.2.4 or Vishniac's original results [92] on an infinitely thin layer with no internal structure at all. Including more effects, such as effects of the variable speed of sound in Section 3.4, also leaves the instability intact. The instability is seen to exist for a broad set of assumptions whenever one has a shock surface hydrodynamically coupled to a surface capable of supporting gravity waves. Removing the deceleration of the frame or removing the degrees of freedom of the non-shock surface which allow it to support waves are conditions seen to remove the instability.

CHAPTER IV

Repeatability Experiments and Data - October 2008, August 2010

4.1 Orthogonal Shots - October 2008

It is in the nature of experiments at the pressures and temperatures with which this thesis concerns itself that most of the laser targets and related structures do not survive from one shock experiment to the next. The experiments described in this chapter took place at the Omega Laser Facility at Laboratory for Laser Energetics [12], and were intended to assess the degree of repeatability of initial conditions and experimental parameters for radiative shock experiments. To this purpose, after some initial shots which served to center the timing of the shock, the experiments were designed to be nominally identical, as described below.

The experiment is designed to repeatably launch strongly radiating shock waves down a xenon-filled tube to a viewing volume, where they are imaged by x-ray radiography. Due to the high density increases (a ratio of approximately 20, as discussed below) over the shock as a result of the radiation transport [73, 24], we can image with great clarity the difference between the unshocked and shocked xenon.

Eleven targets were fired during this campaign. Data produced by radiography are x-ray transmission images captured on film. Figures 4.21 and 4.22 show all the images obtained in October 2008, calibrated to the coordinate system of the shock.

4.1.1 Experimental Design

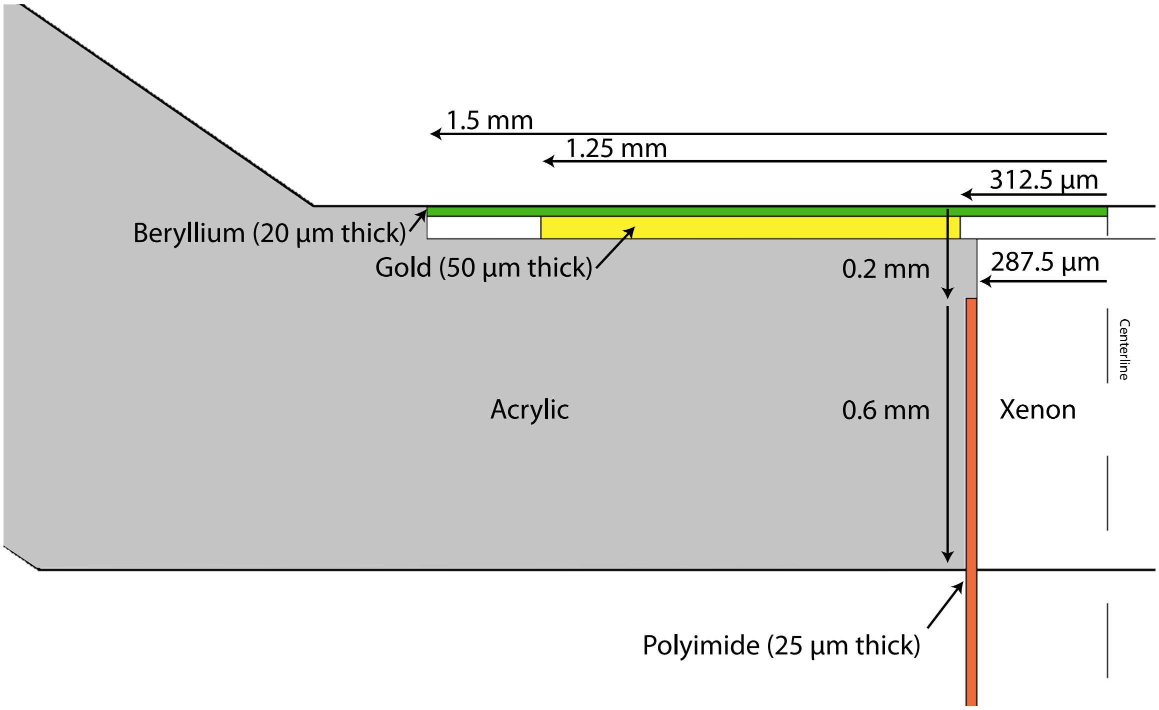

Figure 4.1: Internal structure and dimensions of the nominal October 2008 target design in the vicinity of the drive disc. The image is radially symmetric around the (dashed) centerline on the right side of the image.

Figure 4.1 shows the details of the nominal target. The experimental dimensions are a 21 μm (initially specified at 20, but made 21 due to availability) thick beryllium drive disc, and a polyimide tube 625 μm outer diameter with 25 μm thick walls, filled with xenon at 1.1 atm pressure. The shocks are launched by illuminating the drive disc with 3.8 kJ of laser energy at 351 nm wavelength delivered by 10 drive beams in a 1 ns square pulse over an approximately 840 μm diameter full-width-at-half-maximum of laser irradiance spot. Detailed initial conditions showing the variation in initial conditions from shot to shot are shown in Table 4.1.

A noteworthy feature of these experiments are the large acrylic shield into which the shock tube and drive disc are set. Figure 4.2 shows a schematic of the acrylic shield

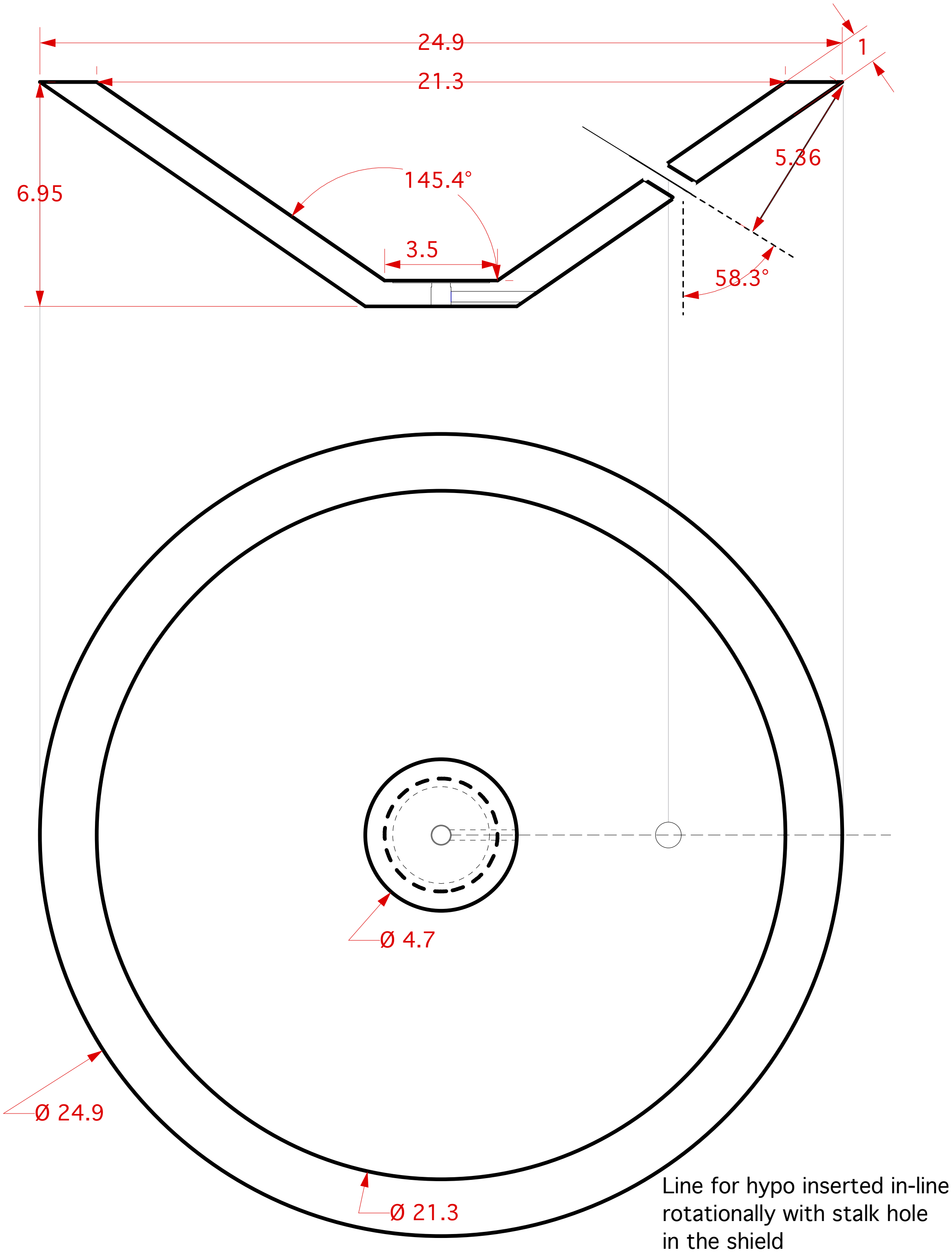

Figure 4.2: Engineering schematic of the acrylic shield for the October 2008 target. Dimensions are shown in mm.

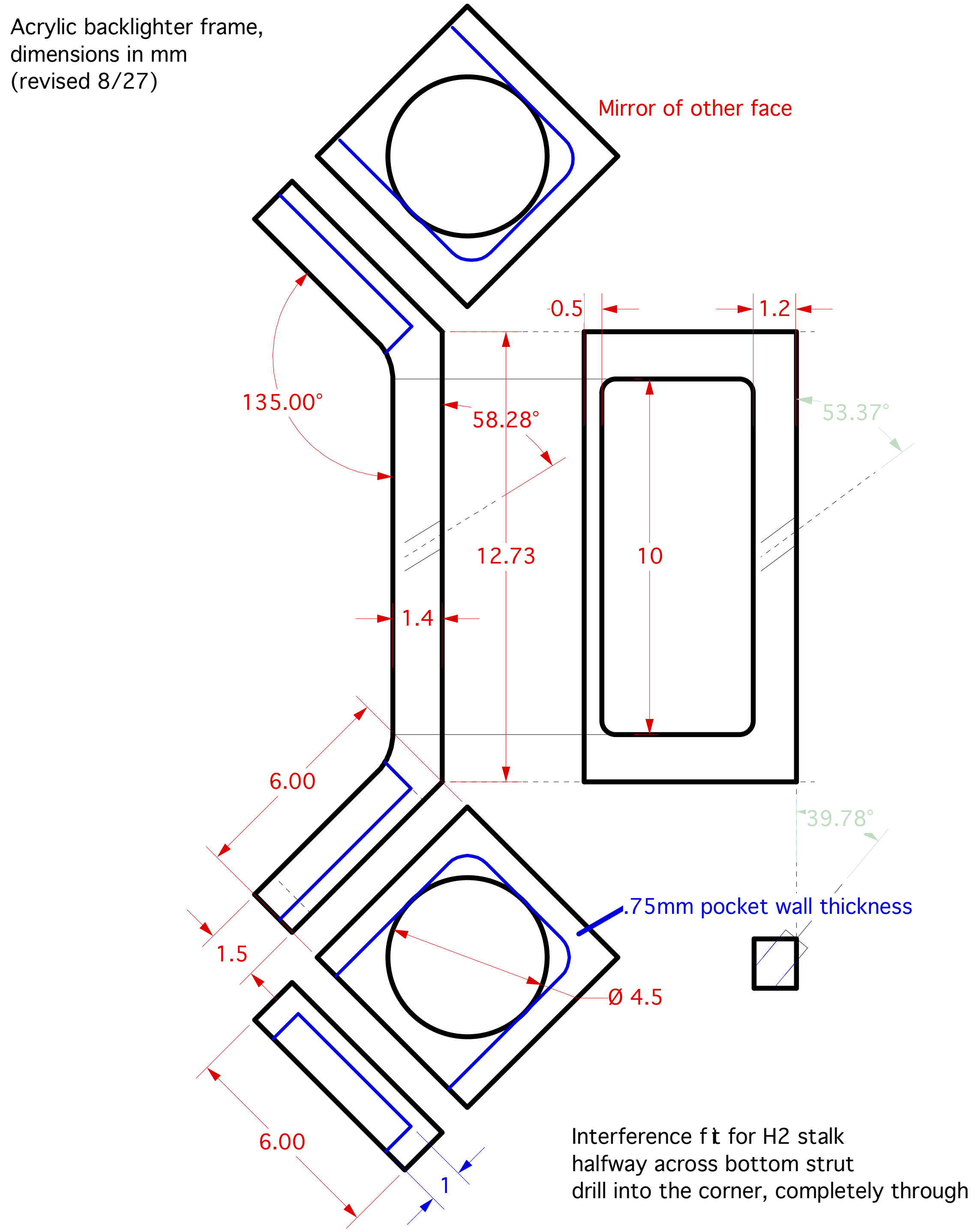

Figure 4.3: Engineering schematic of the acrylic backlighter frame for the October 2008 campaign. Dimensions are in mm. The square platforms each receive one tantalum foil and vanadium x-ray source.

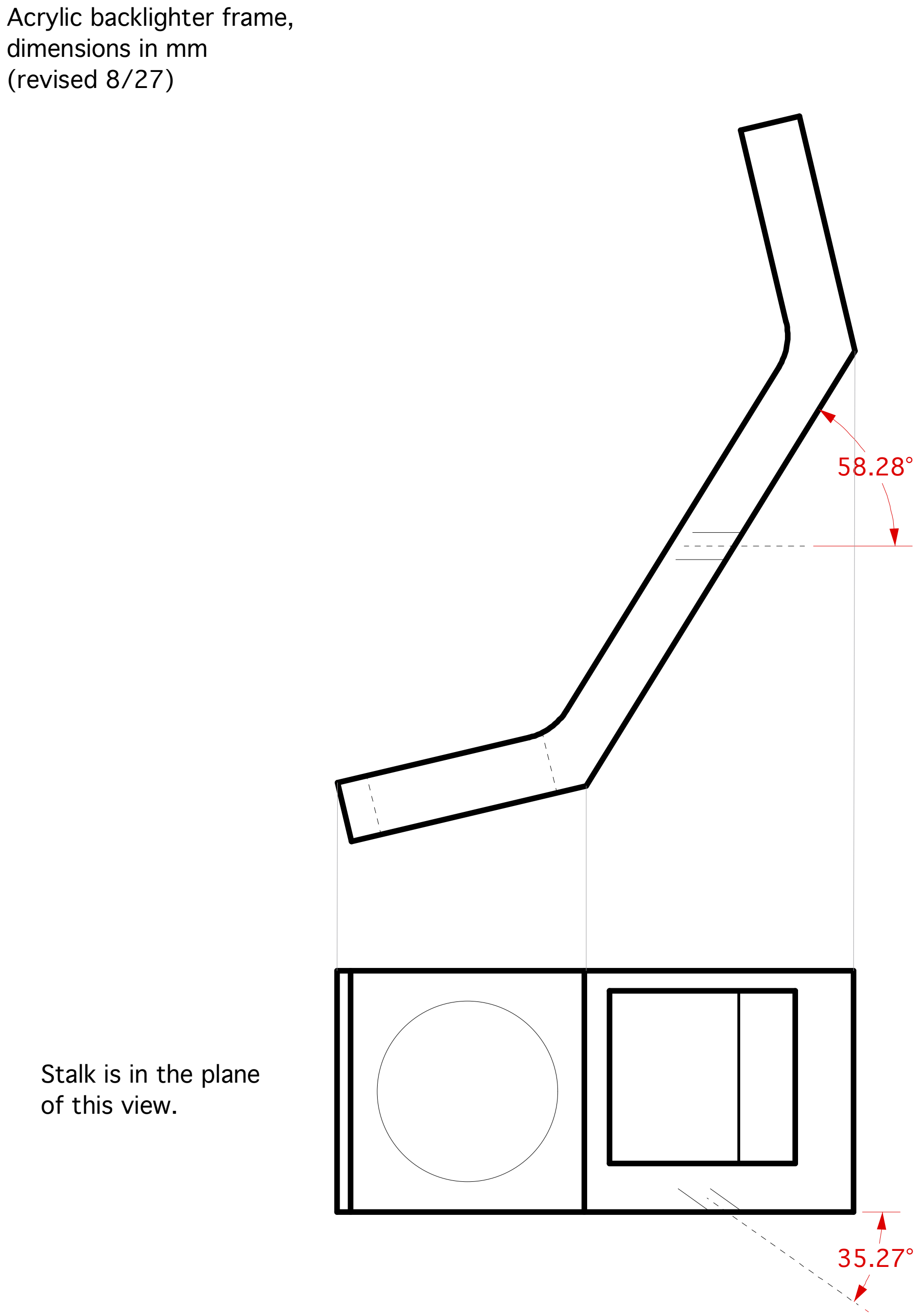

Figure 4.4: Engineering schematic of the acrylic backlighter frame for the October 2008 campaign. Dimensions are in mm. The square platforms each receive one tantalum foil and vanadium x-ray source. (continued from Fig. 4.3)

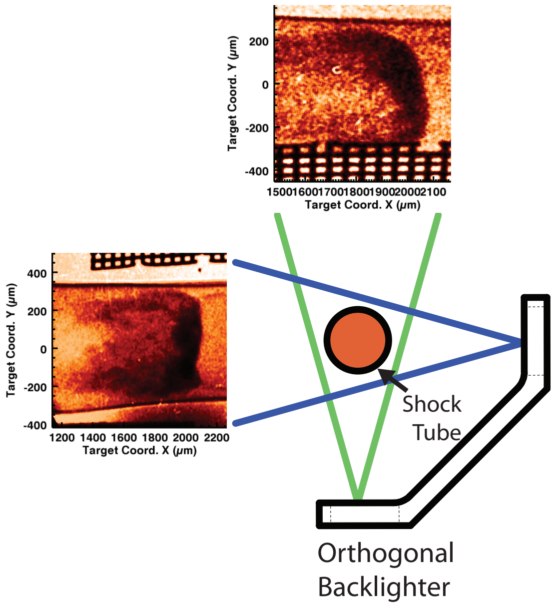

Figure 4.5: Schematic of experimental targets and x-ray paths in the Omega chamber. X-ray images shown are simultaneous images from shot 52667.

structure. The purpose of this shield is to protect the x-ray film, used for diagnosis of the shock, from exposure due to the driving event. The acrylic shield wraps around the area filled by the plasma plume created during the ablation event which drives the shock. This plasma, left unenclosed, emits sufficient radiation to expose the film and prevent the acquisition of data. The acrylic not being sufficient by itself to prevent this, additional shields of 50 μm thick gold are placed on the acrylic between the drive and the diagnostics. This has proven successful in preventing premature exposure of the diagnostics [57].

Approximately 14 ns after the laser drive begins, the set of backlighter beams deliver five beams of 70 J each, also of 351 nm light, to each of two sites on the orthogonal backlighter target, shown in Figure 4.3. Each site contains a 300 μm diameter circular V foil, illuminated by laser beams having an 800 μm spot size for 200 ps. The backlighter emission then projects a cone of x-rays through a 50-μm-to-20-μm tapered pinhole laser drilled in a 5 mm by 5 mm by 50 μm Ta shield. These x-rays pass through the target and into the film stack (Agfa D7 film backed with Fujifilm image plates), as schematically depicted in Figure 4.5. Figure 4.6 shows the overall arrangement of the experiment as placed in the target chamber.

The single backlighter frame comprising two x-ray emitting sites was originally developed for the campaign discussed in Section 5.2. It was utilized in the October 2008 campaign to explore the possible benefits of aligning only two targets (the shock tube target and the backlighter target) in the Omega chamber for each shot, rather than three (two separate backlighter targets and one shock tube target). Aligning a target is a time-consuming process, and for complex geometries often becomes the limiting factor on shot frequency throughout the day. However, the benefits of aligning a single target are weighed against the issues associated with aligning a large target, in which positions of interest are necessarily separated large distances from alignment fiducials. These distances act as lever arms, magnifying the results of small errors in target rotation. This requires the targets to be built to exacting specifications to avoid significant errors in target positioning.

Shot Number	Be Disc	Laser Energy	Pressure
52661	21	3889.6	1.13
52663	21	3882	1.17
52664*	22	3820.1	1.09
52665	21	3892.4	1.13
52667	21	3880.2	1.2
52668	21	3859.8	1.11
52669	21	3846	1.17
52670	21	3841.5	1.17
52671	21	3867.4	1.17

Table 4.1: Detailed initial conditions for the experimental campaign. Beryllium thickness is measured in μm and is accurate to within $\pm .5\mu$m. Laser energy is measured in J accurate to 2% standard deviation. Pre-shot gas pressure is measured in atm to an accuracy of ±0.005 atm. The shot labeled * was known previous to the experiment to have an abnormally large shock tube tilt.

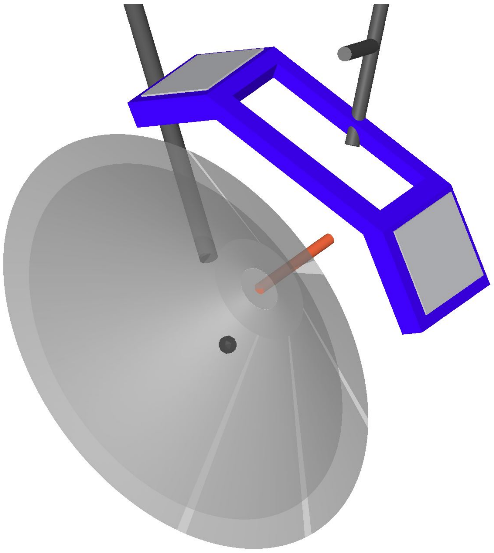

Figure 4.6: CAD model of an assembled October 2008 experiment, as arranged in the Omega target chamber. The piece shown as blue is the orthogonal backlighter frame. The gray is the acrylic shield. The orange is the xenon-filled shock tube. The black circular feature on the shield represents a gold "microdot" used as an alignment reference.

4.1.2 Measured Quantities

The primary output of the experiment was a set of x-ray radiographs. Optimally, each shot could produce two orthogonal radiographs, either simultaneous or displaced in time by 1 to 2 ns. Experimental hazards caused many of the targets to fall short of this ideal, but thirteen usable radiographs were produced.

From the radiographs, we may extract directly, through reference to the spatial fiducial provided by the gold grid, the distances of the shock front from the drive surface (see Figure 4.8). For those shocks with complicated spatial profiles, the shock position is the average distance of the shock front, averaged between the kinks of the wall shock interaction (introduced in Chapter II). This shock position may be used, with the view timing, to calculate the mean speed of the shock. We may also read off the width of the dense xenon layer, the dark layer downstream of the shock front, as averaged by eye. By comparing the dense layer width to the shock position, we learn

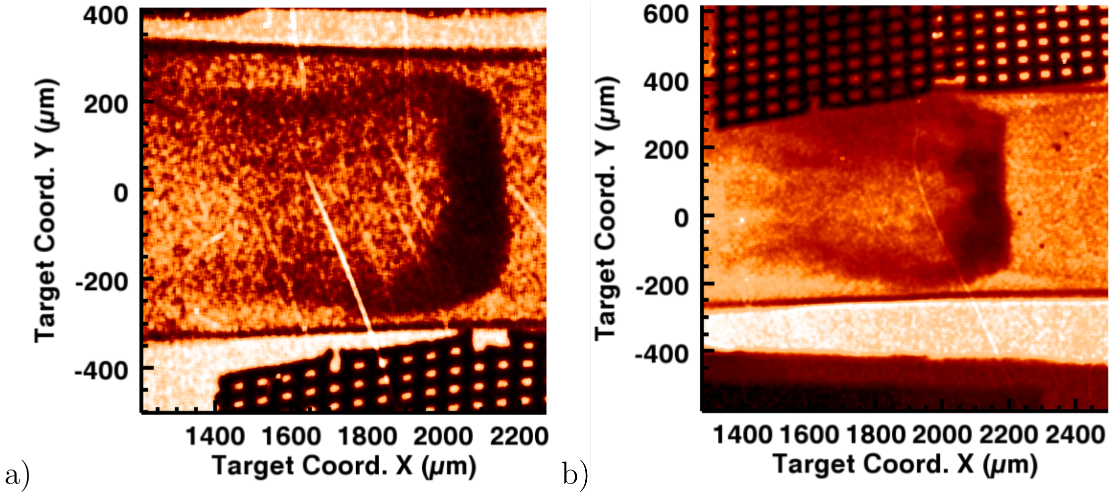

Figure 4.7: Two orthogonal images from Shot 52665, at a) 13 ns and b) 14 ns. The grid squares have a periodicity of 63.5 μm.

the volumes occupied by the same quantity of xenon before and after being shocked, the ratio of which provides a first estimate of the shock compression ratio.

The gold grid fiducial is used with pre-shot metrology to infer a target coordinate system over the experimental image. We use observed inconsistency with a known feature to infer the range of worst-case validity of the coordinate system used. In this section, the location of the center of the shock tube, which should be 0 μm vertically displaced, is used as the reference feature. For example, Figure 4.7(a) has an accurate tube center, while (b) shows some displacement. The absolute distances from the drive tube are therefore known to be correct to within this range of discrepancy. Depending on what processes contributed to the discrepancy (e.g. tube tilt, grid shifting, grid square size variability, etc.), the location may in fact be more accurately measured in the tube length direction than the range reported for that shot. We report in this chapter the maximum range of discrepancy as measured for each experimental image, and for the time being make no further assumptions. We note that in the preparation for experiments, the degree of discrepancy was to some extent able to be anticipated through pre-shot metrology; targets shot earlier in the shot campaign were accordingly prioritized, and it is only the last several shots which suffer from

Shot No.	Position in View 1	Position in View 2	Range in View 1	Range in View 2	Time of View 1	Time of View 2	Xe Width in View 1	Xe Width in View 2
52661	2308	2485	100	70	14	16	125	117
52663	2030		50		13		122	
52664*	1748	1798	100	75	13	13	90	91
52665	2042	2178	25	75	13	14	135	115
52667	2085	2077	≤ 25	≤ 25	13	13	167	136
52668	2098	2310	65	75	13	14	103	137
52669	1940		75		13		150	
52670	2038		275		14		137	
52671	1943		300		13		121	

Table 4.2: Radiographic key data summary for the experiments of October 23, 2008. Spatial data are given in μm. Position refers to the location of the shock front from the initial location of the laser-irradiated surface of the drive disc. Xenon dense layer widths have a resolution limit of $\pm 9\mu$m. The range of possible positional error varies with metrology for each view. Timing data are given in ns. Shot 52664 was unique in that it was a known out-of-spec target, with a drive disc resting at an angle $> 5°$ with respect to the shock tube which generated unusual data.

large fiducial error.

In the case where we have two images of the same shot displaced by 1 ns, relatively free of complex structure, we may extract the local (to within the "shutter speed" of 0.2 ns, corresponding to the x-ray source duration) shock velocity. From the shock images shown in Figure 4.7, we extract a characteristic velocity of 110 km/sec for the shock at this time.

4.1.3 Repeatability

4.1.3.1 Primary Shock Data

Table 4.2 contains the key data parameters discussed above, as measured for each shot. From Table 4.2 we may also extract derived quantities, such as the approximate compression ratio of the shock. Table 4.3 shows the results of the calculation, resulting

Shot Number	Compression Ratio	
52661	18.5	21.2
52663	16.6	
52664	19.4	19.8
52665	15.1	18.9
52667	12.5	15.3
52668	20.4	16.9
52669	12.9	
52670	14.9	
52671	16.1	

Table 4.3: Derived compression ratios from data in Table 4.2. Typical experimental error in this inference is $+6/-1$ ($+5/-0$ from the effect of tilt, $+1/-1$ from the effect of position uncertainty).

in an average compression ratio of 17 for the experiments.

We would like to discuss briefly the possible errors in such a compression ratio. Because we image through an integrated path of chords across the shock tube, any angle by which the shock is misaligned with respect to the plane of tube will appear as an increase in xenon dense layer width. We incorporate this error source approximately as

$$\epsilon_{\text{measured}} = \frac{p}{w}\left(1 - \frac{d}{w}|\theta|\right) \tag{4.1}$$

where ϵ is the compression ratio, p is the shock position, w is the dense layer width, d is the shock tube inner diameter, and θ is the angle of the shock in radians. The values of p and w are readily obtainable from Table 4.2, and d is 575 μm. We see that for a typical shock of $\epsilon_{\text{true}} = p/w = 20$, an angle of 1° would be sufficient to lower the measured ratio to 18. This would suggest that the mean of compression ratios for this experiment likely lies between 17 and 20. We see below that the probable actual value is somewhat larger. In either case, this is consistent with the high density increases one expects from a system with significant radiative losses [24]. The approximation used in Equation 4.1 is valid only for very small angles θ, and will be refined in Section 4.3 below. The approach of Equation 4.1 further depends on the assumption

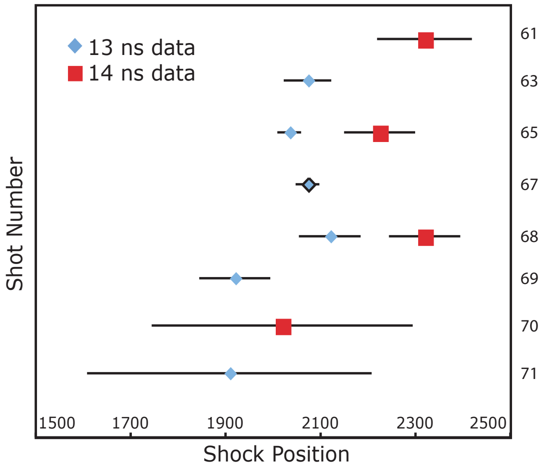

Figure 4.8: Positions of shocks measured experimentally in each shot, measured in distance from drive disc in μm. Error bars shown are worst-case estimates for each piece of data, based on displacement of a known feature (tube center) in target coordinates to a different relative location in radiography coordinates. Shot 52667 contains two points of simultaneous, overlapping, and agreeing data. Not shown: one piece of 16 ns data from Shot 52661.

of negligible radial flow in the bulk of the material, an assumption supported by the predictions of Section 2.3. Simulations of this system also support this conclusion.

Figure 4.9 shows the effect of angular variation on the layer widths obtained in this experiment. To find the actual layer thickness, knowing the measured value (the dashed line) and the angle, one starts from the dashed line at that angle and follows the slope of the diagonal lines leftward to find the intersection with the vertical axis. In most cases here, the angle is not precisely known as the two views are not simultaneous. Also shown in Figure 4.9 is a histogram of angles of the dense layer with respect to the plane of the tube (as measured by a chord following the center of the dense layer, measured against the tube lateral axis). The effect we are describing, which creates apparent layer broadening, is accurate only for small angles. For large angles, integration of opacities through the edges of the layer will begin to fall off and the broadening effect will be diminished. For moderate angles ($< \sim 9°$) we expect the effect to be accurate, and it is possible that a layer of apparent thickness 150μm might be closer to 100μm in actuality.

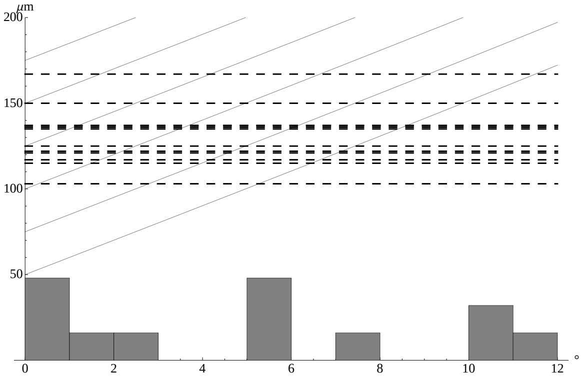

Figure 4.9: Approximate effects of angle with respect to the line of view (horizontal axis, in degrees) on apparent width of the dense xenon layer (vertical axis, in μm). The solid diagonal lines show the trend of angles to produce an dense layer of greater apparent thickness. The dashed lines show data from Table 4.2, with shot 52664 omitted. Additionally, the histogram shows approximate angles observed of the dense layer over different views, with a mean of 5.3°.

Figure 4.8 contains the shock position data from shocks in the 13 to 14 ns range, together with estimated maximum possible error for each shot in the measurement. The shots show approximately a 5% variation in shock position. While parameters such as the drive energy were uniform from shot to shot to within much better accuracy than this, the thickness of the drive disc was verified to only within ±1 μm. For the 20 μm drive disc, this is a 5% variation, which might plausibly have this effect on the speed and overall distance traveled of the shock.

4.1.3.2 Wall Shock Data

Radiographic data of high-energy-density shock tube experiments may contain additional information embedded in the physics of a shock-shock interaction stemming from the *wall shocks.* In Chapter II it was seen that the angles of wall shocks were correlated with and dependent on radiative shock speed and the upstream radiative transport physics at work. Table 2.1 and Figure 2.16 contained measurements from these radiographs, analyzed in the context of radiative-shock-wall-shock interaction.

The point at which the wall shock interacts with the primary shock of the system is often visible in radiographs. The distance of the wall shock interaction point from the wall (the *wall shock amplitude*) may be readily measured, as may, in some cases, the angles of both the wall shock and primary shock deflections in the vicinity of the point. From the former measurement, we obtain a length for which there was derived (Section 2.2.1) a scaling relation relating the wall shock amplitude with the velocity of the primary shock and the material properties of the wall.

Shot Number	Side 1	Side 2	Side 3	Side 4
52661	59.9	73.9 *	45.4	60.2
52663	75	79.6		
52664	37.8			
52665	85.3	73.4	63.7	82.2
52667	72.5 *	63.8	60.9 *	60.9
52668	97.0			75.1
52669	67.8	72.2		
52670	57.6			
52671	59.6	49.0		

Table 4.4: Wall shock amplitudes, measured in μm. Estimated error is on the order of a resolution element, $\pm 9\mu$m. The entries marked * have unusual, three-dimensional structure evident in the image, and are almost certainly not representative of simple scaling laws.

Tables 4.4 contains data extracted from the wall shocks, as discussed above. We see in Table 4.4 the wall shock amplitude is relatively variable from shot to shot and, furthermore, image to image within a shot. This likely reflects a dependence of the physics on higher-dimensional structure, particularly radiation transport away from the shock in potentially complex geometries. A strong dependence on the quantity of radiation expelled from the shock will also result in a complex reading. From the data in Table 4.4, a characteristic amplitude of 67 μm is suggested.

4.2 Hierarchical analysis of 13 ns shock position data

Shot Number	Shock Position	Position Uncertainty
52663	2030	50
52665	2042	25
52667	2085 and 2077	10*
52668	2098	64
52669	1940	75
52671	1943	300

Table 4.5: A subset of the 13 ns data found in Table 4.2. Shot 52664 was omitted due to its out-of-specification nature. *The uncertainty in Shot 52667 benefits from combining simultaneous measurements in orthogonal directions.

The shock position information obtained above gives stronger data as a whole than would an individual point insofar as the experiments were sufficiently similar in design that the information may be correlated. Measurements on the targets before the experiments and ancillary measurements made on the data after the experiments give good estimates of how well the experiments replicated a common set of initial conditions and how much information can be reliably extracted from the radiographs in each case.

The ensuing quantitative analysis combining multiple experiments is fundamentally more complex than combining multiple data points obtained in the same experiment. For best results, one must distinguish between variation in results stemming from random errors in measurement and variation between the experiments. One's measurement scheme may be extremely accurate and yet, if the experiments have variation between them, the accurate measurement of each experiment's true value of output will show variation from point to point. Furthermore, the accuracy of a measurement may itself be one of the parameters which vary from experiment to experiment. An analysis which can accommodate these various complications is desirable.

Analysis with these characteristics has been studied as *hierarchical models* [30].

Fundamentally, one posits both the existence of a parent distribution from which experiments are drawn, and then, for each experiment, a distribution of measurements which one would obtain upon the system. The variation in experiment is encompassed in the parent distribution, and random error in measurement in the second.

As is often the case in statistics, a closed-form analytical solution for the hierarchical model exists when all the distributions involved are normal. Our notation will be that a variable x is said to follow the normal distribution with mean μ and standard deviation σ by writing $x \sim N(\mu, \sigma)$. The parent distribution is written as $N(\mu, \tau)$. True shock positions for an experiment i will be written as $\theta_i \sim N(\mu, \tau)$. Observed data y_i then follows the distributions $y_i \sim N(\theta_i, \sigma_i)$, where σ_i varies for each experiment and is taken from the data.

As data for the hierarchical analysis, we use Table 4.5. For standard shots with data taken at 13 ns, we have written the recorded shock positions and approximate uncertainty in each position. These are our y_i. The uncertainty is estimated by the largest discrepancy between known geometric features located in pre-shot metrology. The large error in the later shots is dominated by issues arising from the tilting of the shock tube. Modeling it as such, the effects of the error become much less random, but for the sake of using the (symmetric, single-peaked, inappropriate) normal model for the moment, we put aside further objections to the assumptions of the model and assign standard deviations σ_i from this column.

The hierarchical Bayesian model takes as its input a set of data and associated standard deviations. It's primary output is the uncertainty of the parent distribution. It is instructive to consider the effect of the parent uncertainty τ on the inference. Figure 4.11 shows expected θ_i as a function of τ. On the far left, when $\tau = 0$, we have the case where there is no experimental variation, and all θ_i are necessarily the same, implying that all experiments reproduced precisely the same actual shock location. This location is necessarily the weighted mean of all the y_i.

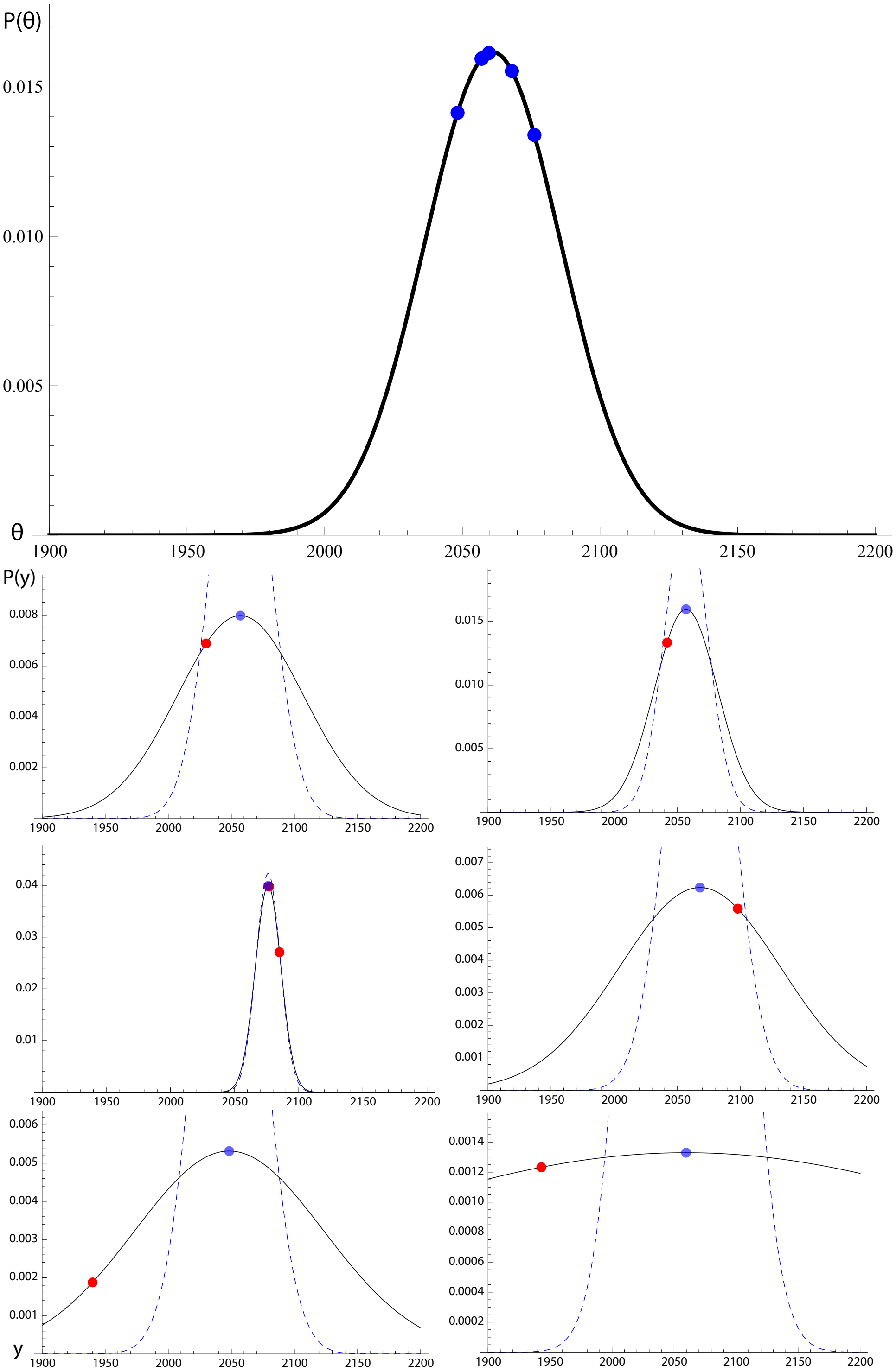

Figure 4.10: Parent (above) and child (below) distributions in the hierarchical Bayes model. The parent distribution $P(\theta)$ is plotted against θ in microns for the expected values of μ and τ. The blue points represent most likely true shock positions θ_i for each experiment i. The child distributions show $P(y)$. The blue dashed lines show $P(\theta_i)$ for that particular experiment. The red points represent observed data quantities y_i.

As we look toward increasing τ, we see that the θ_i are influenced away from the simple weighted mean. Data from experiments with higher σ_i are more influenced by the data with lower uncertainty; if the uncertainty in an experimental measurement is large, probability suggests its true value is likely close to the measurements of other, high accuracy data, and that it is measurement error that makes a data point appear far from the mean. As τ becomes very large, the experiments become uncorrelated, and each θ_i tends toward the associated y_i.

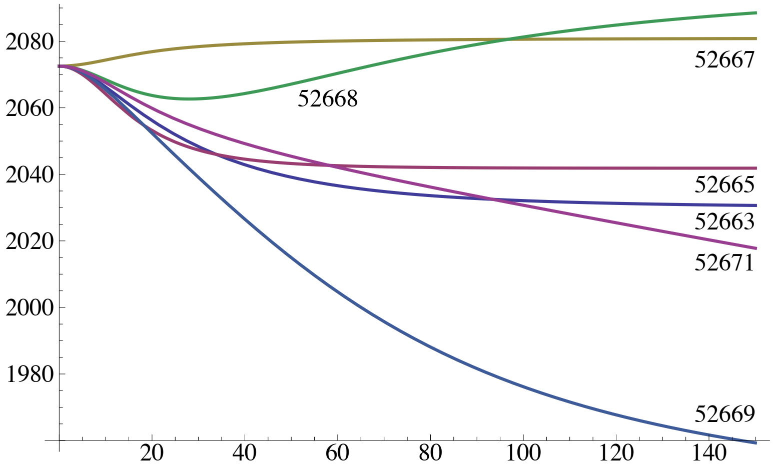

Figure 4.11: Expected value of θ_i for various τ.

We obtain from the model expected values of the true experimental mean μ and experimental variation τ, as well as the most likely θ_i for each experiment. Figure 4.10 plots distributions for these parameters. The expected value of μ, the true mean of shock locations from shot to shot, is 2061 μm. The expected value of τ is 25 μm.

We expect the full range of experimental variation to be approximately 5% of the mean, due to the uncertainty of 1 μm in the drive disc thickness (taking the variation in shock position to be approximately linear with small changes in disc thickness) . In fact, our percentage of uncertainty here is

$$\frac{4 < \tau >}{< \mu >} = 0.0479$$

and the drive disc uncertainty is

$$\frac{1\,\mu\mathrm{m}}{21\,\mu\mathrm{m}} = 0.0476$$

which, while appearing to be a gratifyingly close correspondence, is accurate to a degree that is far greater than is meaningful under the assumptions we have made.

4.3 Analysis of asymmetric error effects on compression data

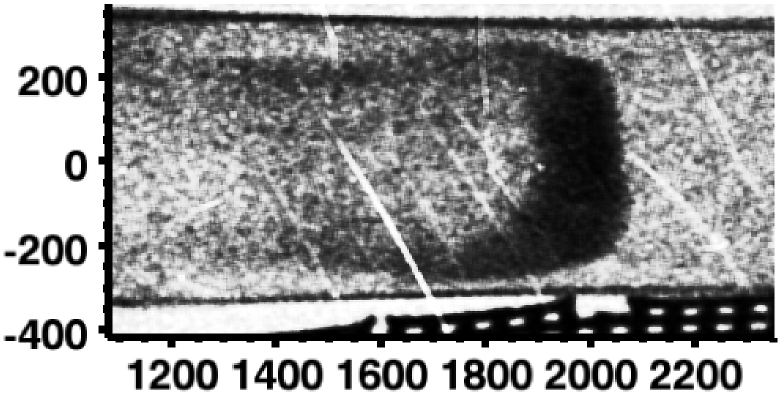

Figure 4.12: X-ray radiograph of the 13 ns image from Shot 52665. Distances from the drive disc are shown in μm. The dark region in the center of the figure is the dense xenon layer. The right edge of the dark layer is the shock front. Behind the layer, the entrained xenon flow can be seen extended downstream. Laterally, the dense layer is seen to stop a finite distance from the tube wall at the wall-shock/primary-shock/deflected-shock triple point. The grid visible in the bottom of the image is a spatial fiducial.

Figure 4.12 shows an example of radiographic shock data obtained in the experimental campaign. Darker regions are areas of lower signal transmitted through the shock tube. Notable features include the dense xenon layer, the shock front which defines the layer's right boundary, and the shock triple points at the layer's top- and bottom-right corners. The triple points are formed from the interaction of the primary shock of the experiment with wall material ablated by the radiative precursor of the shock [23]. Extending downstream from the triple-points are trails of dense, fast, entrained xenon, a consequence of the oblique-shock interactions near the triple point. This entrained xenon appears visually as distinct dark tendrils, due to limb-darkening, but is actually a hollow cylindrical shell.

The post-shock material is sufficiently dense that significant signal may not pass through the dense layer, in which case the shock compression cannot be directly measured by comparing transmitted intensities. A first estimate of the shock compression ratio was obtained above by observing the ratio of the total distance traveled by the shock to the dense post-shock layer width, but small deviations of the angle of the shock with respect to the angle of imaging create large asymmetric errors in observation. A statistical approach to recovering shock compression by appropriately combining data from several experiments is developed in this section.

4.3.1 Data quantization

The shock quantities of interest to this analysis – shock position and average dense layer thickness – are essentially one-dimensional in nature. To define these measurements quantitatively we utilize lineouts averaged over the tube's lateral dimension. For each image a central region of the tube, sufficiently far from the edge effects including the wall shocks that they might be ignored, 150 μm in width and 1 mm long is extracted. The lineout is taken over the distance of 1.5 mm to 2.5 mm from the drive disc for each shot, except for one image which was taken at 16 ns, two to three ns later than the other data points, in which the shock had moved proportionately farther down the tube; that shot was measured from 1.7 to 2.7 mm.

For each of these lineouts we will work with a logarithmic quantity defined as $m = \ln(I_0 - I)$, where I_0 is an intensity taken outside the tube. This maps the intensity lineout to a range of values nearly between 0 and 1. Figure 4.13 shows such a derived log-lineout from Shot 52665. These log-lineouts are effectively described by five regions: (1) a flat area ahead of the shock corresponding to the low density, unshocked xenon; (2) a region of falling transmitted intensity and linearly rising m, including the shock front; (3) an approximately flat region of high density and low transmission within the dense shocked layer; (4) a region of falling m and rising transmitted intensity; and (5) another region of low m and nearly flat intensity, consisting mostly of transparent beryllium. Due to the shell of entrained xenon, we notice that region (5) typically has higher m (lower transmitted intensity) than the pre-shocked region (1).

We define a piecewise function

$$m(x) = \begin{cases} H_1 & x \leq L_1 \\ H_1 + \frac{(x-L_1)}{(L_2-L_1)}(H_2 - H_1) & L_1 < x \leq L_2 \\ H_2 & L_2 < x \leq L_3 \\ H_2 - \frac{(x-L_3)}{(L_3-L_4)}(H_2 - H_3) & L_3 < x \leq L_4 \\ H_3 & x > L_4 \end{cases} \tag{4.2}$$

to capture the shape of the shock in the lineout. We perform a least-squares fit of Equation 4.2 to determine the best-supported values of the four lengths and three heights for each shock. Because of the contamination of the signal behind the shock from the entrained xenon shell, we concentrate our interest on the width of flat signal, $(L_3 - L_2)$, and the rise width, $(L_4 - L_3)$. We also obtain the *average shock position*, $(L_3 + L_4)/2$.

For consistency with the statistical model used in the following section, we define the *apparent shock width*,$2L_4 - L_3 - L_2$, as the flat region width plus twice the rise width, i.e. adding both a rise width and a mirrored “fall width”. This removes the contamination of entrained flow and other disturbances by assuming the projection of the dense layer to be symmetric about the center of the rise width. We note that we expect that the flat width region to be wider than the actual region of flat density, due to depletion of the backlighter signal; the dense layer contains sufficient xenon that no detectable signal typically passes through regions of the layer. Since the analysis will deal with the apparent shock width in total, the deleterious consequences of this depletion are avoided.

We expect the physical shock transition to be substantially shorter than the observed rise width in the mass lineout. Broadening due to finite backlighter pinhole size alone would increase the observed rise width to no more than 20 μm. This long rise width evidently is a result of tilt and curvature of the shock spreading out the projected front of the dense layer. There are three principal components to this rise-broadening: tilt of the shock out of the plane of the image (inclination effect), tilt of the shock in the plane of the image (measurable tilt), and curvature of the shock front. The first of these effects is not directly measurable, and will be addressed below through statistical analysis. Effects of curvature and tilt of the shock within the image may be reduced by reducing the lateral width of the lineout. However, below a lateral width of approximately 50 μm, the signal of many shots becomes too low to reliably fit Equation 4.2. To overcome the effect of tilt in the plane of the image, we perform the fitting algorithm for lineouts of several intermediate widths between 150 and 50 μm in lateral width, and extrapolate by linear regression the parameters and derived quantities for a hypothetical lineout of vanishing width. To minimize the effects of curvature, producing regions of locally thicker dense layers, from biasing the result we perform this analysis for series of lineouts of shrinking width to the top, center, and bottom of the original 150 μm window and average the results.

Of the fourteen experimental images, two were unable to be consistently fit to Equation 4.2, and are omitted from further analysis. Of the remaining shots, we define the *apparent shock compression* as the average shock position divided by the apparent layer width. For an experiment free of inclination effect, these apparent shock compressions would accurately describe the actual shock compression for each

Shot Number (time)	Apparent compression	Posterior mode
52661 (14 ns)	19.52	20.7
52661 (16 ns)	21.19	21.1
52663 (13 ns)	15.22	20.2
52664 (13 ns)	16.61	20.2
52665 (13 ns)	12.40	20.1
52665 (14 ns)	18.32	20.4
52667 (13 ns)	11.16	20.1
52667 (13 ns)	16.74	20.2
52668 (14 ns)	18.76	20.4
52669 (13 ns)	13.64	19.9
52670 (14 ns)	11.06	20.1
52671 (13 ns)	18.95	20.5

Table 4.6: Apparent shock compression ratios for each experimental image, obtained through the fitting procedure described in the text. The approximate time (typical uncertainty of ± 250 ps) relative to the driving event for each image is also indicated. When two images are shown for a single shot, including the two simultaneous shots for Shot 52667, they were taken orthogonally. Also shown is the posterior mode for each data point, found through the method discussed in Section 4.3.3.

shock. The average value of the apparent compression ratios in Table 4.6 is 16.2. This is lower than the average value of the 'by-eye' estimates reported in Table 4.3, which was 17.

4.3.2 Statistical inference

The data of compression ratios inferred by the ratio of distance traveled to average dense layer thickness nominally follows the simple derivation $\epsilon = p/w$, where p is the shock position and w is the dense layer width. However, tilt of the dense layer out of the plane of the shock tube has the asymmetric effect of only increasing the apparent width of the layer, never decreasing it. The geometric relation this effect follows is

$$\epsilon = \frac{p}{w + d \tan|\beta|} \tag{4.3}$$

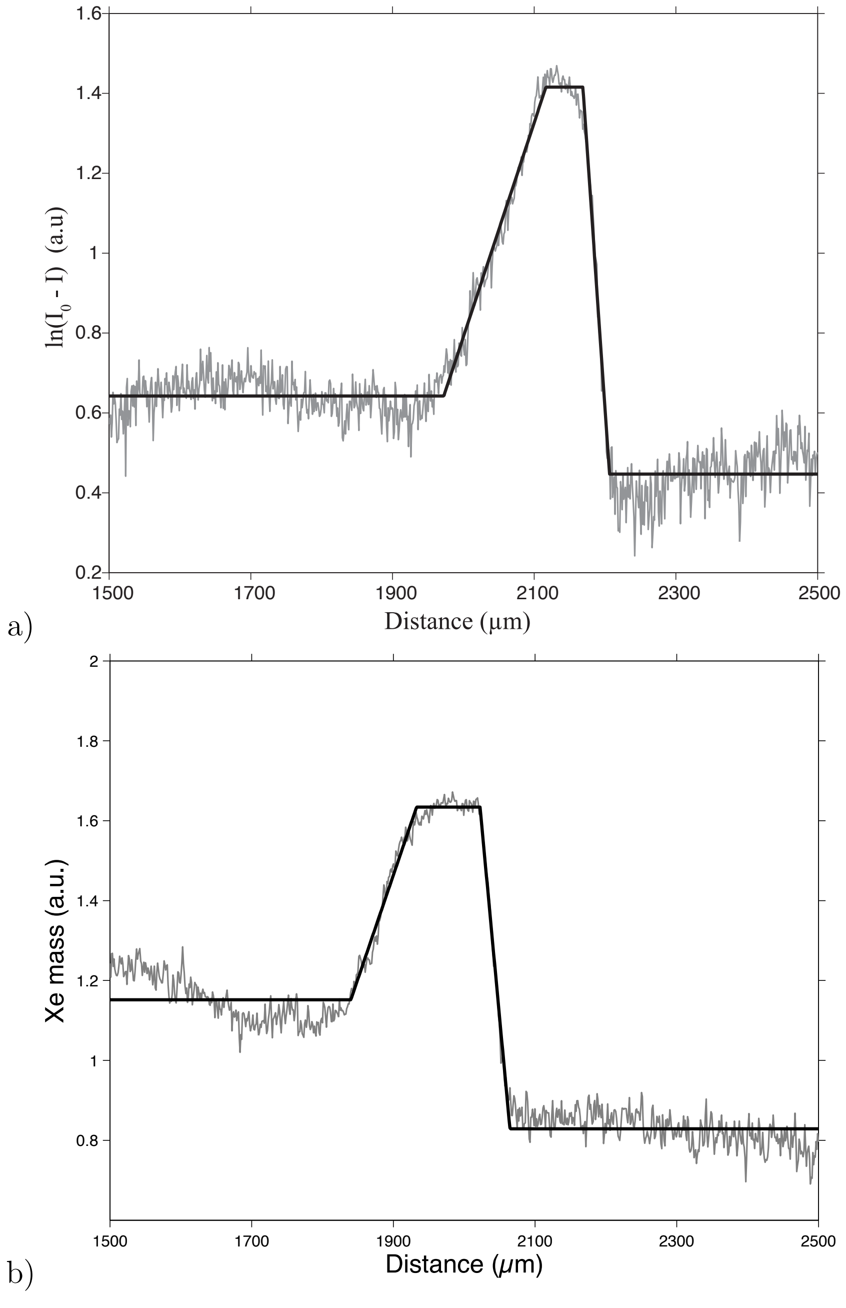

Figure 4.13: Central lineout of the 14 ns radiograph from (a) Shot 52665 and (b) Shot 52670, showing (gray) data averaged over the radial dimension and (black) the five-part piecewise fit to the data. Distance from the experiment's drive disc is shown on the x-axis (in μm), and the derived logarithm of the lineout is shown on the y-axis (in arbitrary units).

where d is the tube diameter and $|\beta|$ is the absolute value of the shock inclination angle. Shock compression is evidently a complicated derived quantity, and even if its constituent functions are treated as normally distributed, ϵ will not be. We will denote a variable x which follows the normal distribution with mean μ and standard deviation σ by $x \sim \mathrm{N}(\mu, \sigma)$.

We develop the model distribution $\mathrm{Tilt}(\theta_\chi)$ for observed compressions ϵ, where θ_χ is the true mean shock compression for the set of experiments, which we wish to determine. We first rewrite Equation 4.3 as

$$\epsilon = \frac{\chi}{1 + \frac{d \cdot \chi}{p} \tan|\beta|} \tag{4.4}$$

where χ is the true compression for a given experiment. Our rewriting w as the product $p\chi^{-1}$ allows us to rescale the 14 and 16 ns data and include them in the same group as the 13 ns data. Of $\mathrm{Tilt}(\theta_\chi)$'s possible parameters, only θ_χ will be considered as an unknown variable. The other parameters will be treated as known experimental facts (or, distributed by empirically known distributions). χ is assumed to vary from experiment to experiment normally, $\chi \sim \mathrm{N}(\theta_\chi, \theta_\chi/80)$, where the second argument is selected to give experiment-to-experiment variation a range of 5%, consistent with manufacturing estimates. Shock position is distributed $p \sim \mathrm{N}(2050\,\mu\mathrm{m}, 25\,\mu\mathrm{m})$. Tube diameter d is set to 575 μm.

The absolute value of shock inclination $|\beta|$ is derived from assuming that the underlying angle β is normally distributed with zero mean. $|\beta|$ is then drawn from a half-normal distribution $\mathrm{HalfN}(\alpha)$, where α is the mean of the half-normal distribution. $\mathrm{HalfN}(\alpha)$ is defined as twice the positive side of $\mathrm{N}(0, \alpha\sqrt{\pi/2})$. We use as the relevant angle measurement for overall shock tilt the angle with respect to the tube radial dimension of the line connecting the two shock triple points, shown tabulated for the dataset in Table 4.7 and compared with the HalfN distribution in Figure 4.14.

We set α to the observed mean of angles of the shocks, $\alpha = 2.36°$.

Table 4.7: Measured angles of the shock with respect to the perpendicular of the tube axis. Shot 52664 created an unusual curved shock in one of its views, and has been omitted.

Shot Number	Shock Angles (°)	
52661	2.0	4.6
52663	8.1	
52665	0.7	0.4
52667	1.9	2.3
52668	1.3	4.8
52669	0.7	
52670	0.4	
52671	1.1	

Values for the distribution Tilt(θ_χ) are now generated computationally. For example, we perform 10^6 draws of parameters from the above distributions with $\theta_\chi = 21.25$, evaluate Equation 4.4 for each, and plot the resulting normalized histogram in Figure 4.15. The dashed line indicates the value of θ_χ. We can see that, as expected, the majority of expected observations fall well to the left of the true underlying mean compression as a consequence of the asymmetric error in observation. The distribution is also moderately skew.

We now consider how well a model with given parameter describes the data. Figure 4.16 shows Tilt(21.25), generated by simulated observations, binned into groups of width 1 with the experimentally observed data overlain on top of it. An appropriate criterion for relative goodness-of-fit for arbitrary density functions is the deviance $\mathcal{D}$, defined as a quantity proportional to the logarithm of the probability of the observed data under the model [30, 47],

$$\mathcal{D} \propto -\ln P(D|H) \tag{4.5}$$

$$= \sum_k n_k \log_{10} \frac{n_k}{np_k}. \tag{4.6}$$

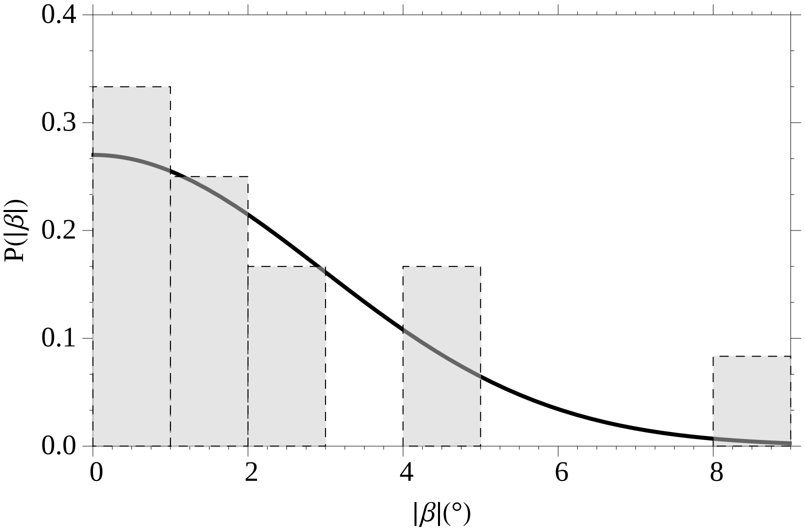

Figure 4.14: Shock angles (dashed) measured in the dataset, in degrees. The histogram is normalized to form a probability density. Also shown (solid) is the probability density function of the half-normal distribution with mean set to the mean of the data.

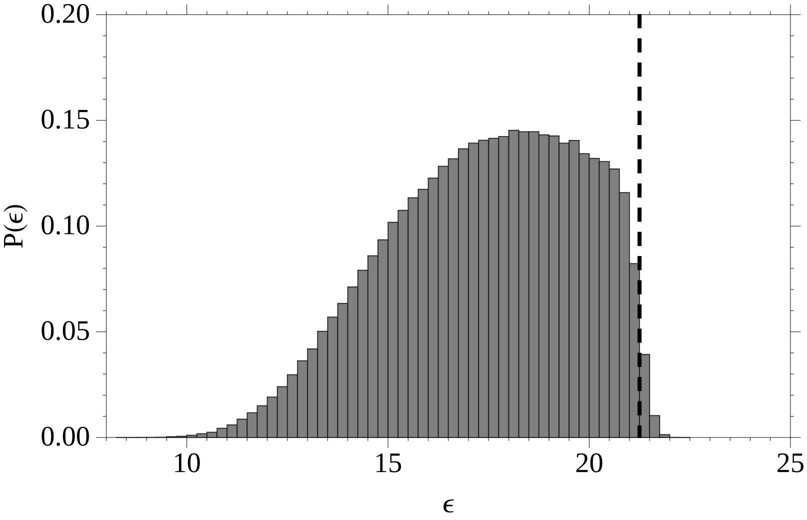

Figure 4.15: Histogram of $\epsilon \sim \text{Tilt}(21.25)$, normalized to form a probability density function for uncorrected observations ϵ. The dashed line shows the value of the underlying true experimental mean for this simulation $\theta_\chi = 21.25$.

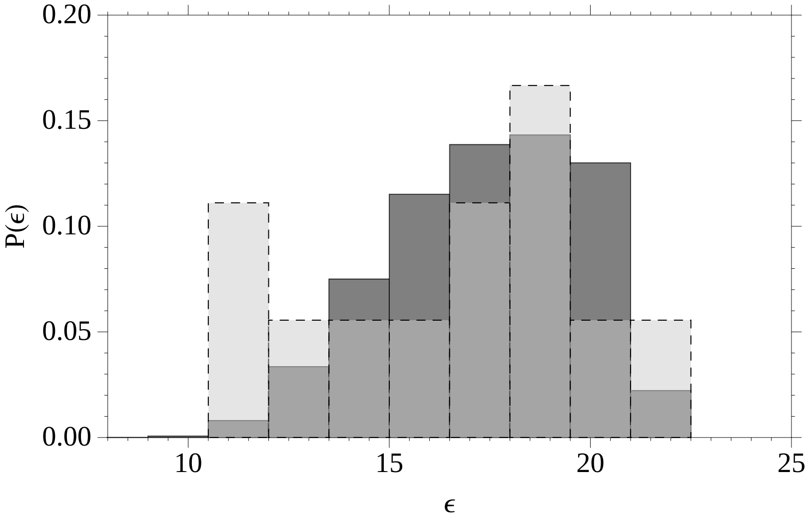

Figure 4.16: Histogram of our model output, $\epsilon \sim$ Tilt(21.25) (solid bars), overlain with compression data (dashed bars).

In Equation 4.6 n is the total number of observations, k is a bin index, n_k is the number of experimental observations falling into a bin k, and p_k is the probability of an observation falling into bin k according to the model being tested.

To infer the most likely value for true mean shock compression θ_χ we repeat the procedure for many values of θ_χ, drawing 10^6 sets of values for the randomly distributed parameters to generate a simulated histogram for a hypothetical large dataset and comparing it to the observed histogram by using Equation 4.6. A bin width of 0.5 is used for calculating the results below. The distribution $P(\theta_\chi)$ is then generated by normalizing the function $P(\theta_\chi) \propto \exp(-\mathcal{D}(\theta_\chi))$.

Figure 4.17 shows the detailed posterior distribution for true mean compression ratio θ_χ, computed within the models $\epsilon \sim \text{Tilt}(\theta_\chi)$, conditioned on the observed data, using a uniform prior. The distribution's mode is at 21.3; this implies that Tilt(21.3) is the parameterization of θ_χ best supported by the data. The 95% confidence interval is between 20.6 and 23. That the difference between mode and high end of the range is larger than that between mode and the low end is reasonable, as it is consistent with the idea that more compressive shocks will have apparent observations indicat-

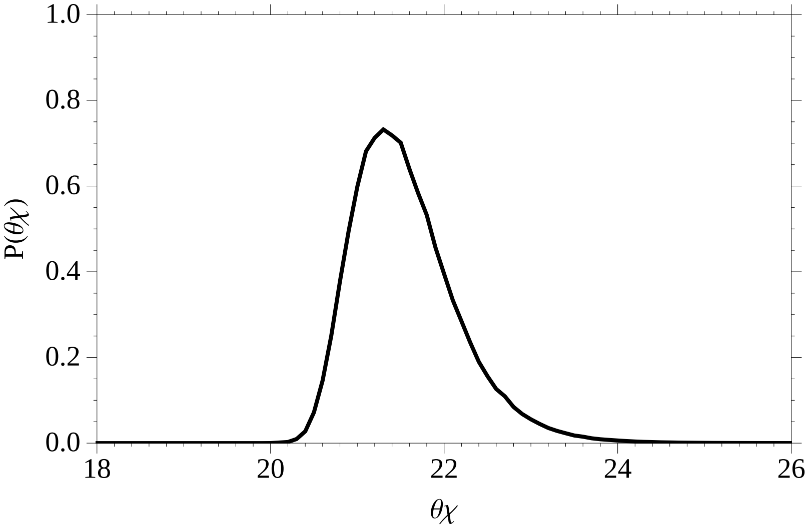

Figure 4.17: Posterior probability density distribution for true mean shock compression θ_χ. The skewness of the distribution reflects the asymmetry of the inclination effect on the data.

ing lower compression far more often than a low mean compression experiment will generate a high (apparent) compression shot. Additionally, there is a 99.99% confidence that $\theta_\chi > 20$, strong evidence that we are well into the regime of radiative collapse.

4.3.3 Posterior distributions for data

Posterior distributions for true shock compressions may be found by calculating

$$P(\chi_j|\eta_j) \propto \int_{-\infty}^{\infty} P(\eta_j|\chi_j)P(\chi_j|\theta_\chi)P(\theta_c hi)\ d\theta_\chi \tag{4.7}$$

where η_j is the observation of an apparent compression ratio from the jth piece of data and χ_j is the unknown true compression ratio for that shock. $P(\theta_\chi)$ is the distribution we obtained using the methods of the previous section. $P(\chi_j|\theta_\chi)$ is the likelihood that $P(\eta_j|\chi_j)$ is the probability of measuring a piece of data to have compression η_j given a true compression χ_j, which was previously computed using random sampling of

Equation 4.4. We now incorporate measurement error by replacing Equation 4.4 with Equation 4.8

$$\epsilon = \frac{\chi}{1 + \frac{d \cdot \chi}{p} \tan|\beta|} + m \tag{4.8}$$

where m is measurement error, $m \sim N(0, \sigma_m)$. We take $\sigma_m = 1$ hereafter (i.e., our data has error ± 1).

The results of these calculations form j posterior distributions; the mode of each distribution is recorded in Table 4.6. It is noteworthy that the mean of the posterior modes is 20.3, which is less than our expected true compression of 21.3. Upon reflection this is not a contradiction; there is no evidence for any one data point in isolation to have indicated a true compression > 21.3, only aggregate evidence for the data set as a whole to contain such points. Evidently when dealing with asymmetric distributions, evaluation of a posterior mean and the average mean of posterior modes are not necessarily identical.

We close with some general comments on the results of this section. In the presence of a strong, asymmetric, random error, one's first inclination is often to take the most extreme measurement in the direction opposite the expected bias as the most likely true value. This analysis supports such intuitions, being informed strongly by the most extreme data point. The largest value in Table 4.6 is 21.2, which is very near the inferred most likely value of 21.3. All other retained apparent compressions are smaller than the most likely compression. The value of this analysis comes both from justifying the intuitive result from underlying, physical processes and also from generating the appropriate confidence in that value. In this case the 95% confidence interval, asymmetrically distributed between 20.6 and 23, would be difficult to generate intuitively.

There is some interest in noting that there is one observation of measurable angle in Figure 4.14 larger than would have been expected for the distribution shown, and also two data points in Figure 4.16 showing lower apparent compressions than would have been expected for the distribution shown. The latter circumstance would be caused by a small number of inclination angles greater than the distribution predicts, much like the excess 8° measurement in Figure 4.14. It is probable that these effects have a common cause, possibly an effect of mismatching of the drive disc normal and shock tube axis, which propagates to form large angles.

4.3.4 Effects of parallax on the measurement

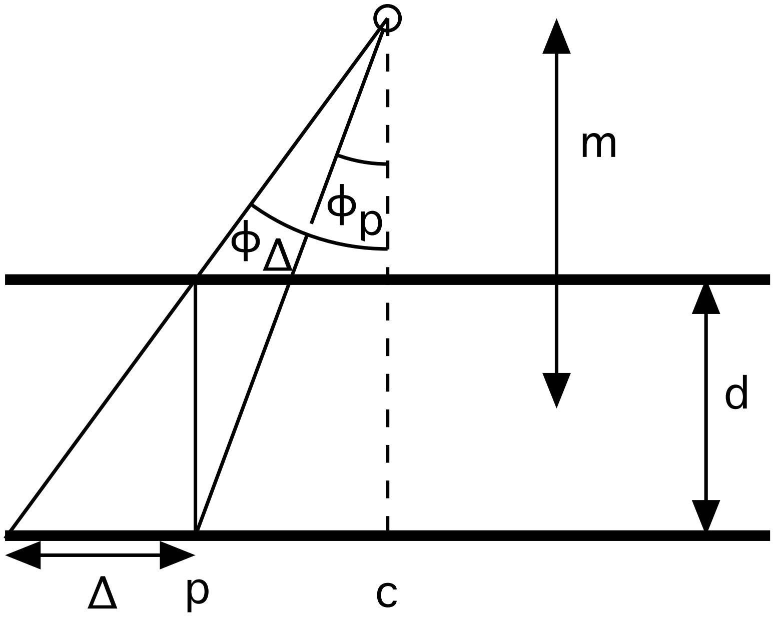

Figure 4.18: Diagram for inferring the effect of parallax on effective shock tilt.

Parallax within the radiographic image can provide an additional source of asymmetric error, providing additional effective tilt between the shock and x-rays as in the shock obliqueness case. Figure 4.18 shows the geometry for determining the additional effect of parallax shifting. The distance from the source to the tube center c is m. It is quickly evident that for a straight shock at location p, the additional apparent increase in apparent shock width Δ is $\Delta = d \tan \phi_\Delta = d \cdot |c - p|/(m - d/2)$.

Performing the same transfer to χ as before and manipulating,

$$\epsilon = \frac{p}{w + d|\tan\beta + \frac{|c-p|}{m-d/2}|} \tag{4.9a}$$

$$= \frac{1}{1 + \frac{\chi}{p}(d|\tan\beta + \frac{|c-p|}{m-d/2}|)} \tag{4.9b}$$

$$= \frac{1}{1 + \frac{\chi}{p}d(|\tan\beta + \tan\phi_\Delta|)}, \text{where } \phi_\Delta = \text{atan}\frac{c-p}{m-d/2} \tag{4.9c}$$

$$= \frac{1}{1 + \frac{\chi}{p}d\left|\frac{\sin(\beta+\phi_\Delta)}{\cos(\beta)\cos(\phi_\Delta)}\right|} \tag{4.9d}$$

$$\simeq \frac{1}{1 + \frac{\chi}{p}d\,|\beta + \phi_\Delta|}, \text{ for small angles.} \tag{4.9e}$$

Now, the new distribution of $c - p$ is dependent on which type of data is under consideration. Previously, moving to $\chi = p/w$ effectively rescaled the data for all times, allowing us to consider only an aggregate p distribution. Now, the induced parallax tilt is explicitly a function of p, so it must be calculated for all data separately.

For all cases, the image was centered at $c = 2000\mu$m, and was $m = 12.5$mm away from the imaging source. For the 13 ns data, $p \sim$ N(2060 μm, 26 μm). For the 14 ns data, $p \sim$ N(2171 μm, 27 μm). For the 16 ns data, $p \sim$ N(2400 μm, 30 μm).

So for the 13 ns data, carrying through the operations, $\phi_\Delta \sim$ N(0.29°, 0.12°). The variance in this distribution is much smaller than that in the obliqueness measurements, $\beta \sim$ N(0, 3°) (this is the distribution which produces $|\beta| \sim$ HalfN(2.4°) in the absolute value). The distribution of the sum $\beta_2 = \beta + \phi_\Delta$ is a normal distribution N(0.29°, 3°), where the variance of the summed distribution $\sqrt{3^2 + 0.12^2}$ has changed only by one part in a thousand. However, β had no mean in its distribution. So, we obtain for the sum of effects a distribution in which the mean comes entirely from the bias from parallax and the variance comes effectively entirely from the random shock obliqueness.

Since an absolute value is in place, we may calculate the distribution $|\beta_2| \sim$

FoldedN(μ, σ). This is the folded normal distribution, which represents a normal distribution with mean μ and standard deviation σ with the probability density of negative values "folded away" by mirroring onto their positive absolute values. When $\mu = 0$, this becomes a representation of the half normal distribution used earlier.

The simplest way to created such a folded distribution is to create an even function of the sum of two normal pdfs, creating a function with total integrated value of 2, and then restrict the distribution only to positive values. When a variable $x \sim$ FoldedN(μ, σ), we define its probability density [62]

$$P(x) = \frac{1}{\sqrt{2\pi}\sigma}\left(e^{-(x-\mu)^2/2\sigma^2} + e^{-(x+\mu)^2/2\sigma^2}\right),\ x > 0. \tag{4.10}$$

We can then calculate for the three sets of data, $|\beta_{2,13}| \sim$ FoldedN(0.3°, 3°), $|\beta_{2,14}| \sim$ FoldedN(0.8°, 3°), $|\beta_{2,16}| \sim$ FoldedN(1.9°, 3°). Pdfs of these distributions are shown in Figure 4.19.

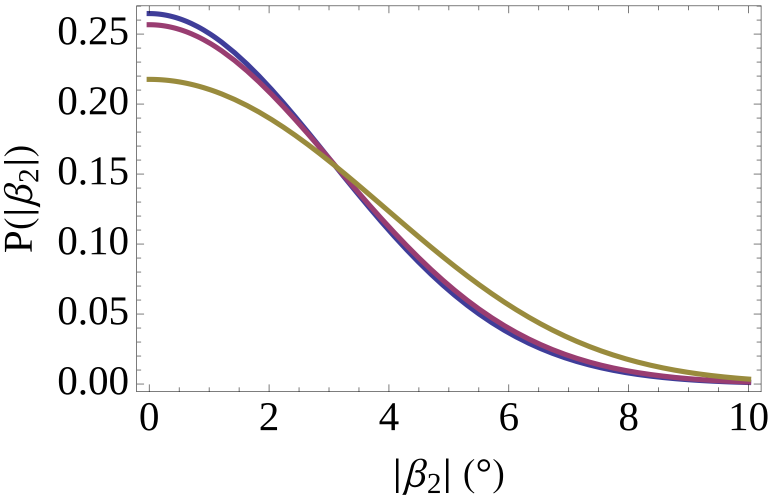

Figure 4.19: Folded distributions with parallax corresponding to (blue) 13 ns, (red) 14 ns, (brown) 16 ns radiographic data. The distribution without parallax was shown in Figure 4.14.

This distribution has some interesting characteristics. Summing the two random variables β and ϕ_Δ before taking the absolute value represents the possibility that the angular tilts might be in opposite directions and cancel each other out. This is captured in a FoldedN distribution by the possible movement of its peak off of the axis. For the HalfN distribution, the most probable output is necessarily 0, the axis of reflection. However, this can only occur if $\mu > \sigma$. To see this, we differentiate Equation 4.10 with respect to x and set it equal to 0, and the non-cancelling terms are

$$e^{-x\mu/\sigma^2}x + e^{x\mu/\sigma^2}x + e^{-x\mu/\sigma^2}\mu - e^{x\mu/\sigma^2}\mu = 0. \tag{4.11}$$

This may be rewritten as

$$x = \mu \tanh\left(\frac{x\mu}{\sigma^2}\right) \tag{4.12}$$

$$\frac{y}{(\mu/\sigma)^2} = \tanh y, \text{where } y = \frac{x\mu}{\sigma^2}. \tag{4.13}$$

There can be an off-axis peak of the folded distribution only if Equation 4.13 has a nonzero solution for y. Since $\tanh y$ never increases as quickly as y, this intersection will exist only if $\mu < \sigma$. Since this does not occur in any of the data distributions, this behavior is not observed in Figure 4.19 (indeed, these are not very different from the $|\beta|$ distribution without parallax ϕ_Δ corrections, with little overall change to the inference).

Additionally, the mean of the distribution μ_f is [62]

$$\mu_f = \sqrt{\frac{2}{\pi}}\sigma e^{-\mu^2/2\sigma^2} + \mu \ \mathrm{erf}\left(\frac{\mu}{\sqrt{2}\sigma}\right) \tag{4.14}$$

where erf is the error function. The implied means for data are $\mu_{f,13} = 2.4°$, $\mu_{f,14} = 2.5°$, $\mu_{f,13} = 2.9°$. This is almost no change at all for the 13 ns data (as it was clustered tightly around the imaging area center), but is a 19 percent increase in effect at 16 ns. This would have had a noticeable effect had more of the data been taken out at the edge of the imaging area. Figure 4.20 summarizes the influence of parallax bias ϕ_Δ on the summed random variable $|\beta + \phi_\Delta|$ under the conditions for β discussed above.

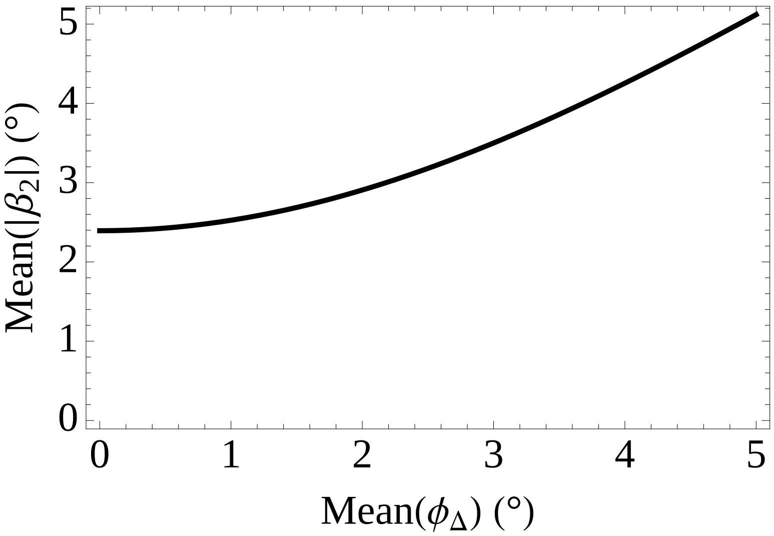

Figure 4.20: The mean of $|\beta_2| = |\beta + \phi_\Delta|$, using Equation 4.14, as a function of the mean of parallax induced effects ϕ_Δ with random obliqueness β having a variance of 3° and a mean of 0.

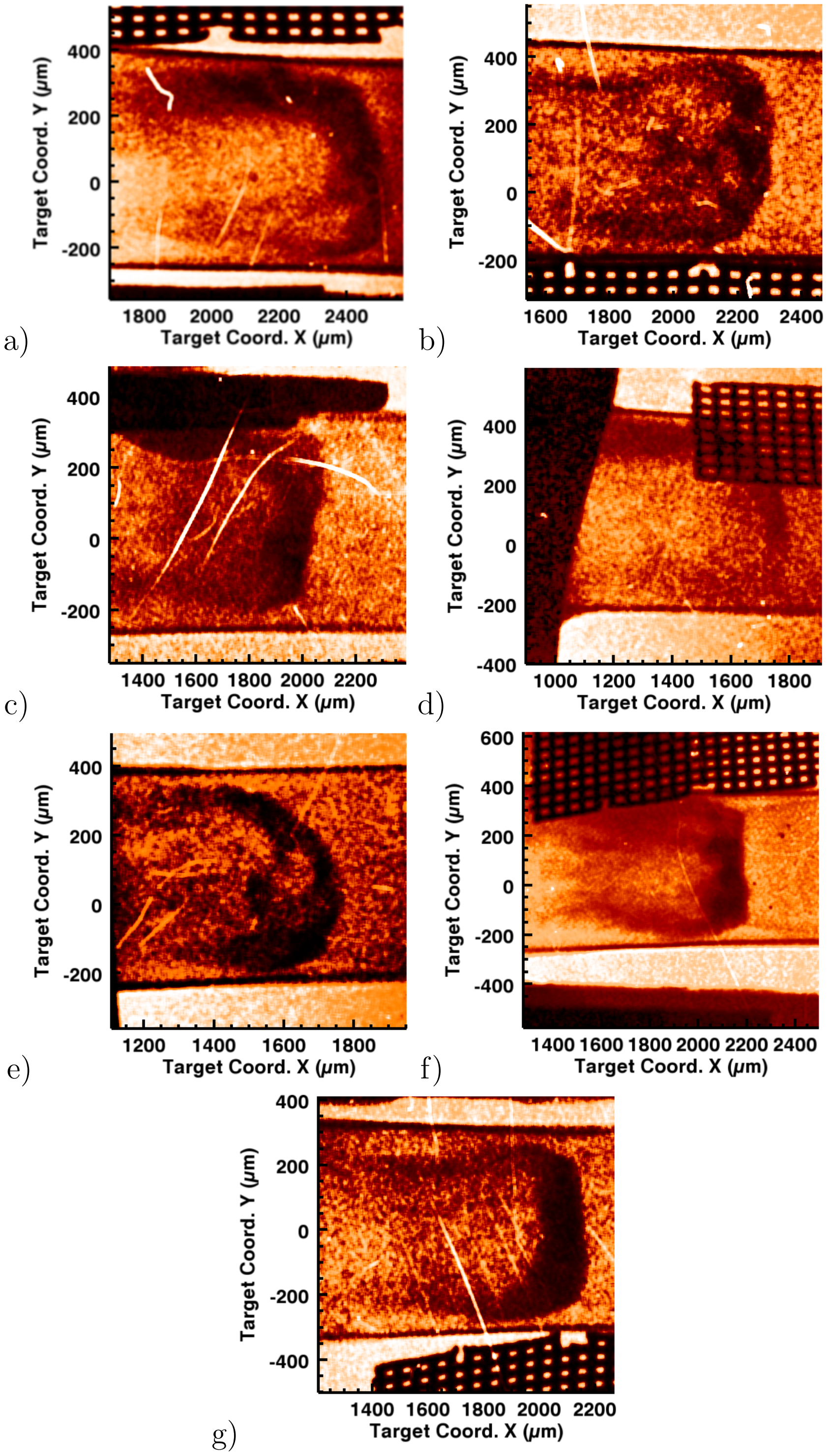

Figure 4.21: Radiography from Shot Number / Omega Port: (a) 52661 TIM-3, (b) 52661 TIM-6, (c) 52663 TIM-6, (d) 52664 TIM-3, (e) 52664 TIM-6, (f) 52665 TIM-3, (g) 52665 TIM-6

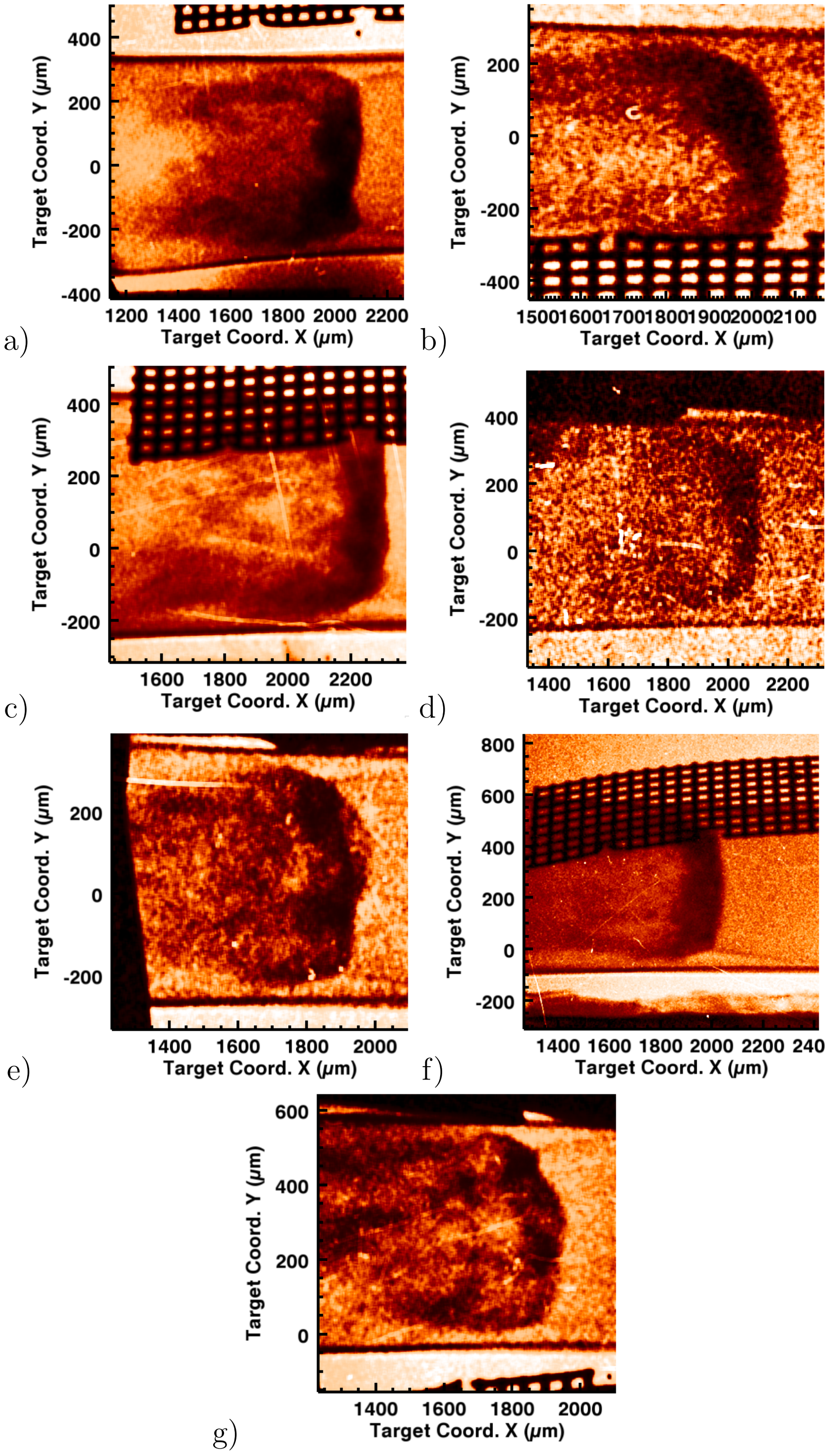

Figure 4.22: Radiography from Shot Number / Omega Port: (a) 52667 TIM-3, (b) 52667 TIM-6, (c) 52668 TIM-3, (d) 52668 TIM-6, (e) 52669 TIM-6, (f) 52670 TIM-3, (g) 52671 TIM-6

4.4 Late Time Repeatability Shots - August 2010

In August 2010, a set of experiments were designed to obtain repeatable data later in the shock's lifetime, at around 26 ns. The purpose of this was to quantify the further evolution of the shock from the 13 ns state to the 26 ns. This would have implications for the shock's overall speed and deceleration, as well as the growth of instabilities in the post-shock layer.

4.4.1 Experimental design

Several changes were made to the design from October 2008 shown in Section 4.1.1, including both changes due to different experimental goals ("physics" changes), and changes to improve methodology and better achieve goals ("repairs"). Documents showing the August 2010 target design are shown in Figures 4.23, 4.24, and 4.25.

In the category of physics-motivated changes, the viewing volume was moved to 3 mm, and the timing was adjusted to nominally view the shock at 26 ns after drive. Beryllium discs of 21 μm thickness were used for the experiment. The targets used x-ray fiducials constructed out of three layers of 25 μm aluminum.

In order to improve upon the October 2008 targets, the sources of possible error were reduced. The large shock uncertainty seen in some targets, as recorded in Table 4.2, was a result of sensitivity of the measurement scheme to small rotations of the polyimide shock tube with respect to the drive disc normal. Because the drive disc is not visible through the acrylic shield during target metrology steps in the shock viewing volume, the far end of the polyimide shock tube was used as a reference location. Since this tube end was over 5000 μm away from the drive disc, small discrepancies in drive tube angle were magnified in the inferred shock position measurements. Unfortunately, in the October 2008 data, the targets were found after construction to have up to three degrees of error in tube alignment in several targets, leading to the large uncertainty in shock location measurement.

This issue was addressed in two ways. First, in order to reduce the angular discrepancies of the shock tubes, the acrylic structure was reworked. Relative to the 2008 design in Figure 4.1, one can see that in Figure 4.24 more acrylic was added (an option which could be implemented due to the increased distance between the viewing volume and the drive disc) and the gas fill line was redesigned to have a very small drill hole in the final layer of acrylic before reaching the shock tube. Previously, a large gas fill hole in the acrylic was mated to a small gas fill hole in the shock tube (kept small to minimize the effect of the hole on the passing shock). However, it is believed that the large hole in the acrylic region responsible for holding the shock tube straight allowed for a systematic bending of the polyimide tube, contributing to much of the observed angular discrepancy of the 2008 shock tubes.

Second, the use of the end of the shock tube was forced in the 2008 design by the absence of any other features on the viewing side of the shield. In this campaign, several corners were machined into the acrylic, as seen in Figure 4.24, with the distances from them to the drive disc kept very consistent. An acrylic column was machined for additional use both as a metrology feature and as a possible alignment feature in the YTVS view at the Omega laser.

For simplicity, the backlighting scheme for these experiments was to use two separate targets as pinhole backlighters. Five beams were again used for each backlighting source, but because the shock was believed to be propagating more slowly at 26 ns after the drive than at 13 ns, a 300 ps pulse was used instead of 200 ps to deliver more total energy and produce more signal with no more blurring than was experienced in the 2008 experiments.

4.4.2 Data and results

Unfortunately, unforeseen experimental difficulties limited the effective length of this campaign to three shots. One of the shots produced a shock image at 20 ns (Fig-

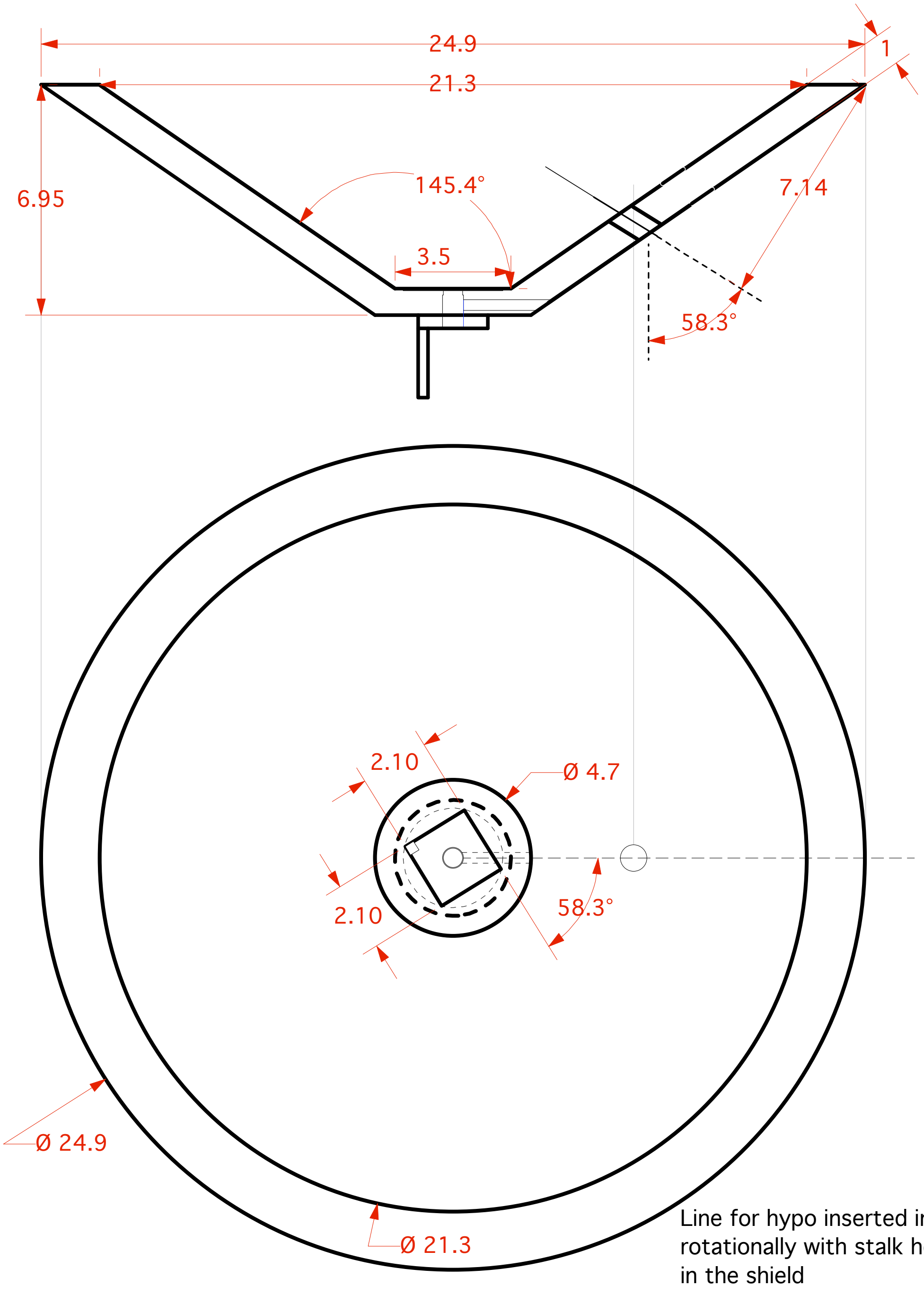

Figure 4.23: Schematics for the large-scale dimensions of the acrylic shield used in the August 2010 campaign. Dimensions are in mm.

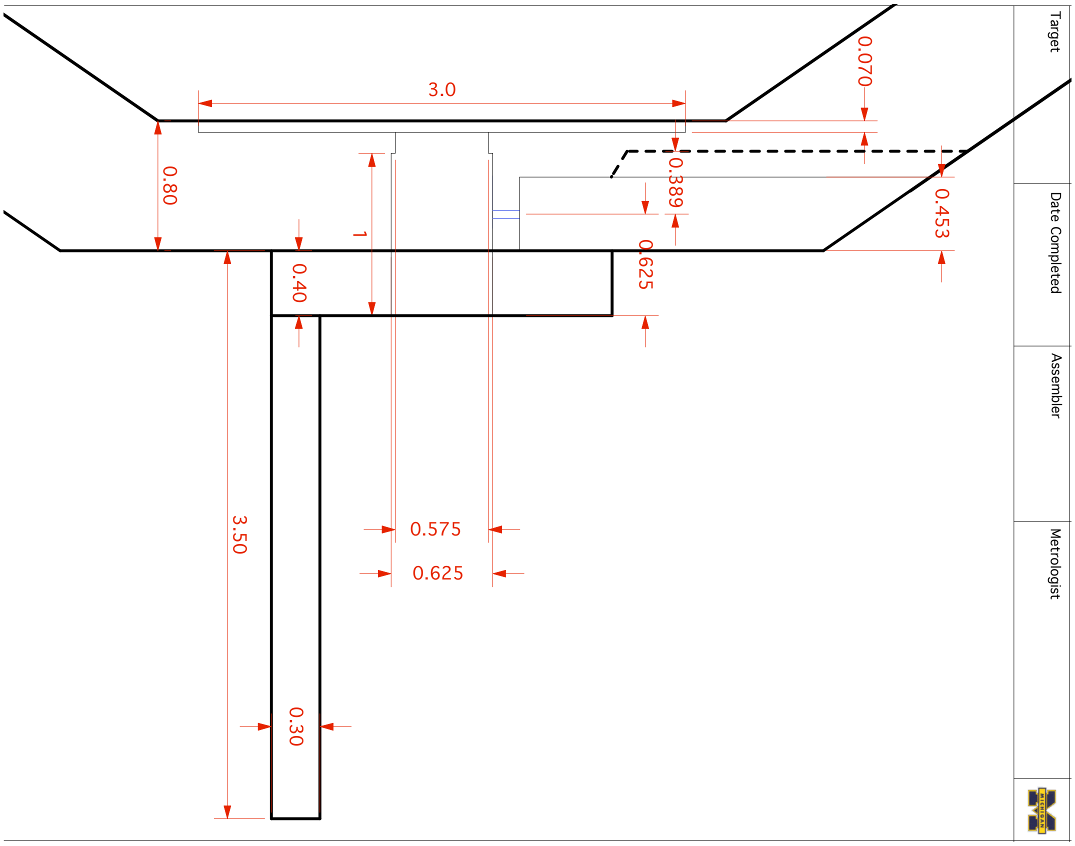

Figure 4.24: Internal structure and dimensions of the August 2010 target design in the vicinity of the drive disc and shock tube. Dimensions are in mm.

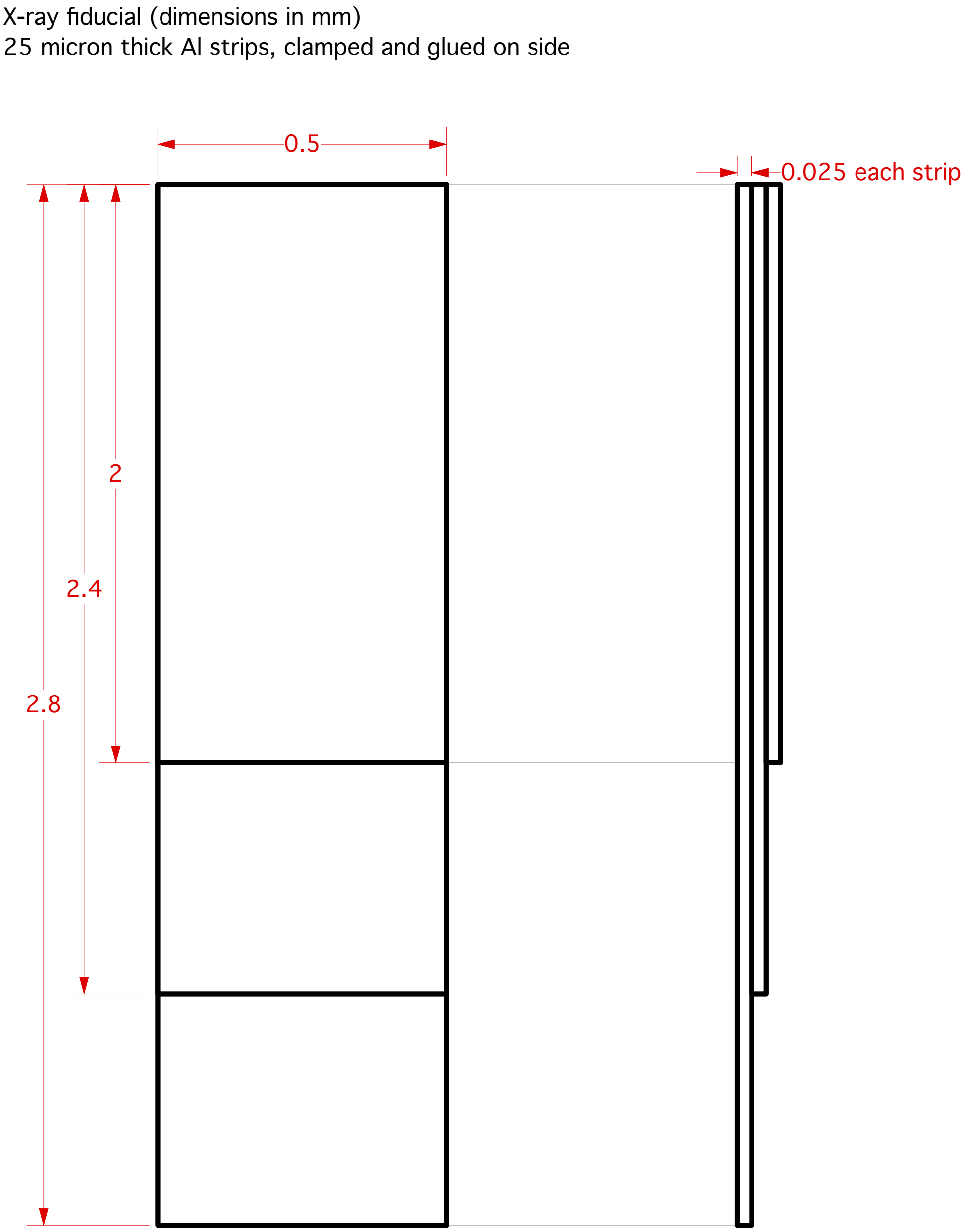

Figure 4.25: X-ray fiducial used in targets.

ure 4.26a), one shot produced an orthogonal pair of images at 26 ns (Figure 4.26b and c), and one produced a "bubble shock" resulting from a tilted drive disc (Figure 4.26d). These results unfortunately undermine the campaign's status as a "repeatability" test, though the data obtained remain valuable in establishing a time sequence of the shock lifetime. In particular, the growth and structure of perturbations observed in the shocked layer from images such as Figures 4.21 and 4.22 at 13 ns to Figure 4.26a at 20 ns and then Figure 4.26b at 26 ns, showing the modulation progress from semi-periodic structures with as many as three maxima visible within the shock tube to a single large dense region near the tube axis, inform and support the conclusions of the instability work in Chapters III and VI.

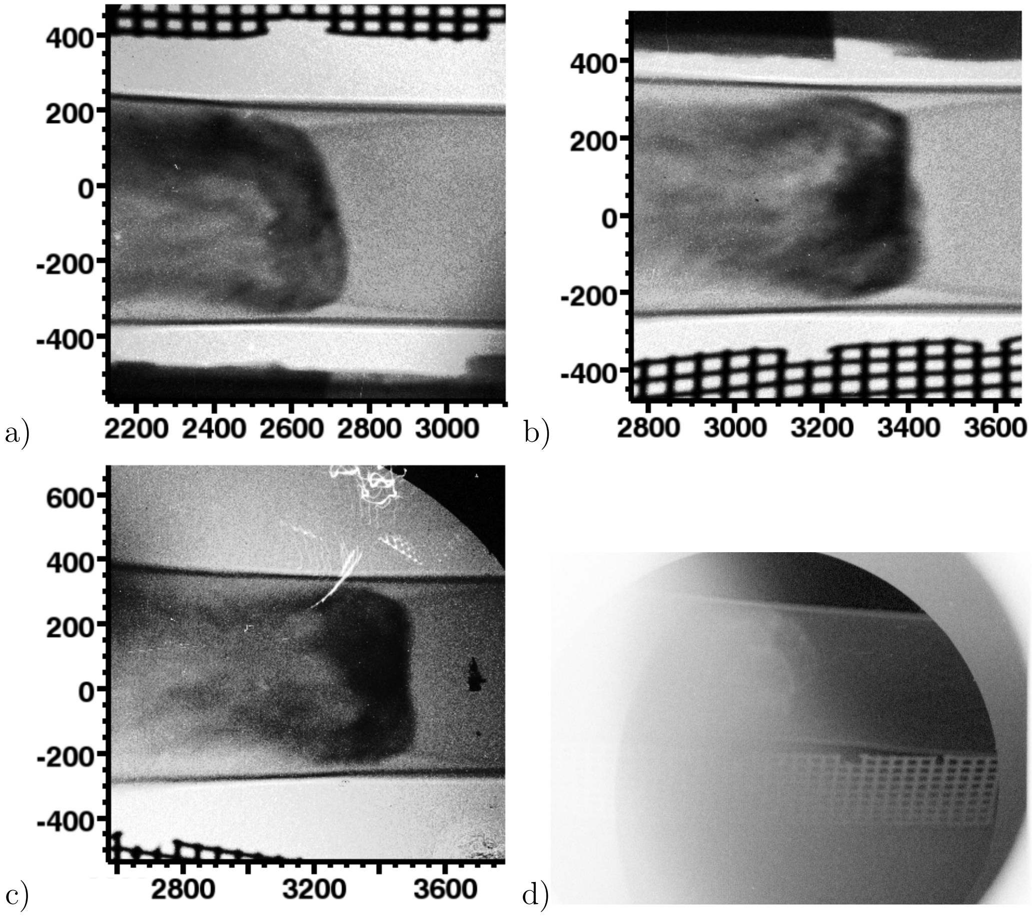

Figure 4.26: Radiography (image plates) from Shot Number / Omega Port: (a) 59026 TIM-3, (b) 59027 TIM-3, (c) 59027 TIM-6, (d) 59029 TIM-6

CHAPTER V

Exploratory Experiments and Data - July 2007, 2008, 2009

Unlike the shot campaigns discussed in Chapter IV, which focused on creating many instances of a single repeatable design, the shot campaigns carried out in the Julys of 2007, 2008, and 2009 attempted to explore the space of target designs and obtain correlated data from several closely related images. These experiments took place later in the tube (3 mm from the drive disc, as opposed to 2 mm in the October 2008 experiments), and fired a range of drive discs (controlling the primary shock's initial speed and time to observation).

Each of the three sections in this chapter describes an experimental campaign on the Omega laser. We describe in each section the unique experimental features for that sequence of targets; for experimental details common to all experiments, we refer the reader to Section 1.1.

5.1 Fast Backlighting Shots - July 2007

The first experimental campaign in which the author participated was an experiment to test the viability of radiography through fast point-projection backlighting onto ungated film as a diagnostic. The radiative gas experiments of Reighard [77] had successfully imaged xenon shocks using long (> 1 ns) area-emission backlighter pulses and x-ray pinhole cameras with an approximately 200 ps "shutter speed." Subsequently, experiments by Kuranz [57] on blast-wave-driven Rayleigh-Taylor instability obtained superior radiography utilizing static ("unshuttered") film and 1 ns backlighting pulses through a pinhole emitter. These long backlighting pulses were appropriate for the dynamic time scale of the Rayleigh-Taylor instability, but were unsuitable for radiative shocks traveling over 100 km/sec, in which a 1 ns exposure would result in > 100 μm of blur. Three shots were used for this campaign.

5.1.1 Experimental design

This experiment sought to reduce the exposure time of the static film technique to durations useful for the radiative shock experiment. The experiment was designed to backlight with 100 ps laser pulses. Beryllium discs of 20 and 10 μm thickness were used as ablators. The viewing volume was 3 mm from the drive, and extrapolation from previous data [77] was used to predict the time at which the shock would enter the viewing volume.

One shot also experimented with the choice of backlighter materials. The usual material used in this and other shots was vanadium, which emits at 5.18 keV. One shot used iron, which would emit at a higher and therefore more probing energy, but which unfortunately did not produce data in that view.

5.1.2 Data and results

The results of the experiment showed two shock images (Figure 5.1), demonstrating that 100 ps backlighting was a possibility. However, the images had noise resulting from lower than expected generation of signal (later rectified by increasing the pulse duration, see Section 5.3). The shocks imaged were also seen at the far drive-side of the viewing volume, discrediting the notion that simple linear extrapolation of the shock location from data at 2 mm would extend to distances of 3 mm. The shock evidently experiences substantial deceleration during this time, despite the fact that the trailing rarefaction has not yet reached the shock front. Obtaining data to illuminate the shock location at long distances and the corresponding changes in shock speed became a major goal of the other experiments described in this chapter.

The targets were also subject to unfortunate design and assembly flaws, some resulting in distortion of the spatial fiducial grid, which complicated the absolute spatial calibration of the data. The primary cause (an undocumented reflection in the target assembly hardware, the implications of which were not understood at the time) was later identified and rectified.

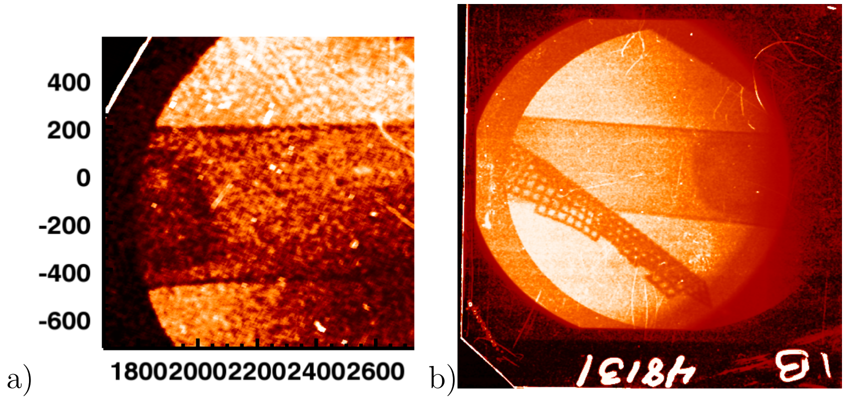

Figure 5.1: Radiography for shot number (a) 48130 and (b) 48131.

5.2 Late Time Stereoscopic Shots - July 2008

The experiments of July 10, 2008 were designed both to test a range of beryllium disc thickness and obtain timing information for shot positions relatively far down the tube (further than 3 mm). Like the shots of July 2007 discussed in Section 5.1, this experiment utilized Omega's 100 ps backlighter driver. These experiments were also the first attempt to obtain stereoscopic images though radiography. Ten targets were fired in this campaign.

5.2.1 Experimental design

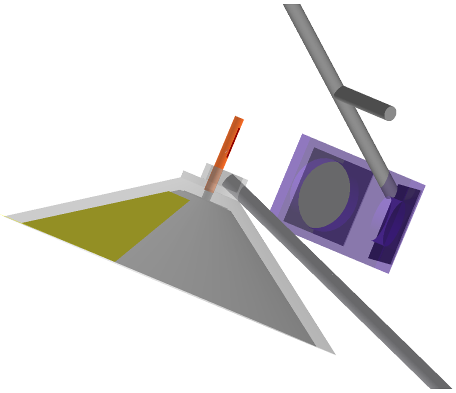

Figure 5.2: CAD image of the July 2008 experimental design as arranged in the Omega target chamber.

Figure 5.2 shows the July 2008 experimental campaign's target design as arranged in the laser's target chamber. The gray structure is the acrylic shield, previously discussed in 4.1.1, with a gold wedge for additional shielding also visible. The orange cylinder is the xenon-filled shock tube. Shown in purple is the stereoscopic backlighter frame, with the two tantalum squares which serve as pinhole substrates shown in gray.

In order to attempt stereoscopic imaging, two backlighter sources were aligned to the nearest two diagnostic ports on Omega, P10 and H3, which are separated by 37.4°. Because this required the two backlighters to be in close proximity, a solution was developed to use a single acrylic frame to hold both backlighters, avoiding issues of complicated geometry to hold and position both backlighters independently. Figure 5.3 shows the schematics for the backlighter frame designed for these targets.

The targets also included new features designed to enhance target metrology. Before the experiment, each target undergoes a measurement and characterization process to determine the exact coordinates of the spatial fiducials provided by the gold grid. Figures 5.4 and 5.5 show the design used for the target's acrylic superstructure. The sharp corners on the material to the shock tube side were used as intermediate metrology points, leading to a reduction in coordinate error.

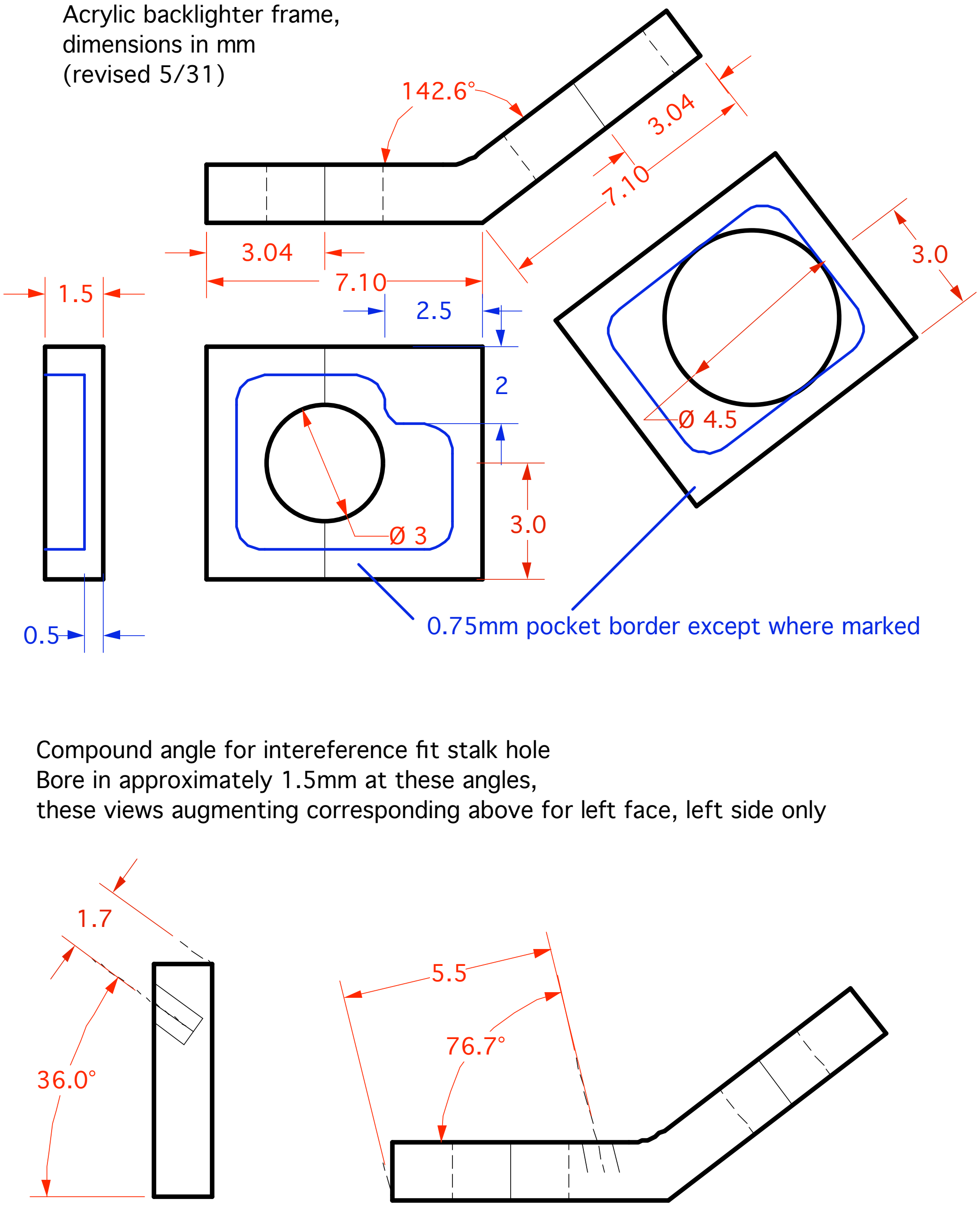

Figure 5.3: Engineering schematics for the backlighter frame used for stereoscopic imaging. Dimensions are shown in mm.

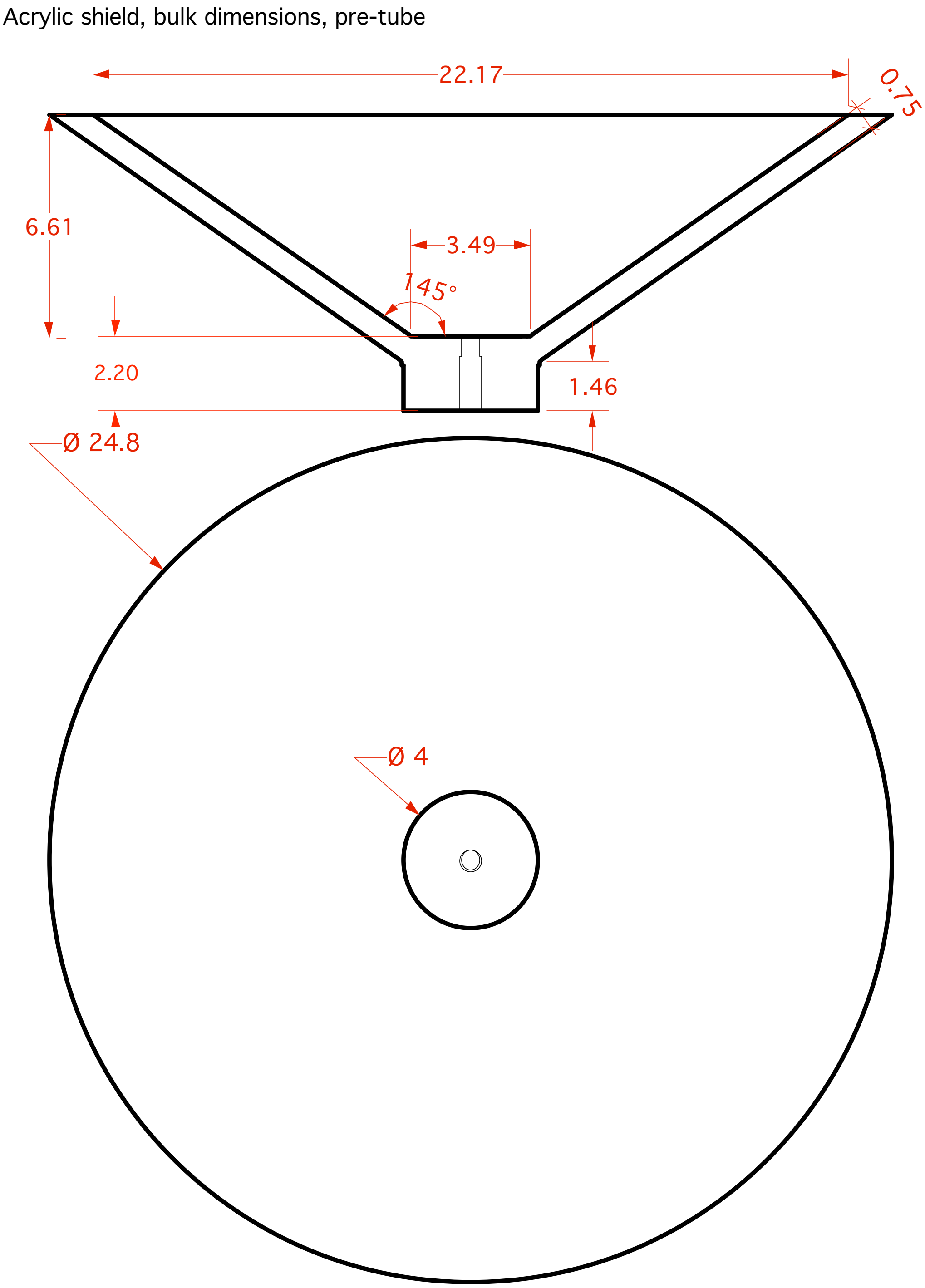

Figure 5.4: Engineering schematics for the acrylic shield used for stereoscopic imaging targets. Dimensions are shown in mm.

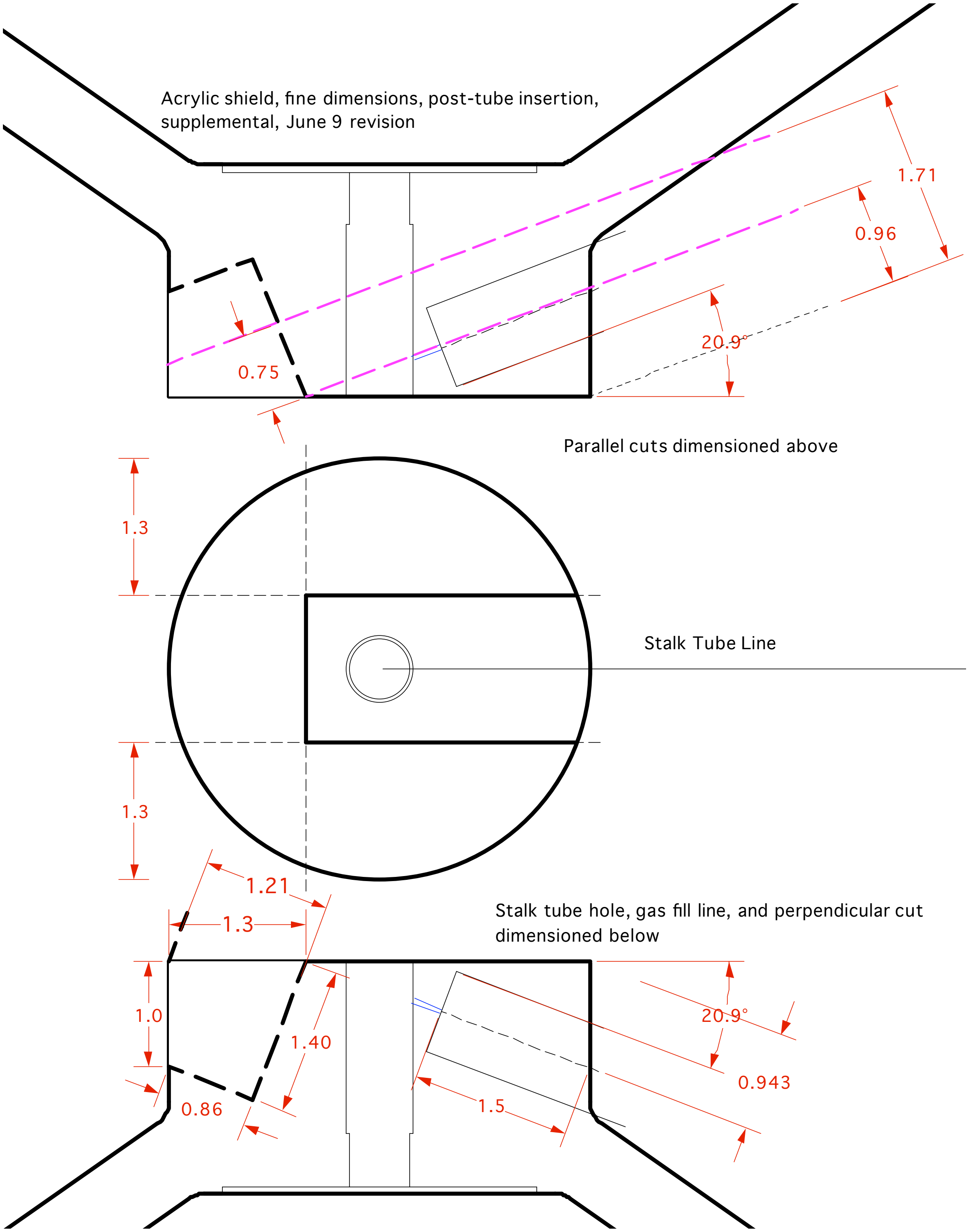

Figure 5.5: Engineering schematics for the acrylic shield in the vicinity of the shock tube. Dimensions are shown in mm.

5.2.2 Data and results

The experiment produced four successful radiographs, shown in Figure 5.6. Several images failed to produce images of shock tubes containing images of shocks. At the time, this was attributed to difficulty in timing the images relative to the drive, assuming that a radiative shock existed in the tube, but was not in the imaged area. However, later data (Section 4.4) validated the timing choices and pointed instead to issues with the experimental gas filling method, implying that the experimental timing was accurate but due to gas contamination no shock existed which could be imaged.

We also discovered what seemed to be a substantial thresholding effect in backlighter energy. Due to the geometry of the target system, nine beams were available for powering the two backlighter sources. Five beams were used to illuminate the backlighter facing the TIM-1 port, and four beams for the source facing the TIM-2 port. The film at TIM-1 obtained substantially clearer and more regularly obtainable data; the film at TIM-2 was often blank and never extremely clear. The backlighting mechanism with 100 ps pulses appears to require most of the four beams' ~ 140 J of energy to establish the plasma which converts additional energy to x-rays. The four-beam geometry produced insufficient photons, while the five-beam geometry on the other backlighter produced good images.

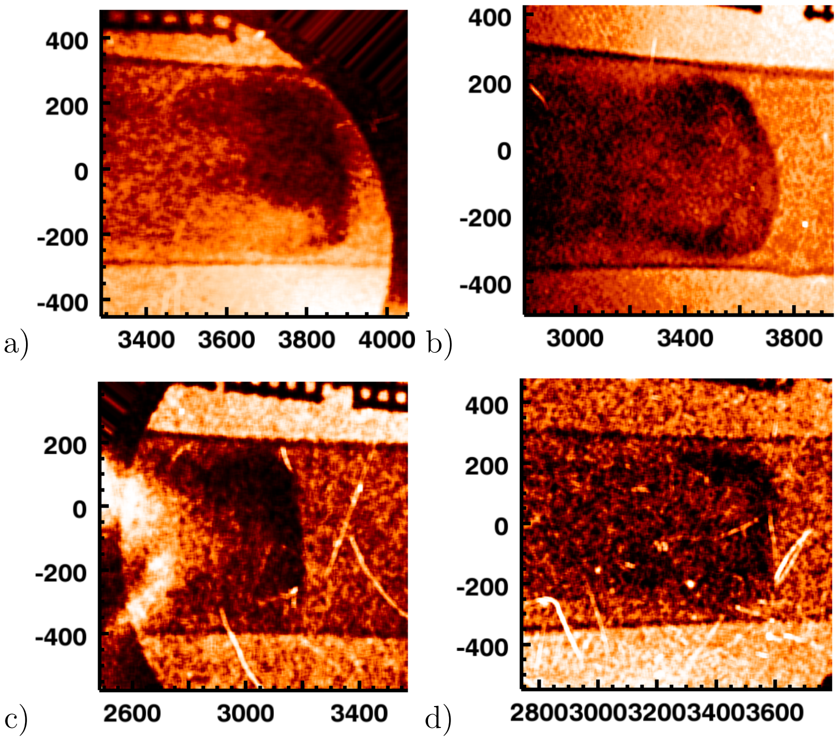

Figure 5.6: Radiography for Shot Number / Omega Port: (a) 51778 TIM-1, (b) 51780 TIM-1, (c) 51782 TIM-1, (d) 51783 TIM-1,

Table 5.1: Data recorded for the experiments of July 10, 2008. Distances and thicknesses are given in microns, times in ns. The column 'fiducial' refers to fiducial discrepancy, a measure of the likely magnitude of measurement uncertainty for that target.

Shot No.	Be thickness	View 1 time	Shock location 1	Fiducial 1
51778	26	31.5	3903	13
51780	18	24.4	3710	74
51782	29	30	3201	118
51783	17	23	3590	22

5.3 Stereoscopic Shots - July 2009

The experiment of July 2009 was designed to revisit the goals of the experiment in July 2008. By the end of the July 2008 campaign, successful timings for shocks produced by variable thicknesses of beryllium ablators had been obtained over 3 mm down the tube. These timings were used in the present experiment to obtain additional data at this distance. Eleven targets were fired in this campaign.

5.3.1 Experimental design

A series of changes to the backlighting scheme was made to address the issue of insufficient energy in the backlighter. First, the laser's driver was changed to 200 ps pulses, which provide sufficiently good temporal resolution for these shocks without the stringent energy requirements. Second, the backlighter geometry was modified to obtain ten beams for backlighting. To do this, one of the backlighter sources was modified to a *tilted pinhole*, in which the pinhole through which the x-rays pass is not normal to the plane of the tantalum substrate. Usually used to direct debris away from the imaging equipment [10], in this case it also was used to change the orientation of one of the backlighting surfaces such that each surface could be powered by five unique beams. The resulting design is shown in Figures 5.7–5.9.

Table 5.2: Data recorded for the experiments of July 21, 2009. Distances are given in microns, times in ns.

Shot No.	Be thickness	View 1 time	Shock location 1	Fiducial 1	View 2 time	Shock location 2	Fiducial 2
54979	23	26	2960	60	27	3120	45
54980	32	31	3359	30	32	3446	18
54982	31	30.5	3635	35	31.5	3739	50
54983	17	22.5	2989	60	23.5	3009	15
54984	22	26	3104	40			
54986	32	31.5	3236	100			
54987	18	25	3168	28			
54988	23	27	2965	40			
54989	21	26	3056	19			

Aside from the backlighter, the same physical target design was used as in July 2008, as shown in Figures 5.4 and 5.5. The only additional component was an x-ray fiducial, consisting of three stepped layers of 25 μm aluminum, used to diagnose x-ray intensity.

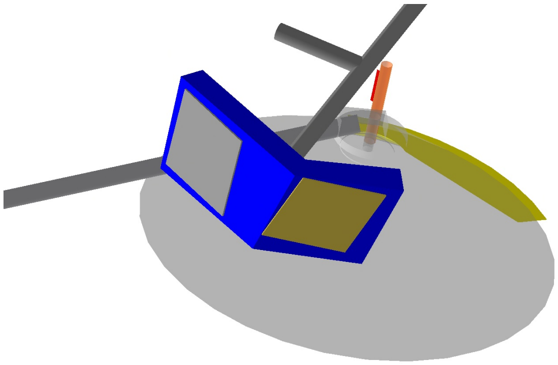

Figure 5.7: CAD image of the July 2009 experimental design as arranged in the Omega target chamber. The blue object is the stereoscopic backlighter with one tilted pinhole.

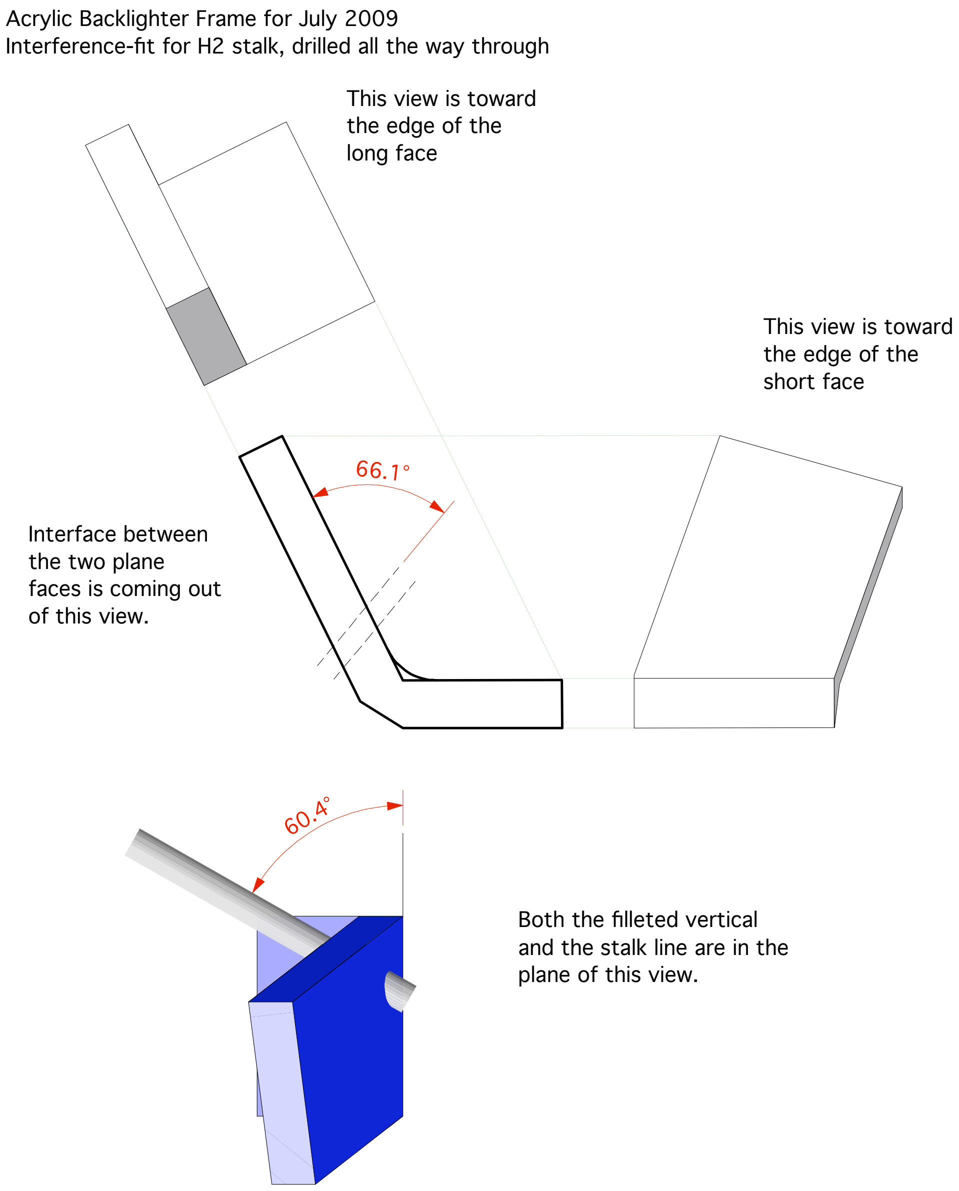

Figure 5.8: Engineering schematic of the July 2009 stereoscopic backlighter frame. Dimensions are shown in mm.

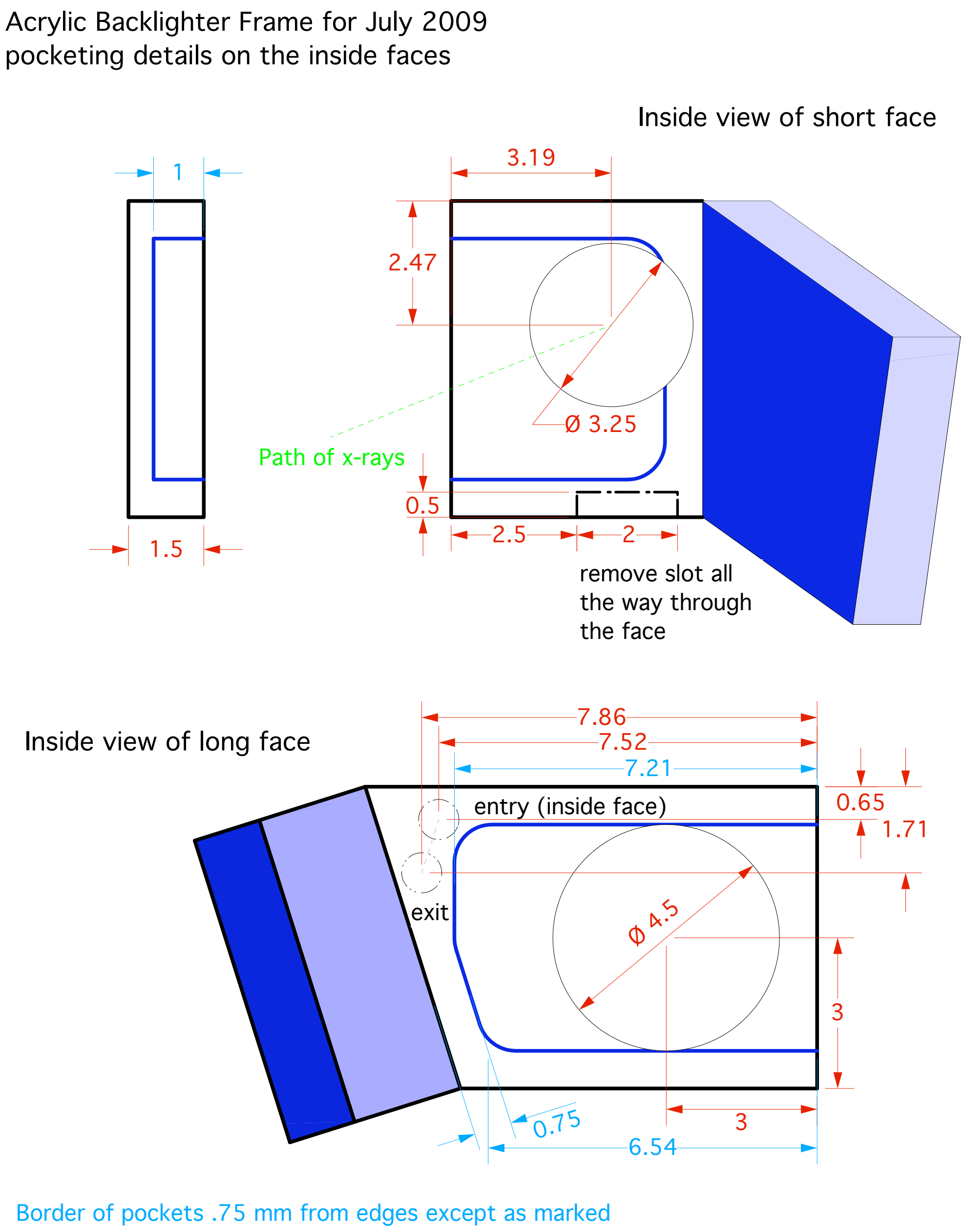

Figure 5.9: Engineering schematic of the July 2009 stereoscopic backlighter frame (continued from Fig. 5.8).

Table 5.3: Wall shock amplitudes for the experiments of July 21, 2009. **Wall shock data was obscured for Shot 54986.

Shot No.	Average Wall Shock Amplitude (μm)	Average Wall Shock Amplitude (view 2) (μm)
54979	53	53
54980	59	51
54982	46.5	49
54983	61	61
54984	45.5	
54986	**	
54987	48	
54988	38	
54989	37	

5.3.2 Data and results

Figures 5.15 and 5.16 show the data gathered in the July 2009 campaign. Table 5.2 shows the shock locations and estimated accuracy taken from each radiograph, along with the measured beryllium disc thickness and image time. In addition to the principal measurements of shock position as a function of time, the maximum wall shock displacement inward from the tube wall was also measured from the radiographs, and recorded in Table 5.3.

Figure 5.10 shows the collected average speed of shocks from both the July 2008 and July 2009 datasets (Tables 5.1 and 5.2). The error bars shown in Figure 5.10 are derived from the measured fiducial discrepancy for each shot (often quite small compared to the total distance the shock has traveled) and 1 μm of uncertainty in disc thickness from the resolution of the micrometer used. Pairs of closely spaced points are typically derived from two radiographs of the same shock.

Looking at the data in Figure 5.10, we see the tendency of average shock speed to fall off with initial disc thickness. We predicted such a relation in Section 1.3.3, where we used Equation 1.15 to predict an initial velocity for each shock. The curved

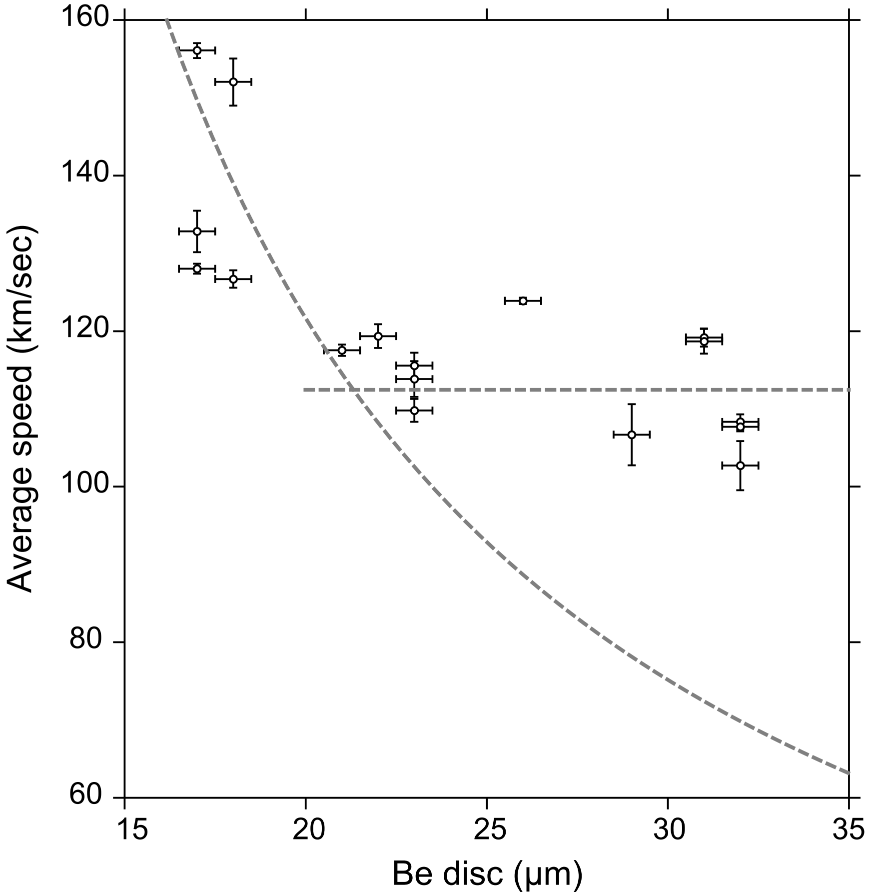

Figure 5.10: Beryllium disc initial thickness in μm against average speed (defined as shock position divided by time since the driving event began) in km/sec for the collected data in Tables 5.1 and 5.2. The curved dashed line represents Equation 5.1 fit to the discs with thickness less than 25 μm. The horizontal dashed line represents 112 km/sec.

dashed line in Figure 5.10 shows the outputs of model in rocket-equation form,

$$v_{ave} = 287.7 \ln\left(\frac{t}{t-6.9}\right) \text{km/sec} \tag{5.1}$$

where t is the disc thickness in μm, 6.9 μm is derived from the results in Section 1.3.3, and the numerical prefactor is fit to the data.

This relation matches the thin beryllium disc data for average speed well, but underpredicts the speed for thick discs, implying that initially slower shocks undergo substantially less deceleration. This is consistent with the hypothesis that the deceleration is largely an effect of radiative cooling, which is proportionately stronger for faster shocks, as discussed in Section 1.2. The dashed line in Figure 5.10 shows the mean value of data from discs thicker than 25 μm, which seems to form the approximate threshold velocity, near 110 km/sec, for strong deceleration.

We wish also to use the data in Tables 5.1 and 5.2 to refine the estimate of initial shock speed as a function of disc thickness from Section 1.3.3. In addition, data for 10 μm shots from previous experiments [77] has been used. In order to investigate, a simple model was constructed in which the shock radiatively decelerates with a power law (with undetermined coefficient α), until it reaches the critical velocity V_c, after which it is steady. This crude model may be written as

$$V_s = \mathrm{Max}\left(V_0 t^{-\alpha}, V_c\right) \tag{5.2}$$

where V_0 is the initial (maximum) velocity of the shock, taken to occur at 1 ns at the time the beams are scheduled to turn off. The initial velocity depends through the standard rocket equation on the thickness of the beryllium disc T, the amount of material ablated during the driving event A, and the velocity with which the ablated material is expelled,

$$V_0 = V_i \ln\left(T/(T-A)\right) \tag{5.3}$$

For a given (measured) beryllium thickness, we obtain as data a position of the shock at a particular time, which are expressed as integrals of Equation 5.2 from 1 ns to the time of observation. From a number of the shots, we can evaluate the positions for various values of the parameters α, A, V_i, V_c and compare them to experiment. A least-squares fit of various shocks gives the values of $\alpha = 0.48, A = 8.0\mu\mathrm{m}, V_i = 435$, and $V_c = 110$ km/sec. Comparing these fits for initial speeds with the average speeds found in Equation 5.1, we see that the average speed of the radiative shocks propagated across a distance of 3 mm is approximately two-thirds their initial speed.

The data is seen to fit to these parameters quite well for both thin discs (which inform primarily α) and thick discs (which are dominated by V_c). The 21 micron data (Figure 5.13) shows the greatest discrepancy with the model, which is reasonable given the model's crudeness. The near-20-micron experiments would be expected to be the ones most reliant on the transition between the two hypothesized velocity phases, a transition which is in this model quite primitive. The model almost certainly overpredicts α, which would be lowered by the inclusion of another deceleration for $V_s < V_c$ proportional to e.g. V_s^β. However, introducing the additional parameter to be fit is found, for the available quantity of data, to make the analysis unusably fragile.

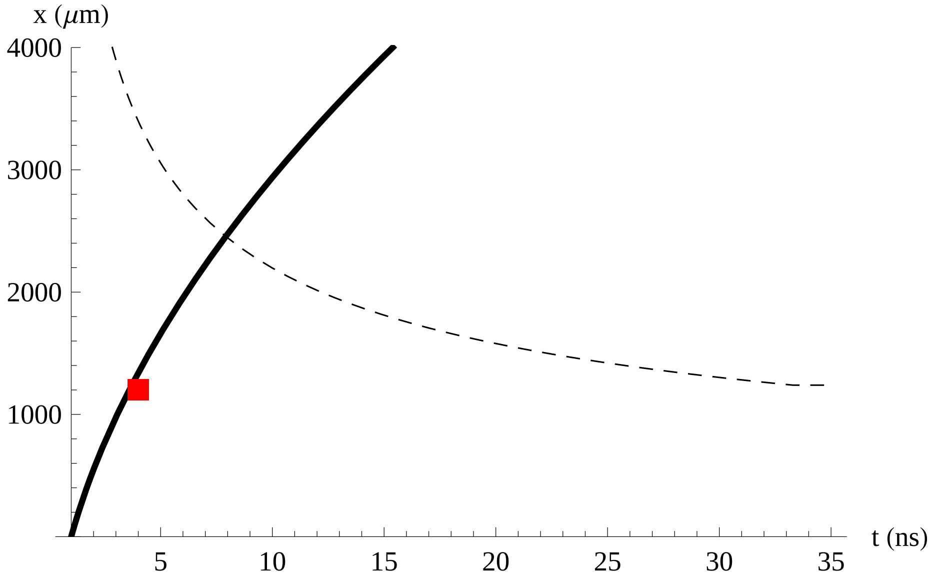

Figure 5.11: Data and model for 10 micron beryllium disc (data from A. Reighard [77]). Dashed line is proportional to modeled velocity at each time.

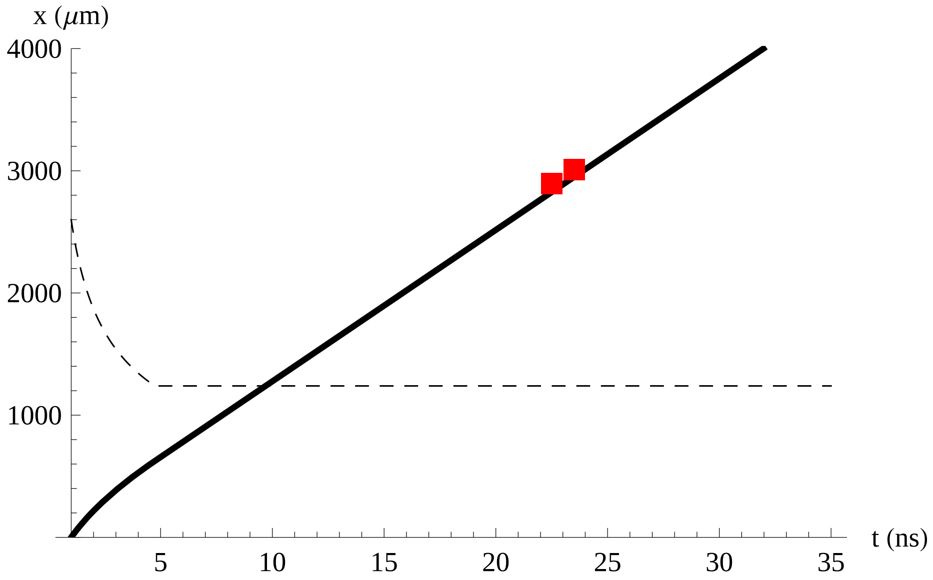

Figure 5.12: Data and model for 17 micron beryllium disc. Dashed line is proportional to modeled velocity at each time.

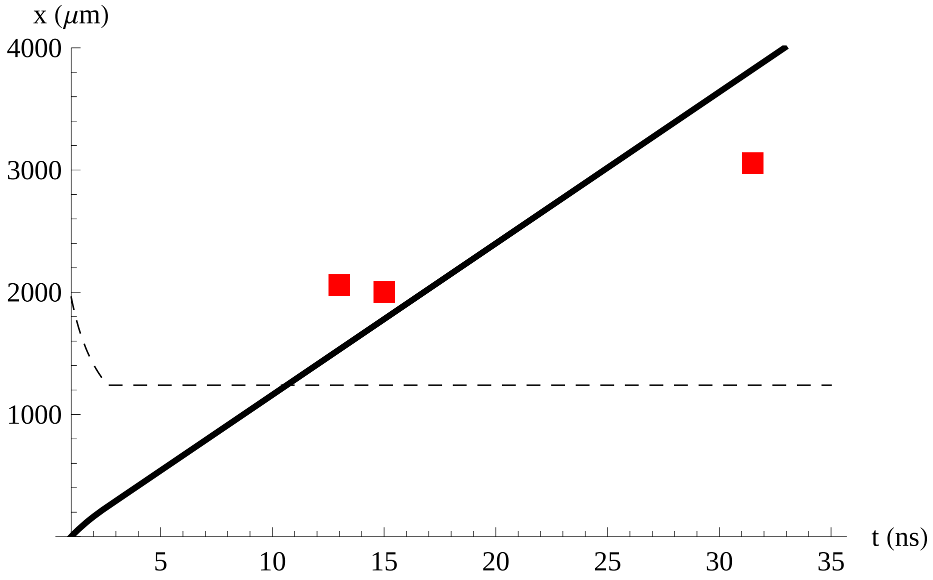

Figure 5.13: Data and model for 21 micron beryllium disc. Leftmost point is consensus for CRASH 13 ns data, rightmost point is from July, center point is consensus of A. Reighard's experiments with 20 micron (approximate) beryllium. Dashed line is proportional to modeled velocity at each time.

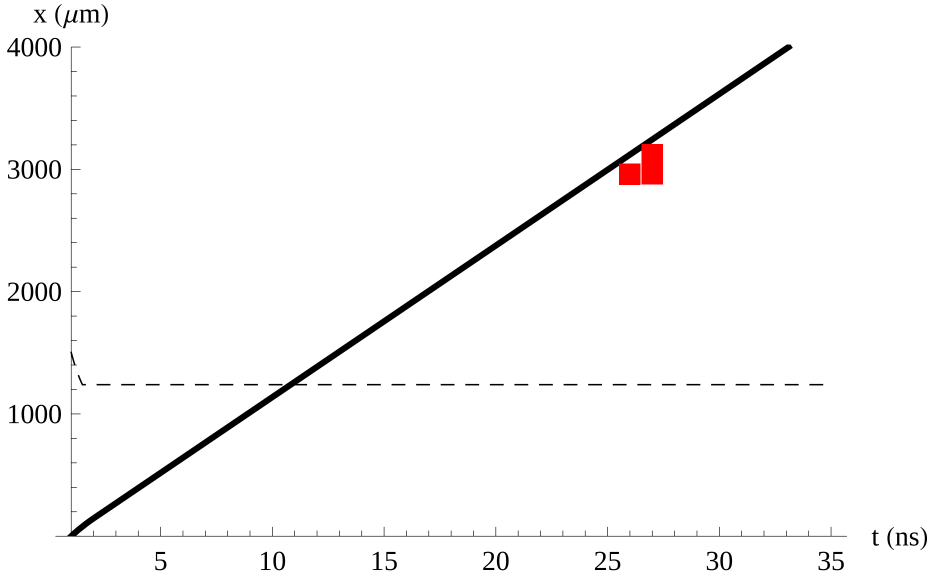

Figure 5.14: Data and model for 23 micron beryllium disc. Dashed line is proportional to modeled velocity at each time.

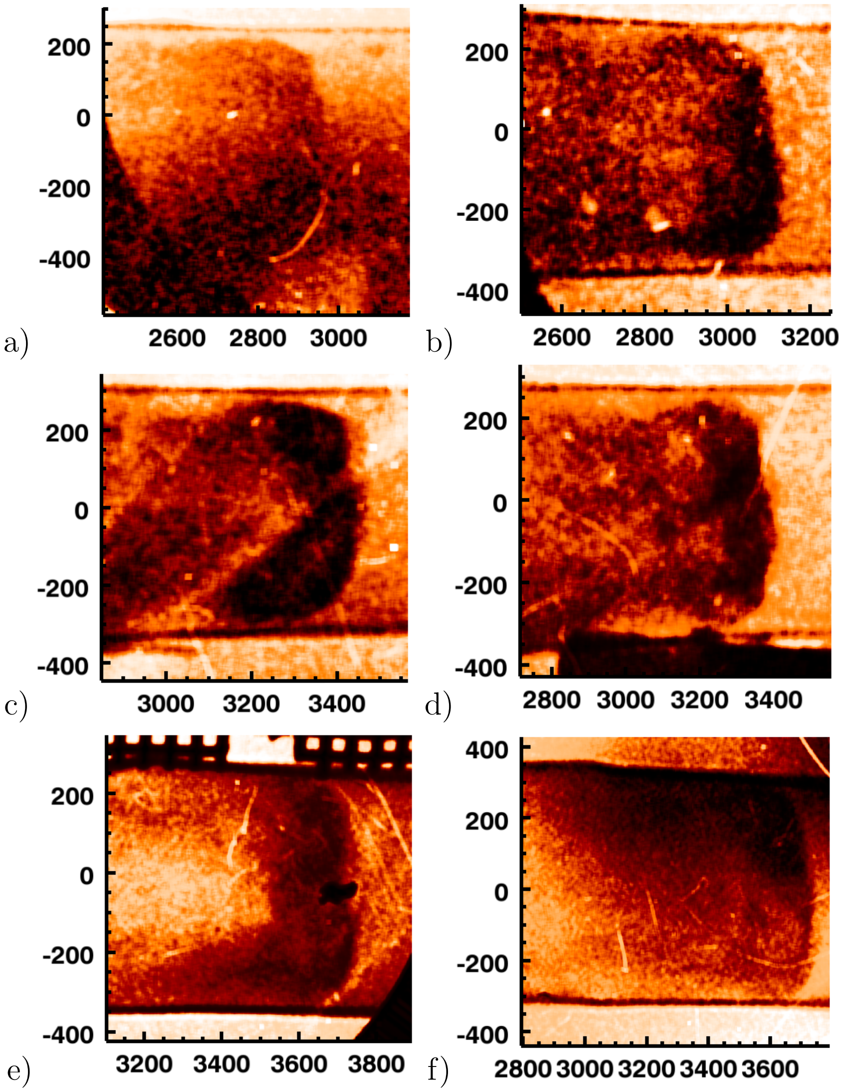

Figure 5.15: Radiography for Shot Number / Omega Port: (a) 54979 TIM-1, (b) 54979 TIM-2, (c) 54980 TIM-1, (d) 54980 TIM-2, (e) 54982 TIM-1, (f) 54982 TIM-2

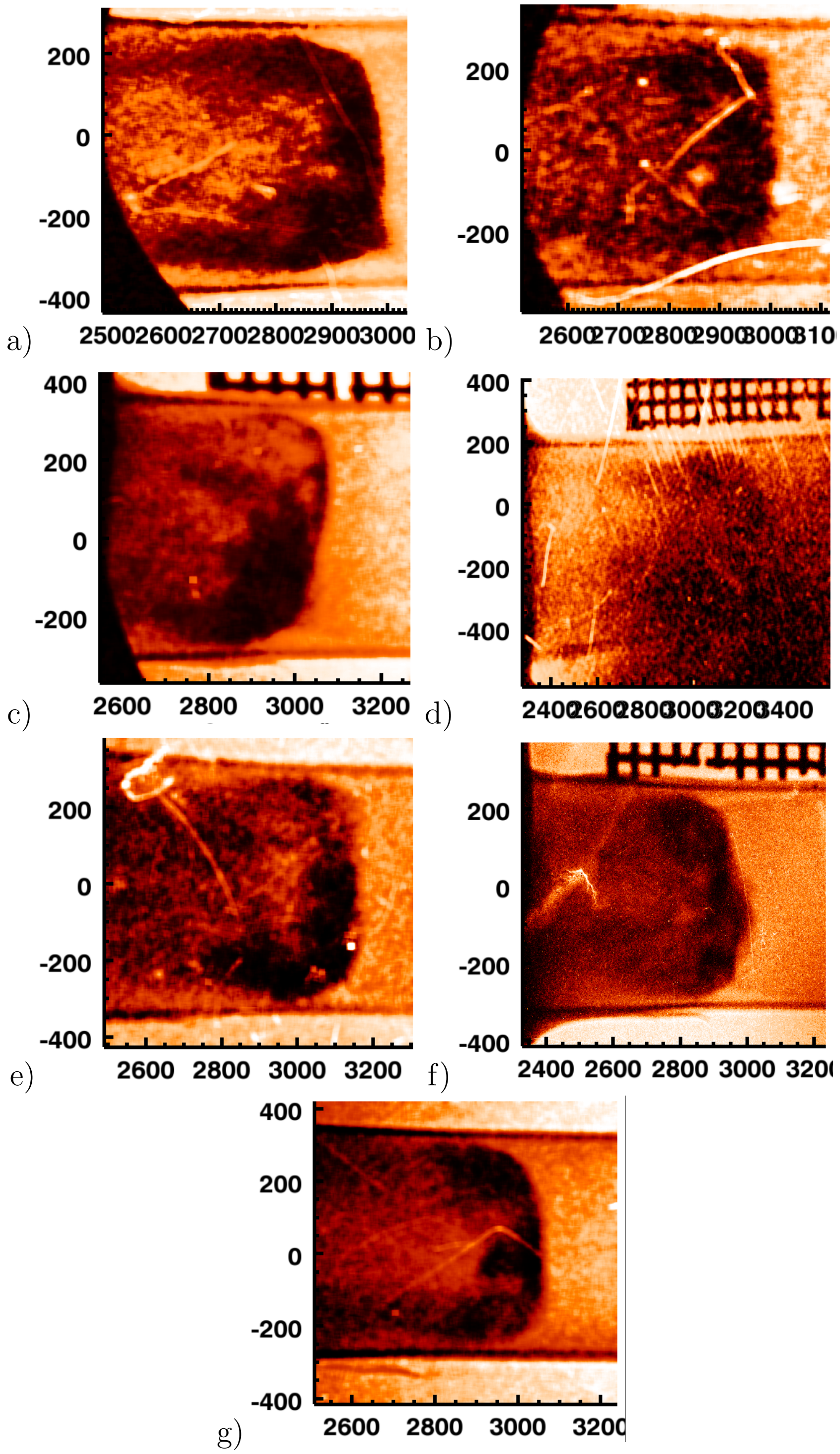

Figure 5.16: Radiography for Shot Number / Omega Port: (a) 54983 TIM-1, (b) 54983 TIM-2, (c) 54984 TIM-1, (d) 54986 TIM-1, (e) 54987 TIM-1, (f) 54988 TIM-1, (g) 54989 TIM-2

CHAPTER VI

Toward a Scaled Astrophysical Instability Experiment

This chapter exists to synthesize the theoretical instability predictions of Chapter III, which should be common to both stars and laboratory systems with powerful, decelerating shocks, with the empirical data of Chapter V. It consists of formal derivations implying how one can build a laser-driven laboratory experiment to test the instability theory of Chapter III under the same physical conditions as astronomers observe in stellar objects.

6.1 Non-dimensionalization of the theory of instabilities

A decelerating shock bound by a material-composition contact discontinuity in a dense post-shock layer is subject to an instability, first investigated by Vishniac [92]. In this instability, the acceleration and density gradients are such that the rear contact discontinuity is stable against the onset of Rayleigh-Taylor instability, but coupling between the shock and rear surfaces of the dense layer leads to the exponential growth of initially low-amplitude perturbations.

Vishniac and Ryu [94] derived their dispersion relation (Equation 14 in their paper) as

$$\omega^4 - \omega^2 k^2 c_s^2 - \frac{k^2 c_s^4}{2L^2}\left(\frac{1+\beta^Q}{1-\beta^Q}Q - 1\right) = 0 \tag{6.1a}$$

where

$$L = \frac{c_s^2}{|\dot{V}_s|}, \tag{6.1b}$$

$$\beta = e^{-H/L}, \tag{6.1c}$$

$$Q = \sqrt{1 + (kL)^2 - \left(\frac{\omega L}{c_s}\right)^2}. \tag{6.1d}$$

In these equations, c_s is the speed of sound throughout the post-shock layer, $|\dot{V}_s|$ is the deceleration of the shock, H is the thickness of the post-shock layer, k is the wavenumber of a sinusoidal mode under consideration, ω is that mode's frequency of oscillation (ω's imaginary part is its growth).

Equation 6.1 can be written in terms of five variables, each having physical dimensions of some powers of length or time. Terms with units of mass do not appear in the dispersion relation. It is a result of the theory of models [61] that Equation 6.1 can be rewritten as an equation in three dimensionless variables. It is convenient to use the set

$$\Pi_1 = \frac{c_s^2}{|\dot{V}_s|H}, \tag{6.2a}$$

$$\Pi_2 = kH, \tag{6.2b}$$

$$\Pi_3 = \frac{c_s}{|\dot{V}_s|}\omega. \tag{6.2c}$$

Π_1 is the ratio of the post-shock material's compressible scale height to the layer width, while Π_2 and Π_3 are non-dimensionalized parameters for specific modes. In terms of these new variables, Equation 6.1 may be rewritten as

$$\Pi_3^4 - \Pi_1^2\Pi_2^2\Pi_3^2 + \frac{1}{2}\Pi_1^2\Pi_2^2\left(\frac{\sqrt{1+\Pi_1^2\Pi_2^2-\Pi_3^2}}{\tanh\left((2\Pi_1)^{-1}\sqrt{1+\Pi_1^2\Pi_2^2-\Pi_3^2}\right)} - 1\right) = 0. \tag{6.3}$$

Equation 6.3 is a fourth order equation in the complex frequency parameter Π_3. The connection between the dispersion relation of Equation 6.3, which includes internal effects to the layer, to the earlier, simpler derivation of Vishniac in 1983 [92], can easily be demonstrated. The relevant approximations are (1) the assumption that the layer is thin compared to the compressible scale height of the system, $\Pi_1 >> 1$, (2) the assumption that wavelengths under consideration are long compared to the layer thickness, $\Pi_2 \lesssim 2$, and (3) sound waves internal to the layer are neglected, allowing the replacement $\sqrt{\Pi_2^2 - (\Pi_3/\Pi_1)^2} \rightarrow \Pi_2$. The last of these is completely analogous to the limiting case in dimensional variables of $j \rightarrow k$ in Section 3.2.4 and applies when $\omega \ll kc_s$. Under these limiting assumptions, Equation 6.3 becomes

$$\Pi_3^4 - \Pi_1^2\Pi_2^2\Pi_3^2 + \Pi_1^3\Pi_2^2 = 0 \tag{6.4}$$

which is the non-dimensional form of the simpler dispersion relation found in Vishniac 1983 [92]. From Equation 6.4 one can readily obtain the approximate cutoff condition for the smallest unstable wavelength as the condition

$$\Pi_{2\text{crit}} = \sqrt{\frac{4}{\Pi_1}}. \tag{6.5}$$

6.2 Non-dimensional parameters for physical systems

Because the dispersion relation 6.3 gives one of the non-dimensional variables as a function of the other two, a system which has been confirmed to scale in two of the three scaling parameters is guaranteed to scale in the third parameter as well. In comparing experimental and astrophysical systems, it will be useful to describe them in terms of two additional dimensionless parameters,

$$A = \Pi_1 = c_s^2/(|\dot{V}_s|H) \tag{6.6a}$$

$$L = 2\pi/\Pi_{2\min} = \lambda_{\max}/H \tag{6.6b}$$

in which we have changed from the "wavenumber-like" lateral parameter Π_2 to the "wavelength-like" lateral parameter L for later ease of interpretation. The axial system scaling parameter A is identical to the non-dimensional variable Π_1, and measures the ratio of the compressible scale length of the gas to the thickness of the post-shock layer. The lateral scaling parameter L compares the maximum lateral (in the sense of "the direction in which periodic wavelengths are aligned") dimension of the system to the layer thickness. L therefore indicates the ratio of the longest allowable wavelength in the system to the layer thickness H.

The variables A and L may be evaluated from experimentally available data both for radiating shock experiments, which form a decelerating, dense, post-shock layer through upstream radiative losses, and for astrophysical systems with spherically diverging shocks.

6.2.1 Experimental data

Experimental data comes in the form of a shock location p at a measured time t after the shock breaks through the laser-ablator material into the gas volume of the system. The experimental system is additionally characterized by the initial thickness of the ablator which, through momentum balance, transfers energy from the laser to the system hydrodynamics. The experimental ablator is a beryllium disc of thickness 17 μm to 32 μm. In all cases, an approximately constant depth of the beryllium is ablated by the laser, driving momentum into the remaining beryllium mass. The initial velocity of the shock launched by the driven ablator as a function of ablator thickness follows the rocket equation

$$V_i(T) = 435 \ln\left(\frac{T}{T - 8\mu m}\right) \mu\text{m/ns} \tag{6.7}$$

where T is the ablator thickness and the numerical factors are empirically determined (see Section 5.3.2).

The scaling parameter A may be estimated for an experiment from the data (p, t, T) by estimating the involved physical parameters. For each data point, one defines an average speed $V_{ave} = p/t$. One may then define a characteristic deceleration $|\dot{V}_s| = (V_i(T) - V_{ave})/(t/2)$. To obtain layer width H, before any broadening by instabilities or geometric effects, H is written the product of inverse shock compression and shock position $\eta \cdot p$. As discussed in Section 4.3, a direct measurement of H is untrustworthy without substantial statistical support. One then obtains the values of η and c_s using the relations from Section 1.2, evaluating them for xenon at 0.006 g/cc using the shock speed V_{ave}. This is sufficient to construct the parameter $A = \Pi_1 = c_s^2/(|\dot{V}_s|\eta p)$. For the second scaling parameter L, one must calculate the longest possible lateral wavelength in the system, which is the tube diameter d less the wall shock amplitudes in the data, which have been recorded in Chapter V, using average values where the data are unclear.

The results of this analysis are summarized in Table 6.1, and are plotted in Figure 6.1. One notes that for discs with $T \gtrsim 30$ the shock deceleration $|\dot{V}_s|$ can be close to 0, reducing the accuracy in calculating A. For other ablator thicknesses, in which all values are of similar magnitudes, the systematic error reduces to the few percent level.

Table 6.1: Data used in generating the profile of non-dimensional experimental values, discussed in Section 6.2.1

Shot No.	T (μm)	Time t (ns)	Position p (μm)	V_{ave} (μm/ns)	V_i (μm/ns)	$\lvert\dot{V}_s\rvert$ (μm/ns^2)	c_s (μm/ns)	1 / η	A	L
51778	26	30.9	3903	126.3	160	2.2	27.2	51	4.4	6.1
51780	18	24.0	3710	154.8	256	8.4	30.7	60	1.8	7.7
51782	29	29.4	3201	109.1	140	2.1	25.0	44	4.0	6.6
51783	17	22.6	3590	158.9	277	10.4	31.2	62	1.6	8.2
54979	23	30.3	2960	116.2	186	5.5	25.9	47	1.9	7.4
54979	23	31.3	3120	117.9	186	5.1	26.1	48	2.0	7.1
54980	32	29.8	3360	110.9	125	0.9	25.2	45	9.1	6.1
54980	32	30.8	3446	110.1	125	1.0	25.1	45	8.5	6.1
54982	31	22.1	3635	121.9	130	0.5	26.7	49	18.1	6.5
54982	31	23.1	3739	121.4	130	0.6	26.6	49	16.7	6.2
54983	17	22.1	2989	135.3	277	12.8	28.4	54	1.1	8.1
54983	17	23.1	3009	130.3	277	12.7	27.7	52	1.0	7.8
54984	22	25.5	3104	121.8	197	5.9	26.7	49	1.9	7.6
54986	32	30.8	3236	105.1	125	1.3	24.4	43	6.1	6.3
54987	18	24.6	3168	128.9	256	10.3	27.6	51	1.2	7.8
54988	23	26.5	2905	112.0	186	5.6	25.4	45	1.8	7.6
54989	21	25.5	3056	119.8	209	7.0	26.4	48	1.6	7.9
59027	21	26.0	3440	132.0	209	5.9	28.0	53	2.0	7.6

6.2.2 Astrophysical data

A supernova remnant is characterized for our purposes by its essentially spherical outbound shock with radius R_s at time t, by its inverse compression ratio η, and by its similarity parameter $\epsilon, R_s \propto t^\epsilon$.

The axial scaling parameter A requires estimates of c_s, H, and $|\dot{V}_s|$. As in the experimental case, $H = \eta R_s$. Through differentiation one finds find the shock's deceleration to be $\dot{V}_s = \epsilon(\epsilon - 1)R_s/t^2$. For a gas with $\gamma = 5/3$, it is found that 3/16 of the shock's energy is transferred to thermal energy [87], allowing one to find the post-shock sound speed $c_s = \sqrt{5/3 \cdot 3/16 \cdot V_s^2}$ yielding $c_s^2 = (5/16)(\epsilon R_s/t)^2$. Constructing the non-dimensional parameter A, all the instances of R_s and t unsurprisingly cancel out, leaving

$$A = \frac{5\epsilon}{16(1-\epsilon)\eta}. \tag{6.8a}$$

The lateral scaling L is simply calculated using the circumference of the remnant as its maximum supportable wavelength, resulting in

$$L = \frac{2\pi}{\eta}. \tag{6.8b}$$

For SN1993J after the first five years of its evolution, estimates derived from Bartel *et al* [5] give $\eta = 0.2, \epsilon = 0.8$. For the Tycho supernova remnant (SN1572), $\eta = 0.07, \epsilon = 0.5$ [45]. The values of Equations 6.8 for these estimates are plotted in Figure 6.1 alongside the non-dimensional parameters for experimental systems.

6.3 Summary and future directions

The results are summarized in Figure 6.1. The Figure shows contours of the growth rate $\mathrm{Im}(\Pi_3)$ as a function of Π_1 and $2\pi/\Pi_2$. The white area designates wavelengths which are stable, and is approximately bounded when $\Pi_1 \gtrsim 1$ by Equation 6.5, shown as the dashed gray line. Additionally, the Figure plots on the same scale the non-dimensional system parameters (A, L) for both experimental and astrophysical systems.

The major result of this analysis is that the experimental system, by controlling ablator thickness, is able to select the axial non-dimensional parameter A shown on the horizontal axis. The vertical axis, which represents the lateral parameter L, is largely informed in the experiment by shock tube diameter. On the current generation of large-energy lasers, L is difficult to increase by the required multipliers, as the required total laser energy scales with the square of the laser spot diameter. However, future generations of lasers should be able to drive tubes of the required ($\sim$ 1 cm) size, allowing one to design, using Figure 6.1, experiments which scale precisely to an astrophysical system, with respect to the Vishniac dispersion relation. In particular, the National Ignition Facility (NIF) is specified to deliver 1.8 MJ of laser energy to its target chamber center. Focusing only on overall energy balance, a hemisphere of NIF could in principle be used to deliver half of that energy to a target for asymmetric planar drive, or 225 times as much total energy. This could be used to drive a target similar to the Omega targets but with 15 times greater L.

When such experiments are designed, it may be useful to consider the time-evolution of the experiments in the non-dimensional space of Figure 6.1. The largest time evolution in the experimental system is the increasing post-shock layer width H as the shock progresses and the shock compression decreases. In the axial parameter A, these changes are approximately balanced by changes in c_s and $|\dot{V}_s|$, so that the resulting motion of the experiment in time is primarily in $L = d/H$. This is evident in the $p = 2$ mm, $t = 13$ ns, $T = 21$ μm data in Figure 6.1, which lies above the aggregate $p = 3$ mm, $t = 26$ ns, $T = 21$ μm data. The stars, in contrast, change only as fast as their governing compression η and scaling ϵ evolve. The scaling parameter ϵ changes as the remnant encounters different density profiles outside the star [80]. The motion of a star in dimensionless space then is primarily horizontal, in A. One might take advantage of this by designing an experiment with cylindrical geometry, having chosen an ablator thickness to align with a star of interest in A, letting the system evolve with L decreasing until both A and L match the star, and then transition to a diverging geometry by opening the shock tube like a horn at the appropriate point. Substantial experimental and numerical modeling would be necessary to predict the appropriate point at which to transition to the diverging geometry and other details, but the resulting experiment should be able to recreate accurately the evolution of Vishniac-caused structures in the post-shock environment.

Finally, there exists the issue of an experimental observation time, t. Its non-dimensional counterpart is the product ωt, the number of growth timescales (e-foldings) which the initial perturbations experience, which should be matched between scaled systems in order to compare data. Since t does not occur explicitly in the dispersion relation, it can be freely chosen for any experiment as necessary without impacting the scaling.

6.4 Conclusions

The results of Chapter VI provide a valuable future direction for radiative shock tube experiments, namely, the investigation of instability growth mechanisms in planar decelerating, radiating shocks. We have shown that the experimental methods described in Chapters IV and V are suitable for this task and, once adapted for the more energetic laser facilities available in the future, will be able to access regimes rigorously relevant to astrophysics.

Chapter II contains important results necessary to diagnose the instability structure that will be generated, by explicating the cylindrical structure imposed by shock-shock tube interactions. The lateral boundary layer in which the shock interacts with the wall shock and the subsequent flow pattern induced in the post-shock flow by

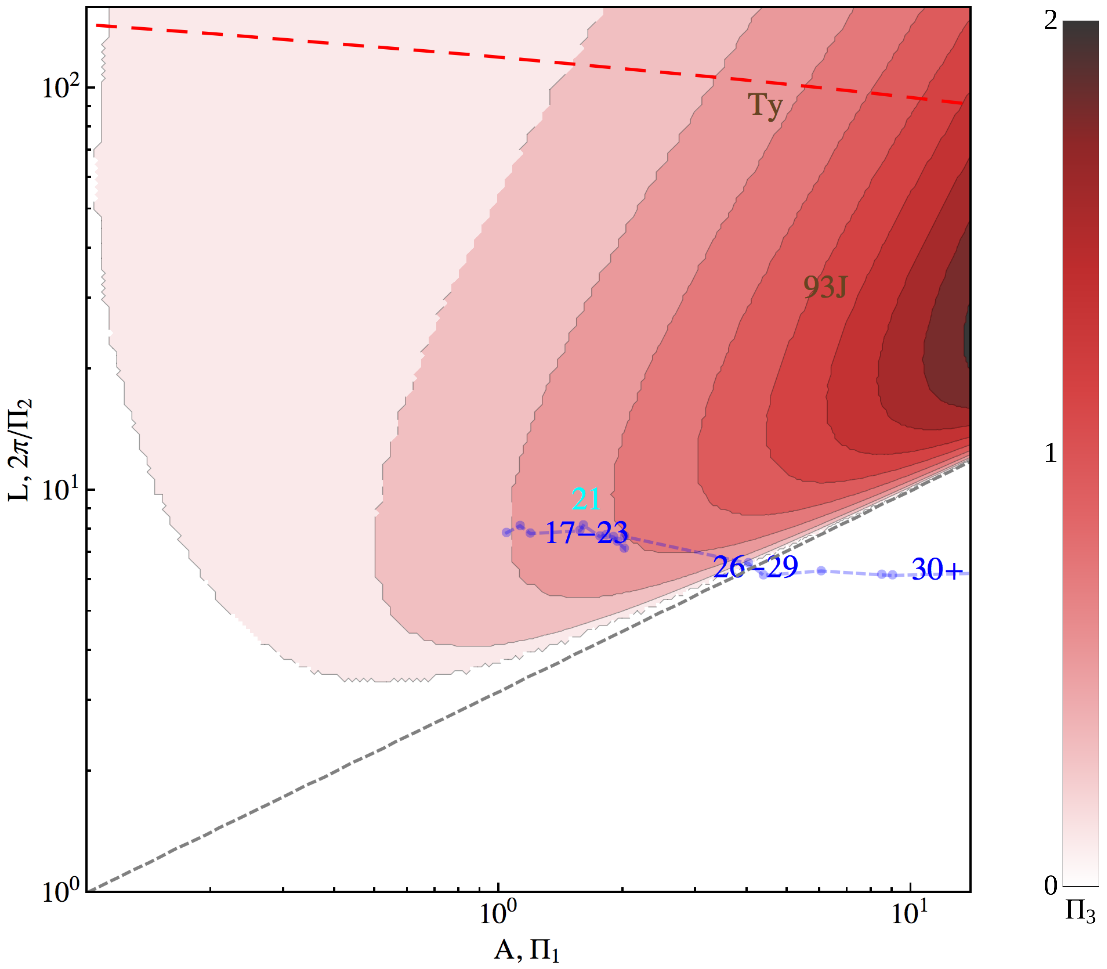

Figure 6.1: The non-dimensional growth parameter $\mathrm{Im}(\Pi_3)$ as a function of dimensionless numbers Π_1 and $2\pi/\Pi_2$, obtained by solving Equation 6.3 for an unstable solution of Π_3. The red contours show the growth rates. Also plotted are experimentally determined values of lateral and axial system parameters L and A for both astrophysical and laboratory systems. The blue numbers show experiments parameterized by ablator thickness (in μm). The dark (light) blue numbers are experiments approximately 3mm (2mm) from the experimental origin. "93J" represents the scaling parameters of Supernova 1993J after 5 years, and "Ty" represents the scaling parameters of the Tycho remnant after 400 years. The red dashed line represents projections for possible experiments on NIF.

shock reflections are substantial corrections to the simple idea of a planar shock propagating down a rigid tube. The Vishniac-related instability structure observed in experiments exists superimposed on these wall effects, and cannot be understood without knowledge of these wall effects. The precise interaction between the instability and the wall shocks, in particular what lateral boundary condition would be imposed on the instability theory explored in Chapter III, remains undetermined, the subject of possible future research. It is likely that further non-radiographic research into the present radiative shock systems, both experimental and computational, will also benefit from understanding the nature of the wall shocks and their consequences.

APPENDICES

APPENDIX A

July 2007 Shot Request Form

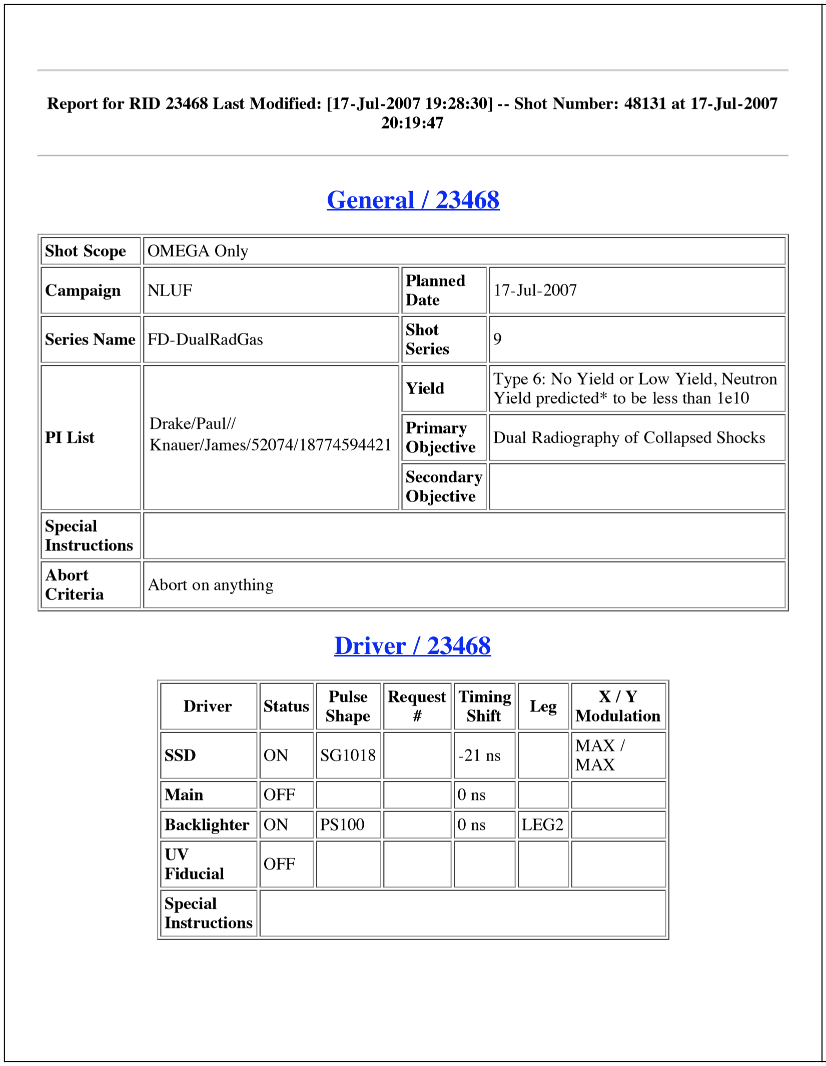

Report for RID 23468 Last Modified: [17-Jul-2007 19:28:30] -- Shot Number: 48131 at 17-Jul-2007 20:19:47

General / 23468

Shot Scope	OMEGA Only		
Campaign	NLUF	**Planned Date**	17-Jul-2007
Series Name	FD-DualRadGas	**Shot Series**	9
PI List	Drake/Paul// Knauer/James/52074/18774594421	**Yield**	Type 6: No Yield or Low Yield, Neutron Yield predicted* to be less than 1e10
		Primary Objective	Dual Radiography of Collapsed Shocks
		Secondary Objective	
Special Instructions			
Abort Criteria	Abort on anything		

Driver / 23468

Driver	Status	Pulse Shape	Request #	Timing Shift	Leg	X / Y Modulation
SSD	ON	SG1018		-21 ns		MAX / MAX
Main	OFF			0 ns		
Backlighter	ON	PS100		0 ns	LEG2	
UV Fiducial	OFF					
Special Instructions						

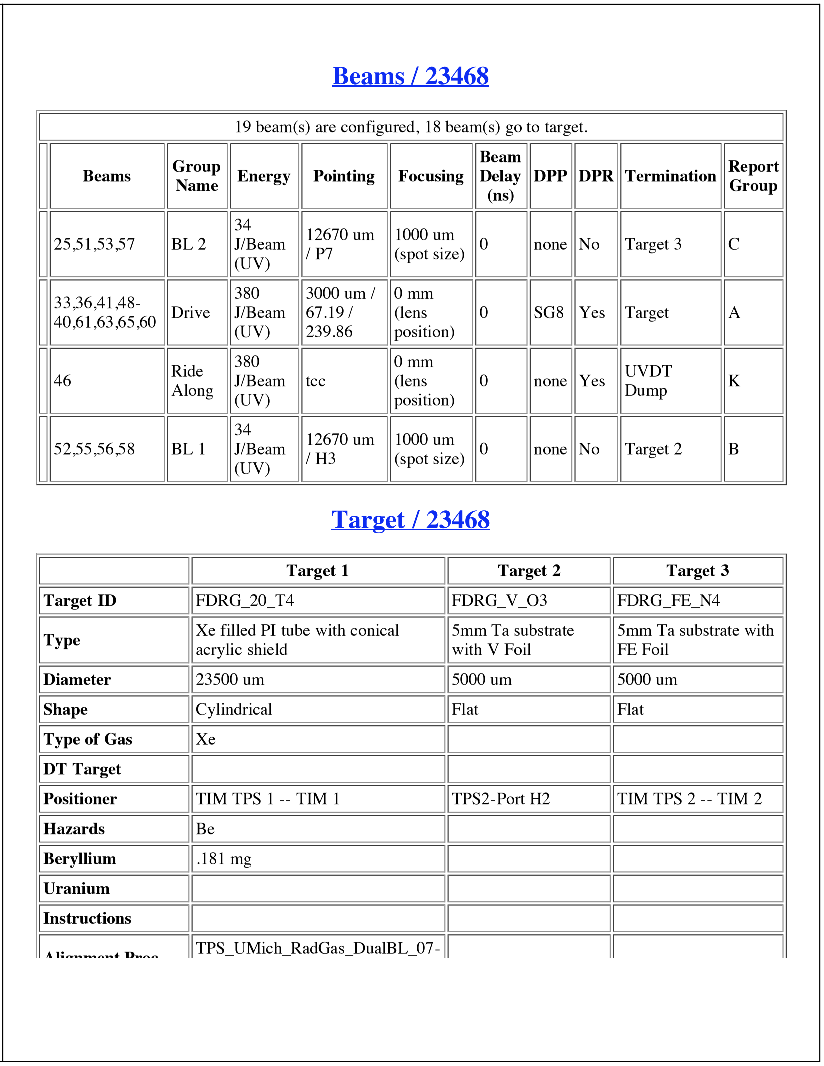

Beams / 23468

19 beam(s) are configured, 18 beam(s) go to target.

Beams	Group Name	Energy	Pointing	Focusing	Beam Delay (ns)	DPP	DPR	Termination	Report Group
25,51,53,57	BL 2	34 J/Beam (UV)	12670 um / P7	1000 um (spot size)	0	none	No	Target 3	C
33,36,41,48-40,61,63,65,60	Drive	380 J/Beam (UV)	3000 um / 67.19 / 239.86	0 mm (lens position)	0	SG8	Yes	Target	A
46	Ride Along	380 J/Beam (UV)	tcc	0 mm (lens position)	0	none	Yes	UVDT Dump	K
52,55,56,58	BL 1	34 J/Beam (UV)	12670 um / H3	1000 um (spot size)	0	none	No	Target 2	B

Target / 23468

	Target 1	Target 2	Target 3
Target ID	FDRG_20_T4	FDRG_V_O3	FDRG_FE_N4
Type	Xe filled PI tube with conical acrylic shield	5mm Ta substrate with V Foil	5mm Ta substrate with FE Foil
Diameter	23500 um	5000 um	5000 um
Shape	Cylindrical	Flat	Flat
Type of Gas	Xe		
DT Target			
Positioner	TIM TPS 1 -- TIM 1	TPS2-Port H2	TIM TPS 2 -- TIM 2
Hazards	Be		
Beryllium	.181 mg		
Uranium			
Instructions			
Alignment Proc	TPS_UMich_RadGas_DualBL_07-		

Alignment Proc.	07		
Soft Rough Pumping	Y	N	N
	300 Sec.		
Target Detection?	Y		
Record Target Pressure?	Y	N	N
Cryogenic Target	No		
MCTC			

TIM / 23468

Location	Priority	Description	Contact
TIM 1	Primary	LLNL TIM Target Positioner System - 1	Sorce, C.
TIM 2	Primary	LLNL TIM Target Positioner System - 2	Sorce, C.
TIM 3	Primary	Static Pinhole Camera Array - 1	Sorce, C.
TIM 4	Primary	Static Pinhole Camera Array - 2	Sorce, C.

Fixed Diagnostics / 23468

Port	Priority	Description	Contact
H8D	Secondary	Visible Camera (3)	Kowaluk, E.
P2A	Secondary	Visible Camera (2)	Kowaluk, E.
H13C	Secondary	XR Pinhole Camera (H13)	Marshall, F.
H8C	Secondary	XR Pinhole Camera (H8)	Marshall, F.
H12C	Secondary	XR Pinhole Camera (H12)	Marshall, F.

TIM 3 - SPCA 1 / 23468 Operating Procedures

Description	Static Pinhole Camera Array

Optics

Nosecone Type	LLNL
Magnification	MPBL

Pinhole Size	9mm
Blast Shield	8 mil Be
Standoff Distance	9 in.
Frame Type	
Pinhole Substrate	
Rear Filter	20milBe+12.5umV
Film Filter	2 mil
Film Type	DEF
Pieces of Film	2

Steering	tcc
Comments	Use AWE nosecone. Use D7 in front of DEF.

TIM 4 - SPCA 2 / 23468 Operating Procedures

Description	Static Pinhole Camera Array

Optics

Nosecone Type	LLNL
Magnification	MPBL
Pinhole Size	9mm
Blast Shield	8 mil Be
Standoff Distance	9 in.
Frame Type	
Pinhole Substrate	
Rear Filter	20milBe+12.5umFe
Film Filter	2 mil
Film Type	DEF
Pieces of Film	2

Steering	tcc
Comments	Use AWE nosecone. Use D7 in front of DEF.

FIXED H12C - XRPHC H12 / 23468 Operating Procedures

Description	XR Pinhole Camera

Blast Shield	0.004" Be
Vacuum Window	0.001" Be
Pinhole to image	648 mm
Pinhole diameter	10 um
Pinhole to target	162.5 mm
Detector	CID
Magnification	4.0
Fixed Filtration	0.005" Be
Rear Filter	.001" Be

FIXED H13C - XRPHC H13 / 23468 Operating Procedures

Description	XR Pinhole Camera
Blast Shield	0.004" Be
Vacuum Window	0.001" Be
Pinhole to image	648 mm
Pinhole diameter	10 um
Pinhole to target	162.5 mm
Detector	CID
Magnification	4.0
Fixed Filtration	0.005" Be
Rear Filter	.001" Be

FIXED H8C - XRPHC H8 / 23468 Operating Procedures

Description	XR Pinhole Camera
Blast Shield	0.004" Be
Vacuum Window	0.001" Be
Pinhole to image	648 mm before 4/28/2009, 1296 mm after
Pinhole diameter	10 um before 4/28/2009, 20 um after
Pinhole to target	162.5 mm before 4/28/2009, 628.8 mm after
Detector	CID
Magnification	4.0 before 4/28/2009, 2.1 after
Fixed Filtration	0.005" Be
Rear Filter	.001" Be

APPENDIX B

July 2008 Shot Request Form

Report for RID 25917 Last Modified: [10-Jul-2008 12:46:00] -- Shot Number: 51775 at 10-Jul-2008 13:48:09

General / 25917

Shot Scope	OMEGA Only		
Campaign	NLUF	**Planned Date**	10-Jul-2008
Series Name	RadGas Stereoscopic	**Shot Series**	3
PI List	Drake/Paul// Knauer/James/52074/18774594421 Sorce/Chuck/50134/	**Yield**	Type 6: No Yield or Low Yield, Neutron Yield predicted* to be less than 1e10
		Primary Objective	To obtain stereoscopic dual backlit images of radiating shocks
		Secondary Objective	
Special Instructions			
Abort Criteria	Abort on anything		

Driver / 25917

Driver	Status	Pulse Shape	Request #	Timing Shift	Leg	X / Y Modulation
SSD	ON	SG1018		-35.5 ns		MAX / MAX
Main	OFF			0 ns		
Backlighter	ON	PS100		0 ns	LEG3	
UV Fiducial	OFF					
Special Instructions						

Beams / 25917

20 beam(s) are configured, 19 beam(s) go to target.

Beams	Group Name	Energy	Pointing	Focusing	Beam Delay (ns)	DPP	DPR	Termination	Report Group
30	BL 2	34 J/Beam (UV)	12400 um / H18	800 um (spot size)	0	none	Yes	Target 2	D
33,34,36-38	BL 1	34 J/Beam (UV)	12400 um / P10	-800 um (spot size)	0	none	Yes	Target 2	B
35,39,64	BL 2	34 J/Beam (UV)	12400 um / H18	-800 um (spot size)	0	none	Yes	Target 2	C
42-45,49-51,53,54,57	Drive	380 J/Beam (UV)	3200 um / 121.72 / 198	0 um (spot size)	0	SG8	Yes	Target	A
46	Ride Along	380 J/Beam (UV)	tcc	0 mm (lens position)	0	none	Yes	UVDT Dump	K

Target / 25917

	Target 1	Target 2	Target 3
Target ID	RGS_T31_3	RGS_BL_3	
Type	Xe filled PI tube with conical acrylic shield	Acrylic/Ta substrate with two mounted V foils	
Diameter	23500 um	14200 um	
Shape	Other	Other	
Type of Gas			
DT Target			
Positioner	TIM TPS 1 -- TIM 5	TPS2-Port H2	
Hazards			
Beryllium	.181 mg		

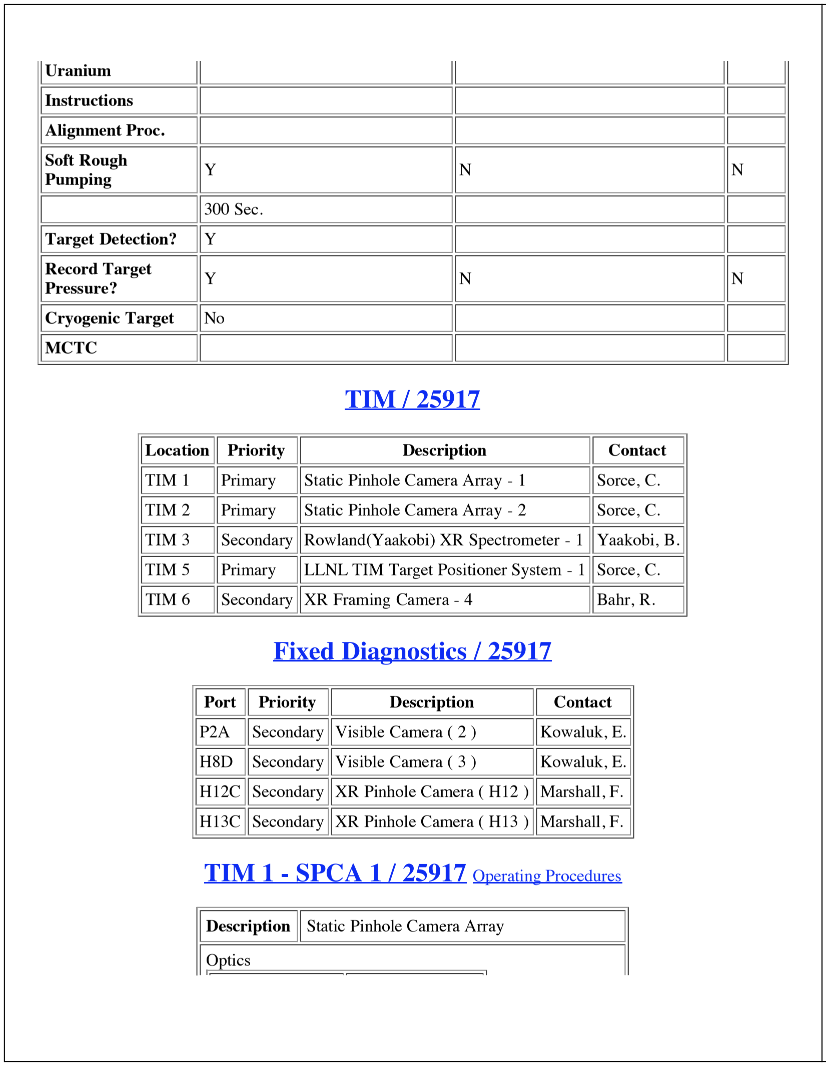

Uranium			
Instructions			
Alignment Proc.			
Soft Rough Pumping	Y	N	N
	300 Sec.		
Target Detection?	Y		
Record Target Pressure?	Y	N	N
Cryogenic Target	No		
MCTC			

TIM / 25917

Location	Priority	Description	Contact
TIM 1	Primary	Static Pinhole Camera Array - 1	Sorce, C.
TIM 2	Primary	Static Pinhole Camera Array - 2	Sorce, C.
TIM 3	Secondary	Rowland(Yaakobi) XR Spectrometer - 1	Yaakobi, B.
TIM 5	Primary	LLNL TIM Target Positioner System - 1	Sorce, C.
TIM 6	Secondary	XR Framing Camera - 4	Bahr, R.

Fixed Diagnostics / 25917

Port	Priority	Description	Contact
P2A	Secondary	Visible Camera (2)	Kowaluk, E.
H8D	Secondary	Visible Camera (3)	Kowaluk, E.
H12C	Secondary	XR Pinhole Camera (H12)	Marshall, F.
H13C	Secondary	XR Pinhole Camera (H13)	Marshall, F.

TIM 1 - SPCA 1 / 25917 Operating Procedures

Description	Static Pinhole Camera Array

Optics

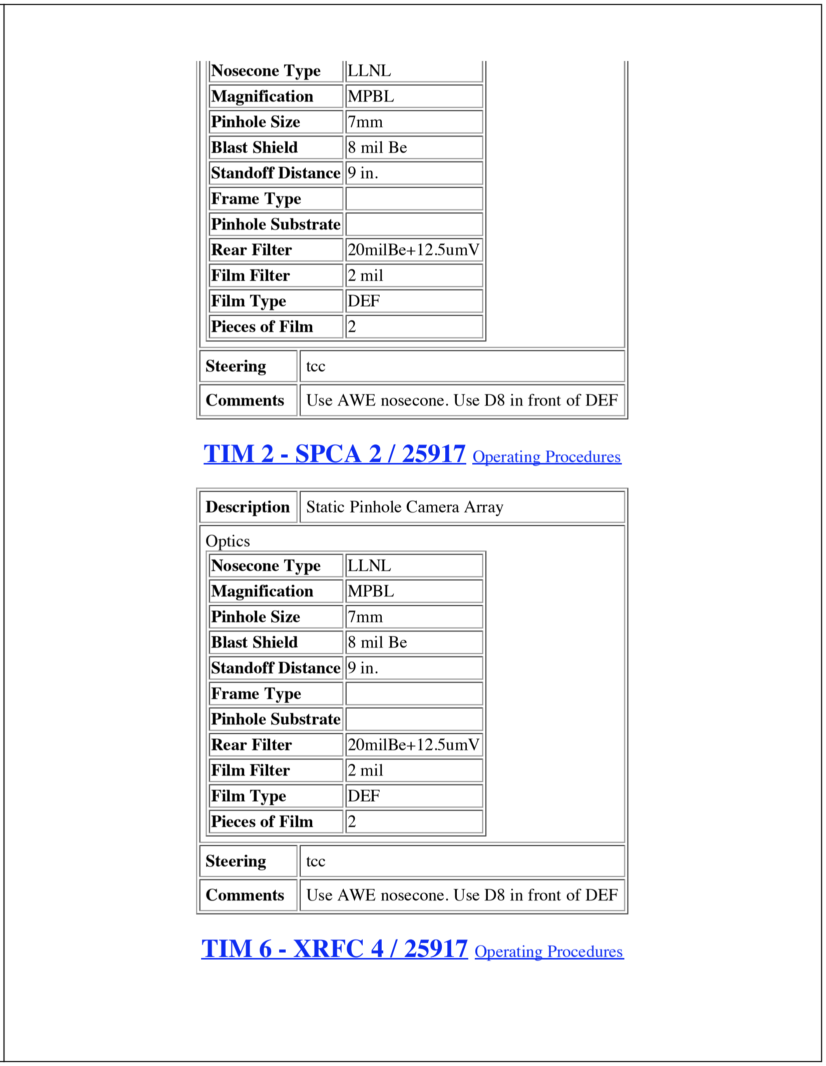

Nosecone Type	LLNL
Magnification	MPBL
Pinhole Size	7mm
Blast Shield	8 mil Be
Standoff Distance	9 in.
Frame Type	
Pinhole Substrate	
Rear Filter	20milBe+12.5umV
Film Filter	2 mil
Film Type	DEF
Pieces of Film	2

Steering	tcc
Comments	Use AWE nosecone. Use D8 in front of DEF

TIM 2 - SPCA 2 / 25917 Operating Procedures

Description	Static Pinhole Camera Array

Optics

Nosecone Type	LLNL
Magnification	MPBL
Pinhole Size	7mm
Blast Shield	8 mil Be
Standoff Distance	9 in.
Frame Type	
Pinhole Substrate	
Rear Filter	20milBe+12.5umV
Film Filter	2 mil
Film Type	DEF
Pieces of Film	2

Steering	tcc
Comments	Use AWE nosecone. Use D8 in front of DEF

TIM 6 - XRFC 4 / 25917 Operating Procedures

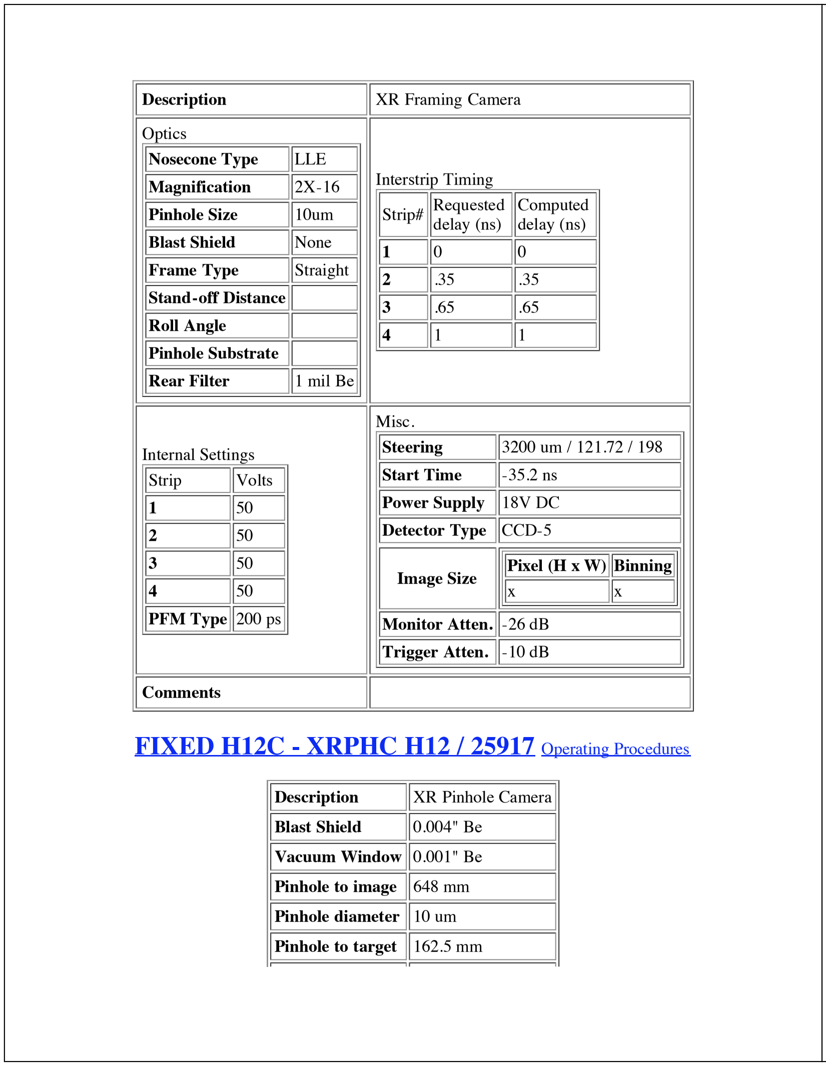

Description	XR Framing Camera

Optics

Nosecone Type	LLE
Magnification	2X-16
Pinhole Size	10um
Blast Shield	None
Frame Type	Straight
Stand-off Distance	
Roll Angle	
Pinhole Substrate	
Rear Filter	1 mil Be

Interstrip Timing

Strip#	Requested delay (ns)	Computed delay (ns)
1	0	0
2	.35	.35
3	.65	.65
4	1	1

Internal Settings

Strip	Volts
1	50
2	50
3	50
4	50
PFM Type	200 ps

Misc.

Steering	3200 um / 121.72 / 198
Start Time	-35.2 ns
Power Supply	18V DC
Detector Type	CCD-5
Image Size	**Pixel (H x W)**: x **Binning**: x
Monitor Atten.	-26 dB
Trigger Atten.	-10 dB

Comments	

FIXED H12C - XRPHC H12 / 25917 Operating Procedures

Description	XR Pinhole Camera
Blast Shield	0.004" Be
Vacuum Window	0.001" Be
Pinhole to image	648 mm
Pinhole diameter	10 um
Pinhole to target	162.5 mm

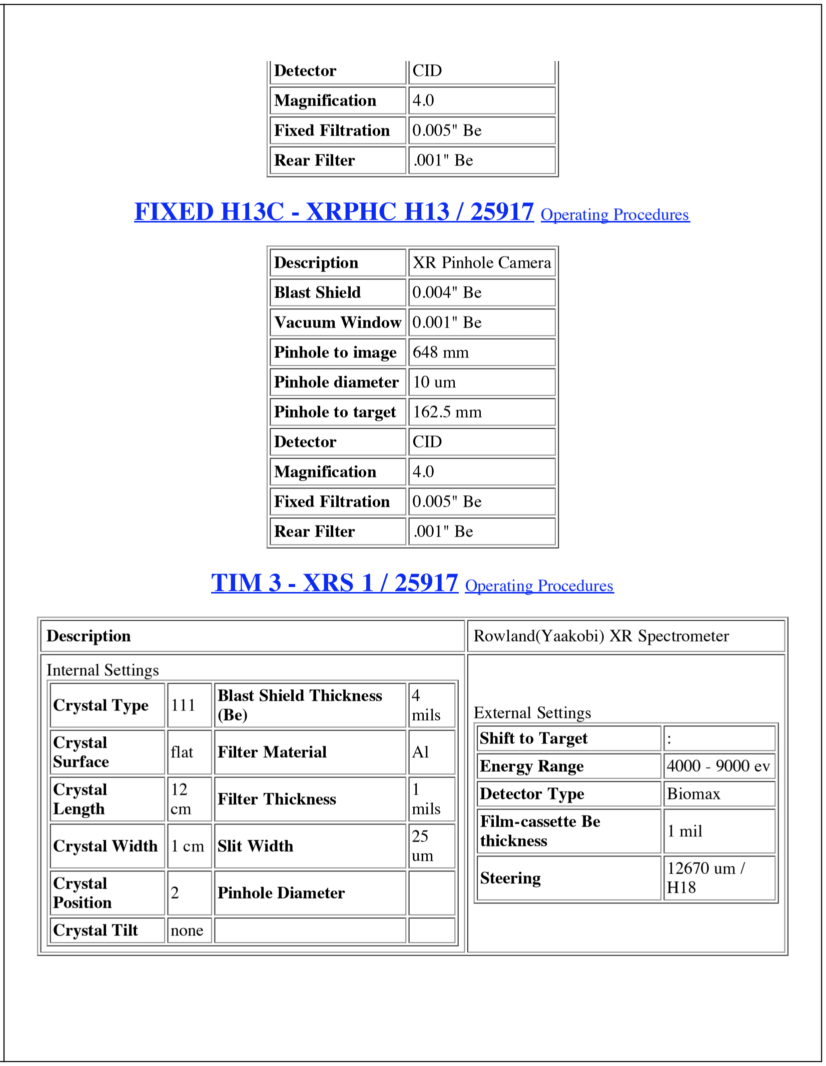

Detector	CID
Magnification	4.0
Fixed Filtration	0.005" Be
Rear Filter	.001" Be

FIXED H13C - XRPHC H13 / 25917 Operating Procedures

Description	XR Pinhole Camera
Blast Shield	0.004" Be
Vacuum Window	0.001" Be
Pinhole to image	648 mm
Pinhole diameter	10 um
Pinhole to target	162.5 mm
Detector	CID
Magnification	4.0
Fixed Filtration	0.005" Be
Rear Filter	.001" Be

TIM 3 - XRS 1 / 25917 Operating Procedures

Description	Rowland(Yaakobi) XR Spectrometer

Internal Settings

Crystal Type	111	**Blast Shield Thickness (Be)**	4 mils
Crystal Surface	flat	**Filter Material**	Al
Crystal Length	12 cm	**Filter Thickness**	1 mils
Crystal Width	1 cm	**Slit Width**	25 um
Crystal Position	2	**Pinhole Diameter**	
Crystal Tilt	none		

External Settings

Shift to Target	:
Energy Range	4000 - 9000 ev
Detector Type	Biomax
Film-cassette Be thickness	1 mil
Steering	12670 um / H18

APPENDIX C

October 2008 Shot Request Form

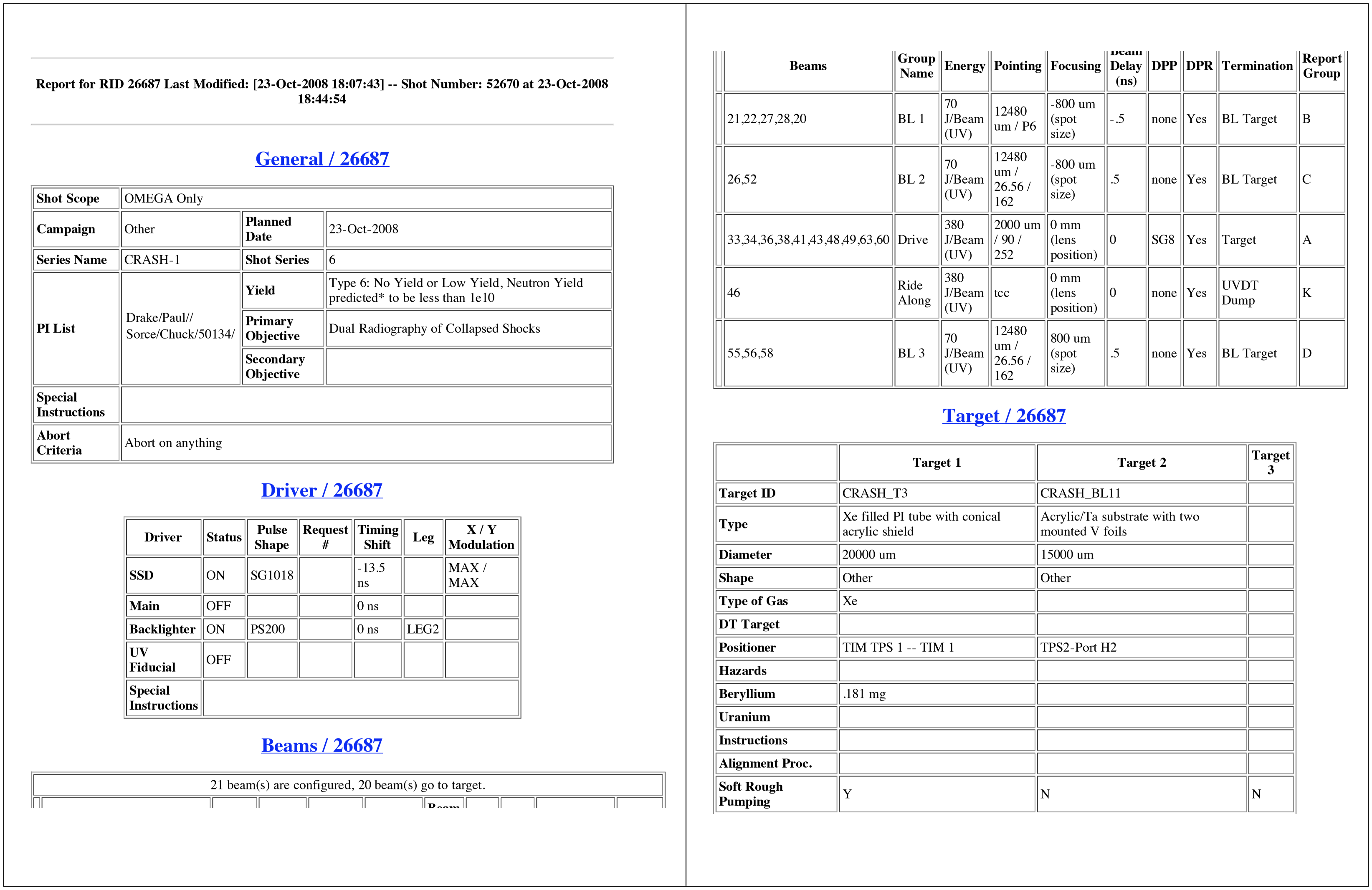

Report for RID 26687 Last Modified: [23-Oct-2008 18:07:43] -- Shot Number: 52670 at 23-Oct-2008 18:44:54

General / 26687

Shot Scope	OMEGA Only		
Campaign	Other	**Planned Date**	23-Oct-2008
Series Name	CRASH-1	**Shot Series**	6
PI List	Drake/Paul// Sorce/Chuck/50134/	**Yield**	Type 6: No Yield or Low Yield, Neutron Yield predicted* to be less than 1e10
		Primary Objective	Dual Radiography of Collapsed Shocks
		Secondary Objective	
Special Instructions			
Abort Criteria	Abort on anything		

Driver / 26687

Driver	Status	Pulse Shape	Request #	Timing Shift	Leg	X / Y Modulation
SSD	ON	SG1018		-13.5 ns		MAX / MAX
Main	OFF			0 ns		
Backlighter	ON	PS200		0 ns	LEG2	
UV Fiducial	OFF					
Special Instructions						

Beams / 26687

21 beam(s) are configured, 20 beam(s) go to target.

Beams	Group Name	Energy	Pointing	Focusing	Beam Delay (ns)	DPP	DPR	Termination	Report Group
21,22,27,28,20	BL 1	70 J/Beam (UV)	12480 um / P6	-800 um (spot size)	-.5	none	Yes	BL Target	B
26,52	BL 2	70 J/Beam (UV)	12480 um / 26.56 / 162	-800 um (spot size)	.5	none	Yes	BL Target	C
33,34,36,38,41,43,48,49,63,60	Drive	380 J/Beam (UV)	2000 um / 90 / 252	0 mm (lens position)	0	SG8	Yes	Target	A
46	Ride Along	380 J/Beam (UV)	tcc	0 mm (lens position)	0	none	Yes	UVDT Dump	K
55,56,58	BL 3	70 J/Beam (UV)	12480 um / 26.56 / 162	800 um (spot size)	.5	none	Yes	BL Target	D

Target / 26687

	Target 1	Target 2	Target 3
Target ID	CRASH_T3	CRASH_BL11	
Type	Xe filled PI tube with conical acrylic shield	Acrylic/Ta substrate with two mounted V foils	
Diameter	20000 um	15000 um	
Shape	Other	Other	
Type of Gas	Xe		
DT Target			
Positioner	TIM TPS 1 -- TIM 1	TPS2-Port H2	
Hazards			
Beryllium	.181 mg		
Uranium			
Instructions			
Alignment Proc.			
Soft Rough Pumping	Y	N	N

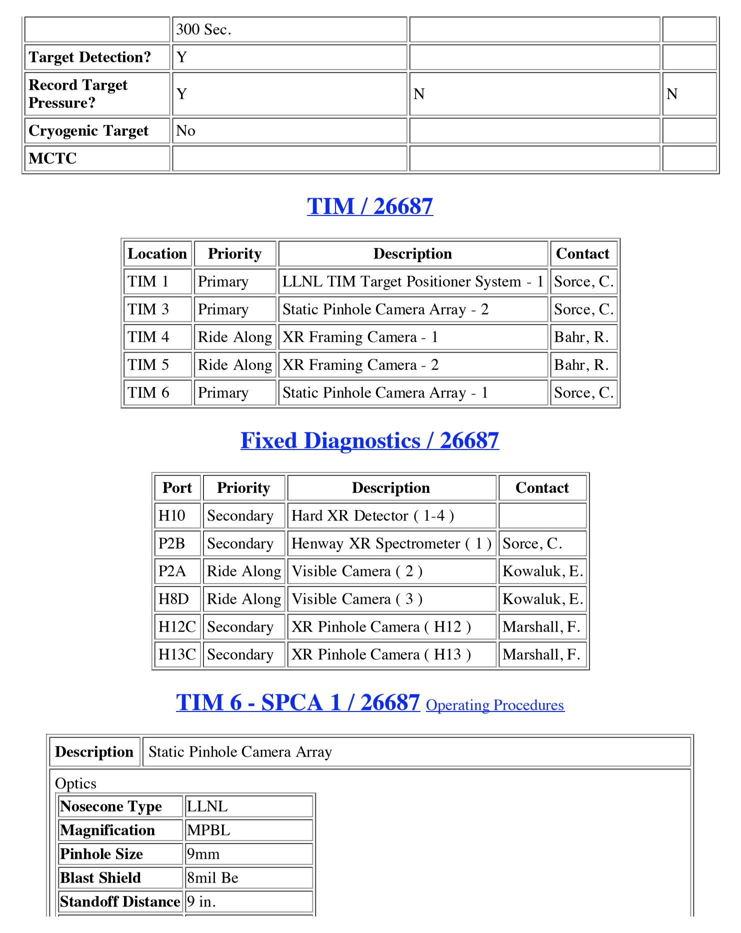

	300 Sec.		
Target Detection?	Y		
Record Target Pressure?	Y	N	N
Cryogenic Target	No		
MCTC			

TIM / 26687

Location	Priority	Description	Contact
TIM 1	Primary	LLNL TIM Target Positioner System - 1	Sorce, C.
TIM 3	Primary	Static Pinhole Camera Array - 2	Sorce, C.
TIM 4	Ride Along	XR Framing Camera - 1	Bahr, R.
TIM 5	Ride Along	XR Framing Camera - 2	Bahr, R.
TIM 6	Primary	Static Pinhole Camera Array - 1	Sorce, C.

Fixed Diagnostics / 26687

Port	Priority	Description	Contact
H10	Secondary	Hard XR Detector (1-4)	
P2B	Secondary	Henway XR Spectrometer (1)	Sorce, C.
P2A	Ride Along	Visible Camera (2)	Kowaluk, E.
H8D	Ride Along	Visible Camera (3)	Kowaluk, E.
H12C	Secondary	XR Pinhole Camera (H12)	Marshall, F.
H13C	Secondary	XR Pinhole Camera (H13)	Marshall, F.

TIM 6 - SPCA 1 / 26687 Operating Procedures

Description	Static Pinhole Camera Array

Optics

Nosecone Type	LLNL
Magnification	MPBL
Pinhole Size	9mm
Blast Shield	8mil Be
Standoff Distance	9 in.

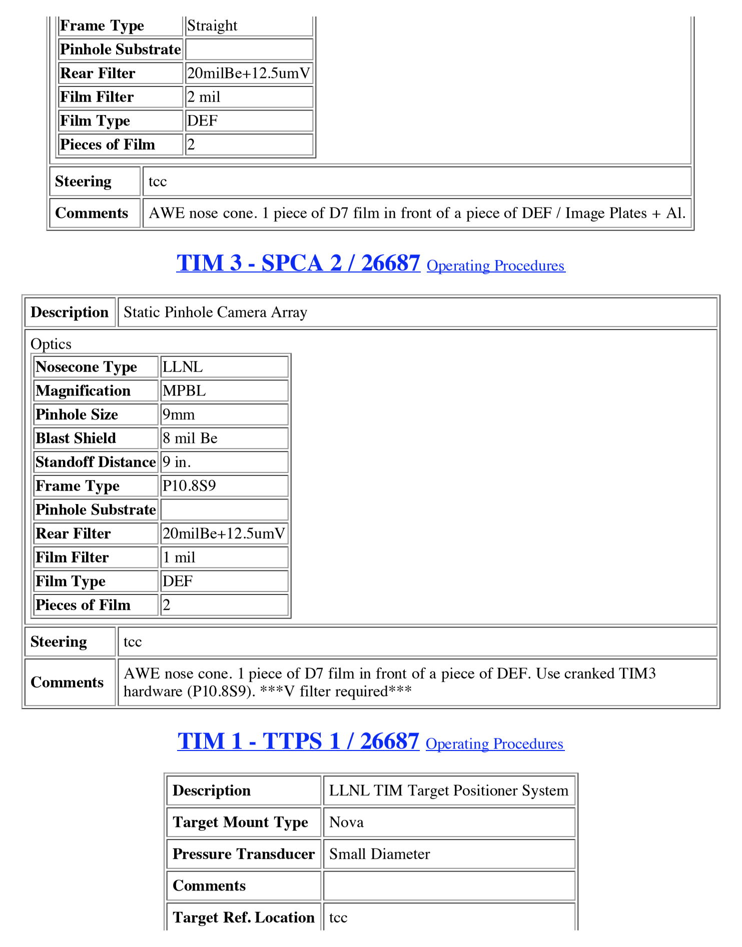

Frame Type	Straight
Pinhole Substrate	
Rear Filter	20milBe+12.5umV
Film Filter	2 mil
Film Type	DEF
Pieces of Film	2

Steering	tcc
Comments	AWE nose cone. 1 piece of D7 film in front of a piece of DEF / Image Plates + Al.

TIM 3 - SPCA 2 / 26687 Operating Procedures

Description	Static Pinhole Camera Array

Optics

Nosecone Type	LLNL
Magnification	MPBL
Pinhole Size	9mm
Blast Shield	8 mil Be
Standoff Distance	9 in.
Frame Type	P10.8S9
Pinhole Substrate	
Rear Filter	20milBe+12.5umV
Film Filter	1 mil
Film Type	DEF
Pieces of Film	2

Steering	tcc
Comments	AWE nose cone. 1 piece of D7 film in front of a piece of DEF. Use cranked TIM3 hardware (P10.8S9). ***V filter required***

TIM 1 - TTPS 1 / 26687 Operating Procedures

Description	LLNL TIM Target Positioner System
Target Mount Type	Nova
Pressure Transducer	Small Diameter
Comments	
Target Ref. Location	tcc

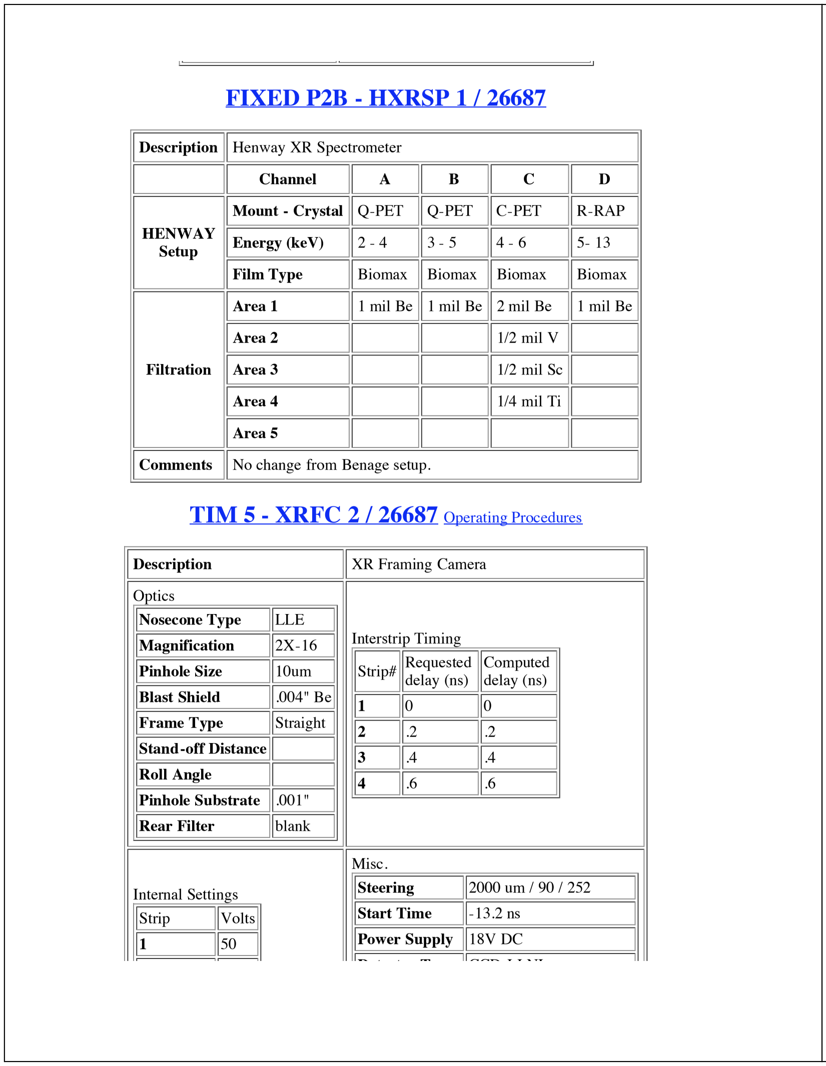

FIXED P2B - HXRSP 1 / 26687

Description	Henway XR Spectrometer				
	Channel	**A**	**B**	**C**	**D**
HENWAY Setup	**Mount - Crystal**	Q-PET	Q-PET	C-PET	R-RAP
	Energy (keV)	2 - 4	3 - 5	4 - 6	5- 13
	Film Type	Biomax	Biomax	Biomax	Biomax
Filtration	**Area 1**	1 mil Be	1 mil Be	2 mil Be	1 mil Be
	Area 2			1/2 mil V	
	Area 3			1/2 mil Sc	
	Area 4			1/4 mil Ti	
	Area 5				
Comments	No change from Benage setup.				

TIM 5 - XRFC 2 / 26687 Operating Procedures

Description	XR Framing Camera

Optics

Nosecone Type	LLE
Magnification	2X-16
Pinhole Size	10um
Blast Shield	.004" Be
Frame Type	Straight
Stand-off Distance	
Roll Angle	
Pinhole Substrate	.001"
Rear Filter	blank

Interstrip Timing

Strip#	Requested delay (ns)	Computed delay (ns)
1	0	0
2	.2	.2
3	.4	.4
4	.6	.6

Internal Settings

Strip	Volts
1	50

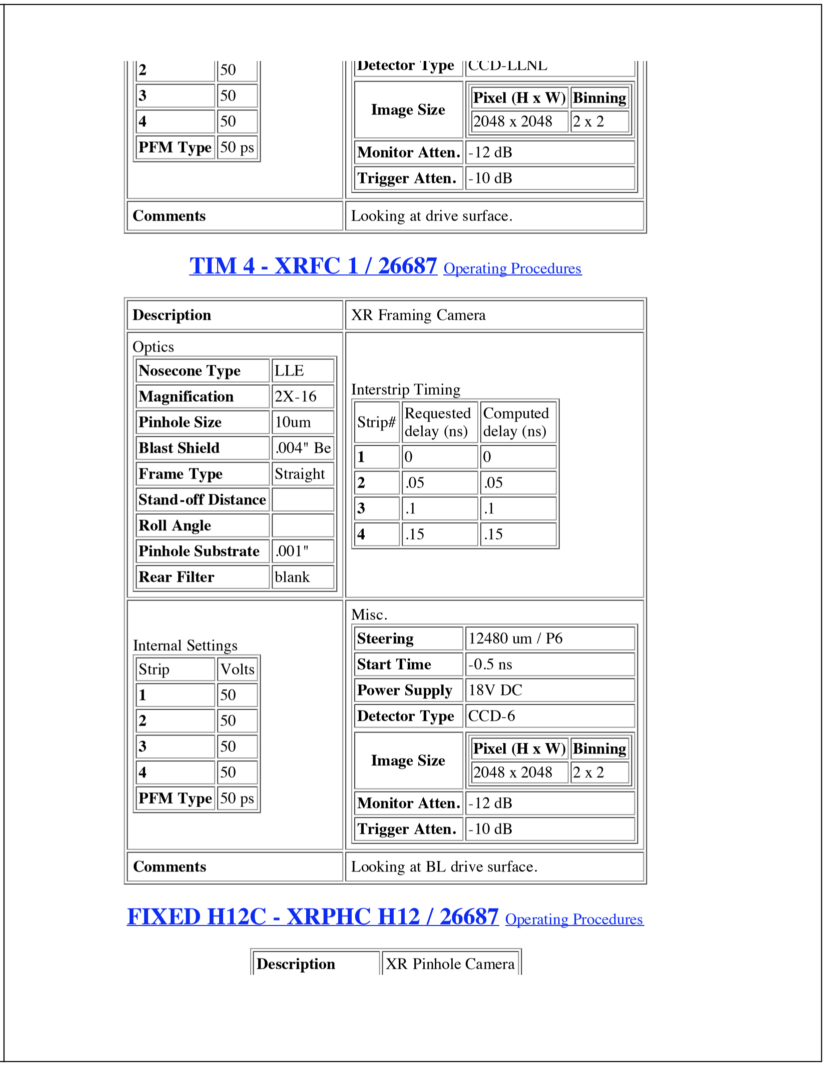

2	50
3	50
4	50
PFM Type	50 ps

Misc.

Steering	2000 um / 90 / 252
Start Time	-13.2 ns
Power Supply	18V DC
Detector Type	CCD-LLNL
Image Size	**Pixel (H x W)**: 2048 x 2048 **Binning**: 2 x 2
Monitor Atten.	-12 dB
Trigger Atten.	-10 dB

Comments	Looking at drive surface.

TIM 4 - XRFC 1 / 26687 Operating Procedures

Description	XR Framing Camera

Optics

Nosecone Type	LLE
Magnification	2X-16
Pinhole Size	10um
Blast Shield	.004" Be
Frame Type	Straight
Stand-off Distance	
Roll Angle	
Pinhole Substrate	.001"
Rear Filter	blank

Interstrip Timing

Strip#	Requested delay (ns)	Computed delay (ns)
1	0	0
2	.05	.05
3	.1	.1
4	.15	.15

Internal Settings

Strip	Volts
1	50
2	50
3	50
4	50
PFM Type	50 ps

Misc.

Steering	12480 um / P6
Start Time	-0.5 ns
Power Supply	18V DC
Detector Type	CCD-6
Image Size	**Pixel (H x W)**: 2048 x 2048 **Binning**: 2 x 2
Monitor Atten.	-12 dB
Trigger Atten.	-10 dB

Comments	Looking at BL drive surface.

FIXED H12C - XRPHC H12 / 26687 Operating Procedures

Description	XR Pinhole Camera

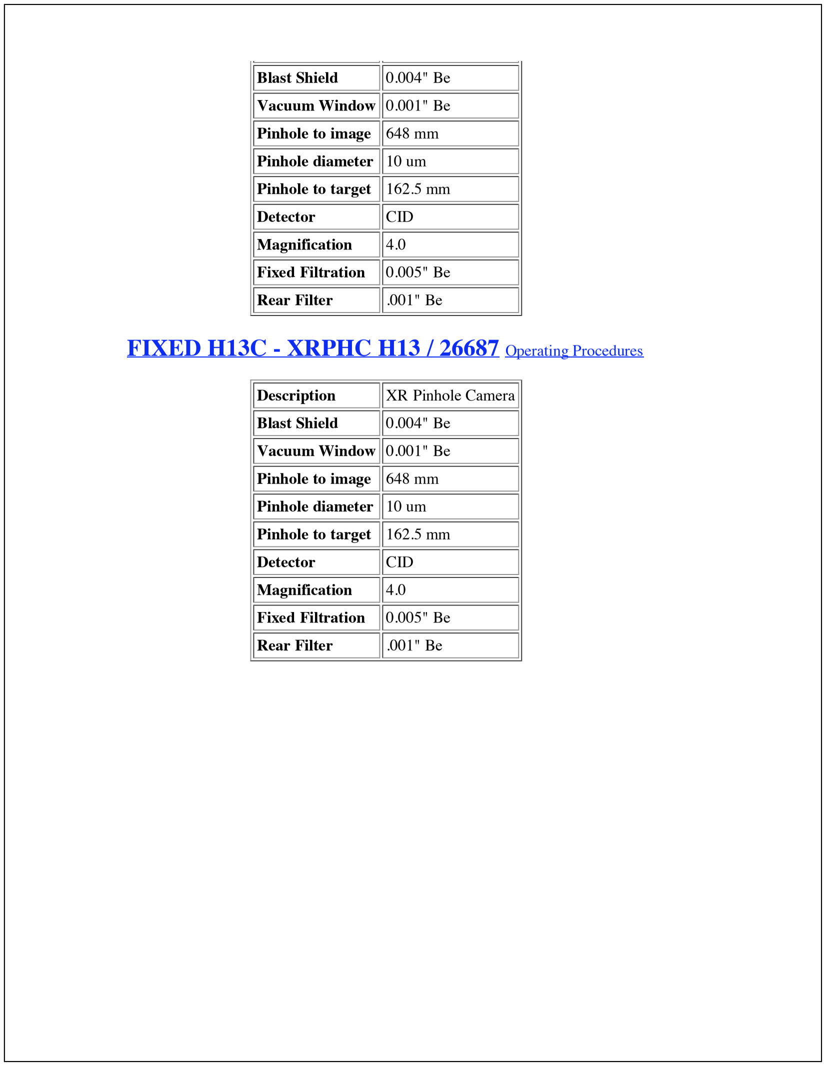

Blast Shield	0.004" Be
Vacuum Window	0.001" Be
Pinhole to image	648 mm
Pinhole diameter	10 um
Pinhole to target	162.5 mm
Detector	CID
Magnification	4.0
Fixed Filtration	0.005" Be
Rear Filter	.001" Be

FIXED H13C - XRPHC H13 / 26687 Operating Procedures

Description	XR Pinhole Camera
Blast Shield	0.004" Be
Vacuum Window	0.001" Be
Pinhole to image	648 mm
Pinhole diameter	10 um
Pinhole to target	162.5 mm
Detector	CID
Magnification	4.0
Fixed Filtration	0.005" Be
Rear Filter	.001" Be

APPENDIX D

July 2009 Shot Request Form

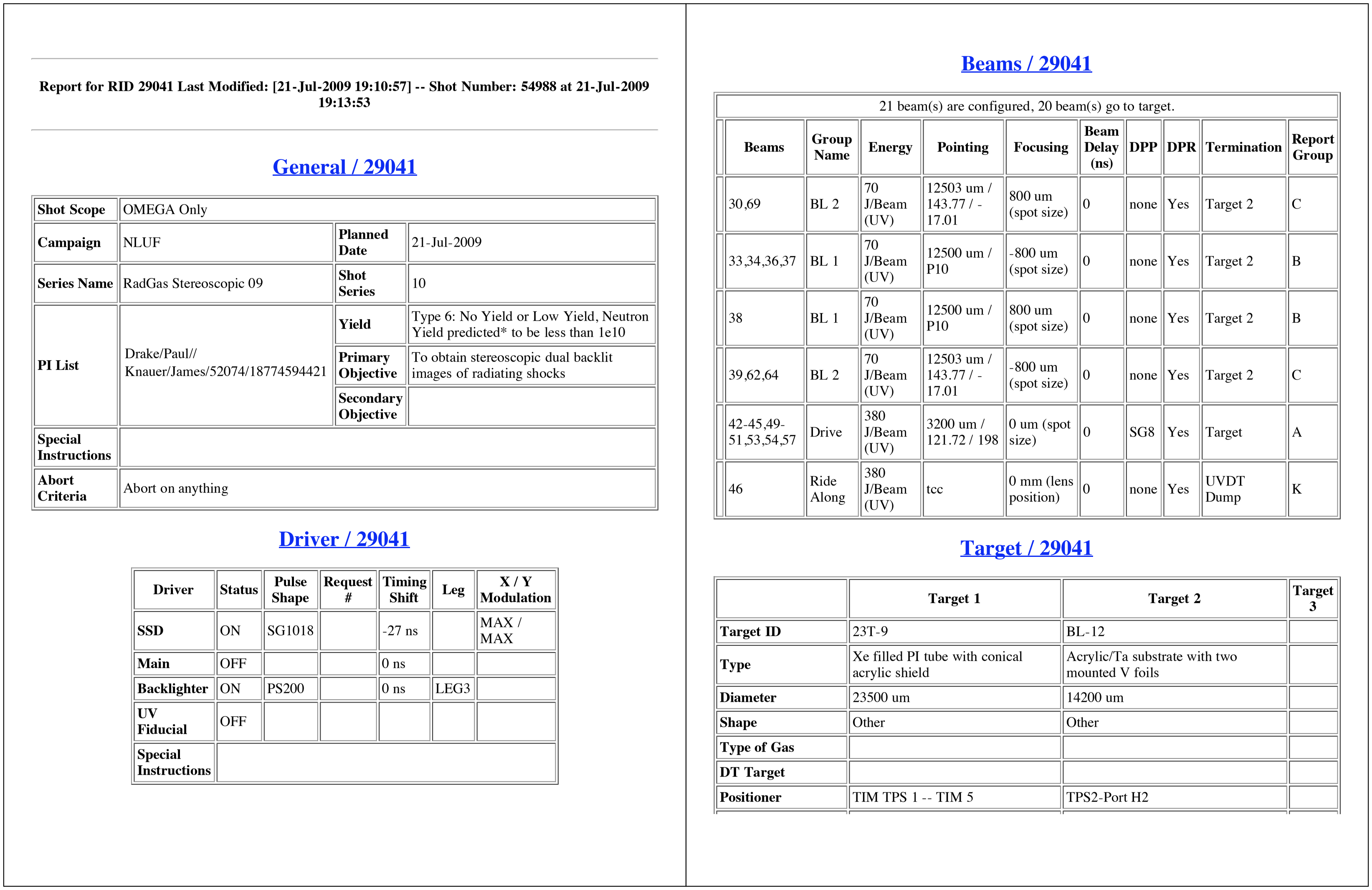

Report for RID 29041 Last Modified: [21-Jul-2009 19:10:57] -- Shot Number: 54988 at 21-Jul-2009 19:13:53

General / 29041

Shot Scope	OMEGA Only		
Campaign	NLUF	**Planned Date**	21-Jul-2009
Series Name	RadGas Stereoscopic 09	**Shot Series**	10
PI List	Drake/Paul// Knauer/James/52074/18774594421	**Yield**	Type 6: No Yield or Low Yield, Neutron Yield predicted* to be less than 1e10
		Primary Objective	To obtain stereoscopic dual backlit images of radiating shocks
		Secondary Objective	
Special Instructions			
Abort Criteria	Abort on anything		

Driver / 29041

Driver	Status	Pulse Shape	Request #	Timing Shift	Leg	X / Y Modulation
SSD	ON	SG1018		-27 ns		MAX / MAX
Main	OFF			0 ns		
Backlighter	ON	PS200		0 ns	LEG3	
UV Fiducial	OFF					
Special Instructions						

Beams / 29041

21 beam(s) are configured, 20 beam(s) go to target.

Beams	Group Name	Energy	Pointing	Focusing	Beam Delay (ns)	DPP	DPR	Termination	Report Group
30,69	BL 2	70 J/Beam (UV)	12503 um / 143.77 / -17.01	800 um (spot size)	0	none	Yes	Target 2	C
33,34,36,37	BL 1	70 J/Beam (UV)	12500 um / P10	-800 um (spot size)	0	none	Yes	Target 2	B
38	BL 1	70 J/Beam (UV)	12500 um / P10	800 um (spot size)	0	none	Yes	Target 2	B
39,62,64	BL 2	70 J/Beam (UV)	12503 um / 143.77 / -17.01	-800 um (spot size)	0	none	Yes	Target 2	C
42-45,49-51,53,54,57	Drive	380 J/Beam (UV)	3200 um / 121.72 / 198	0 um (spot size)	0	SG8	Yes	Target	A
46	Ride Along	380 J/Beam (UV)	tcc	0 mm (lens position)	0	none	Yes	UVDT Dump	K

Target / 29041

	Target 1	Target 2	Target 3
Target ID	23T-9	BL-12	
Type	Xe filled PI tube with conical acrylic shield	Acrylic/Ta substrate with two mounted V foils	
Diameter	23500 um	14200 um	
Shape	Other	Other	
Type of Gas			
DT Target			
Positioner	TIM TPS 1 -- TIM 5	TPS2-Port H2	

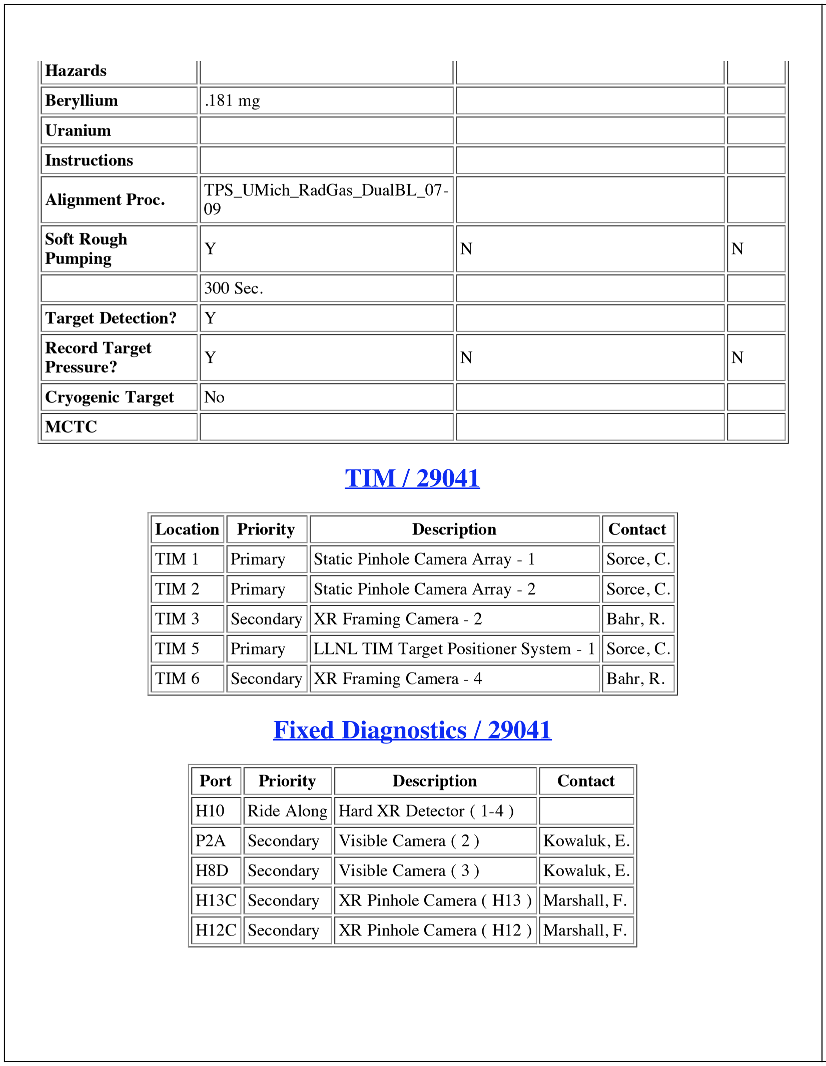

Hazards			
Beryllium	.181 mg		
Uranium			
Instructions			
Alignment Proc.	TPS_UMich_RadGas_DualBL_07-09		
Soft Rough Pumping	Y	N	N
	300 Sec.		
Target Detection?	Y		
Record Target Pressure?	Y	N	N
Cryogenic Target	No		
MCTC			

TIM / 29041

Location	Priority	Description	Contact
TIM 1	Primary	Static Pinhole Camera Array - 1	Sorce, C.
TIM 2	Primary	Static Pinhole Camera Array - 2	Sorce, C.
TIM 3	Secondary	XR Framing Camera - 2	Bahr, R.
TIM 5	Primary	LLNL TIM Target Positioner System - 1	Sorce, C.
TIM 6	Secondary	XR Framing Camera - 4	Bahr, R.

Fixed Diagnostics / 29041

Port	Priority	Description	Contact
H10	Ride Along	Hard XR Detector (1-4)	
P2A	Secondary	Visible Camera (2)	Kowaluk, E.
H8D	Secondary	Visible Camera (3)	Kowaluk, E.
H13C	Secondary	XR Pinhole Camera (H13)	Marshall, F.
H12C	Secondary	XR Pinhole Camera (H12)	Marshall, F.

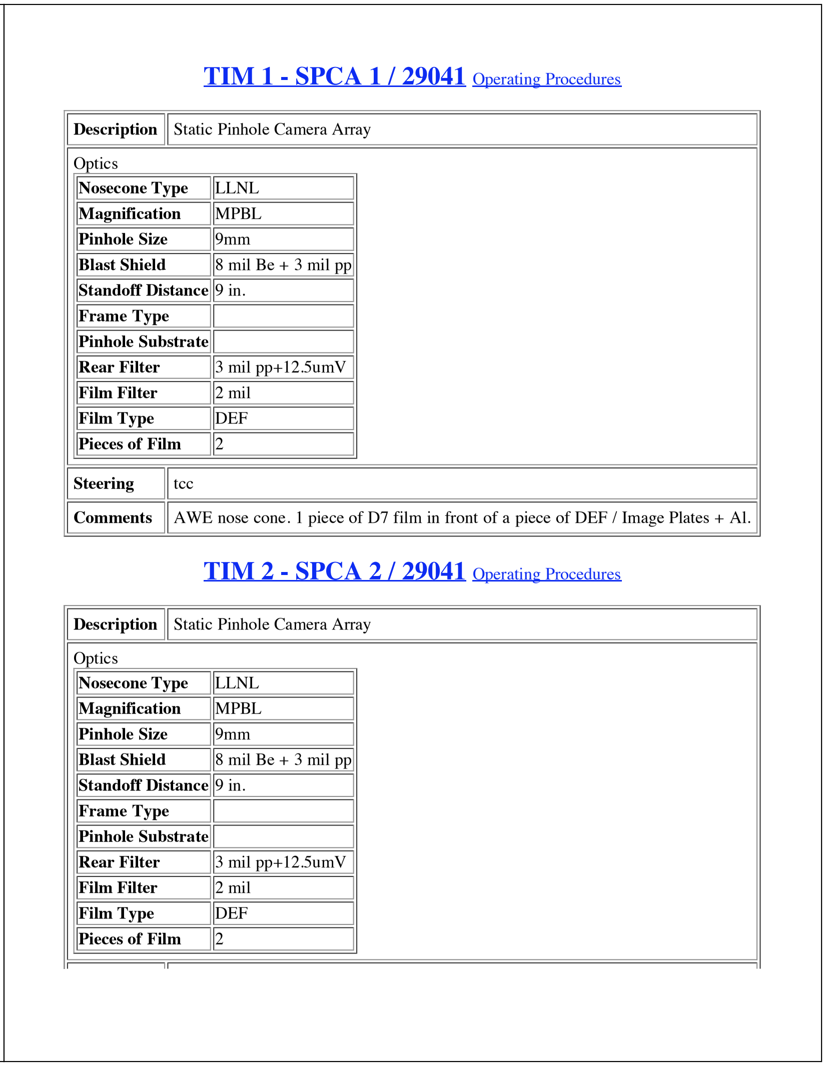

TIM 1 - SPCA 1 / 29041 Operating Procedures

Description: Static Pinhole Camera Array

Optics

Nosecone Type	LLNL
Magnification	MPBL
Pinhole Size	9mm
Blast Shield	8 mil Be + 3 mil pp
Standoff Distance	9 in.
Frame Type	
Pinhole Substrate	
Rear Filter	3 mil pp+12.5umV
Film Filter	2 mil
Film Type	DEF
Pieces of Film	2

Steering: tcc

Comments: AWE nose cone. 1 piece of D7 film in front of a piece of DEF / Image Plates + Al.

TIM 2 - SPCA 2 / 29041 Operating Procedures

Description: Static Pinhole Camera Array

Optics

Nosecone Type	LLNL
Magnification	MPBL
Pinhole Size	9mm
Blast Shield	8 mil Be + 3 mil pp
Standoff Distance	9 in.
Frame Type	
Pinhole Substrate	
Rear Filter	3 mil pp+12.5umV
Film Filter	2 mil
Film Type	DEF
Pieces of Film	2

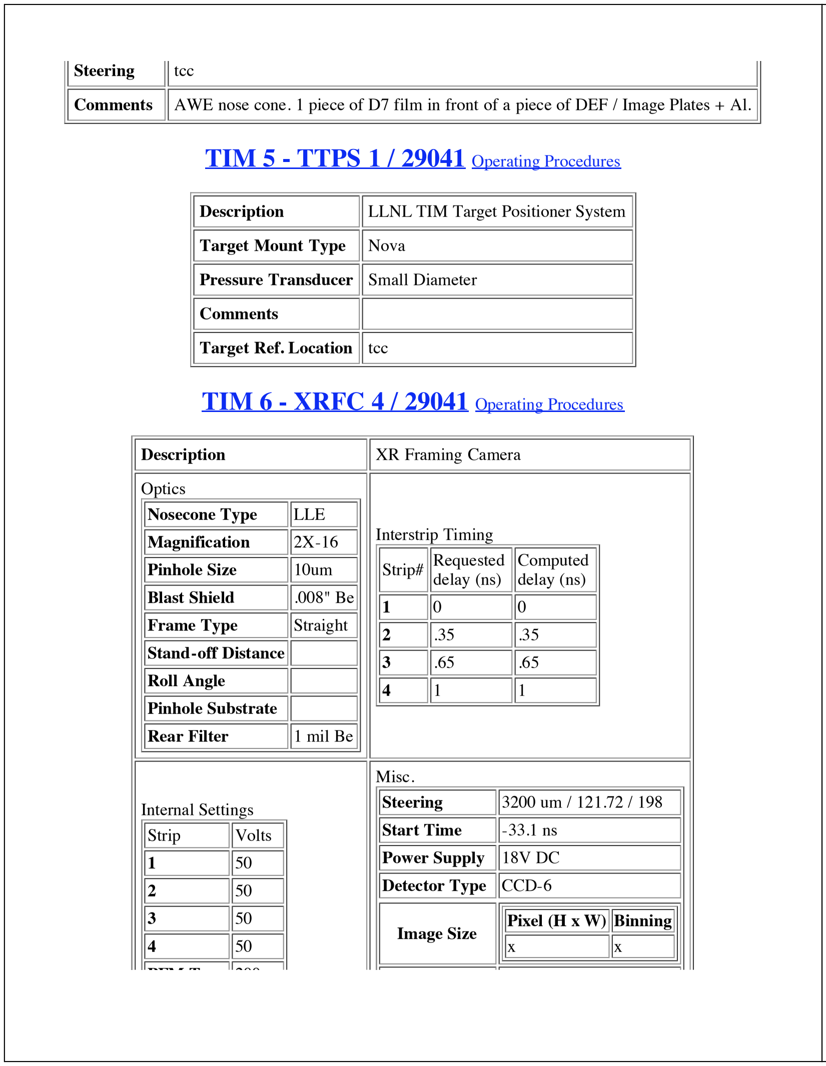

Steering	tcc
Comments	AWE nose cone. 1 piece of D7 film in front of a piece of DEF / Image Plates + Al.

TIM 5 - TTPS 1 / 29041 Operating Procedures

Description	LLNL TIM Target Positioner System
Target Mount Type	Nova
Pressure Transducer	Small Diameter
Comments	
Target Ref. Location	tcc

TIM 6 - XRFC 4 / 29041 Operating Procedures

Description	XR Framing Camera

Optics

Nosecone Type	LLE
Magnification	2X-16
Pinhole Size	10um
Blast Shield	.008" Be
Frame Type	Straight
Stand-off Distance	
Roll Angle	
Pinhole Substrate	
Rear Filter	1 mil Be

Interstrip Timing

Strip#	Requested delay (ns)	Computed delay (ns)
1	0	0
2	.35	.35
3	.65	.65
4	1	1

Internal Settings

Strip	Volts
1	50
2	50
3	50
4	50

Misc.

Steering	3200 um / 121.72 / 198
Start Time	-33.1 ns
Power Supply	18V DC
Detector Type	CCD-6
Image Size	**Pixel (H x W)**: x **Binning**: x

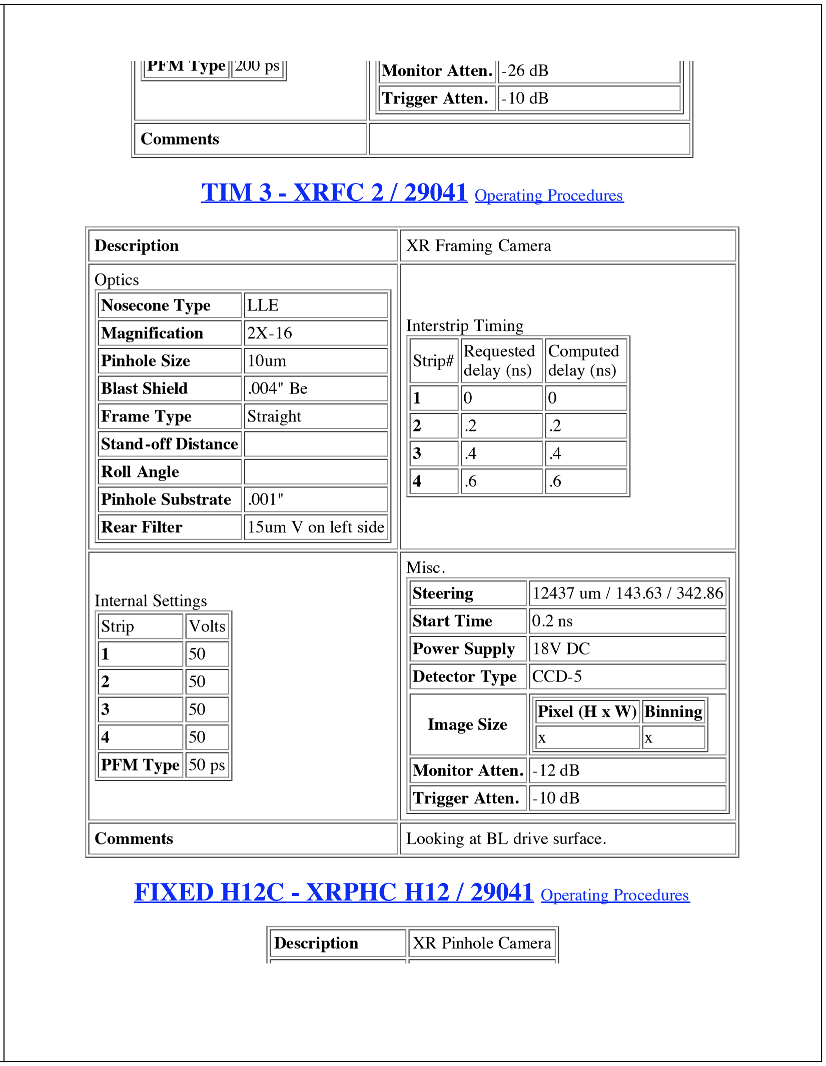

PFM Type	200 ps
Monitor Atten.	-26 dB
Trigger Atten.	-10 dB
Comments	

TIM 3 - XRFC 2 / 29041 Operating Procedures

Description	XR Framing Camera

Optics

Nosecone Type	LLE
Magnification	2X-16
Pinhole Size	10um
Blast Shield	.004" Be
Frame Type	Straight
Stand-off Distance	
Roll Angle	
Pinhole Substrate	.001"
Rear Filter	15um V on left side

Interstrip Timing

Strip#	Requested delay (ns)	Computed delay (ns)
1	0	0
2	.2	.2
3	.4	.4
4	.6	.6

Internal Settings

Strip	Volts
1	50
2	50
3	50
4	50
PFM Type	50 ps

Misc.

Steering	12437 um / 143.63 / 342.86
Start Time	0.2 ns
Power Supply	18V DC
Detector Type	CCD-5
Image Size	**Pixel (H x W)**: x **Binning**: x
Monitor Atten.	-12 dB
Trigger Atten.	-10 dB

Comments	Looking at BL drive surface.

FIXED H12C - XRPHC H12 / 29041 Operating Procedures

Description	XR Pinhole Camera

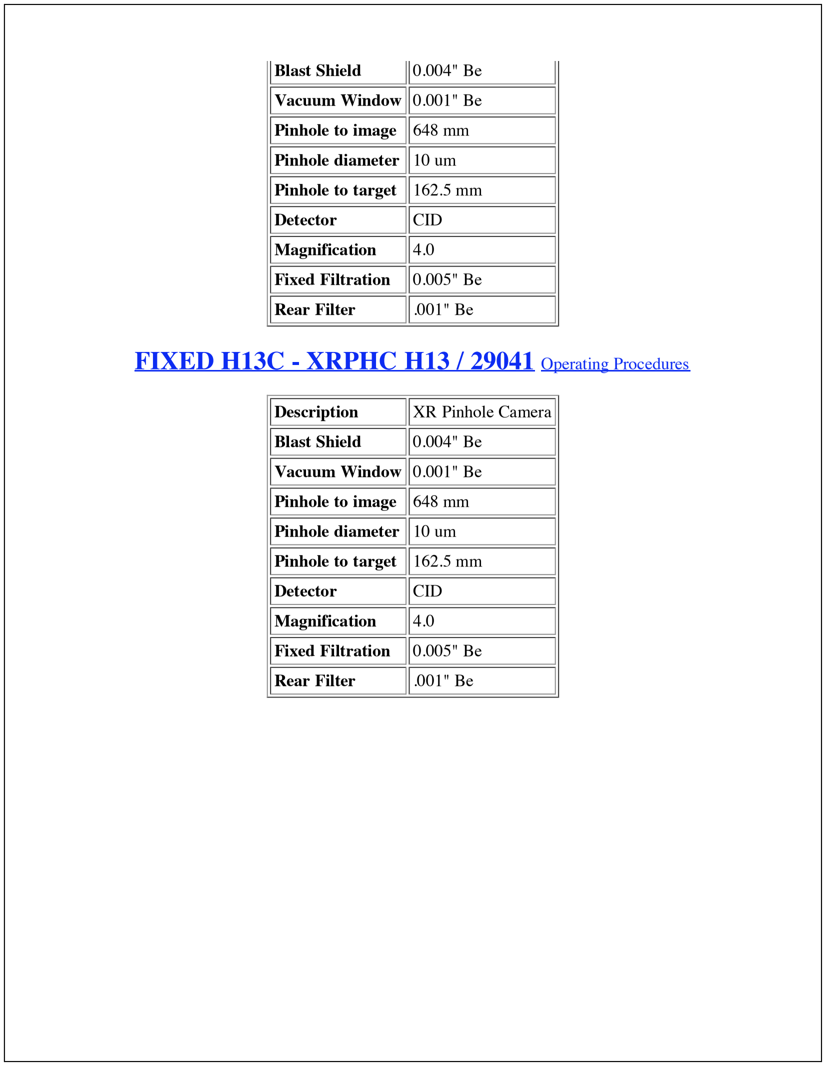

Blast Shield	0.004" Be
Vacuum Window	0.001" Be
Pinhole to image	648 mm
Pinhole diameter	10 um
Pinhole to target	162.5 mm
Detector	CID
Magnification	4.0
Fixed Filtration	0.005" Be
Rear Filter	.001" Be

FIXED H13C - XRPHC H13 / 29041 Operating Procedures

Description	XR Pinhole Camera
Blast Shield	0.004" Be
Vacuum Window	0.001" Be
Pinhole to image	648 mm
Pinhole diameter	10 um
Pinhole to target	162.5 mm
Detector	CID
Magnification	4.0
Fixed Filtration	0.005" Be
Rear Filter	.001" Be

APPENDIX E

August 2010 Shot Request Form

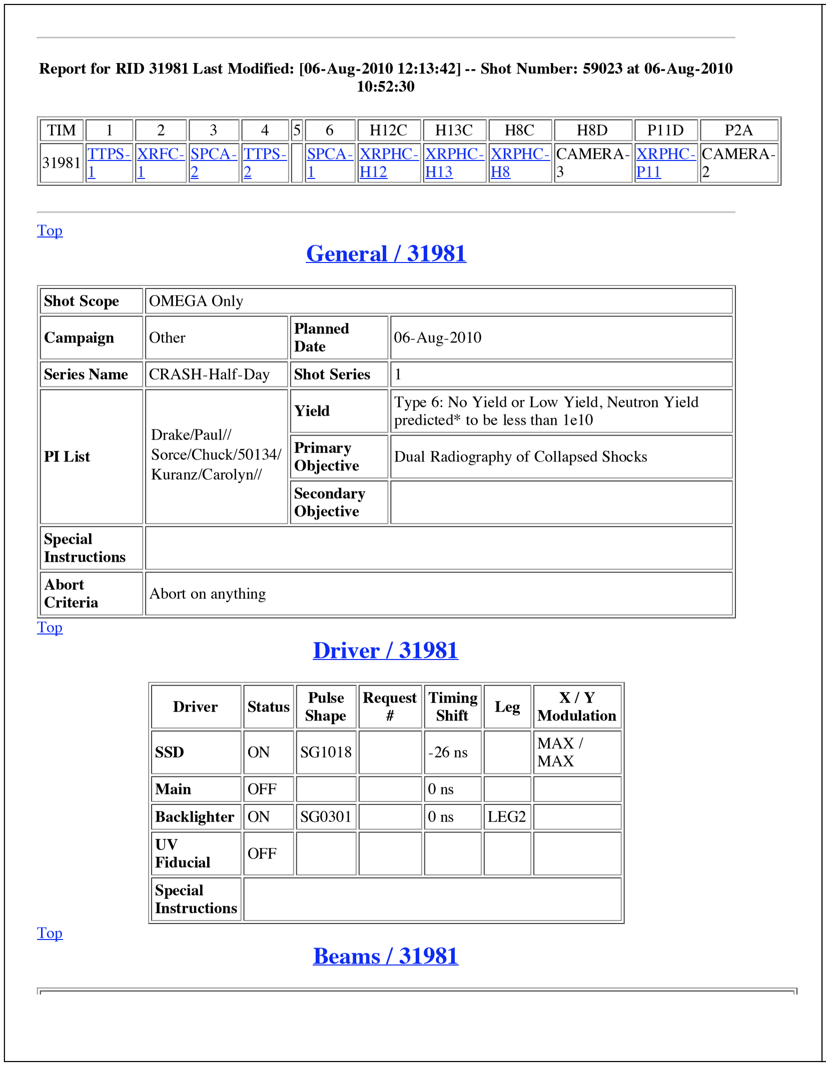

Report for RID 31981 Last Modified: [06-Aug-2010 12:13:42] -- Shot Number: 59023 at 06-Aug-2010 10:52:30

TIM	1	2	3	4	5	6	H12C	H13C	H8C	H8D	P11D	P2A
31981	TTPS-1	XRFC-1	SPCA-2	TTPS-2		SPCA-1	XRPHC-H12	XRPHC-H13	XRPHC-H8	CAMERA-3	XRPHC-P11	CAMERA-2

Top

General / 31981

Shot Scope	OMEGA Only		
Campaign	Other	**Planned Date**	06-Aug-2010
Series Name	CRASH-Half-Day	**Shot Series**	1
PI List	Drake/Paul// Sorce/Chuck/50134/ Kuranz/Carolyn//	**Yield**	Type 6: No Yield or Low Yield, Neutron Yield predicted* to be less than 1e10
		Primary Objective	Dual Radiography of Collapsed Shocks
		Secondary Objective	
Special Instructions			
Abort Criteria	Abort on anything		

Top

Driver / 31981

Driver	Status	Pulse Shape	Request #	Timing Shift	Leg	X / Y Modulation
SSD	ON	SG1018		-26 ns		MAX / MAX
Main	OFF			0 ns		
Backlighter	ON	SG0301		0 ns	LEG2	
UV Fiducial	OFF					
Special Instructions						

Top

Beams / 31981

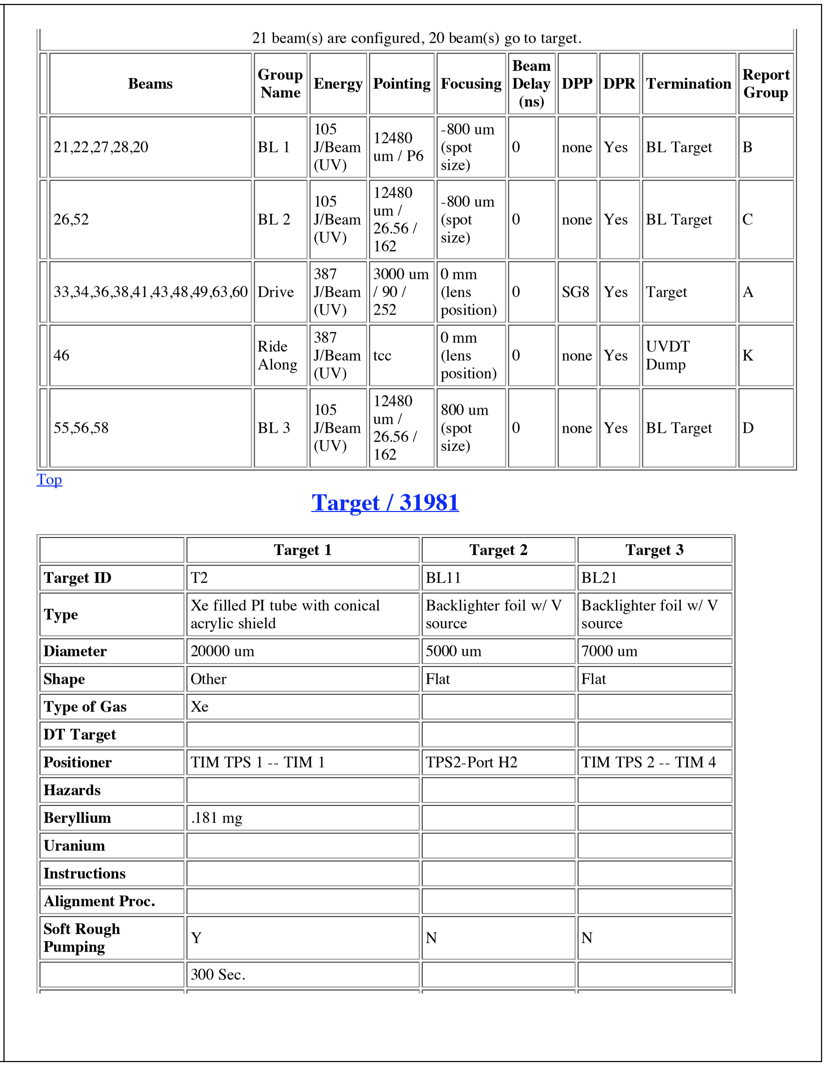

21 beam(s) are configured, 20 beam(s) go to target.

Beams	Group Name	Energy	Pointing	Focusing	Beam Delay (ns)	DPP	DPR	Termination	Report Group
21,22,27,28,20	BL 1	105 J/Beam (UV)	12480 um / P6	-800 um (spot size)	0	none	Yes	BL Target	B
26,52	BL 2	105 J/Beam (UV)	12480 um / 26.56 / 162	-800 um (spot size)	0	none	Yes	BL Target	C
33,34,36,38,41,43,48,49,63,60	Drive	387 J/Beam (UV)	3000 um / 90 / 252	0 mm (lens position)	0	SG8	Yes	Target	A
46	Ride Along	387 J/Beam (UV)	tcc	0 mm (lens position)	0	none	Yes	UVDT Dump	K
55,56,58	BL 3	105 J/Beam (UV)	12480 um / 26.56 / 162	800 um (spot size)	0	none	Yes	BL Target	D

Top

Target / 31981

	Target 1	Target 2	Target 3
Target ID	T2	BL11	BL21
Type	Xe filled PI tube with conical acrylic shield	Backlighter foil w/ V source	Backlighter foil w/ V source
Diameter	20000 um	5000 um	7000 um
Shape	Other	Flat	Flat
Type of Gas	Xe		
DT Target			
Positioner	TIM TPS 1 -- TIM 1	TPS2-Port H2	TIM TPS 2 -- TIM 4
Hazards			
Beryllium	.181 mg		
Uranium			
Instructions			
Alignment Proc.			
Soft Rough Pumping	Y	N	N
	300 Sec.		

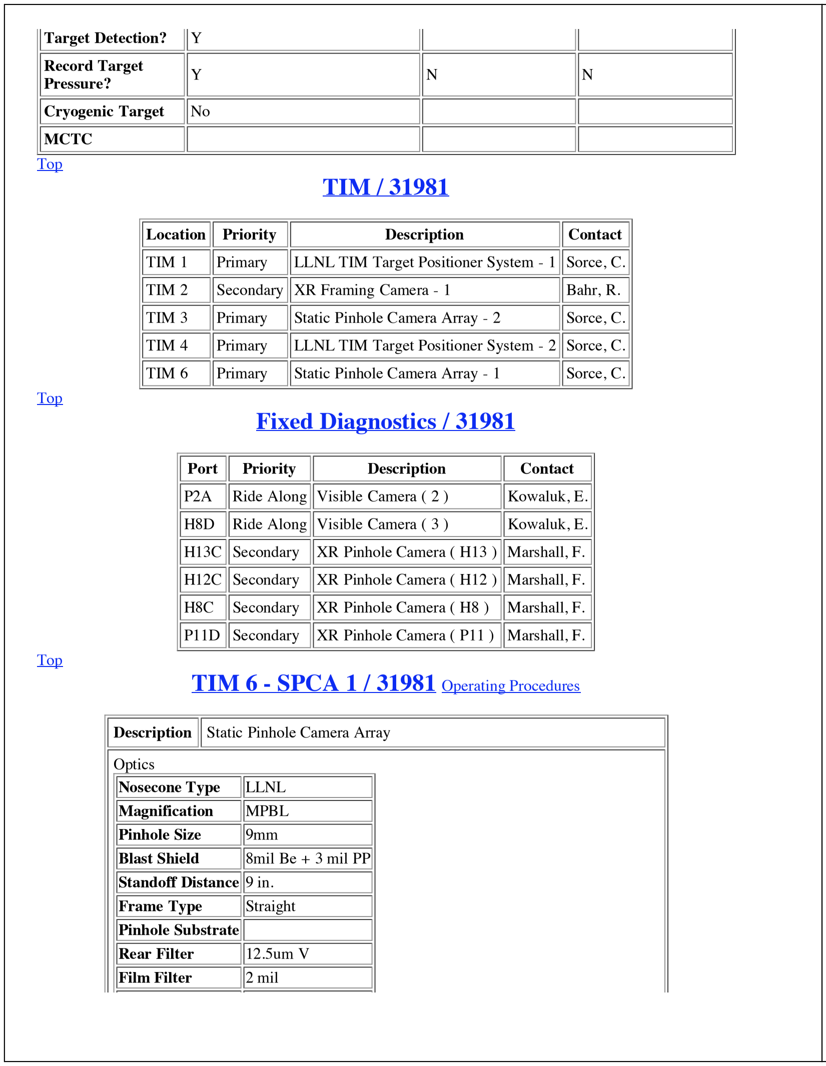

Target Detection?	Y		
Record Target Pressure?	Y	N	N
Cryogenic Target	No		
MCTC			

Top

TIM / 31981

Location	Priority	Description	Contact
TIM 1	Primary	LLNL TIM Target Positioner System - 1	Sorce, C.
TIM 2	Secondary	XR Framing Camera - 1	Bahr, R.
TIM 3	Primary	Static Pinhole Camera Array - 2	Sorce, C.
TIM 4	Primary	LLNL TIM Target Positioner System - 2	Sorce, C.
TIM 6	Primary	Static Pinhole Camera Array - 1	Sorce, C.

Top

Fixed Diagnostics / 31981

Port	Priority	Description	Contact
P2A	Ride Along	Visible Camera (2)	Kowaluk, E.
H8D	Ride Along	Visible Camera (3)	Kowaluk, E.
H13C	Secondary	XR Pinhole Camera (H13)	Marshall, F.
H12C	Secondary	XR Pinhole Camera (H12)	Marshall, F.
H8C	Secondary	XR Pinhole Camera (H8)	Marshall, F.
P11D	Secondary	XR Pinhole Camera (P11)	Marshall, F.

Top

TIM 6 - SPCA 1 / 31981 Operating Procedures

Description	Static Pinhole Camera Array

Optics

Nosecone Type	LLNL
Magnification	MPBL
Pinhole Size	9mm
Blast Shield	8mil Be + 3 mil PP
Standoff Distance	9 in.
Frame Type	Straight
Pinhole Substrate	
Rear Filter	12.5um V
Film Filter	2 mil

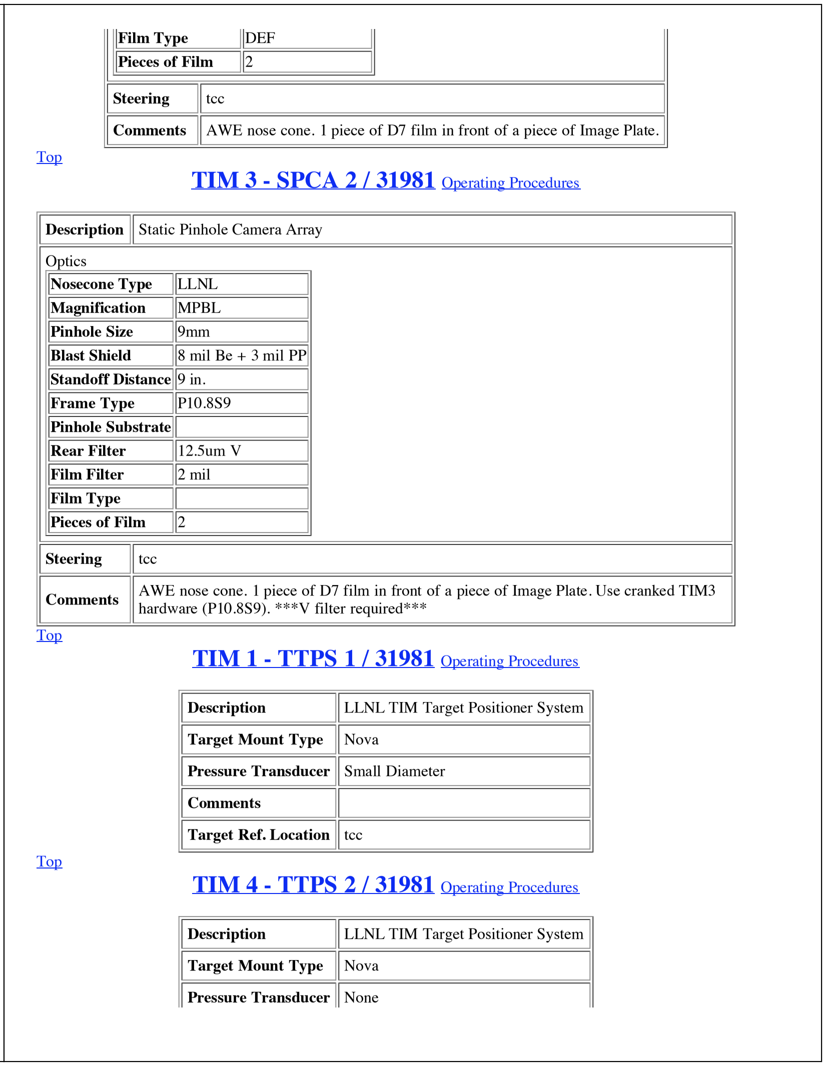

Film Type	DEF
Pieces of Film	2

Steering	tcc
Comments	AWE nose cone. 1 piece of D7 film in front of a piece of Image Plate.

Top

TIM 3 - SPCA 2 / 31981 Operating Procedures

Description	Static Pinhole Camera Array

Optics

Nosecone Type	LLNL
Magnification	MPBL
Pinhole Size	9mm
Blast Shield	8 mil Be + 3 mil PP
Standoff Distance	9 in.
Frame Type	P10.8S9
Pinhole Substrate	
Rear Filter	12.5um V
Film Filter	2 mil
Film Type	
Pieces of Film	2

Steering	tcc
Comments	AWE nose cone. 1 piece of D7 film in front of a piece of Image Plate. Use cranked TIM3 hardware (P10.8S9). ***V filter required***

Top

TIM 1 - TTPS 1 / 31981 Operating Procedures

Description	LLNL TIM Target Positioner System
Target Mount Type	Nova
Pressure Transducer	Small Diameter
Comments	
Target Ref. Location	tcc

Top

TIM 4 - TTPS 2 / 31981 Operating Procedures

Description	LLNL TIM Target Positioner System
Target Mount Type	Nova
Pressure Transducer	None

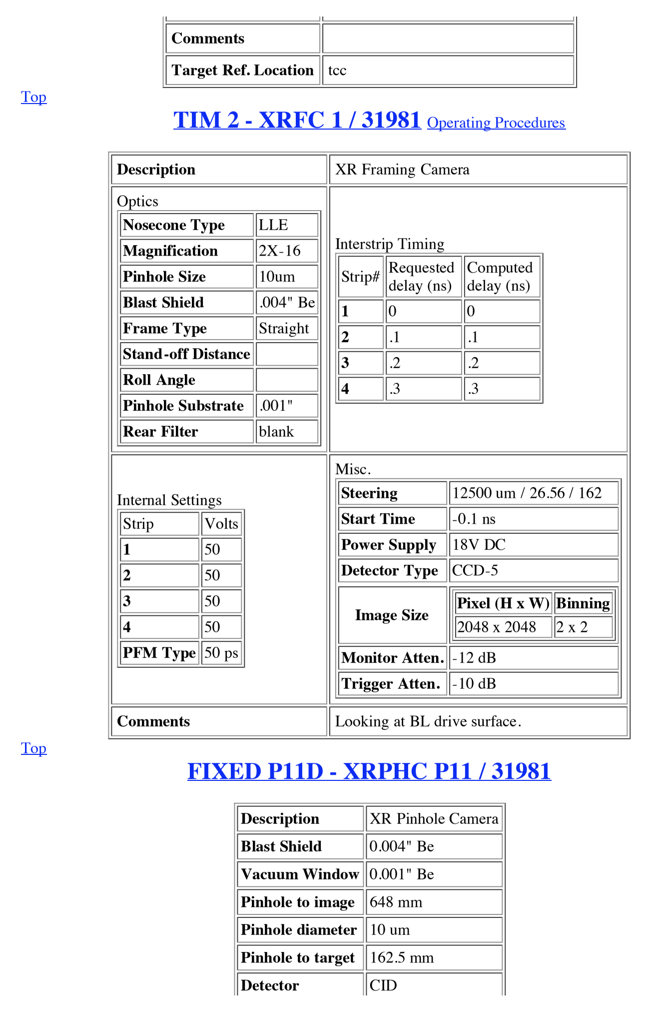

Comments	
Target Ref. Location	tcc

Top

TIM 2 - XRFC 1 / 31981 Operating Procedures

<table>
<tr><td>Description</td><td>XR Framing Camera</td></tr>
<tr><td>Optics
<table>
<tr><td>Nosecone Type</td><td>LLE</td></tr>
<tr><td>Magnification</td><td>2X-16</td></tr>
<tr><td>Pinhole Size</td><td>10um</td></tr>
<tr><td>Blast Shield</td><td>.004" Be</td></tr>
<tr><td>Frame Type</td><td>Straight</td></tr>
<tr><td>Stand-off Distance</td><td></td></tr>
<tr><td>Roll Angle</td><td></td></tr>
<tr><td>Pinhole Substrate</td><td>.001"</td></tr>
<tr><td>Rear Filter</td><td>blank</td></tr>
</table></td>
<td>Interstrip Timing
<table>
<tr><td>Strip#</td><td>Requested delay (ns)</td><td>Computed delay (ns)</td></tr>
<tr><td>1</td><td>0</td><td>0</td></tr>
<tr><td>2</td><td>.1</td><td>.1</td></tr>
<tr><td>3</td><td>.2</td><td>.2</td></tr>
<tr><td>4</td><td>.3</td><td>.3</td></tr>
</table></td></tr>
<tr><td>Internal Settings
<table>
<tr><td>Strip</td><td>Volts</td></tr>
<tr><td>1</td><td>50</td></tr>
<tr><td>2</td><td>50</td></tr>
<tr><td>3</td><td>50</td></tr>
<tr><td>4</td><td>50</td></tr>
<tr><td>PFM Type</td><td>50 ps</td></tr>
</table></td>
<td>Misc.
<table>
<tr><td>Steering</td><td>12500 um / 26.56 / 162</td></tr>
<tr><td>Start Time</td><td>-0.1 ns</td></tr>
<tr><td>Power Supply</td><td>18V DC</td></tr>
<tr><td>Detector Type</td><td>CCD-5</td></tr>
<tr><td>Image Size</td><td><table><tr><td>Pixel (H x W)</td><td>Binning</td></tr><tr><td>2048 x 2048</td><td>2 x 2</td></tr></table></td></tr>
<tr><td>Monitor Atten.</td><td>-12 dB</td></tr>
<tr><td>Trigger Atten.</td><td>-10 dB</td></tr>
</table></td></tr>
<tr><td>Comments</td><td>Looking at BL drive surface.</td></tr>
</table>

Top

FIXED P11D - XRPHC P11 / 31981

Description	XR Pinhole Camera
Blast Shield	0.004" Be
Vacuum Window	0.001" Be
Pinhole to image	648 mm
Pinhole diameter	10 um
Pinhole to target	162.5 mm
Detector	CID

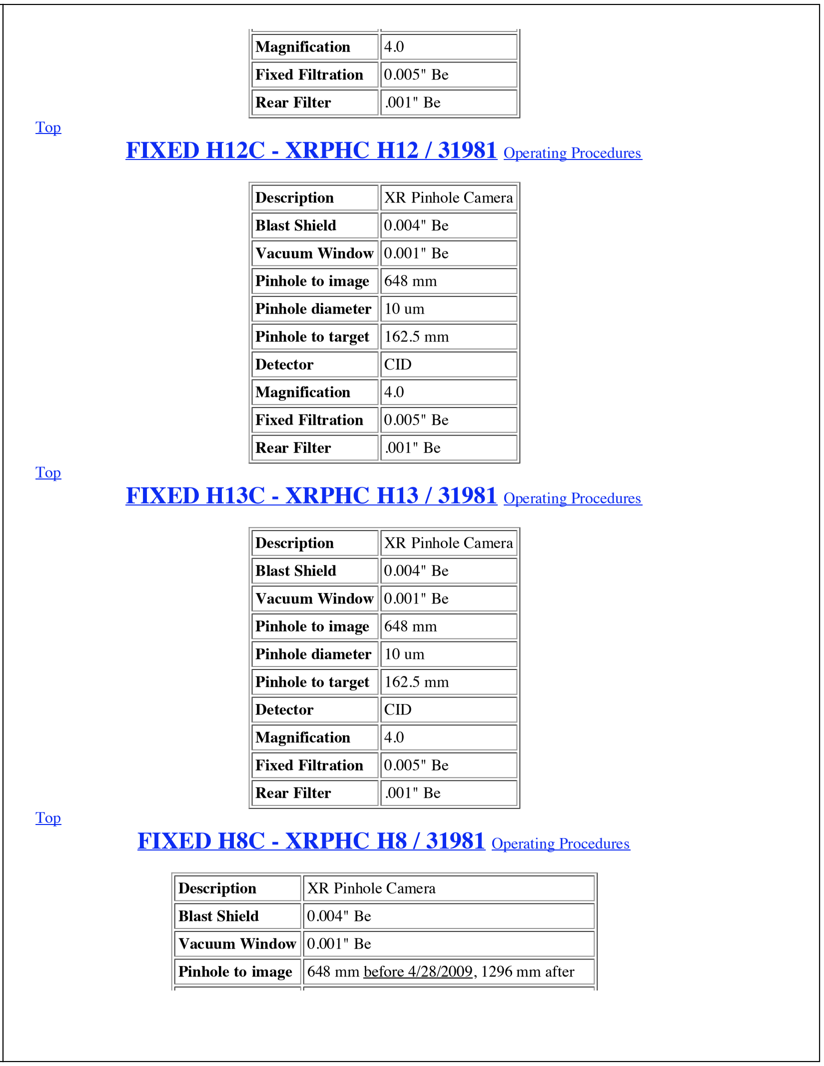

Magnification	4.0
Fixed Filtration	0.005" Be
Rear Filter	.001" Be

Top

FIXED H12C - XRPHC H12 / 31981 Operating Procedures

Description	XR Pinhole Camera
Blast Shield	0.004" Be
Vacuum Window	0.001" Be
Pinhole to image	648 mm
Pinhole diameter	10 um
Pinhole to target	162.5 mm
Detector	CID
Magnification	4.0
Fixed Filtration	0.005" Be
Rear Filter	.001" Be

Top

FIXED H13C - XRPHC H13 / 31981 Operating Procedures

Description	XR Pinhole Camera
Blast Shield	0.004" Be
Vacuum Window	0.001" Be
Pinhole to image	648 mm
Pinhole diameter	10 um
Pinhole to target	162.5 mm
Detector	CID
Magnification	4.0
Fixed Filtration	0.005" Be
Rear Filter	.001" Be

Top

FIXED H8C - XRPHC H8 / 31981 Operating Procedures

Description	XR Pinhole Camera
Blast Shield	0.004" Be
Vacuum Window	0.001" Be
Pinhole to image	648 mm before 4/28/2009, 1296 mm after

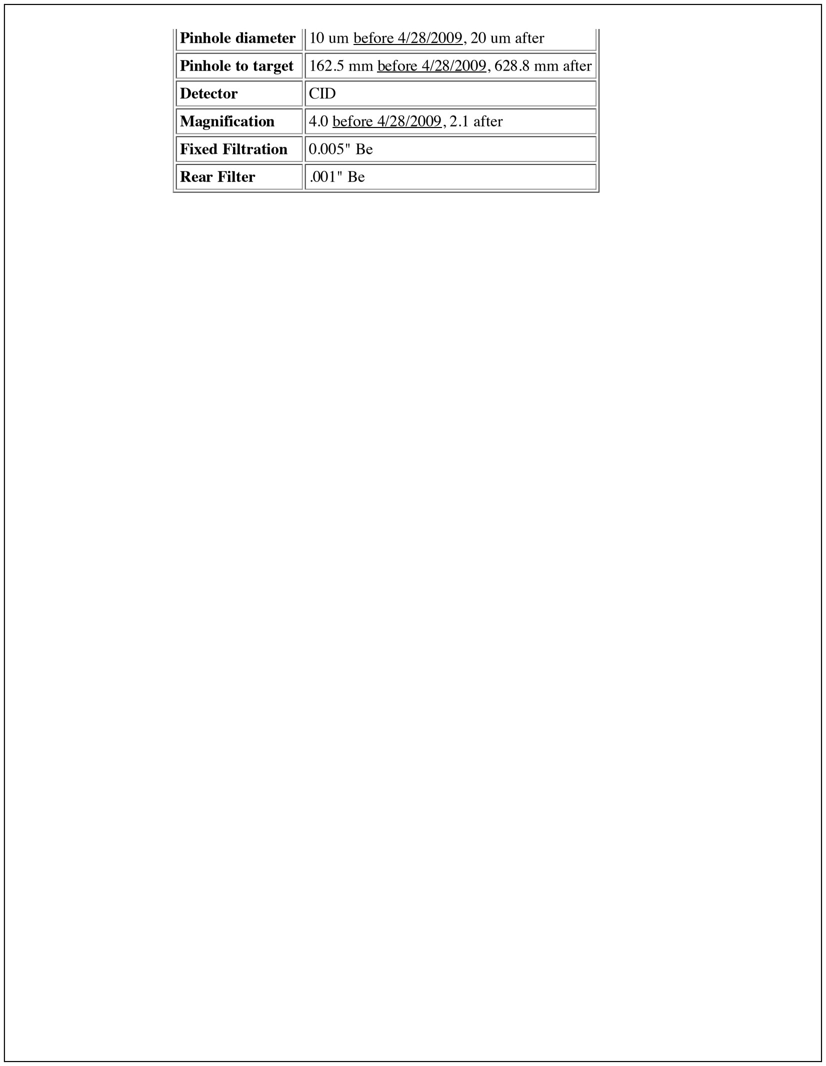

Pinhole diameter	10 um before 4/28/2009, 20 um after
Pinhole to target	162.5 mm before 4/28/2009, 628.8 mm after
Detector	CID
Magnification	4.0 before 4/28/2009, 2.1 after
Fixed Filtration	0.005" Be
Rear Filter	.001" Be

BIBLIOGRAPHY

BIBLIOGRAPHY

[1] V. I. Artem'ev, V. I. Bergel'son, S. A. Medvedyuk, I. V. Nemchinov, T. I. Orlova, V. A. Rybakov, and V. M. Khazins. Vortex flows induced by interaction of a shock wave with thin regions of finite length and reduced density. *Izvestiya Rossiiskoi Akademii Nauk, Mekhanika Zhidkosti i Gaza*, (3):149–153, 1993.

[2] V. I. Artem'ev, V. N. Bergel'son, A. A. Kalmykov, I. V. Nechinov, T. I. Orlova, V. A. Rybakov, V. A. Smirnov, and V. M. Khazins. Development of a forerunner in interaction of a shock wave with a layer of reduced density. *Prikladnoi Mekhaniki i Tekhnicheskoi Fiziki*, (2):158–163, 1988.

[3] Stefano Atzeni and Jurgen Meyer ter Vehn. *The Physics of Inertial Fusion: Beam Plasma Interaction, Hydrodynamics, Hot Dense Matter*. Oxford University Press, 2009.

[4] J. E. Bailey, G. A. Chandler, S. A. Slutz, I. Golovkin an P. W. Lake, J. J. Macfarlane, R. C. Mancini, T. J. Burris-Mog, G. Cooper, R. J. Leeper, T. A. Mehlhorn, T. C. Moore, T. J. Nash, D. S. Nielsen, C. L. Ruiz, D. G. Schroen, and W. A. Varnum. Hot dense capsule-implosion cores produced by z-pinch dynamic hohlraum radiation. *Physical Review Letters*, page 085002, February 2004.

[5] N. Bartel, M. F. Bietenholz, M. P. Rupen, A. J. Beasley, D. A. Graham, V. I. Altunin, T. Venturi, G. Umana, W. H. Cannon, and J. E. Conway. The changing morphology and increasing deceleration of supernova 1993j in m81. *Science*, 287:112, 2000.

[6] Gabi Ben-Dor. *Shock Wave Reflection Phenomena*. Springer, 2007.

[7] A. Benuzzi, M. Koenig, B. Faral, J. Krishnan, F. Pisani, D. Batani, S. Bossi, D. Beretta, T. Hall, S. Ellwi, S. Hüller, J. Honrubia, and N. Grandjouan. Preheating study by reflectivity measurements in laser-driven shocks. *Physics of Plasmas*, 5(6):2410, 1998.

[8] V. I. Bergel'son, Yu. N. Kiselev, V. A. Klumov, I. V. Nemchinov, T. I. Orlova, V. B. Rozhdestvenskii, and V. M. Khazins. Interaction of a shock wave with a boundary layer. *Prikladnoi Mekhaniki i Tekhnicheskoi Fiziki*, (3):32–40, 1993.

[9] E. Bertschinger. On the structure and stability of radiative shock waves. *Astrophysical Journal*, 304:154 – 177, May 1986.

[10] B. E. Blue, J. F. Hansen, M. T. Tobin, D. C. Eder, and H. F. Robey. Debris mitigation in pinhole-aperatured point-projection backlit imaging. *Review of Scientific Instruments*, 75(11):4775, 2004.

[11] B. E. Blue, H. F. Robey, S. G. Glendinning, M. J. Bono, S. C. Burkhart, J. R. Celeste, R. F. Coker, R. L. Costa, S. N. Dixit, J. M. Foster, J. F. Hansen, C. A. Haynam, M. R. Hermann, J. P. Holder, W. W. Hsing, D. H. Kalantar, N. E. Lanier, D. A. Latray, H. Louis, B. J. MacGowan, G. R. Maggelssen, C. D. Marshall, E. I. Moses, A. J. Nikitin, D. W. O'Brien, T. S. Perry, M. W. Poole, V. V. Rekow, P. A. Rosen, M. B. Schneider, P. E. Stry, B. M. Van Wonterghem, R. Wallace, S. V. Weber, B. H. Wilde, D. T. Woods, and B. K. Young. Three-dimensional hydrodynamic experiments on the national ignition facility. *Physics of Plasmas*, 12(5):056313, 2005.

[12] T. R. Boehly, D .L. Brown, R. S. Craxton, R. L. Keck, J. P. Knauer, J. H. Kelly, T. J. Kessler, S. A. Kumpman, S.J. Loucks, S. A. Letzring, F. J. Marshall, R. L. McCrory, S. F. B. Morse, W. Seka, J. M. Soures, and C. P. Verdon. Initial performance results of the omega laser system. *Optics-Communications*, 133:495, 1994.

[13] S. Bouquet, C. Stehlé, M. Koenig, J.-P. Chièze, A. Benuzzi-Mounaix, D. Batani, S. Leygnac, X. Fleury, H. Merdji, C. Michaut, F. Thais, N. Grandjouan, T. Hall, E. Henry, V. Malka, and J.-P. J. Lafon. Observation of laser driven supercritical radiative shock precursors. *Physical Review Letters*, 92(22):225001, Jun 2004.

[14] Serge Bouquet, Romain Teyssier, and Jean Pierre Chieze. Analytical study and structure of a stationary radiative shock. *Astrophysical Journal Supplement Series*, 127:242, April 2000.

[15] J. C. Bozier, G. Thiell, J. P. Le Breton, S. Azra, M. Decroisette, and D. Schirmann. Experimental observation of a radiative wave generated in xenon by a laser-driven supercritical shock. *Physical Review Letters*, 57(11):1304–1307, Sep 1986.

[16] C. J. Chapman. *High Speed Flow.* Cambridge University Press, 2000.

[17] J. Clarke and M. Onorato. Normal shock waves structured by nonequilibirum radiative and collisional ionization. *Journal of Applied Mechanics*, page 783, September 1970.

[18] J. H. Clarke and C. Ferrari. Gas dynamics with nonequilibrium radiative and collisional ionization. *Physics of Fluids*, 8(12):2121, 1965.

[19] R. Courant and K. O. Friedrichs. *Supersonic Flow and Shock Waves.* Interscience, 1948.

[20] John P. Cox and R. Thomas Giuli. *Principles of Stellar Structure.* Gordon and Breach, 1968.

[21] F. W. Doss, R. P. Drake, and C. C. Kuranz. Repeatability in radiative shock tube experiments. *High Energy Density Physics*, 6:157–161, 2010.

[22] F. W. Doss, R. P. Drake, and E. S. Myra. Oblique radiative shocks, including their interactions with non-radiative polytropic shocks. *Physics of Plasmas*, 18(5):to appear.

[23] F. W. Doss, H. F. Robey, R. P. Drake, and C. C. Kuranz. Wall shocks in high-energy-density shock tube experiments. *Physics of Plasmas*, 16(11):112705, 2009.

[24] R. Paul Drake. *High-Energy-Density Physics*. Springer, 2006.

[25] M. J. Edwards, A. J. MacKinnon, J. Zweiback, K. Shigemori, D. Ryutov, A. M. Rubenchik, K. A. Keilty, E. Liang, B. A. Remington, and T. Ditmire. Investigation of ultrafast laser-driven radiative blast waves. *Physical Review Letters*, 87:085004, August 2001.

[26] Shalom Eliezer, Ajoy K. Ghatak, and Heinrich Hora. *Fundamentals of Equations of State*. World Scientific, 2002.

[27] C. Ferrari and M. Onorato. Structure of a strong normal shock wave due to nonequilibrium radiation and collisional ionization. *Meccanica*, page 207, September 1969.

[28] X. Fleury, S. Bouquet, C. Stehlé, M. Koenig, D Batani, A. Benuzzi-Mounaix, J.-P. Chièze, N. Grandjouan, J. Greiner, T. Hall, E. Henry, J.-P. Lafon, . Leygnac, V. Malka, B. Marchet, H. Merdji, C. Michaut, and F. Thais. ”a laser experiment for studying radiative shocks in astrophysics”. *Laser and Particle Beams*, 20:263, 2002.

[29] N. C. Freeman. A Theory of the Stability of Plane Shock Waves. *Royal Society of London Proceedings Series A*, 228:341–362, March 1955.

[30] Andrew Gelman, John B. Carlin, Hal S. Stern, and Donald B. Rubin. *Bayesian Data Analysis, Second Edition (Texts in Statistical Science)*. Chapman & Hall/CRC, 2003.

[31] Irvin Glassman. *Combustion, Third Edition*. Academic Press, 1996.

[32] J. Grun, R. Burris, G. Joyce, S. Slinker, J. Huba, K. Evans, C. K. Manka, J. R. Barthel, and J. W. Wierhe. Small-scale laboratory measurement and simulation of a thermal precursor shock. *Journal of Applied Physics*, 83(5):2420, 1998.

[33] J. Grun, J. Stamper, C. Manka, J. Resnick, R. Burris, J. Crawford, and B. H. Ripin. Instability of taylor-sedov blast waves propagating through a uniform gas. *Physical Review Letters*, 66(21):2738, May 1991.

[34] G. Guderley. Powerful spherical and cylindrical compression shocks in the neigbourhood of the center of the sphere and of the cylindrical axis. *Luftfahrtforschung*, 19:302, 1942.

[35] J. F. Hansen, M. J. Edwards, D. Froula, G. Gregori, A. Edens, and T. Ditmire. Laboratory simulations of supernova shockwave propagation. *Astrophysics and Space Sciences*, 298:61 67, July 2005.

[36] Wallace Hayes and Ronald Probstein. *Hypersonic Flow Theory*. Academic Press, 1966.

[37] C A Haynam, R A Sacks, P J Wegner, M W Bowers, S N Dixit, G V Erbert, G M Heestand, M A Henesian, M R Hermann, K S Jancaitis, K R Manes, C D Marshall, N C Mehta, J Menapace, M C Nostrand, C D Orth, M J Shaw, S B Sutton, W H Williams, C C Widmayer, R K White, S T Yang, and B M Van Wonterghem. The national ignition facility 2007 laser performance status. *Journal of Physics: Conference Series*, 112(3):032004, 2008.

[38] L. F. Henderson and R. Menikoff. Triple-shock entropy theorem and its consequences. *Journal of Fluid Mechanics*, 366:179, 1998.

[39] L.F. Henderson. The refraction of a plane shock wave at a gas interface. *J. Fluid Mech.*, 26(3):607, 1966.

[40] L.F. Henderson, Ma Jia-Huan, Sakurai Akira, and Takayama Kazuyoshi. Refraction of a shock wave at an air–water interface. *Fluid Dynamics Research*, 5(5-6):337 – 350, 1990.

[41] B. L. Henke, E. M. Gullikson, and J.C. Davis. X-ray interactions: photoabsorption, scattering, transmission, and reflection at $e = 50 - 30000$ eV, $z = 1 - 92$. *Atomic Data and Nuclear Data Tables*, 54(2):181–342, July 1993.

[42] H. Hornung. Regular and Mach reflection of shock waves. *Ann. Rev. Fluid Mech.*, 18:33–58, 1986.

[43] Eugene Isaacson and Herbert Bishop Keller. *Analysis of Numerical Methods*. Dover Publications, 1994.

[44] R. Ishizaki and K. Nishimura. Propagation of a rippled shock wave driven by nonuniform laser ablation. *Physical Review Letters*, 78:1920, 1997.

[45] Department of Physics Jack Hughes and Rutgers University Astronomy. personal communication, 2010.

[46] R. G. Jahn. The refraction of shock waves at a gaseous interface. *Journal of Fluid Mechanics*, 1(05):457–489, 1956.

[47] E.T. Jaynes. *Probability Theory: The Logic of Science*. Cambridge University Press, 2003.

[48] S. Kaliski. The 'isothermal' shock wave. *Bulletin de l'Academie Polonaise des Sciences Series des Sciences Mathematiques Astronomiques et Physiques*, 24:463, 1976.

[49] Edison Liang and Katherine Keilty. An analytic approximation to radiative blast wave evolution. *Astrophysical Journal*, 533:890, 2000.

[50] P. A. Keiter, R. P. Drake, T. S. Perry, H.F. Robey, B. A. Remington, C. A. Iglesias, R. J. Wallace, and J. Knauer. Observation of a hydrodynamically driven, radiative-precursor shock. *Physical Review Letters*, 89(16):165003, Sep 2002.

[51] Yu. N. Kiselev, V. A. Klumov, V. B. Rozhdestvenskii, and V. L. Yur'ev. Formation of boundary disturbances during shock-wave propagation in tubes made of different materials. *Prikladnoi Mekhaniki i Tekhnicheskoi Fiziki*, (1):116–120, 1986.

[52] M. Koenig, T. Vinci, A. Bennuzi-Mounaix, N. Ozaki, A. Ravasio, L. Boireau, C. Michaut, S. Bouquet, S. Atzeni, A. Schiavi, O. Peyrusse, and D. Batani. Radiative shocks: An opportunity to study laboratory astrophysics. *Physics of Plasmas*, 13:056504, 2006.

[53] William Kruer. *The Physics of Laser Plasma Interactions*. Westview Press, 2001.

[54] C. C. Kuranz, B. E. Blue, R. P. Drake, H. F. Robey, J. F. Hansen, J. P. Knauer, M. J. Grosskopf, C. Krauland, and D. C. Marion. Dual, orthogonal, backlit, pinhole radiography in omega experiments. *Review of Scientific Instruments*, 77:10E327 1–4, 2006.

[55] C. C. Kuranz, R. P. Drake, K. K. Dannenberg, P. J. Susalla, D. J. Kremer, T. Boehly, and J. Knauer. Preheat issues in hydrodynamic HEDLA experiments. *Astrophysics and Space Science*, page 267, 2005.

[56] C. C. Kuranz, R. P. Drake, E. C. Harding, M. J. Grosskopf, H. F. Robey, B. A. Remington, M. J. Edwards, A. R. Miles, T. S. Perry, T. Plewa, N. C. Hearn, J. P. Knauer, D. Arnett, and D. R. Leibrandt. 2d rayleigh-taylor instability: experiment and simulation. *Astrophysics Journal*, 696:749–759, 2009.

[57] Carolyn C. Kuranz. *Blast-Wave-Driven, Multidimensional Rayleigh-Taylor Instability Experiments*. PhD thesis, University of Michigan, 2009.

[58] C.C. Kuranz, F.W. Doss, R.P. Drake, M.J. Grosskopf, and H.F. Robey. Using wall shocks to measure preheat in laser-irradiated, high-energy-density, hydrodynamics experiments. *High Energy Density Physics*, 6(2):215 – 218, 2010. ICHED 2009 - 2nd International Conference on High Energy Density Physics.

[59] D. Kushnir, E. Waxman, and D. Shvarts. The Stability of Decelerating Shocks Revisited. *Astrophysical Journal*, 634:407–418, November 2005.

[60] L. D. Landau and E. M. Lifshitz. *Fluid Mechanics*. Elsevier, 1987.

[61] Henry L. Langhaar. *Dimensional Analysis and Theory of Models*. John Wiley and Sons, 1951.

[62] F. C. Leone, L. S. Nelson, and R. B. Nottingham. The folded normal distribution. *Technometrics*, 3(4):pp. 543–550, 1961.

[63] M. J. Lighthill. The position of the shock wave in certain aerodynamic problems. *Quarterly Journal of Mechanics and Applied Mathematics*, 1:309–318, 1948.

[64] M. M. Marinak, G. D. Kerbel, N. A. Gentile, O. Jones, D. Munro, S. Pollaine, T. R. Dittrich, and S. W. Haan. Three-dimensional hydra simulations of national ignition facility targets. *Physics of Plasmas*, 8:2275, 2001.

[65] Ryan McClarren, R. Paul Drake, J. E. Morel, and James Paul Holloway. Theory of radiative shocks in the mixed, optically thick-thin case. *Physics of Plasmas*, 17:093301, 2010.

[66] R. L. McCrory, D. D. Meyerhofer, R. Betti, R. S. Craxton, J. A. Delettrez, D. H. Edgell, V. Yu. Glebov, V. N. Goncharov, D. R. Harding, D. W. Jacobs-Perkins, J. P. Knauer, F. J. Marshall, P. W. McKenty, P. B. Radha, S. P. Regan, T. C. Sangster, W. Seka, R. W. Short, S. Skupsky, V. A. Smalyuk, J. M. Soures, C. Stoeckl, B. Yaakobi, D. Shvarts, J. A. Frenje, C. K. Li, R. D. Petrasso, and F. H. Séguin. Progress in direct-drive inertial confinement fusion. *Physics of Plasmas*, 15(5):055503, 2008.

[67] T. Meyer. Über zweidimensionale bewegungsvorgänge in einem gas, das mit überschallgeschwindigkeit strömt. Doctoral dissertation, Georg-August Universitt, Gttingen, 1908.

[68] D. Mihalas and B. Weibel-Mihalas. *Foundations of Radiation Hydrodynamics*. Dover, 1984.

[69] A. S. Moore, E. T. Gumbrell, J. Lazarus, M. Hohenberger, J. S. Robinson, R. A. Smith, T. J. A. Plant, D. R. Symes, and M. Dunne. Full-trajectory diagnosis of laser-driven radiative blast eaves in search of thermal plasma instabilities. *Physical Review Letters*, 100:055001, 2008.

[70] R. M. More. Atomic physics in inertial confinement fusion. Technical Report UCRL-84991 Part 1, Lawrence Livermore National Laboratory, March 1981.

[71] Edward I. Moses and Craig R. Wuest. The national ignition facility: Status and plans for laser fusion and high-energy-density experimental studies. *Fusion Science and Technology*, 43(3):420–427, 2003.

[72] W. J. Macquorn Rankine. On the thermodynamic theory of waves of finite longitudinal disturbance. *Phil. Trans. R. Soc. Lond.*, 160:277–288, January 1870.

[73] A. B. Reighard, R. P. Drake, K. K. Dannenberg, D. J. Kremer, M. Grosskopf, E. C. Harding, D. R. Leibrandt, S. G. Glendinning, T. S. Perry, B. A. Remington, J. Greenough, J. Knauer, T. Boehly, S. Bouqet, L. Boireau, M. Koenig, and T. Vinci. Observation of collapsing radiative shocks in laboratory experiments. *Physics of Plasmas*, 13:082901, 2006.

[74] A. B. Reighard, R. P. Drake, K. K. Dannenberg, D. J. Kremer, B. A. Remington, C. A. Iglesias, R. J. Wallace, D. D. Ryutov, J. Greenough, J. Knauer, T. Boehly, S. Bouquet, A. Calder, R. Rosner, B. Fryxell, D. Arnett, M. Koenig, and N. Grandjouan. Collapsing radiative shocks in xenon gas on the omega laser. In *Inertial Fusions Sciences and Applications 2003*. American Nuclear Society, 2003.

[75] A. B. Reighard, R. P. Drake, T. Donjakowski, M. J. Grosskopf, K. K. Dannenberg, D. Froula nd S. Glenzer, J. S. Ross, and J. Edwards. Thomson scattering from a shock front. *Review of Scientific Instruments*, 77:10E504 1, 2006.

[76] A.B. Reighard and R. P. Drake. The formation of a cooling layer in partially optically thick shock. *Astrophysics and Space Science*, 307:121, 2007.

[77] Amy B. Reighard. *Collapsing Radiative Shock Experiments on the Omega Laser*. PhD thesis, University of Michigan, 2007.

[78] B. A. Remington, J. Kane, R. P. Drake, S. G. Glendinning, K. Estabrook, R. London, J. Castor, R. J. Wallace, D. Arnett, E. Liang, R. McCray, A. Rubenchik, and B. Fryxell. Supernova hydrodynamics experiments on the nova laser. volume 4, pages 1994–2003. AIP, 1997.

[79] G. A. Rochau, J. E. Bailey, Y. Maron, G. A. Chandler, G. S. Dunham, D. V. Fisher, V. I. Fisher, R. W. Lemke, J. J. MacFarlane, K. J. Peterson, D. G. Schroen, S. A. Slutz, and E. Stambulchik. Radiating shock measurements in the z-pinch dynamic hohlraum. *Physical Review Letters*, 100(12):125004, Mar 2008.

[80] P. L. Sachdev. *Shock Waves and Explosions*, volume 132 of *Monographs and Surveys in Pure and Applied Mathematics*. Chapman and Hall / CRC, 2004.

[81] S. D. Sadov. Deformation mechanism of a shock radiating front during its motion in a channel. *Prikladnoi Mekhaniki i Tekhnicheskoi Fiziki*, (5):30, 1989.

[82] E. B. Saloman. Energy levels and observed spectral lines of xenon, Xe I through Xe LIV. *J. Phys. Chem. Ref. Data*, 33(3):765, 2004.

[83] David Salzmann. *Atomic Physics in Hot Plasmas*. Oxford University Press, 1998.

[84] W. R. Sears, editor. *General Theory of High-Speed Aerodynamics*, volume 6 of *High Speed Aerodynamics and Jet Propulsion*. Princeton, 1954.

[85] L. I. Sedov. Propagation of strong shock waves. *Journal of Applied Mathematics and Mechanics*, 10:241 – 250, 1946.

[86] R. G. Shreffler and R. H. Christian. Boundary disturbances in high-explosive shock tubes. *Journal of Applied Physics*, 25(3):324, 1954.

[87] F. H. Shu. *The Physics of Astrophysics: Gas Dynamics.* University Science Books, 1992.

[88] D.R. Symes, M. Hohenberger, J. Lazarus, J. Osterhoff, A.S. Moore, R.R. Fustlin, A.D. Edens, H.W. Doyle, R.E. Carley, A. Marocchino, J.P. Chittenden, A.C. Bernstein, E.T. Gumbrell, Mike Dunne, R.A. Smith, and T. Ditmire. Investigations of laser-driven radiative blast waves in clustered gases. *High Energy Density Physics*, 6(2):274, 2010.

[89] Sir Geoffrey Ingram Taylor. The formation of a blast wave by a very intense explosion. ii. the atomic explosion of 1945. *Proceedings of the Royal Society of London. Series A, Mathematical and Physical Sciences*, 201(1065):175 – 186, March 1950.

[90] H. S. Tsien and M. Finston. Interaction between parallel streams of subsonic and supersonic velocities. *Journal of the Aeronautical Sciences*, 16(9):515, 1949.

[91] T. Vinci, M. Koenig, A. Bennuzi-Mounaix, C. Michaut, L. Boireau, S. Leygnac, S. Bouquet, O. Peyrusse, and D. Batani. Temperature and electron density measurements on laser driven radiative shocks. *Physics of Plasmas*, 13:010702, 2006.

[92] E. T. Vishniac. The dynamic and gravitational instabilities of spherical shocks. *Astrophysical Journal*, 274:152–167, November 1983.

[93] E. T. Vishniac. Linear and nonlinear waves in shock-bounded slabs. *New York Academy Sciences Annals*, 773:70–79, January 1995.

[94] E. T. Vishniac and D. Ryu. On the stability of decelerating shocks. *Astrophysical Journal*, 337:917–926, February 1989.

[95] Gerald Beresford Whitham. *Linear and Nonlinear Waves.* Wiley-Interscience, 1974.

[96] Ya. B. Zeldovich and Yu. P. Razier. *Physics of Shock Waves and High-Temperature Hydrodynamic Phenomena.* Academic Press, 1967.